Running-in and residual stress: finite element contact analysis of as measured rough surfaces and comparison with experiment

Michael Bryant

Thesis submitted in candidature
for the degree of Doctor of Philosophy
at Cardiff University

Tribology and Contact Mechanics Group
Institute of Mechanics and Advanced Materials
Cardiff School of Engineering
Cardiff University

July 2013

Declaration

This work has not previously been accepted in substance for any degree and is not being concurrently submitted in candidature for any degree.

Signed: _____ (candidate)

Date: _____

Statement 1

This thesis is being submitted in partial fulfilment of the requirements for the degree of PhD.

Signed: _____ (candidate)

Date: _____

Statement 2

This thesis is the result of my own independent work / investigation, except where otherwise stated. Other sources are acknowledged by explicit references.

Signed: _____ (candidate)

Date: _____

Statement 3

I hereby give consent for my thesis, if accepted, to be available for photocopying and for inter-library loading, and for the title and summary to be made available to outside organisations.

Signed: _____ (candidate)

Date: _____

Summary

The principal aim of this thesis was to investigate the contact and deformation of rough surfaces such as those found on the teeth of gears. Freshly manufactured surfaces undergo a process known as “running-in”, in which the surface geometry is altered as a result of contact under load. Plastic deformation can occur which induces significant residual stresses, and it has been suggested that these may have implications for the subsequent fatigue life of the surfaces. In this thesis, finite element analysis (FEA) has been used to perform full elastic-plastic contact analysis based on profiles from gear teeth which are used in micropitting tests in order to determine the detailed nature of deformation and the magnitude and distribution of the residual stresses.

FEA was performed using Abaqus, and the techniques were first developed using known contact problems of smooth elastic bodies. Plastic behaviour was subsequently introduced, guided by previous studies in the literature. Profiles from real surfaces were then used to study the behaviour of typical gear surfaces under load. Experiments were carried out in which the rough surfaces of crowned steel discs were loaded together, with relocated profiles taken before and after loading. The aim was to provide experimental verification of the residual deformations predicted by FEA. Good agreement was found between the analysis and experiments carried out at different loads.

Regions of surface and subsurface residual tensile stress were predicted to occur in proximity to heavily loaded asperity contacts. Greater plastic deformation resulted in increased magnitudes of residual stress. Significant residual tensile stresses were predicted in regions where crack initiation has been shown to occur in practice at depths typical of micropitting failures in gears. It is concluded that residual effects of initial plastic deformation taking place during running-in can be a significant factor in micropitting failures in gears.

Acknowledgements

I would first of all like to thank Prof. Pwt Evans and Prof. Ray Snidle, firstly for giving me the opportunity to pursue this PhD, and for their supervision and guidance ever since. This thesis would not have been possible without their continuous support and encouragement. Credit must also go to Dr. Kayri Sharif for his assistance throughout. I would also like to thank Cardiff University and in particular the School of Engineering, where I have spent a significant proportion of my time over the last four years as a postgraduate and the four years preceding that as an undergraduate. Gratitude must also go to the EPSRC, whose funding made the project possible.

My friends Russell Gay and Grant Dennis have provided both assistance and distraction, although both end in credit. Much amusement was had in our office, most of which is probably left unsaid. I would also like to thank a multitude of colleagues that I shared my time with in the research group; Amjad Al Hamood, Anton Manoylov, Ben Wright, Ingram Weekes, Matteo Carli and Sergey Khausov. All of you at some point provided insight or inspiration for me. For those of you who have already finished, congratulations, and for those still working, good luck.

Aside from my academic work, Formula Student has been a thoroughly enjoyable experience throughout my time in Cardiff, and I am eternally grateful for the memories that I will cherish for many years to come. Not only was it intensely enjoyable, but an incredible learning experience. There are too many people to name here for their contribution to that experience, but I would like to thank Lee Treherne in particular. As a mainstay of the team, he has helped make Formula Student at Cardiff what it is.

My parents have given me love and support throughout my life, and without them I would not be where I am today. I am eternally grateful for everything they have given me, and am forever indebted to them. Last but not least, I would like to thank my girlfriend Michelle who has been supportive and understanding, and put up with me during the highs and lows of this project.

Contents

Nomenclature

Symbol	Description	Units
A	Contact area	m^2
A_c	Contact area at initial yield	m^2
A^*	A/A_c	-
a	Major axis contact semi-dimension	m
a_c	Major axis contact semi-dimension at initial yield	m
a^*	a/a_c	-
b	Minor axis contact semi-dimension (elliptical contact only)	m
d	Non-contact semi-dimension (wavy surface contact)	m
E	Elastic modulus	Pa
E'	Reduced elastic modulus: $\frac{2}{E'} = \frac{(1-\nu_1^2)}{E_1} + \frac{(1-\nu_2^2)}{E_2}$	Pa
E_T	Tangential modulus	Pa
F	Tangential load	N
F_{max}	Tangential load at frictional limit (i.e. full slip)	N
G	Shear modulus	Pa
g	Standard gravity	m/s^2
H	Vickers hardness	kgf/mm^2
$L_{residual}$	Residual asperity land width	m
p	Contact pressure	Pa
p_0	Maximum contact pressure	Pa
$(p_0)_y$	Maximum contact pressure at initial yield	Pa
$\bar{p}$	Mean contact pressure	Pa
p^*	Mean contact pressure at initial complete contact of sinusoidal surface	Pa
R	Radius of hemisphere/cylinder	m
U_x	Deformation in x-direction	m
U_y	Deformation in y-direction	m
U_z	Deformation in z-direction	m
UR_x	Rotation about x-axis	rad
UR_y	Rotation about y-axis	rad
UR_z	Rotation about z-axis	rad
w	Load	N
w_c	Load at initial yield	N
w^*	w/w_c	-
w'	Load per unit length	N/m
w'_c	Load per unit length at initial yield	N/m
w'^*	w'/w'_c	-

x	Co-ordinate tangential to the contact	m
y	Co-ordinate perpendicular to the contact	m
z	Co-ordinate normal to the contact	m
γ	Shear strain	-
Δz_{avg}	Average residual asperity deflection normal to the surface	m
Δz_{max}	Maximum residual asperity deflection normal to the surface	m
δ	Contact interference for sinusoidal surface analysis	m
δ_c	Contact interference for complete contact of sinusoidal surface	m
δ^*	δ/δ_c	-
ε	Strain	-
ε_{nom}	Nominal strain	-
ε_{true}	True strain	-
ε_{true}^{pl}	True plastic strain	-
ε_{xx}	Direct strain in the x-direction	-
ε_{yy}	Direct strain in the y-direction	-
ε_{zz}	Direct strain in the z-direction	-
λ	Wavelength of sinusoid surface	m
μ	Coefficient of friction	-
ν	Poisson's ratio	-
σ	Stress	Pa
σ_{nom}	Nominal stress	Pa
σ_{true}	True stress	Pa
σ_1	Maximum principal stress	Pa
σ_2	Middle principal stress	Pa
σ_3	Minimum principal stress	Pa
σ_{vM}	Von Mises stress	Pa
σ_{xx}	Direct stress in the x-direction	Pa
σ_y	Yield strength	Pa
σ_{yy}	Direct stress in the y-direction	Pa
σ_{zz}	Direct stress in the z-direction	Pa
τ	Shear stress	Pa
τ_{xy}	Shear stress in the x-y plane	Pa
τ_y	Yield shear stress	Pa
τ_{yz}	Shear stress in the y-z plane	Pa
τ_{zx}	Shear stress in the z-x plane	Pa
ω	Contact interference	m
ω_c	Contact interference at initial yield	m
ω^*	ω/ω_c	m

Introduction

1.1. Introduction

This thesis is concerned with the contact and deformation of rough surfaces such as those found on the teeth of gears. During the initial period of operation of these machine elements "running in" rapidly occurs in which the surfaces become somewhat smoother, and this is thought to be largely the result of plastic deformation and partial flattening of the most prominent asperity features. The process is usually regarded as beneficial, but it has also been suggested that as a result of significant plastic strains the induced residual stresses may have an adverse influence on the subsequent fatigue life of the surfaces involved. In order to gain a better understanding of the residual effects of running in of engineering surfaces the thesis therefore describes a full elastic-plastic contact analysis based on profiles from gear teeth which are used in micropitting tests. This chapter introduces tribology and contact mechanics and briefly reviews the existing literature in the field of elastic/plastic contact simulation, which ranges from the study of single idealised contacts to surfaces on which roughness is present.

1.2. A brief history of Tribology

The origin of the term "tribology" is in classic Greek, deriving from *τριβοσ*, or tribos, meaning "to rub". However, the coining of the term and its usage is a relatively modern occurrence. It is widely thought to have first appeared in a committee report from the UK Government Department of Education and Science in 1966, commonly referred to as the "Jost Report" after the committee chair, Peter Jost. The report identified the possible savings that could be achieved as a result of better tribological practices (Jost 1966). The committee's report concluded that more than £500 million (approximately equivalent to £6.5 billion in 2012) could be saved by reducing maintenance,

replacements and breakdowns, increasing machine life, and reducing frictional losses, amongst others. The report officially defined tribology as:

> *"The science and technology of interacting surfaces in relative motion and the practices related thereto."*

While this may have been the birth of the terminology, to say that this was the birth of tribology itself would be untrue. Indeed, tribological concepts have been implemented by mankind over thousands, if not hundreds of thousands, of years. Ancestors of modern humans, for example, used heat generated by friction to create fire. Estimates of when this first occurred range from 200,000 to 1.5 million years ago (James 1989). In more recent history, evidence of the use of tribological principles can be found in ancient Egypt, using lubrication (Dowson 1979a) and rolling elements (Carnes *et al*. 2005) to aid the transport of statues and blocks of stone. In Europe, some of the earliest evidence on the use of gears around the second century can be seen in the Antikythera mechanism (Freeth *et al*. 2006), while Roman ships from approximately AD50 have been found with evidence of tapered rolling element bearings (Hamrock and Anderson 1983).

During the Middle Ages technological advancements slowed before the emergence of Leonardo da Vinci (1452-1519), a man of great artistic as well as technical genius. Da Vinci studied a number of the concepts and principles that are now considered as tribological, such as friction, wear and bearings (Dowson 1977). He was the first to discover laws of friction that are still recognisable today; the link between normal and frictional load, and the lack of dependence on apparent contact area. He also investigated wear patterns and designed bush and rolling element bearings, including the necessity of a cage to separate elements.

It was almost two hundred years before advancements of da Vinci's work occurred, with Guillaume Amontons (1663-1705) in France, where the development of machinery was gaining momentum. His interest was in machines and he even claimed to have designed an engine with the power of thirty-

nine horses using air expansion to force water to rotate a wheel (Bowden and Tabor 1964). His research resulted in the defining of the laws of friction that we still recognise today (Amontons 1699):

Amontons' 1st Law - Frictional force is proportional to the normal load.

Amontons' 2nd Law - Friction is independent of the apparent contact area.

A third law, known as Coulomb's Law is also still in use today (Teer and Arnell 1975a):

Coulomb's Law – Kinetic friction is nearly independent of the speed of sliding.

Charles Augustin Coulomb (1736-1806) was one of many who followed Amontons' work due to scepticism over his second law. Nonetheless, Coulomb's work confirmed and strengthened these findings. Many of the friction theories in France depended upon contact and interaction of asperities, while in England, Jean Theophile Desaguliers (1683-1744) was a proponent of the idea of adhesion of surfaces causing friction, noting that polished surfaces do not slide more easily as might be expected.

Later, almost simultaneously, Nikolai Petrov (1836-1920) and Beauchamp Tower (1845-1904) experimentally investigated lubricated bearings. Petrov (1883) found that viscosity was a crucial lubricant property, as well as the relationship between frictional force and bearing area and clearance as well as sliding speed. Meanwhile, experimentation by Tower (1883; 1885) proved for the first time that lubricant could completely separate surfaces moving relative to one another, i.e. full-film hydrodynamic lubrication. Just a few years later, Osborne Reynolds (1842-1912) used the Navier-Stokes equation to provide the theory behind the experimental findings (Reynolds 1886). This resulted in the following equation, known as the Reynolds equation:

$$\frac{\partial}{\partial x}\left(\frac{\rho h^3}{\mu}\frac{\partial p}{\partial x}\right)+\frac{\partial}{\partial y}\left(\frac{\rho h^3}{\mu}\frac{\partial p}{\partial y}\right)=6U\frac{\partial(\rho h)}{\partial x}+12\frac{\partial(\rho h)}{\partial t}$$

While such work in lubricated contacts was evolving, Heinrich Hertz (1857-1894), perhaps more widely known for his research on electromagnetic waves, published work on the dry contact of

elastic solids (Hertz 1882). Hertz used interference phenomena as a result of the change in geometry of glasses lenses to determine contact stresses and deformations. His work is based upon several assumptions; that the contact area is small compared to the radius of relative curvature, and the size of the contacting bodies, and that the contact is frictionless. The results of his research still provide the basis for studies on non-conforming contacts today.

Developments in lubrication continued with widespread use of the Reynolds equation (Williams 1994). Arnold Sommerfeld (1868-1951) gave an approximation for lubrication pressure distribution in journal bearings (Sommerfeld 1904) and Anthony Michell (1870-1959) and Albert Kingsbury (1863-1943) who independently, but concurrently developed thrust pad bearings (Michell 1950; Kingsbury 1914).

The hydrodynamic lubrication effect in such bearings is considered to completely separate the surfaces. Sir William Bate Hardy (1864-1934) investigated “dry” or “greasy” surfaces (Hardy and Doubleday 1922) and was the first to coin the term “boundary lubrication” (Dowson 1979b). It was found that even the smallest amount of lubricant between surfaces could significantly reduce the friction between them. The effects of boundary lubrication on friction between bodies have since been studied extensively, and most famously, by Bowden and Tabor (1950; 1964).

In the bearing applications that the Reynolds equation had been applied to, the contacts were highly conformal. In applying the same methods to non-conformal contacts such as those found in gear tooth contacts or in rolling element bearings, conditions suggested film thicknesses smaller than the scale of surface roughness, or even the size of lubricant molecules (Williams 1994). Despite this, components experiencing such conditions operated successfully with little evidence of surface distress. A solution to this apparent inconsistency was first proposed by Grubin and Vinogradova (1949) who combined the effects of pressure on lubricant viscosity and elastic deformation of surfaces into the earliest theory of elastohydrodynamic lubrication (Whomes and Halling 1975). Further significant developments of elastohydrodynamic lubrication theory were made by Dowson

and Higginson (1959). More recently the subject has benefitted from the use of high speed computers which have enabled the introduction of the real effects of non-Newtonian lubricant behaviour and, most importantly, the presence of roughness which is present on real engineering surfaces. An excellent review of the topic has recently been given by (Lugt and Morales-Espejel 2011).

1.3. Review of relevant literature

1.3.1. Introduction

One of the key issues facing tribology is the drive to reduce frictional losses as energy efficiency becomes more critical. As a result less viscous lubricants will be required in hydrodynamically lubricated bearings causing thinner lubricant films, resulting in bearings which no longer operate under full film conditions, but in a state of "mixed lubrication" in which there is a significant interaction, and possibly direct contact, between asperity features on the two opposed rough surfaces. Therefore, it will become increasingly important to consider the nature of such contacts and their potential effects on the condition of the surface, and the life of machine elements such as bearings and gears. Various techniques, both experimental and theoretical, can be used in the study of rough surfaces and their contact under both dry and lubricated conditions.

The work described in this thesis was concerned with the detailed behaviour of asperity/asperity contacts under both elastic and elastic-plastic conditions using finite element (FE) simulations. The ultimate aim of this study was to investigate the effect of loaded contact on the residual stresses retained in the surface and subsurface material once the load was removed. Subsequent analysis to assess the relationship between residual deflection and residual stresses and the potential for connotations on surface fatigue life could then be considered.

In this section, the literature relating to surfaces and their contact is reviewed, focussing upon areas particularly relevant to this work. This encompasses both tribological problems, and the methods

used to solve them. Currently, little work exists regarding the contact analysis of real rough surfaces. Many studies have been performed considering single asperity contacts, before being extended in statistical models, while idealised rough surfaces have also been studied. Neither of these gives a truly representative account of the interaction between asperity contacts of surfaces typically found on ground gears. The work in this thesis will therefore aim to develop robust contact analysis techniques, allowing this kind of situation to be analysed further.

1.3.2. Individual contacts

1.3.2.1. Circular and elliptical contacts

The basis for contact mechanics theory originates from the research of Hertz on the elastic contact of semi-infinite bodies. When studying optical interference fringes, Hertz (1882) considered the deformation of the glass lenses under an applied load, as shown in Figure 1.1. He solved the problem of elastic non-conforming contacts, and obtained simple expressions for the contact stresses and deformations, subject to the following assumptions:

- Contact surfaces are continuous and non-conforming.
- The strains as a result of the loaded contact are small.
- Each contact body can be considered as a perfectly elastic, infinite half space.
- Contact surfaces are frictionless.
- The shape of the surfaces in the region of their contact is paraboloidal.

Hertz found that in general, contacts are elliptical in shape and the contact pressure distribution is semi ellipsoidal. This form of pressure distribution is now widely referred to as “Hertzian”. Much of the work in contact mechanics has essentially been directed towards eliminating the simplifications in Hertzian contact theory.

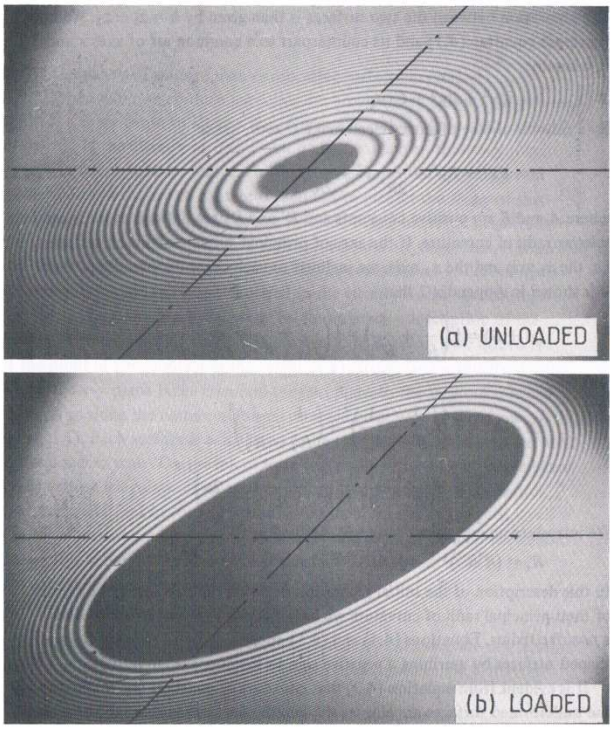

Figure 1.1 - Interference fringes at the contact of two equal cylindrical lenses with their axes inclined at 45°: a) unloaded, b) loaded (Johnson 1985).

Much of the early research on single point contacts loaded beyond the elastic limit was driven by interest in the Brinell hardness test, in which a hard steel ball is pressed normally on the surface of interest. This resulted in a number of studies focussed upon the indentation of a soft half space by a harder, or rigid, spherically-tipped indenter.

Ishlinksky (1944) solved the problem of a rigid sphere indenting a purely plastic half space, and a number of studies followed considering elastic-plastic behaviour (Hardy *et al*. 1971; Lee *et al*. 1972; Follansbee and Sinclair 1984; Sinclair *et al*. 1985; Hill *et al*. 1989). Finite element techniques were used to simulate the loading of a rigid sphere into an elastic-plastic half space, over a range of loads, using experimental results obtained by Tabor (1951) and Johnson (1968), but also from the experiments of the authors themselves. Several patterns in behaviour were found to occur in these early studies. As the load was increased, contact pressures were found to evolve from a Hertzian distribution to a flatter, more rectangular shape, as shown in Figure 1.2. The region of yielding material was found to grow, leaving a small region of elastic material at the surface in the centre of

the contact, surrounded by plastic material. This can be seen in Figure 1.3, where N/N^* is the ratio of applied load to the load to cause initial yield, and in Figure 1.2 where σ_z/τ_{yp} is the contact pressure normalised by the yield point shear strength. After the load was removed residual negative deflections were found to occur, with positive displacements occurring just outside the contact region.

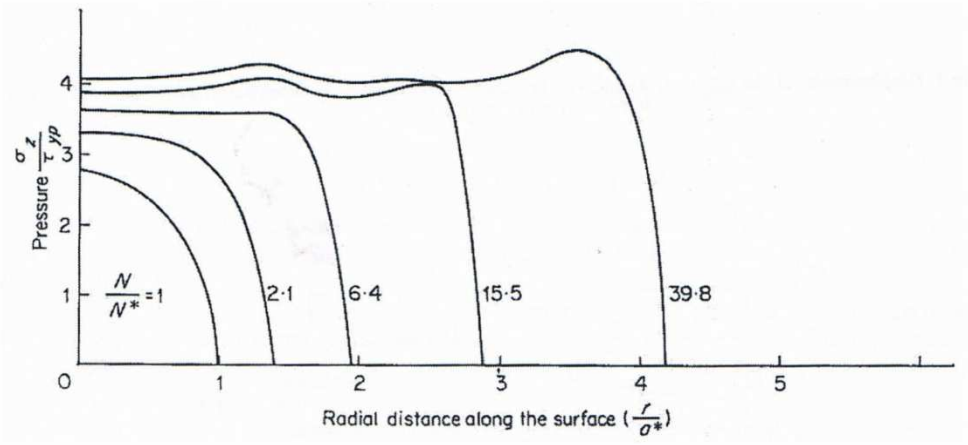

Figure 1.2 - Pressure distribution in the contact area (Hardy *et al*. 1971).

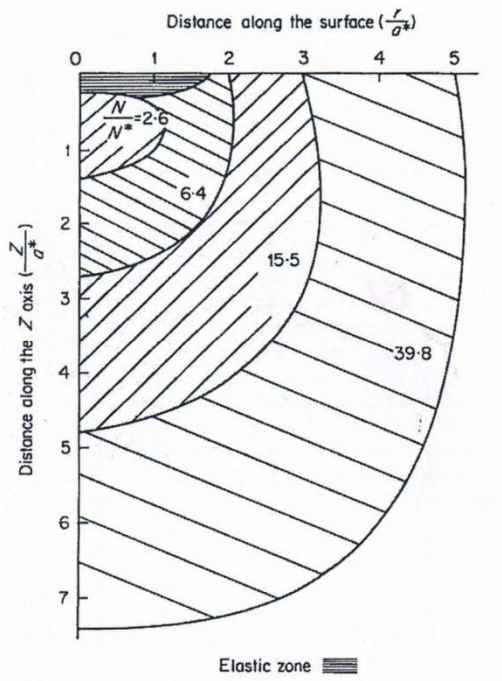

Figure 1.3 - Progressive yielding of the half space under loading conditions. The elastic zone is shown around the origin (Hardy *et al*. 1971).

Kral *et al*. (1993) used the commercially available finite element software package Abaqus to simulate a similar indentation problem, whilst also investigating the effect of varying elastic and plastic properties by changing the elastic modulus and strain hardening behaviour. Similar trends were found to occur as previously mentioned, while little difference was found to occur due to the changes made to the elastic properties. However, introducing strain hardening resulted in higher peak contact pressures and smaller contact areas. Also investigated was the effect of repeated loadings. The size and shape of the yielding areas were not found appreciably to change with subsequent loadings, although small amounts of further plastic strain were found to occur. The authors later extend the analysis to consider the indentation of layered materials (Kral *et al*. 1995a; Kral *et al*. 1995b). The additional, stiffer surface layers resulted in contact pressures peaking at the edge of the contact, and also resulted in increased stresses at the layer interface. Kulkarni *et al*. (1990; 1991) performed work investigating multiple rolling contacts, and it was found that most plastic behaviour occurred during the first load cycle. In their comparison of elastic-perfectly plastic and strain hardening materials, higher peak stresses were found to occur in the materials with strain hardening properties.

As part of wider research into powder compaction, Mesarovic and Fleck (1999; 2000) investigated a wider range of axisymmetric contact scenarios. These included the contact of a deformable sphere with deformable and rigid spheres and half spaces, as well as the indentation of a deformable half space with a rigid spherical indenter as already discussed. The results show that the case of a rigid indenter contacting a deformable half space, and a deformable sphere pressed into a rigid flat, are different. As a result, the increasing research into elastic-plastic asperity contact for incorporation into Greenwood and Williamson (GW) stochastic-type models (Greenwood and Williamson 1966) has concentrated on the contact of deformable spheres rather than rigid indentation. Chang *et al*. (1987) (CEB model), Chang (1997) and Zhao *et al*. (2000) (ZMC model) mathematically manipulated the behaviour in the elastic-plastic regime to complete the transition between classical purely elastic and plastic contact behaviour for implementation in statistical models of rough surface contact. This

section of the chapter is concerned with individual contacts, so aspects of these studies, and those to be discussed, focussing upon the statistical models, can be found in Section 1.3.3.1.

An alternative commercially available finite element software package, ANSYS was used by Kogut and Etsion (2002) to study the contact of a deformable steel sphere with a rigid flat. The elastic-plastic behaviour of the deformable steel was determined by the von Mises yield criterion, while the yield strength varied as a proportion of the elastic modulus, which was not explicitly stated. Load was applied in the form of a specified interference, or approach distance. The maximum interference applied was 110 times that for first yield (the critical interference). As previously found in indentation studies, as the load was increased, and the amount of plastic material increased, a small region of elastic material remained at the surface in the centre of the contact. This elastic region eventually disappeared at a sufficiently high interference. The authors then compared results of the study against the mathematically manipulated elastic-plastic regimes proposed by Chang *et al*. (1987) and Zhao *et al*. (2000) in their statistical models. The constant mean contact pressure of plastic contacts assumed in the CEB model was criticised, while the ZMC models results were found to provide a good approximation to the finite element analysis, but predict a fully plastic contact occurring at a lower load. Both models were found to overestimate contact size after a critical interference ratio of around 30. Based on curve fit data, two discontinuous empirical formulations were defined for the relationships between interference and contact load and contact dimension.

In a subsequent study, Etsion *et al*. (2005) investigated the residual effects of loading single spherical asperities. Also investigated was a range of materials to determine the validity of normalising parameters against critical values at initial yield. In this study, a small amount of linear strain hardening was used to ensure better convergence of the solutions. The dimensionless model presented suggests a consistent behaviour across the materials tested. In the contact itself, the size of the residual indentation as result of the contact was smaller than the loaded contact dimension, as would be expected. Additional regions of yielding material were found to occur at the edge of the

contact at the surface after heavy loading. The authors also suggest that the unloading phase is fully reversible upon subsequent application of the same interference. Preliminary testing of repeated loading indicated that this was the case, but further investigation was proposed.

A further investigation was carried out by Kadin *et al*. (2006a). It was found that the majority of plastic flow occurs during the first loading. For high values of interference, some yielding occurs in the first unloading as previously discussed. Subsequently, even in the second load cycle, the material remains fully elastic. A range of materials was tested as before, and this behaviour was found to be typical. Changing material properties such as Poisson's ratio and strain hardening behaviour resulted in changes in material yield in the unloading phase. A suggestion of future work was the introduction of kinematic hardening behaviour rather than isotropic, which is thought to be a factor in reducing plasticity in subsequent load cycles.

Two studies by Jackson and Green (2005) and Jackson *et al*. (2005) also investigated the loading and unloading of a single asperity contact, respectively. A similar finite element model was created using ANSYS, contacting a deformable sphere with a rigid flat using a specified interference. The sphere was then moved away from the rigid flat to obtain residual results. Typical elastic material properties of steel were used, with a range of yield strengths tested. Finite element results were found to follow Hertzian behaviour at small interferences, diverging once plastic behaviour became more dominant. Good agreement was generally found with the empirical formulations of Kogut and Etsion (2002), (KE), albeit with a discontinuity. As previously discussed, the ZMC model predicts a fully plastic contact prematurely. These comparisons can be seen in Figure 1.4. It was also found that the average contact pressure was limited to approximately $2.84\sigma_y$ as indicated by Williams (1994), or approximately $3\sigma_y$ as stated by Tabor (1951). However, for higher yield strength materials, this limit was found to be lower, ranging from $2.7\sigma_y$ to $2.4\sigma_y$ as yield strength increased. The authors attributed this behaviour to the evolution of the contact geometry, as the deformable sphere tended towards a deformable blunt rod. Again, empirical formulations were determined for the

relationships between key parameters, interference, load and contact area as well as average contact pressure.

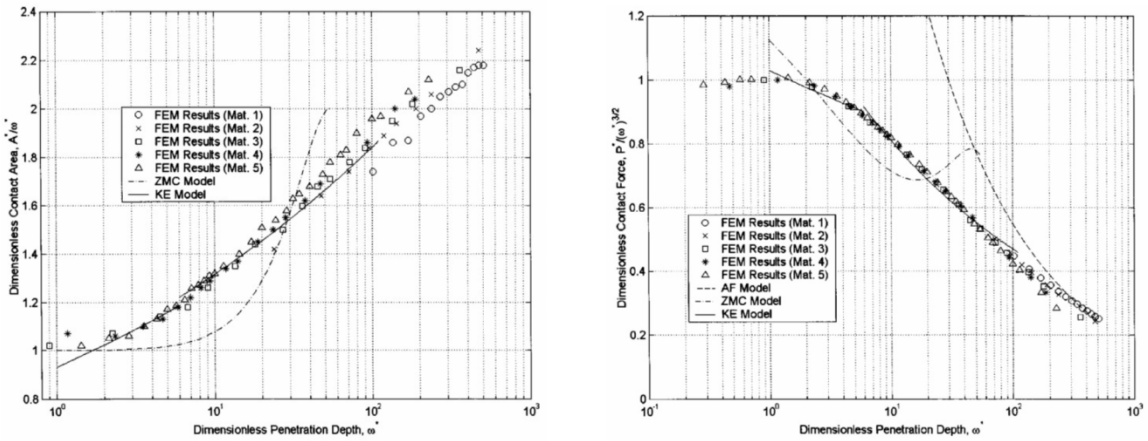

Figure 1.4 – FEM predicted contact area (left) and contact force (right) (Jackson and Green 2005).

In the study of residual effects (Jackson *et al*. 2005), the magnitude of negative residual deformations were found to be highly dependent on the loaded displacement, as would be expected. Furthermore, increased loaded displacement resulted in increased positive residual deformation, or pile up, at the contact edge. Also discussed were the residual stresses found in the material of the deformable sphere. Regions of tensile radial stresses were found to occur at the surface in the region of the contact edge, aligned with the regions of residual pile up. A region of subsurface tension was also found directly beneath the surface. Tensile axial stress was also found slightly beneath the surface at the edge of the contact. These stress distributions can be seen in Figure 1.5.

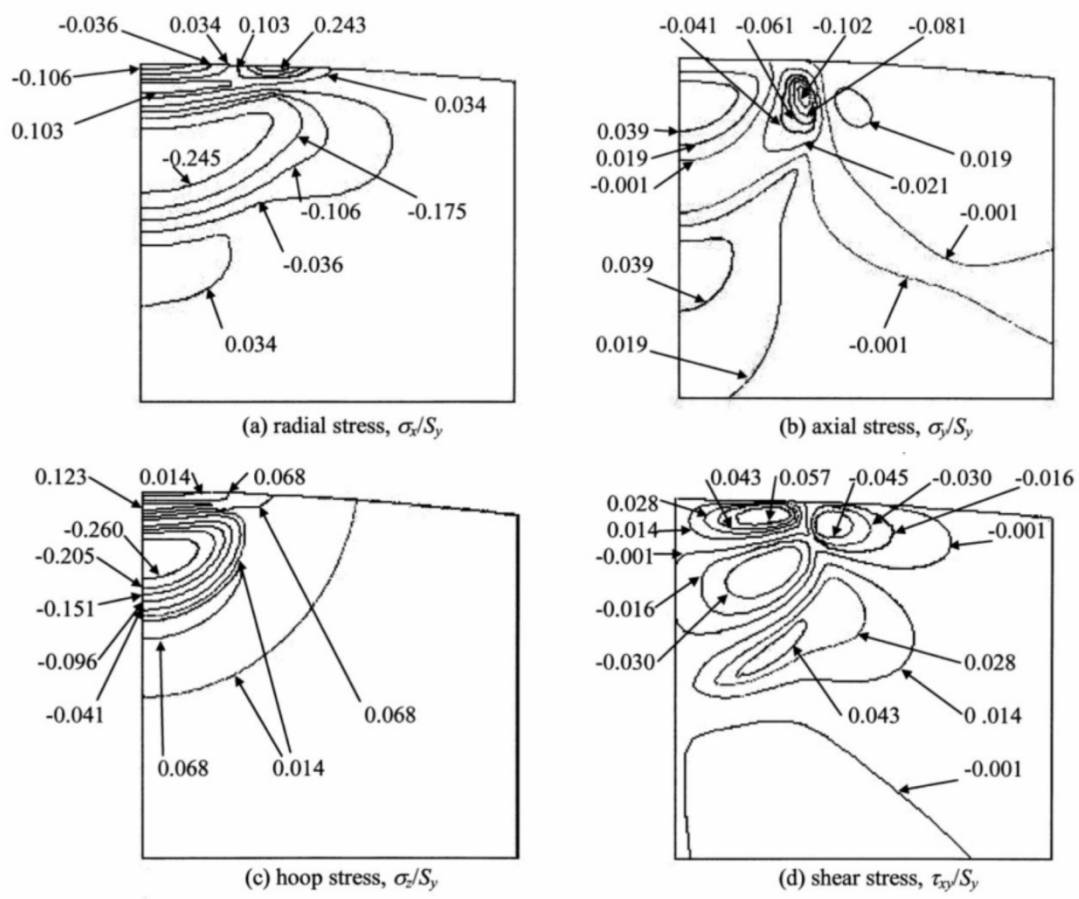

Figure 1.5 - Contour plots of the complete stress tensor for a hemispherical contact unloaded from $\omega^* = 3.92$; a) radial stress σ_{xx} / σ_y, b) axial stress, σ_{yy} / σ_y, c) hoop stress, σ_{zz} / σ_y, d) shear stress, τ_{xy} / σ_y (Jackson *et al*. 2005).

Another group studying single spherical contacts looked more specifically at the effect of strain hardening (Shankar and Mayuram 2008a; 2008b). The first study directly compared results to those achieved by Kogut and Etsion (2002) and Jackson and Green (2005). Differences were found to occur primarily in the interferences required to cause the region of surface elastic core to emerge, and subsequently disappear. Aside from this, good agreement was generally found to occur, in particular with Jackson and Green. Upon introduction of linear strain hardening, contact pressures could exceed the proposed limits of $2.8\sigma_y$ to $3.0\sigma_y$. Small differences in contact areas and the emergence and disappearance of the surface elastic core were also founded to occur. An experimental validation of the analysis techniques used was performed using a rigid indenter model (as opposed

to the deformable sphere model described). Aluminium and brass specimens were indented using a hard ball, and material properties imported to ANSYS. Good agreement was shown between experimental and finite element results, as shown in Figure 1.6.

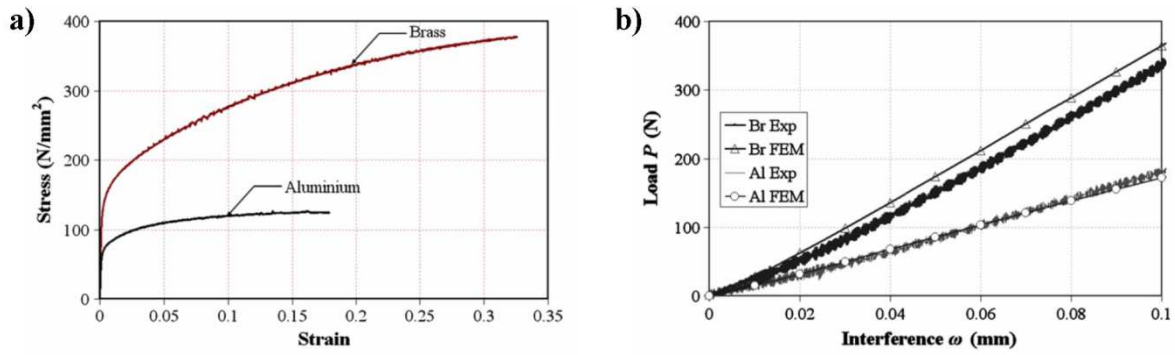

Figure 1.6 - a) Stress-strain curve for the tested base specimens, b) Comparison of the FEM and experimental contact load results (Shankar and Mayuram 2008b).

Ovcharenko *et al*. (2007) performed an experimental study, contacting copper and stainless steel spheres against a sapphire flat. Testing of the materials showed that the materials approximated elastic-perfectly plastic and linear strain hardening materials respectively. A microscope and CCD camera set up allowed images to be taken *in situ*, giving images of contact areas during the loading and unloading phases. Loaded and residual results showed good agreement with results obtained by Kogut and Etsion (2002) and Etsion *et al*. (2005), respectively. When the spheres were first unloaded, discrepancies were founded to occur however. The authors attributed this to the change in the loading relationships in the residual study. However, the original relationship proposed a discontinuity in behaviour that seems counterintuitive, and so the revised relationship appears more appropriate. Under cyclic loading, the steel specimens took approximately five loadings before insignificant additional growth in residual contact area occurred. For copper specimens this took more than the ten cycles shown. This is in contrast to the findings of Kadin *et al*. (2006a). The authors proposed this difference to be in the perfect slip contact condition of the finite element study, although the defined plastic materials constants could also be a source of the differences.

Another experimental study was performed by Jamari and Schipper (2006b), who subsequently used the mathematically manipulated elastic-plastic regime proposed by Zhao *et al*. (2000) to study the loading and unloading of spherical contacts (Jamari and Schipper 2006a; 2007). Copper and aluminium spheres were loaded against a silicon carbide flat, with surface measurements taken by an optical interference microscope before and after loading. Loads were such that the results were predominantly in the plastic region only. Results were compared with model predictions of Abbott and Firestone (1933), Chang *et al*. (1987)and Jackson and Green (2005) (AF, CEB and JG). Agreement between these models and the experimental data was relatively poor, as can be seen from Figure 1.7. The experimental data seem to show a constant mean contact pressure in agreement with that of the AF and CEB models. However, some reservations have been expressed by Jackson and Green (2007), concerning measurement of contact dimension from residual surface measurements and the calculation of the yield strength in the JG model.

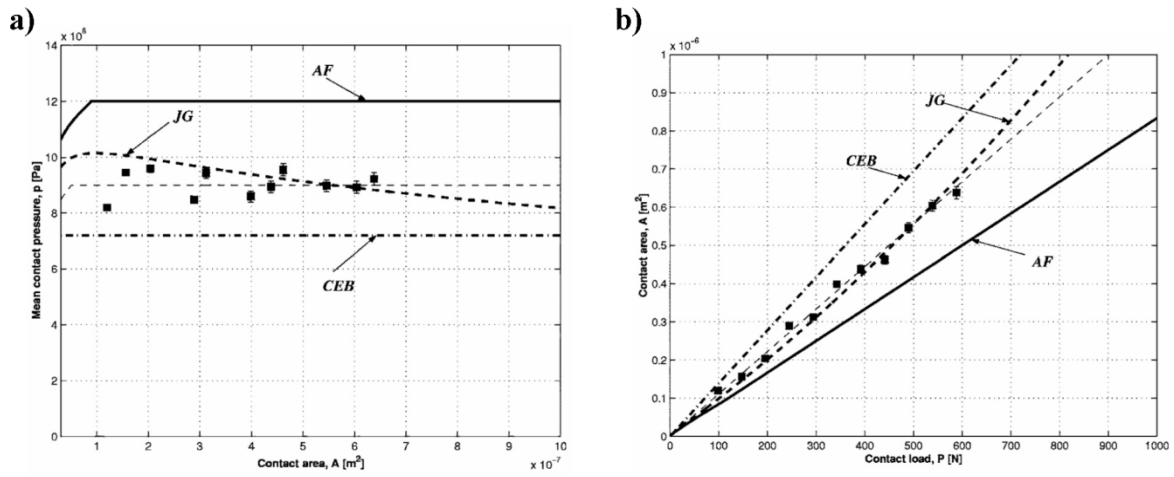

Figure 1.7 - a) Mean contact pressure versus contact area, b) Contact area as a function of normal load. Plotted points (▪) are experimental data (Jamari and Schipper 2006b).

Jamari and Schipper (2006a) then developed a theoretical model based on the approach to the elastic-plastic regime of Zhao *et al*. (2000), using the experimental results of Chaudhri *et al*. (1984) for validation, rather than their own, to include contacts in the elastic and elastic-plastic regions. These experiments contacted phosphor-bronze and brass spheres with a flat of sapphire. For each

material the author's model provided the best agreement with the experimental data. For the softer phosphor-bronze, the JG model had the best approximation of those considered. For the harder brass, each of the models considered were more tightly grouped, with the KE model providing the closest predictions.

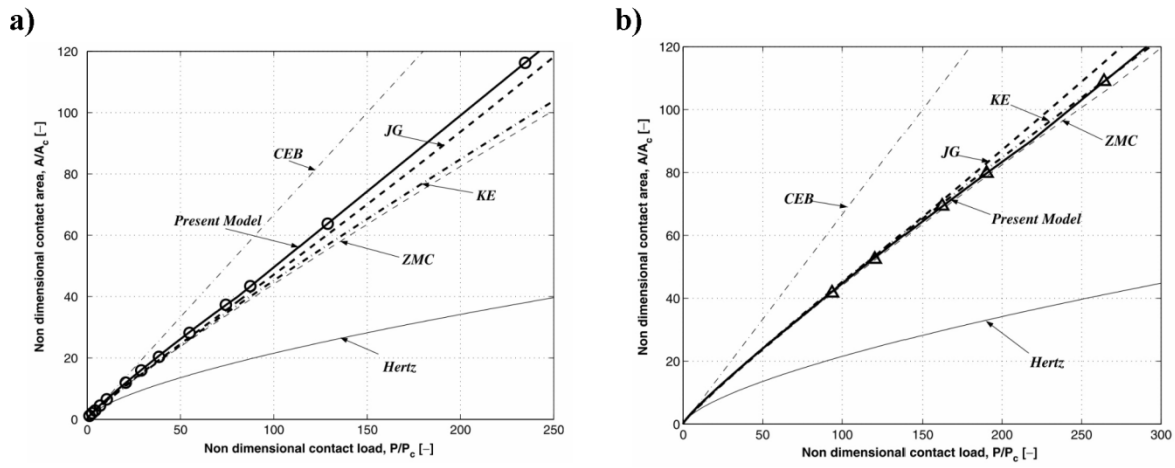

Figure 1.8 - Non-dimensional contact area versus non-dimensional contact load; a) phosphor-bronze, b) brass. ○ and Δ are experimental data (Jamari and Schipper 2006a).

In the residual study, Jamari and Schipper (2007) compared their theoretical residual results against those found in their own experimental study using copper and aluminium spheres. As before, better agreement was found in the comparisons between the proposed model and experimental results using the harder material, in this case aluminium, as can be seen in Figure 1.9.

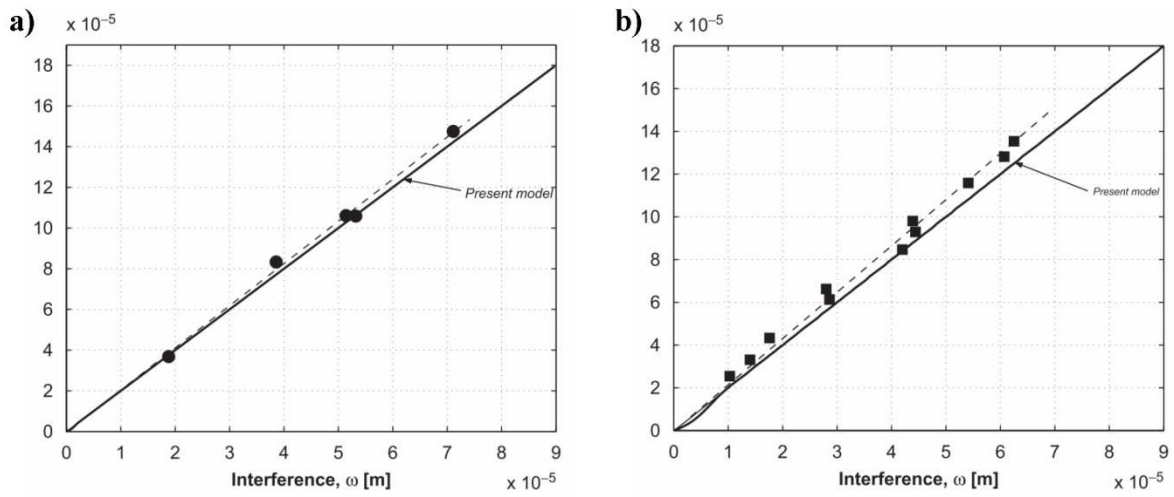

Figure 1.9 - Plastic contact area versus interference of spheres; a) aluminium, b) copper. • and ▪ are experimental data (Jamari and Schipper 2007).

The contact of a deformable sphere is essentially a special case of an elliptical contact whereby the two contact semi dimensions are equal. The problem of the contact of a deformable ellipsoid is significantly less frequented in the literature. When considering finite element analysis, this may be due at least in part to the requirement of modelling in three dimensions. A spherical contacting body can be modelled using two dimensional axisymmetric elements. At least ¼ of the ellipsoid surface must be modelled in three dimensions, with symmetrical boundaries along the major and minor axes. Therefore, significantly more elements and nodes are required to analyse the problem, increasing computational resource requirements. Nonetheless, the directionality of many machining processes means that asperities are unlikely to be ideally shaped point or lines contacts. Therefore, elliptical contacts should not be neglected.

Lin and Lin (2006) first studied spherical contacts using ANSYS, and later extended their work to investigate the contact of ellipsoids (2007). Some of the findings are relatively intuitive. For example, for a more elongated elliptical body, the contact area is more elliptical too. However, at low interferences, the contact area was found to be more elliptical than the contacting body. For elliptical bodies of ratios 1 (spherical), 0.5 and 0.2, the ellipticity of the contact area was 1, 0.4 and 0.126 respectively. With increasing load, the ellipticity of the contact tends towards that of the body.

Contact pressures are found to be higher in more spherical contacts, while larger interferences are required for more eccentric elliptical bodies to cause transition from elastic to elastic-plastic and elastic-plastic to fully plastic regimes. Chung (2010) shows the evolution of elliptical contacts, tending from spherical contacts to line contacts, as material yield initially occurs at larger depths in more eccentric elliptical contacts.

Much of the research in this area has utilised the finite element method and commercially available finite element analysis software packages. Other methods have also been developed, such as those used by Hu *et al*. (1999) and Wang *et al*. (2010). Each of these studies used a numerical method based on fast Fourier transforms, minimisation of complementary energy and the conjugate gradient method. Initially, the method was tested using a purely elastic model, using known results from the Hertzian contact solution for contact pressure and subsurface stress distributions (Hu *et al*. 1999). Elastic-plastic behaviour was later considered, from finite element analysis results using Abaqus as a validation method. Good agreement was found between the numerical method and finite element for a variety of parameters including contact dimensions and pressures, loaded and residual von Mises stress distributions, and displacements. The largest discrepancies were found for elastic-perfectly plastic material in regions of plasticity.

Wang and Keer (2005) also developed a semi-analytical method, although this was used to investigate the indentation of a deformable half space by a rigid indenter. A range of strain hardening materials was used, and it was found that an increased tangent modulus resulted in increased stresses and reduced contact areas. Chen *et al*. (2008) extended the study to repeated indentations of a deformable half space. Kinematic hardening behaviour was defined. Most plastic deformation occurred in the first load cycle, with increasingly small additional plastic strain in subsequent load cycles. Details of the techniques used were published by Liu *et al*. (2000).

A number of studies have also been performed examining sliding and rolling contacts of individual spherical bodies. These have used finite element analysis (Faulkner and Arnell 2000; Mulvihill *et al*.

2011), semi-analytical methods (Boucly *et al*. 2007) and combinations of the two (Jackson *et al*. 2007). Common findings include asymmetric distributions of normal and shear forces when normal axes are aligned. Forces are typically found to be higher in the first half of the sliding cycle. Increasing friction coefficient increases shear forces, but normal forces remain relatively unchanged.

1.3.2.2. Line contacts

Circular point contacts and line contacts are the two extreme limits of elliptical contacts; one where the principal radii are equal, and the other where one radius is infinite. While much research has been performed on circular point contacts, as already discussed, contact of cylinders and line contacts have been less extensively researched. However, as previously stated, the directionality of many machining processes (such as grinding, extensively used to finish the teeth of gears) means that asperities of long elliptical shape are perhaps more applicable to the study of rough surface contacts in practice. A line contact is an approximation to a highly eccentric elliptical contact, but with simpler contact geometry and is less computationally intensive. This section will discuss studies that have focussed upon this contact configuration.

Hertz (1882) considered a line contact to be the limiting case of an elliptical contact when the major axis contact dimension became very large compared to the minor axis contact dimension. Johnson (1985) considers the configuration as a problem in its own right, and solves the elastic problem, deriving formulae for contact dimension, contact pressure distribution and the subsurface stress distributions as in Figure 1.10.

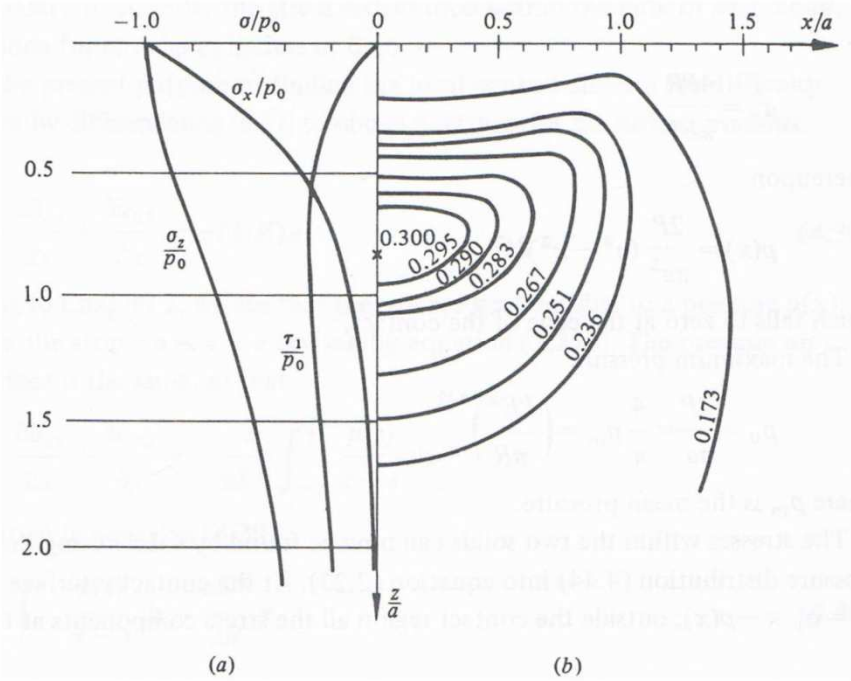

Figure 1.10 - Contact of cylinders: a) subsurface stresses along the axis of symmetry, b) contours of principal shear stress (Johnson 1985).

Similar indentation studies to those discussed for rigid spheres have also been performed considering a rigid cylinder in contact with a deformable half space, with researchers generally choosing to use the finite element method. Akyuz and Merwin (1968) were one of the first to do so, noting significant flattening of the contact pressure profile, deviating from the elliptical Hertzian distribution as the load was increased as shown in Figure 1.11. This is behaviour found also in spherical body contacts. However, the study only covered loads such that the plastically deforming region was confined beneath the surface.

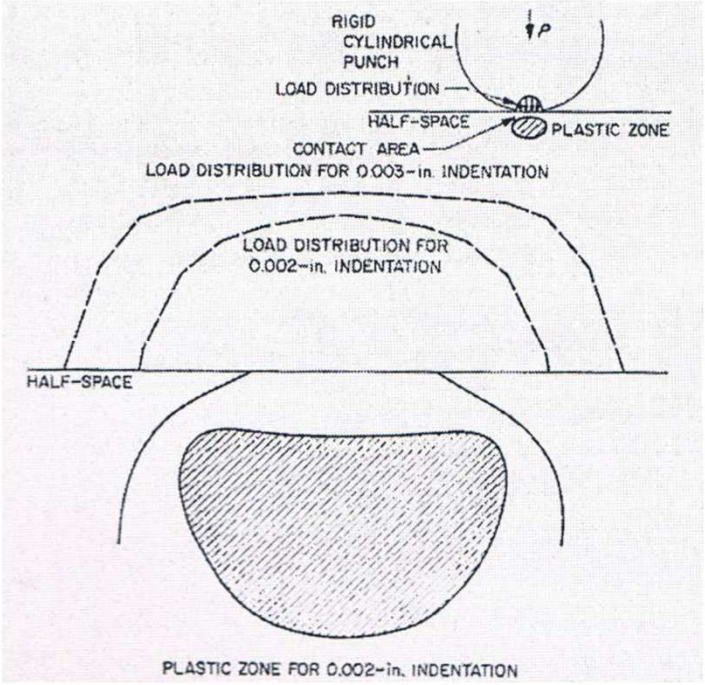

Figure 1.11 - Load distribution and plastic zone in plane strain state for rigid circular punch of R = 50 in (Akyuz and Merwin 1968).

The indentation problem was also studied by Lee and Kobayashi (1970). Dumas and Baronet (1971) and Lin and Tseng (1998). Similar patterns of behaviour were found to those already discussed for a rigid spherical indenter. In the elastic-plastic regime, a small region of elastic material was found to remain at the surface at the centre of the contact. This was then found to disappear in materials with strain hardening behaviour. Strain hardening behaviour also resulted in relatively larger contact pressures and loaded stresses, but reduced contact areas and residual deformations and stresses.

Tian and Saka (1991) extended the indentation problem by considering a multi layered deformable half space, consisting of layers of gold, nickel and copper as found in electrical contacts. The gold top layer and copper substrate thicknesses were maintained while the nickel interlayer thickness was varied. Contact pressures distributions were found to be dictated by the degree of plasticity, which in turn was found to depend upon the thickness of the interlayer. The distribution became flatter for increasing thickness, before becoming reduced again for the maximum thickness tested. For thinner layers, the layer interface faces act as stress raisers, and plastic strains can be seen to occur in their

vicinity. For the thickest interlayer, it is sufficiently far away that only small amounts of plasticity occur between the top two layers.

For spherical contacts, Mesarovic and Fleck (2000) showed that the case of a rigid indenter and deformable half space differed from that of a deformable body and rigid flat. Unfortunately, no equivalent study for a line contact has been found but it would not be unreasonable to expect similar findings. Liu *et al*. (2001) initially studied the contact of a deformable cylinder with a rigid flat in order to validate their theoretical model, before analysis of rough surfaces. The Hertzian solution was used for elastic contact validation, while for elastic-plastic behaviour, finite element analysis was used. Good agreement was found for their model for elastic and elastic-plastic behaviour.

Much of the analysis of the contact of cylinders is concerned with rolling contacts. One of the first of these studies was performed by Merwin and Johnson (1963), who investigated repeated loading of a rigid cylinder on an elastic-plastic half space. For loads below a defined shakedown limit, only small increases in residual stress were found to occur after the first loading cycle. For loads above this shakedown limit, larger increases were found to occur in subsequent cycles. However, these residual stress increases were restricted to a narrow band of the region in which they first occurred, as shown in Figure 1.12.

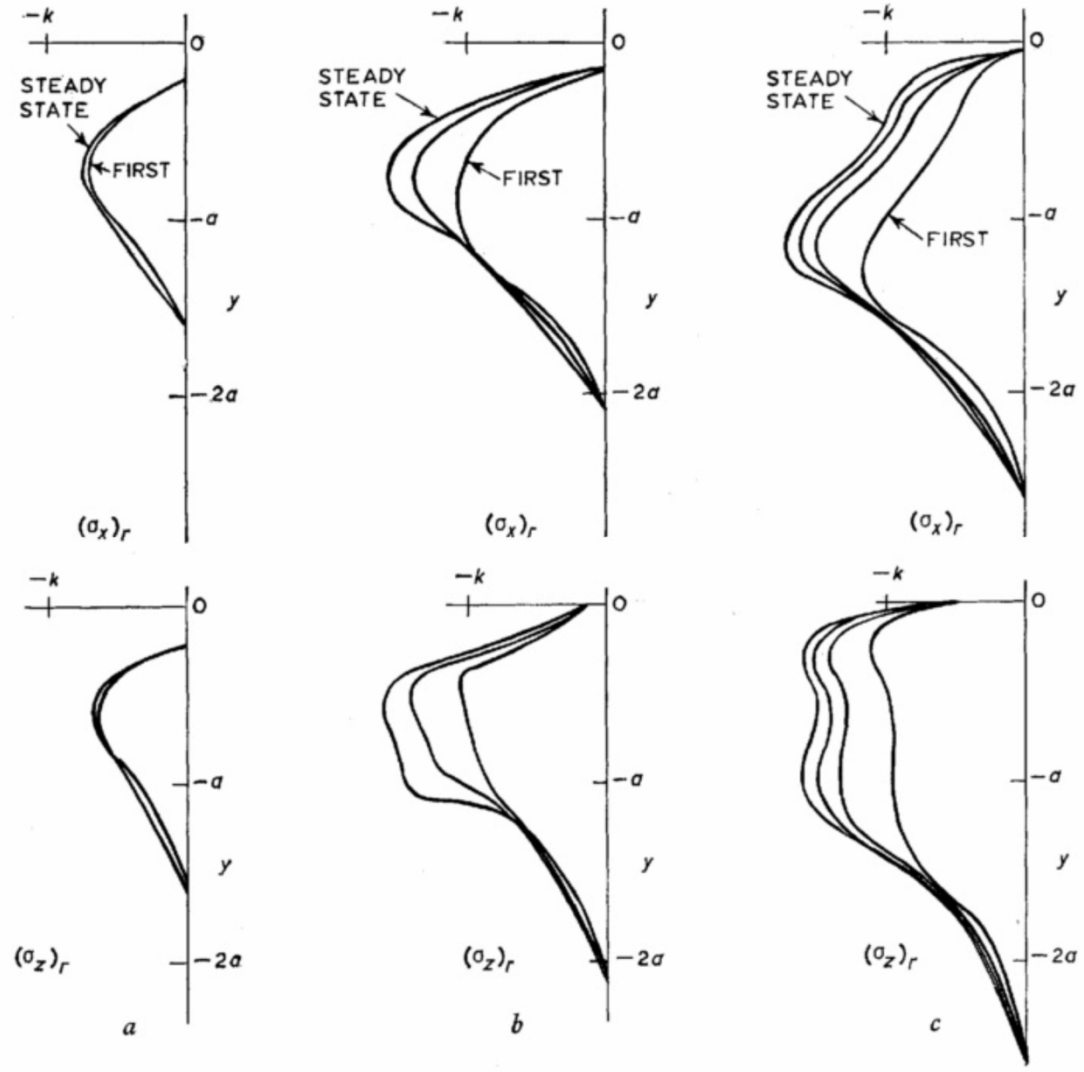

Figure 1.12 - Build-up of residual stress $(\sigma_x)_r$ and $(\sigma_z)_r$ with repeated passages of the load; a) p_0 = 4.0k (shakedown limit), b) p_0 = 4.8k, c) p_0 = 5.5k (Merwin and Johnson 1963).

Two studies by Bhargava *et al*. (1985a; 1985b) also considered the rolling contact of cylinders, for single and multiple contacts, respectively. The Abaqus software was used to apply a Hertzian pressure distribution to a deformable half space. For single contacts (Bhargava *et al*. 1985a), the finite element analysis was first verified for elastic behaviour using the Hertz solution, and for elastic-plastic behaviour using the indentation work by Dumas and Baronet (1971) previously discussed. Rolling contact was simulated by translating the applied pressure distribution along the deformable half space. Figure 1.13 shows the initial (light lines) and residual (heavy lines) meshes used in one of the load cases in the study. As can be seen from the final shape of the half space, it

appears that a static indentation is a more severe form of loading than the rolling contact. The initial indentation occurs at the left side of the half space, with the applied pressure being translated across the surface to the right. When the pressure distribution is again stationary, larger displacements are again seen to occur. However, these displacements are smaller than the initial indentation as a result of "ploughing"; the pushing of material ahead of the rolling sphere. This behaviour is also reflected in the residual stress and plastic strain distributions. For single contacts, higher residual stresses are typically found than in equivalent results shown by Merwin and Johnson (1963).

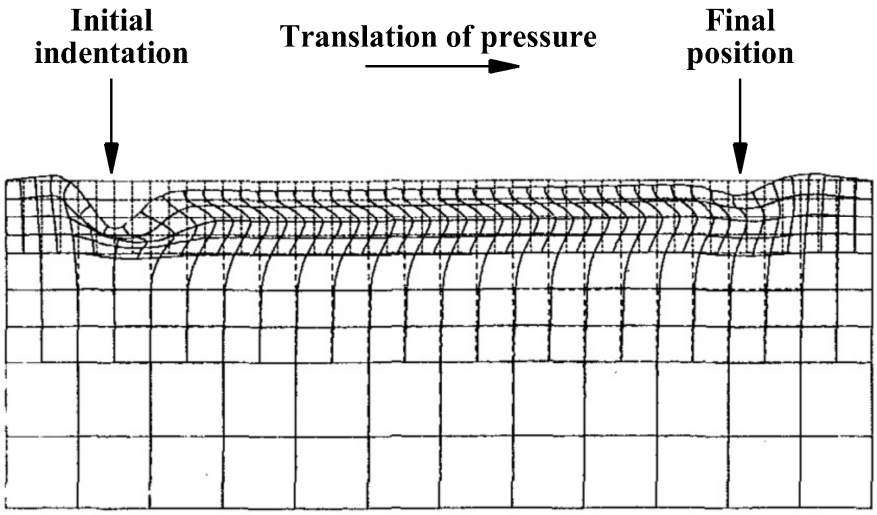

Figure 1.13 - The residual displacement with the load removed, mag. factor 117.8 (Bhargava *et al*. 1985a).

For repeated contacts (Bhargava *et al*. 1985b), direct comparisons to the results of Merwin and Johnson (1963) were made. A lower shakedown limit was found for the finite element analysis. As for the single loading, larger peak residual stresses were found to occur, although the trends in the distributions were similar. It was concluded that a steady state was achieved after typically two loading cycles.

A criticism of each of these rolling contact studies is the use of an elliptical Hertzian pressure distribution for loads that results in material plasticity. It has already be discussed how contact

pressure distributions become somewhat “flattened” as a result of material yield and the contact pressure distributions used are therefore not ideal. However, at low loads where small amounts of plasticity occur, the Hertz distribution is relatively similar. But major discrepancies will occur at higher degrees of deformation.

Vijaywargiya and Green (2007) used a commercially available finite element analysis software package, utilising 2D plane strain elements to investigate sliding contact of deformable cylinders. Similar to previously discussed studies, normal loading was performed by way of a vertical interference or approach distance. The interference at initial yield was that derived by Green (2005). Cylinders were offset in from one another before a specified translation moved one cylinder across the other. A schematic of the loading scheme can be seen in Figure 1.14.

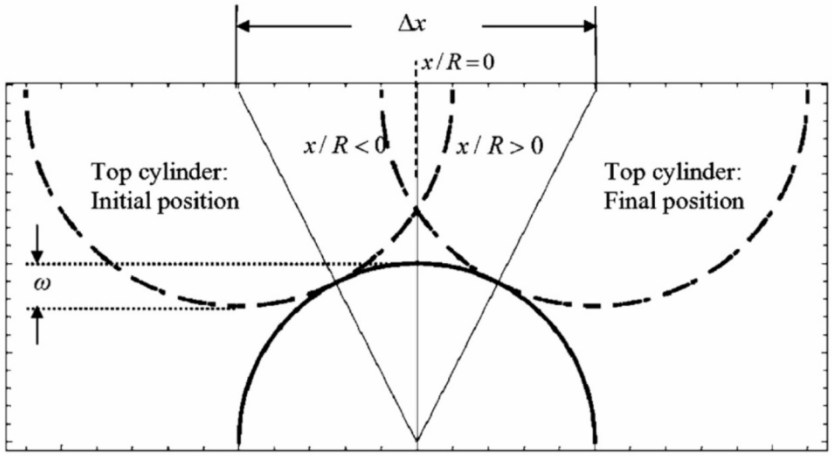

Figure 1.14 - Schematics of the sliding process (Vijaywargiya and Green 2007).

As the interference was increased, the normal and tangential reaction forces also increased. The distribution of these forces became increasingly asymmetric also. Toward the end of the sliding contact, the tangential reaction forces changes direction. Initially positive, resisting the sliding contact, the reaction become negative essentially pushing the opposing cylinder past. The ratio of horizontal to normal reaction force also grows with increased interference. When friction was introduced the reaction forces increased. The normal reaction increased slightly and the tangential

reaction significantly. Residual deflections were also found to be increased as a result of the introduction of friction.

Mulvihill *et al*. (2011) also studied the problem of cylindrical sliding contact. However these authors chose to utilise 3D elements, allowing the use of a ductile material failure model in Abaqus. This 3D model was compared with an equivalent 2D plane strain model, and results were found to be essentially identical. Load distributions were again found to be asymmetric.

Further contact phenomena were studied by Hu *et al*. (1999), who used their numerical model based on fast Fourier transforms and minimisation of complementary energy to simulate the contact of a cylinder of finite length. This resulted in increased contact pressures at the edge of cylinder.

1.3.3. Rough contacts

1.3.3.1. Stochastic contact models

Zhuravlev (1940) provided an approximation of purely elastic contact of flat rough surfaces by proposing a random distribution of asperity heights, each with a constant radius. An almost directly proportional relationship was found to occur between the real contact area and the load. This statistical approach to the analysis of rough surface contact is often attributed to Greenwood and Williamson (1966), and is commonly referred to as the GW model. While the method had previously been proposed, they did introduce several new aspects not found in Zhuravlev's work, such as the discussion of the transition from elastic to plastic contact and experimenting with the adoption of both exponential and Gaussian distributions of asperity heights. The exponential distribution was found to give an exactly proportional relationship between load and real contact area, although a Gaussian distribution was found to be more representative of the geometry of real rough surfaces. Subsequent experimental research has shown that within the range of elastic deformation, and considering quasi-isotropic surfaces, the GW model provides a good approximation of real rough surface contact behaviour (Handzel-Powierza *et al*. 1992).

Stochastic GW type models have subsequently been applied to other contact problems. Greenwood and Tripp (1967) extended the model to consider the contact of rough spherical surfaces, as did Mikic (1974), while Lo (1969) and later Gelinck and Schipper (1999) studied the contact of rough cylinders. Greenwood and Tripp (1970) again broadened their research in this area by considering the contact of two rough surfaces. It was found that models with both surfaces rough give indistinguishable results from single rough surface models.

A limitation of these GW type models is the manner in which material plasticity is approached, considering asperities to be either elastic or plastic, with little transition behaviour. Furthermore, the plastic contact model adopted was based upon that of Abbott and Firestone (1933). This predicts the contact area to be calculated by truncating asperities at the intersection of the original surfaces, with uniform contact pressure equal to the hardness. This model of plasticity neglects volume conservation in the deformed material (Ford 1963).

Studies by Williamson and Hunt (1972) and Pullen and Williamson (1972) actively investigated plasticity in rough contacts. Positive as well as negative deformation of the rough surface was discussed, as shown in Figure 1.15. Conservation of volume was proposed to occur by a uniform positive displacement across non-contacting regions of the rough surface. This resulted in a new non-linear approximation of the relationship between contact area and load. The proposed solution showed good agreement at low and high loads, where elastic and plastic behaviour dominate. However, the transitory state between elastic and plastic behaviour is poorly approximated.

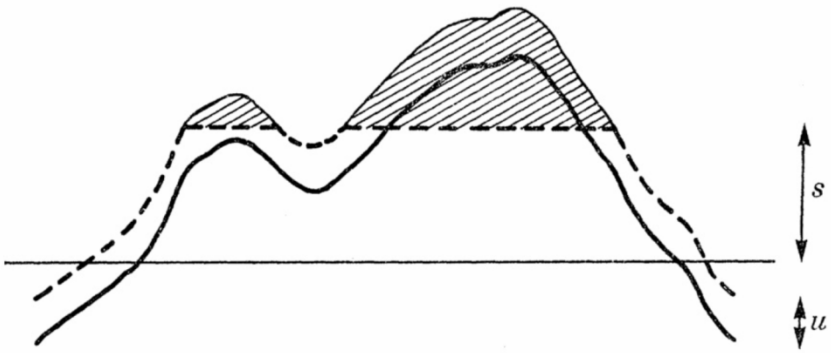

Figure 1.15 - The manner in which metal is redistributed during the crushing of a rough surface by a flat (Pullen and Williamson 1972).

A further limit is that these models each considered asperities to be spherically tipped, with constant radius of curvature. A study of surface topography by Whitehouse and Archard (1970) resulted in an alternative theory to describe asperity shape. The asperity distribution and radius assumptions were discarded, replaced by two new surface parameters to characterise asperity height and wavelength structure. Onions and Archard (1973) proceeded to use these parameters to create a stochastic model comparable to the GW model. This resulted in slightly different behaviour between load and contact area, as shown in Figure 1.16, and very different mean contact pressures, as shown in Figure 1.17. Bush and Gibson (1975) also modified the shape of asperities, considering elliptical paraboloid tips, rather than spherical.

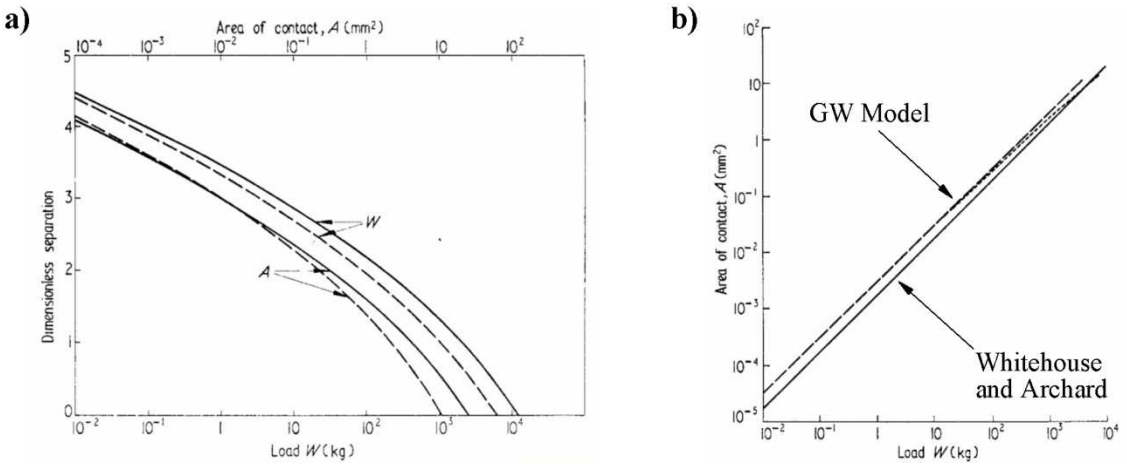

Figure 1.16 - Comparison of Greenwood Williamson model and Whitehouse and Archard model; a) Area of contact as a function of separation, b) Relation between the area of contact and the load (Onions and Archard 1973).

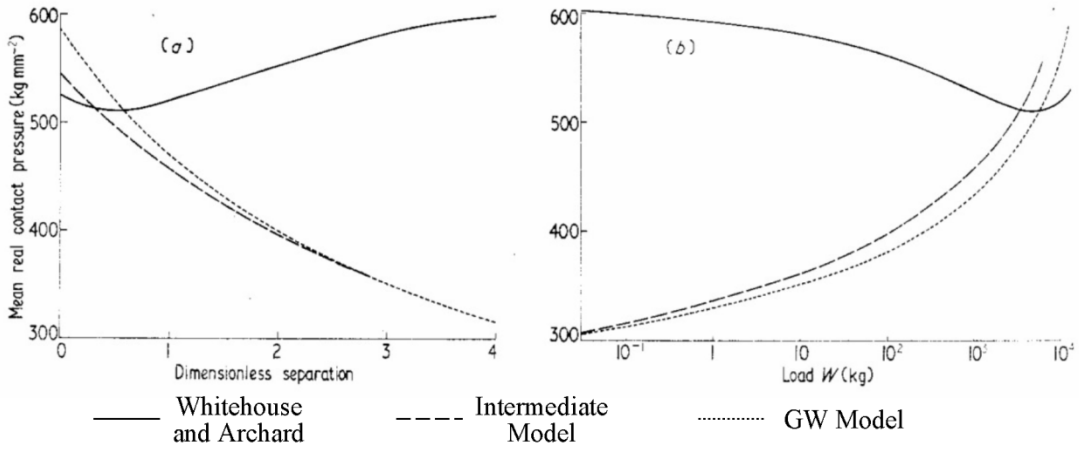

Figure 1.17 - Mean pressure at the real area of contact as a function of a) separation, b) load (Onions and Archard 1973).

More recently, a similar type of model has been used for a number of other problems. McCool (1986) compared the standard GW model to other isotropic and anisotropic models, before later introducing more deviations in the form of skewed asperity distributions to represent different finishing techniques as well as studying coated surfaces (McCool 2000).

As discussed, the original GW model and subsequent refinements provide a good solution for rough surface contact for predominantly elastic or plastic behaviour. The transitory region in between is

not accurately represented. As a result, significant research has been performed investigating elastic-plastic behaviour. Many of the authors discussed hereafter have performed work on single contacts, before introducing their suggested elastic-plastic regime into a GW type model. The single contact aspects of these studies have previously been discussed in Section 1.3.2; this section focuses on the stochastic implementation.

One of the first models to attempt to bridge this transition range was proposed by Chang *et al*. (1987), which is commonly referred to as the CEB model. Based on work by Tabor (1951), a critical interference, or approach distance was calculated at which material yield first occurs. Until this critical value is reached, purely elastic Hertzian contact is assumed, while afterwards, a model based upon volume conservation over a region dependent on the interference is used to simulate plastic behaviour. Hertzian contact pressures were assumed for elastic contacts, while plastically deforming asperities were subject to constant contact pressures proportional to the hardness. This effectively tied together the purely elastic and plastic models, while doing little to describe any transitory regime in between, leading to discontinuities in the results of the rough surface contact. Horng (1998) performed a related study, considering elliptical contacts with a range of asperity tip radii, with the trends in behaviour found similar to that found by the CEB model. However, discontinuities between elastic and plastic behaviour were still present, with nothing done to address the transition.

Evseev *et al*. (1991) proposed an alteration to the contact pressure distribution where only the pressure at the centre of the contact remained constant. The pressure at the edges of the contact followed a Hertzian distribution. This removed the discontinuity found in previously discussed models, but the authors recommended further investigation after comparison with experiment.

Kucharski *et al*. (1994) used a finite element method to solve the contact of an elastic-plastic, spherically tipped, single asperity, as discussed in Section 1.3.2. The behaviour found for the single contact was then used in a statistical model as in the GW and CEB formulations, and the results compared, as in Figure 1.18. While none of the three shown models provides particularly good

agreement with experimental results, it can be seen that the results achieved using the finite element model give the closest approximation.

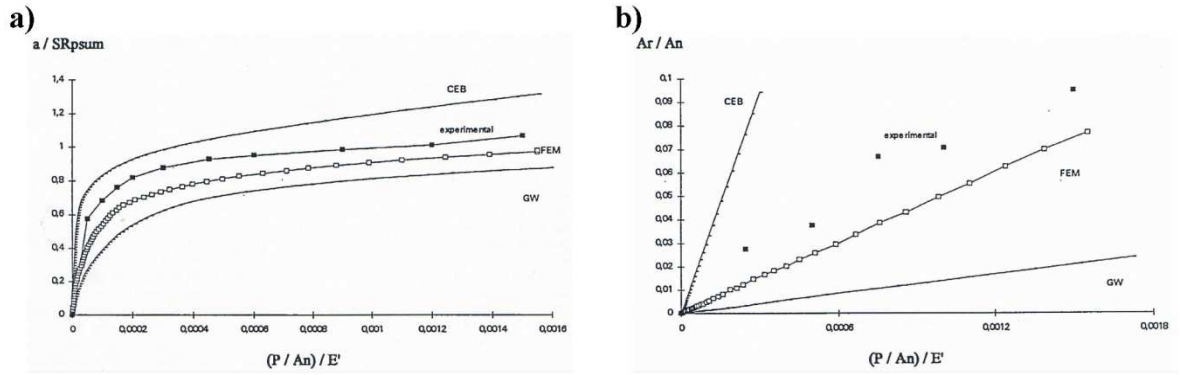

Figure 1.18 - a) Dimensionless approach vs. dimensionless load for sand-blasted surface, b) real contact area vs. dimensionless load for sand-blasted surface (Kucharski *et al*. 1994).

While considering coated surfaces, Chang (1997) returned to further develop the CEB model to remove the previous discussed discontinuity between elastic and plastic behaviour. A linear transition between the onset of plasticity and fully plastic behaviour was introduced, using a function of the interference. Zhao *et al*. (2000) used mathematical manipulation to smooth the transition between elastic, elastic-plastic and fully plastic behaviour. Comparisons were made with the original GW and CEB models. All three models showed good agreement when elastic behaviour dominated the contact. Despite the improvements, the new model showed results similar to those of the original CEB model even with increased levels of plasticity. The authors attributed this to inaccuracies in the CEB model cancelling to provide a good approximation.

Kogut and Etsion (2003) and Jackson and Green (2006) both implemented the results of their finite element studies of single contacts (Kogut and Etsion 2002; Jackson and Green 2005) in GW type statistical models. Both found good agreement with the CEB model where elastic behaviour dominates the contact. For increasing levels of plasticity, both diverge from the CEB model, but maintain good agreement with each other. It is only at high levels of plasticity, where large deformations occur, that the two models differ. Jackson and Green proffer that their individual

contact model is more valid, considering material and geometric effects not accounted for by Kogut and Etsion. Abdo and Farhang (2005) present a mathematical model that shows good agreement with the experimental results from Kucharski *et al*. (1994) previously discussed.

Ciavarella *et al*. (2008) attempted to include asperity interaction in a statistical model that considered only elastic behaviour. At low loads, asperity interaction was assumed to be negligible. At high loads, asperity interaction was introduced with the assumption that asperity contacts are uniformly distributed and uniformly deformed. The results of the new model were presented alongside a discrete implementation of the model (Ciavarella *et al*. 2006) and the original GW model, showing the effect of asperity interaction. The authors highlight sealing as being particularly affected by asperity interaction, with smaller contact areas predicted for a given separation.

A number of studies have been performed considering different aspects to those so heavily investigated. Greenwood *et al*. (2011) and Franse *et al*. (1985) each considered cylindrically tipped asperities rather than the traditional spherically tipped, resulting in significantly reduced contact pressures. The latter also investigated the effect of the coefficient of friction of sliding surfaces. Faulkner and Arnell (2000) tackled this problem also, comparing the results from Franse *et al*. (1985) with those obtained using spherically tipped asperities. They performed finite element analysis, as others did for static contacts, of an individual asperity contact, before incorporating the behaviour into a statistical model. Overall coefficients of friction were found to depend upon asperity shape, with smaller values found for spherically tipped asperities. Mulvihill *et al*. (2011) also applied the results of the finite element analysis of sliding cylindrical contacts to a statistical model, finding similar trends in behaviour to those of Franse *et al*. 1985).

Kadin *et al*. (2006) appear to be one of the few groups to have considered the residual state of a surface in a GW type model. They investigated the effect of the applied load of the distribution of asperity heights, finding that the larger the degree of plasticity, the larger amount of skewness was found in the residual asperity distribution.

1.3.3.2. Idealised contacts

One of the earliest idealised models of rough surface contact was that of Westergaard (1939) who considered the contact of smooth surfaces with a two dimensional sinusoidal form. At low loads, the contact pressure distribution followed Hertzian theory; at higher loads it became sinusoidal, reflecting the form of the surface. This approach is further discussed by Johnson (1985), who examines the development of the ratio of real contact area to apparent contact area with increasing load. Each of these phenomena can be seen in Figure 1.19.

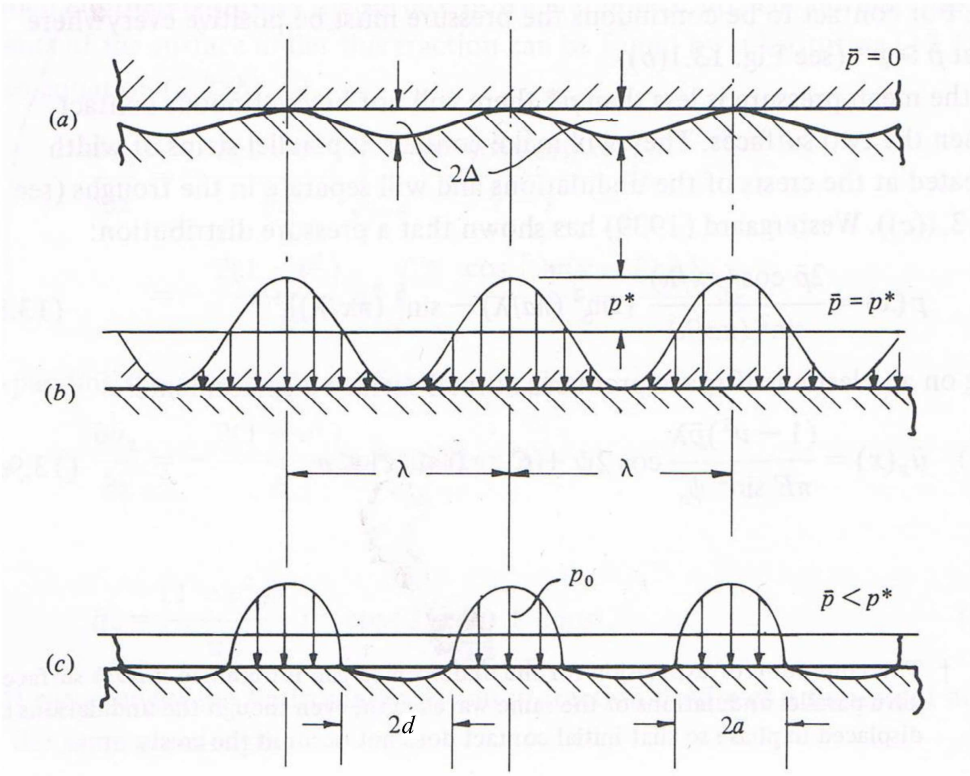

Figure 1.19 - Contact of a one-dimensional wavy surface with an elastic half space; a) unloaded, b) complete contact, c) partial contact (adapted from Johnson 1985).

Vergne *et al*. (1985) examined how neighbouring asperity features on such a surface can interact with one another during contact, considering a two dimensional elastic sinusoidal profile of two peaks in close proximity in contact with a rigid plane. At low loads, the asperities did not interact, resulting in Hertzian pressure and stress distributions. As the load was increased, interaction between neighbouring contacts was seen to occur. Pressures and stresses were “drawn” towards

each other as seen in Figure 1.20. This illustrates one of the problems with statistic models of rough surface contact, such as the GW model in which interaction between asperities is not accounted for.

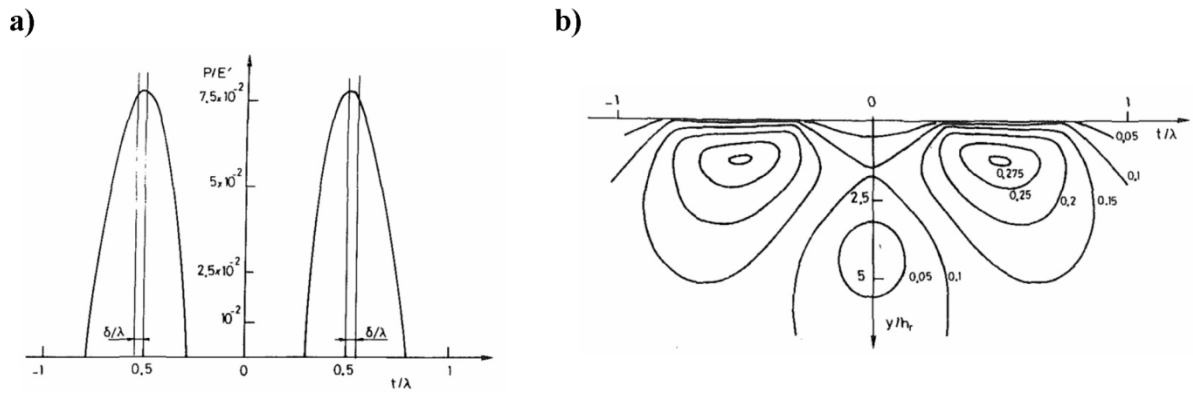

Figure 1.20 - a) Comparison between pressure fields, b) τ_{max} / P_{max} for c / λ = 0.497 (Vergne *et al.* 1985).

Seabra and Berthe (1987) superimposed a range of two-dimensional sinusoidal profiles onto a cylindrical surface and thereby analysed the contact of elastic cylinders having a wavy surface with a plane. Under load, the contact pressure distributions of the two separate problems became combined, as illustrated in Figure 1.21. The effects of including this idealised roughness can be seen in both the peak contact pressures and in the contact dimensions. In each case, the peak pressure exceeds that of the equivalent smooth cylinder, whilst the location of local profile peaks results in the edges of contact moving. This can result in either smaller or larger contacts, or a translation of the contact centre.

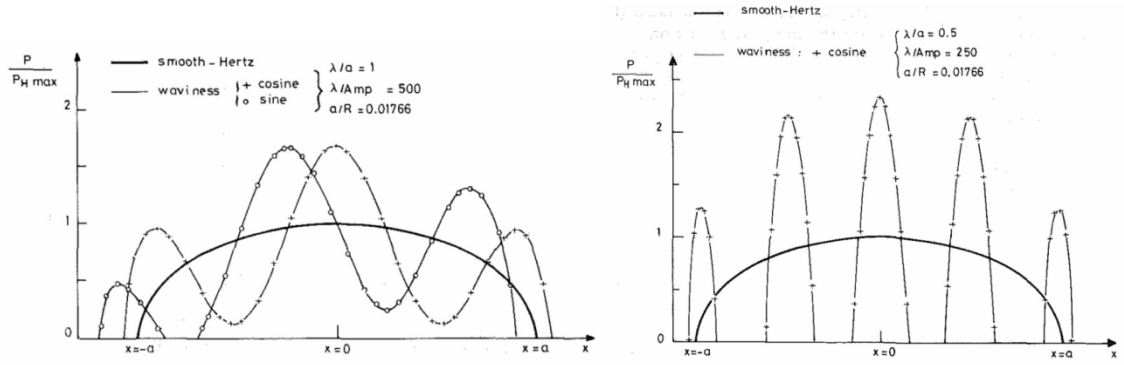

Figure 1.21 - Pressure for elastic wavy cylinder/plane contact (Seabra and Berthe 1987).

Nowell and Hills (1989) attempted to approximate a cylinder with a ground surface by superimposing a periodic array of two dimensional asperities of constant height and radius onto a smooth cylinder. The distance between asperities was varied and the load was increased, resulting in additional asperities contacting and interaction occurring. It was shown that asperity interaction occurred predominantly at the surface. In the subsurface region, stress distributions were similar to those found in smooth cylinder contacts.

Komvopoulos and Choi (1992) used Abaqus to model a periodic array of rigid cylindrical asperities of equal radius, with the number of asperities, and distance between asperity centres, varied. This was loaded against a deformable elastic half space by applying a range of vertical displacements, or interferences, to the rigid surface. As previously discussed, contacts under small interferences followed Hertzian theory closely, with little interaction between neighbouring asperities and their associated stress fields. At higher interferences, increased interaction was found to occur. For more closely grouped asperities, interaction was more apparent in regions closer to the surface. When spaced further apart, interaction could be seen at greater depths. Additionally for more closely group asperities, the subsurface material showed increased magnitudes of stress.

Sundaram and Farris (2009) performed a similar study using a numerical method based on singular integral equations. A number of idealised rough surface contact problems were discussed, including

an eight degree polynomial surface punch as well as a sinusoidally rough cylinder and a flat punch with rounded edges. Similar patterns were seen to occur in the contact pressures as previously described, with peak contact pressures exceeding those of equivalent smooth contacts. Interaction of stress fields of neighbouring asperities can be seen in Figure 1.22.

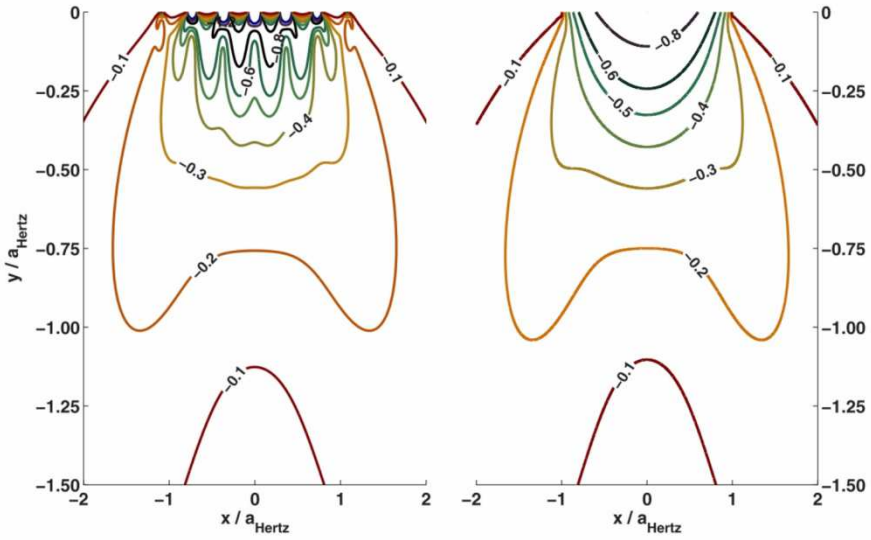

Figure 1.22 - Normalised subsurface stresses σ_{xx} / ${p_{Hz}}^{max}$ for the rough cylinder (left) and smooth cylinder (right) for the same applied load, material properties and cylinder radius (Sundaram and Farris 2009).

Gao *et al*. (2006) introduced elastic-plastic behaviour to the problem of a two dimensional sinusoidal contact, using Abaqus to simulate contact with a rigid flat. The amplitude and wavelength of the sinusoidal surface were varied to assess the differences in behaviour for differently shaped features. The ratio of elastic modulus to yield strength was varied also to test a range of material properties. By varying these parameters an indentation map detailing contact behaviour was created. The model schematic and indentation map can be seen in Figure 1.23.

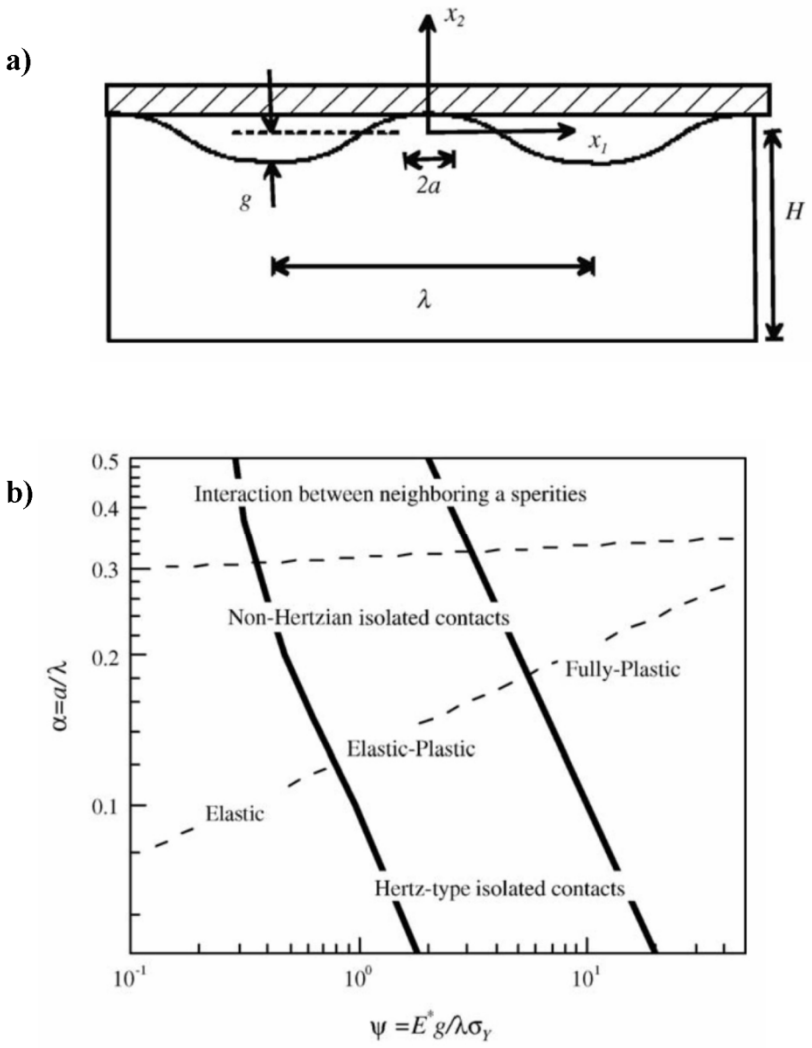

Figure 1.23 - a) Schematic illustration of a sinusoidal rough surface by a rigid indenter, with notation and sign convention, b) A schematic map showing the behaviour of a sinusoidal elastic-perfectly plastic surface under contact loading (Gao *et al*. 2006).

It was found that for most partial contact situations the normalised mean pressure was limited to approximately $3\sigma_y$, as proposed by Tabor (1951) and Williams (1994). However, as complete contact was approached, and yielding regions began to interact, contact pressures increased rapidly, to approximately twice this proposed limit, $6\sigma_y$. The authors report this to be due to the interactions preventing lateral expansion of the plastic zone. This behaviour was most pronounced in the case of small amplitude, large wavelength surfaces, of relatively low yield strength materials. However, the proposed limit was still exceeded for more practical engineering material properties, but not to the same extent. After the contact was unloaded, cases of complete contact result in predominantly

compressive residual stresses. For more realistic degrees of contact, regions of tensile direct stress in the tangential direction were found to occur both at the surface and in the subsurface material. Manners (2008) further discussed this seemingly higher mean contact pressure, using upper and lower bound solutions to conclude that the predicted behaviour is acceptable. Contact pressure is limited to approximately $3\sigma_y$, until the proportion of the area in contact is approximately two thirds. Further increase in area results in a sharp increase in the contact pressure limit, as shown in Figure 1.24. This is as material beneath the surface is under a state of hydrostatic stress.

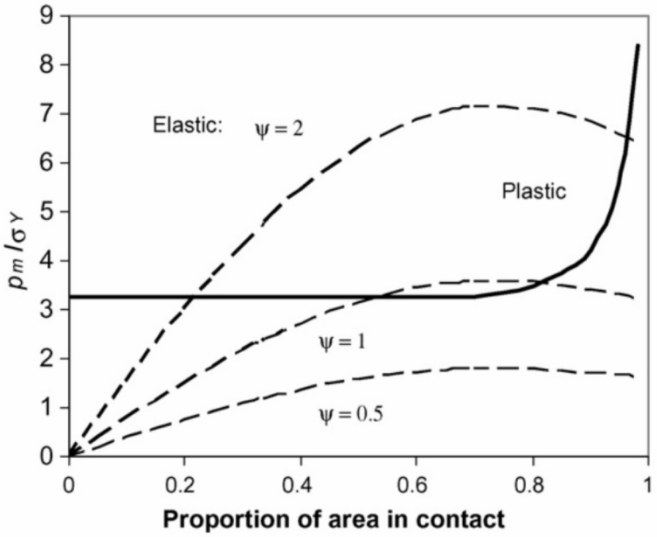

Figure 1.24 - Contact pressure and contact area (Manners 2008).

In two studies, Krithivasan and Jackson (2007) and Jackson *et al*. (2008) considered a similar sinusoidal surface elastic-plastic contact, only in three dimensions rather than two. Their finite element model was compared with analysis by Johnson *et al*. (1985) and Tripp *et al*. (2003), who determined the contact pressure and stress distributions for contact of a purely elastic three-dimensional sinusoidal surface. Good agreement was found between these results and those from the finite element analysis for elastic behaviour. As previously found, at high contact area ratios the average contact pressure was found to exceed the limit of approximately $3\sigma_y$. This limit was exceeded at lower contact ratios for lower yield strength materials. Lower yield strength materials

also exceeded the proposed limit the most when complete contact was achieved, at just over $6\sigma_y$, similar to that previously found by Gao *et al*. (2006). Finite element results were subsequently used in a comparison against several analytical models that predicted higher average contact pressures as the yield strength was further reduced.

The elastic-plastic regime was also studied in work by Sabelkin and Mall (2007). Using a two dimensional finite element model created using Abaqus, the contact of a multi asperity cylinder was considered. This cylinder was contacted with a deformable counter face by itself, as with up to six additional cylindrical asperities superimposed onto its surface. Relationships between total contact area and contact load were examined. These were found to be complex, depending upon the number of asperities, the shape of asperities and their location relative to the contact. These factors also affect the amount of interaction between asperities under load.

Gong and Komvopoulos (2003) created a similar finite element model using Abaqus to simulate a contact of layered media as in Figure 1.25. While considering a magnetic recording disk as the motivation for the study, the effects of multiple layers of materials with different mechanical properties is relevant to the study of gear contacts. Gears are typically subject to a wide range of treatments that alter the surface properties in particular, such as carburising or nitriding, which could have potentially result in differences to an isotropic material. This study considered surfaces with both squared features and a sinusoidal profile. The squared features were used as a surface representative of patterned media for high density magnetic recording. In this study, the rigid curved body, labelled asperity, was slid across the rough surface. Contact pressures were found to be raised at the trailing edge of the squared roughness features. This effect was exacerbated by increasing the height of the features. Contact pressures were also found to increase as a result of an increase in the amplitude of the sinusoid, as a result of reduced contact areas. Due to the continuity of the surface, no such stress raisers cause such dramatic changes in the contact pressure distribution. Similar

patterns were found to occur in the stresses found to occur at the surface. As in previous studies of contact of layered bodies, the interface between layers acted as a stress raiser.

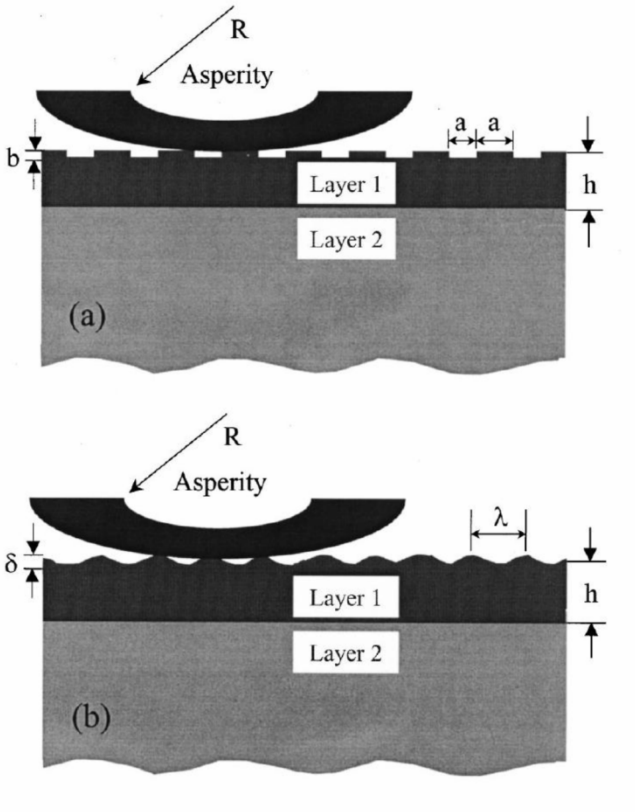

Figure 1.25 - Schematics of layered media with a) meandered and b) sinusoidal surfaces (Gong and Komvopoulos 2003).

As well as sliding contacts, rolling contacts have been considered by Ismail *et al*. (2010), who aimed to investigate running in. Using Abaqus, a rigid cylinder was displaced vertically into a deformable rough surface of cylindrical asperities. This rigid cylinder was then rolled across the surface before being removed. This load cycle was repeated a total of five times. Plastic deformation was found to be limited to the first two cycles. However, as the load was applied in the form of a defined displacement, after the plastic deflection of the first load cycle, it is though that the load would be inconsistent between cycles. As a result of the rolling contact, the lateral residual displacements are different to the pure static loading. In a static loading, lateral displacements were symmetrical, while in rolling contact, the displacements were larger in the direction of rolling.

The idea of superimposing cylindrical asperities on a cylindrical body is a basic form of a fractal surface. Fractal geometry is based on the assumption that surface features repeat themselves at a range of scales. The models already discussed have only considered fractal geometry of an "order" of two, i.e. two levels of cylinders. However, larger orders have been considered in an attempt to simulate real surface geometry. Work by Archard (1957) was one of the earliest such studies, considering a number of fractal surfaces (although Archard did not use the term "fractal"), as shown in Figure 1.26. This investigation considered up to three levels of fractals, with equidistant spherical asperities of radius R_1, which have asperities of a smaller radius R_2, which in turn have asperities of a smaller radius of R_3. The relationship between contact area and load tended to converge towards a linear relationship as the "order" or asperities was increased, i.e. $A \propto W$.

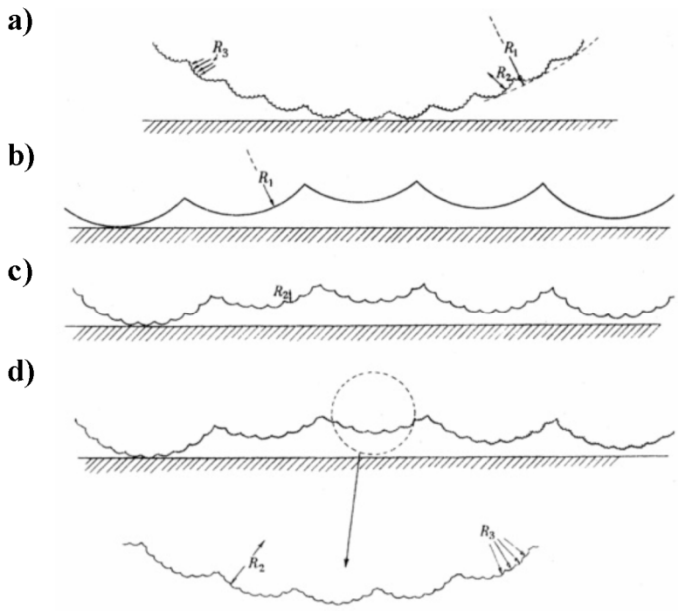

Figure 1.26 - Models used in the theory under zero load; The deduced relations between A and W for these models are a) $A \propto W^{26/27}$, b) $A \propto W^{4/5}$, c) $A \propto W^{14/15}$, d) $A \propto W^{44/45}$ (Archard 1957).

Majumdar and Bhushan (1990) examined three-dimensional surface profiles measured via profilometry and used a Weierstrass-Mandelbrot wave function to provide fractal approximations. Majumdar and Bhushan (1991) then used an analytical model to simulate the elastic-plastic contact

of these surfaces. Both the fractal surface model and the GW model were compared against a range of experimental results (Yamada *et al*. 1978; Bhushan 1985; Bhushan and Dugger 1990). The fractal approximation of a rough surface was found to agree better with experimental results, particularly at relatively low loads. More deviation occurred as load was increased. The authors suggest this difference to be attributable to the lack of consideration of asperity interaction in the fractal model. The linear relationship between contact area and load in the GW model is not seen experimentally, and is not seen in the fractal analysis either.

Weierstrass profiles of superimposed sinusoidal wave functions of different amplitude and wavelength have been considered by Ciavarella *et al*. (2000) in a linear elastic contact model to determine contact areas and contact pressure distributions. This model was extended to determine the contact stiffness and electrical contact resistance. A similar surface contact model was created by Wilson *et al*. (2010), with several key differences. Rather than consider a two dimensional perfectly fractal surface, the authors modified the methodology to consider a three dimensional measured surface. This measured surface was then approximated using a Fourier series, giving a surface that is not perfectly fractal.

A number of other studies of elastic-plastic fractal surface contact have been performed, such as those by Warren and Krajcinovic (1996) and Larsson *et al*. (1999), using experimental work by Handzel-Powierza *et al*. (1992) and Kucharski *et al*. (1994), respectively as means for comparison. Warren and Krajcinovic (1996) found good agreement at low levels of applied vertical displacements. Deviation appeared to grow at increased displacements, but the theoretical model failed to cover the same range as the experimental results. Larsson *et al*. (1999) also show good agreement at lower loads, as illustrated in Figure 1.27. Agreement is seen across a wider range of nominal pressures for the rougher surface, (E30).

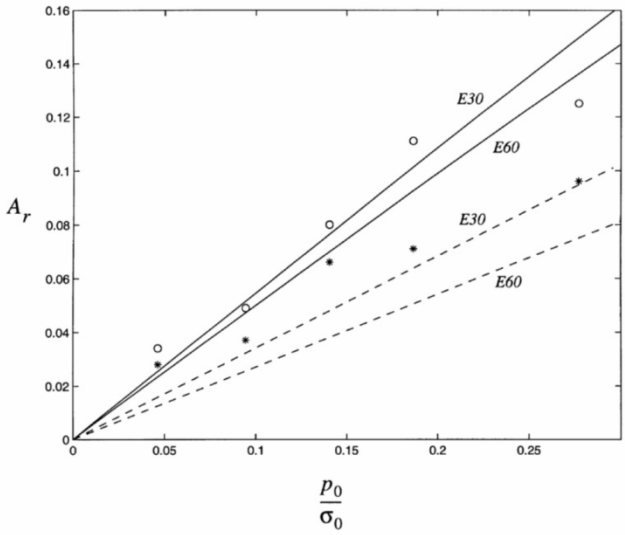

Figure 1.27 - Relative contact area, A_r, versus dimensionless nominal pressure, p_0 / σ_0, from experimental observations by Kucharski *et al*. (1994) for two different surface, E30 (○) and E60 (*), in comparison with prediction of fractal theory (solid) and Kucharski *et al*. (dashed) (Larsson *et al*. 1999).

Hyun *et al*. (2004) considered the elastic contact of three dimensional fractal surfaces using the finite element method, before extending the analysis to include elastic-plastic behaviour (Pei *et al*. 2005). Despite nonlinearity of the material properties, the contact area was found to increase linearly with load. As the surface initially contacts in relatively few locations, only small loads were found to be required to cause plastic deformation in asperity contacts. More asperity contacts were found to occur once a material yield strength was determined, as the surface could not maintain the pressures found in the elastic analysis. This load was distributed between other asperities.

A number of methods for generating rough surfaces similar to those created by manufacturing processes, with Gaussian or non-Gaussian distributions are available. Two studies in particular have been adopted by those performing contact analysis, using linear transformations on random matrices (Patir 1978) or digital filter techniques (Hu and Tonder 1992).

Yu and Bhushan (1996) generated nine surfaces based upon the methods of Patir (1978). It was found that at small loads, asperity contacts act as point loads on the surface. The maximum von Mises stress was found to occur at or near the surface, exceeding that beneath the surface.

Therefore, as load increases, it is found that plastic deformation first occurs at the surface, causing residual asperity deflection.

Mihailidis *et al*. (2001) considered the contact of two rough cylinders, each with generated surface roughness, to evaluate the subsurface stress fields. The stress distributions for the rough surface contact significantly differed from those for the equivalent smooth contact. Local maximum shear stresses were found to occur just beneath the surface of loaded asperity features, coexisting with the subsurface maximum associated with Hertzian contact theory. As the load was increased, the maximum shear stress associated with asperities exceeded the subsurface maximum. This is found to occur at lighter loads for rougher surfaces. The depth of these maximum stresses is found to correlate with the typical depth of micropitting failures.

Kim *et al*. (2006), using the surface generation methods of Hu and Tonder (1992), also investigated subsurface stresses in rough surface contact. They too found that local maximum stresses occurred near the surface of loaded asperities. Lower peak stresses were found to occur when the kurtosis of the surface was reduced, due to less aggressive peaks. Introducing a larger friction coefficient at the surface resulted in the local maximum stresses moving closer towards the surface. It was proposed that it is impossible to define the typical behaviour of rough surfaces in contact, as each surface and each asperity contact are unique.

1.3.3.3. Real rough surface contacts

Early studies of analysis of real rough surfaces used elastic behaviour, with validation based on comparison with smooth Hertzian theory, before introducing measured two dimensional roughness profiles. Webster and Sayles (1986) were among the first to do this, followed later by Seabra and Berthe (1987) and Snidle and Evans (1994), who each used numerical methods to investigate rough surfaces. Contact pressures were found to differ significantly from the smooth case, as shown in Figure 1.28. Peak pressures are achieved that are often several times that of Hertzian theory. Nonetheless, the general trend can still be seen to loosely follow the Hertzian pressure distribution,

and contact dimensions are similar. Nominal contact area was found to be approximately proportional to applied load.

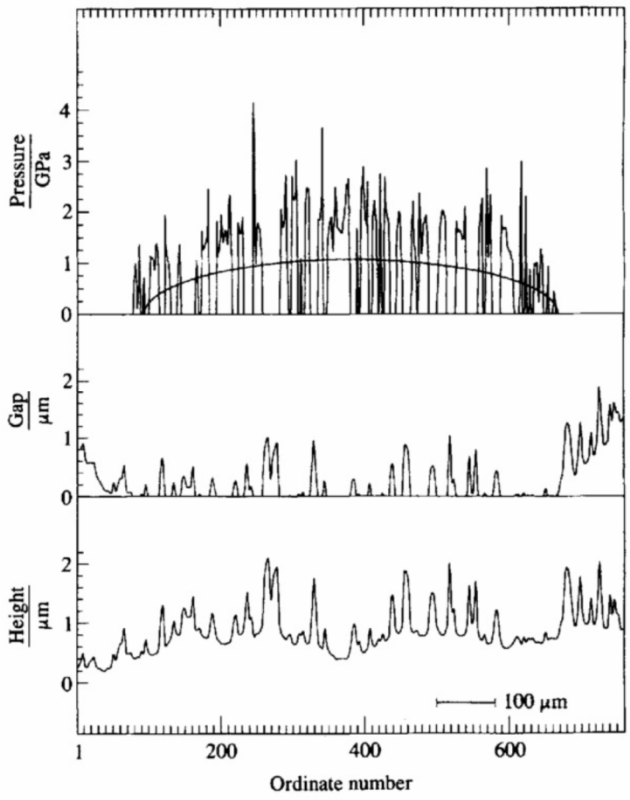

Figure 1.28 - Results of simulated contact between a run-in, ground elastic surface and a rigid flat. Radius of relative curvature = 19 mm; E' = 227.3 GPa; load = 600 kN/m; ordinate spacing 1.25 µm. Lower graph shows the original, undeformed rough surface relative to a straight line datum. Note that Hertzian pressure is also shown (Snidle and Evans 1994).

Bailey and Sayles (1991) and Cole and Sayles (1992) later extended the work of Webster and Sayles (1986) to consider sliding friction and layered bodies, respectively. As previously discussed for generated rough surfaces, maximum stresses were found to occur in close proximity to the surface, as shown in Figure 1.29. For the range of rough surfaces considered, the rougher surfaces showed these stresses to be larger in magnitude, with stresses exceeding the yield strength commonplace in the elastic material. Introducing a surface shear with a defined friction coefficient resulted in the peak stresses moving towards the surface, while the bulk subsurface stresses deviated in a similar

manner as in smooth contact. In considering layered bodies, it was found that the introduction of a thin surface layer had a greater effect on contact behaviour for rough contact than smooth.

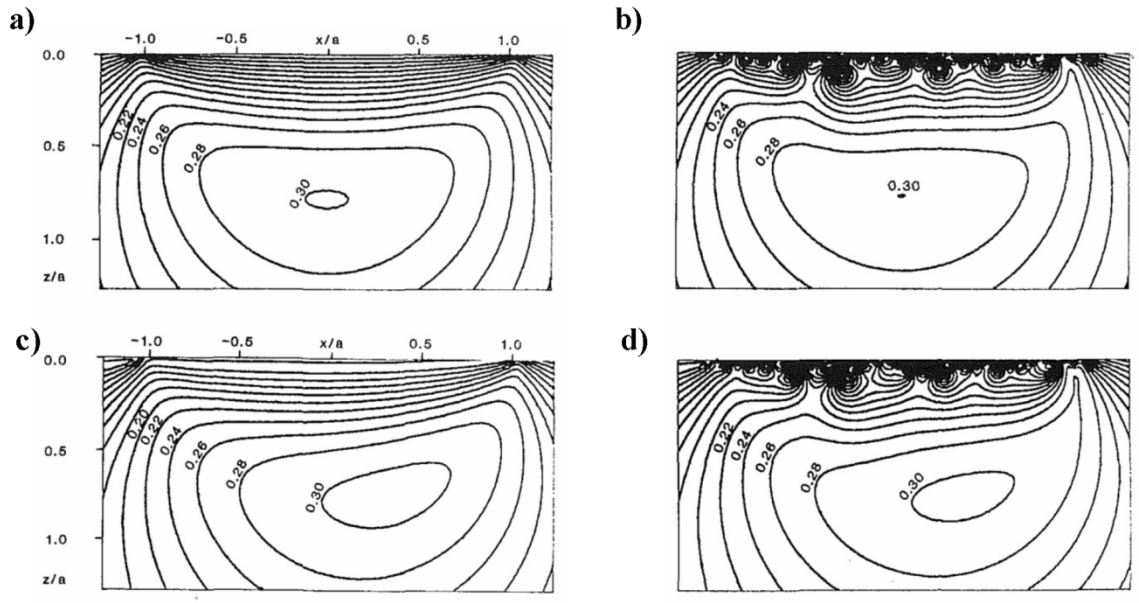

Figure 1.29 - Distribution of subsurface principal shear stress for elastic contact; a) smooth - normal load, b) rough - normal load, c) smooth - normal load and surface shear (μ = 0.1), d) rough - normal load and surface shear (μ = 0.1) (Bailey and Sayles 1991).

Considerations of three dimensional geometry and material plasticity were subsequently introduced by Poon and Sayles (1994a; 1994b). The two dimensional roughness surface profiles were extruded over a finite length before being contacted with a smooth sphere. Plasticity was introduced by limiting the contact pressure to the material hardness, with contact pressures truncated. A total of 110 different rough surfaces were created, considering a range of R_q values. It was found that smoother surfaces, with smaller R_q values, tended towards completely elastic contact. Increasing the roughness of the surface resulted in increased plasticity.

Jackson and Green (2011) considered the elastic contact of as-measured roughness using a FFT-based deterministic model based on the methods of Stanley and Kato (1997). Investigating three surfaces with different surface finishes, a near linear relationship between contact area and load was found. Some agreement was seen in the comparisons made with stochastic models, such as the Greenwood and Williamson (1966) model. However, the authors comment that real rough surfaces

do not appear to follow any proposed mathematical structures and so these types of models should not be expected accurately to predict contact behaviour. While this may imply that deterministic models are more suitable, they too have their drawbacks. The authors particularly highlight the effect of mesh density. In their assessment of the effect of mesh density, the general trends in behaviour can be found regardless, but the mesh density can affect the details. It was found that a coarser mesh density resulted in a prediction of larger contact areas, and thus reduced contact pressures, than those obtained with a finer mesh.

In a series of studies, the plastic contact of rough surfaces was investigated (Jamari *et al*. 2007; Jamari and Schipper 2007a; 2008). The methods were based on those used for the single spherical contact work already discussed in Section 1.3.2.1. A smooth silicon carbide ball was used as an indenter in a contact with a rough aluminium surface. The rough surface was measured using an optical interference microscope before and after application of the load. Good agreement between the proposed model and experiment was found to occur, as illustrated in Figure 1.30. Also, a relationship was developed to determine the nature of a contact. This described whether a contact will be dominated by asperity or bulk deformation.

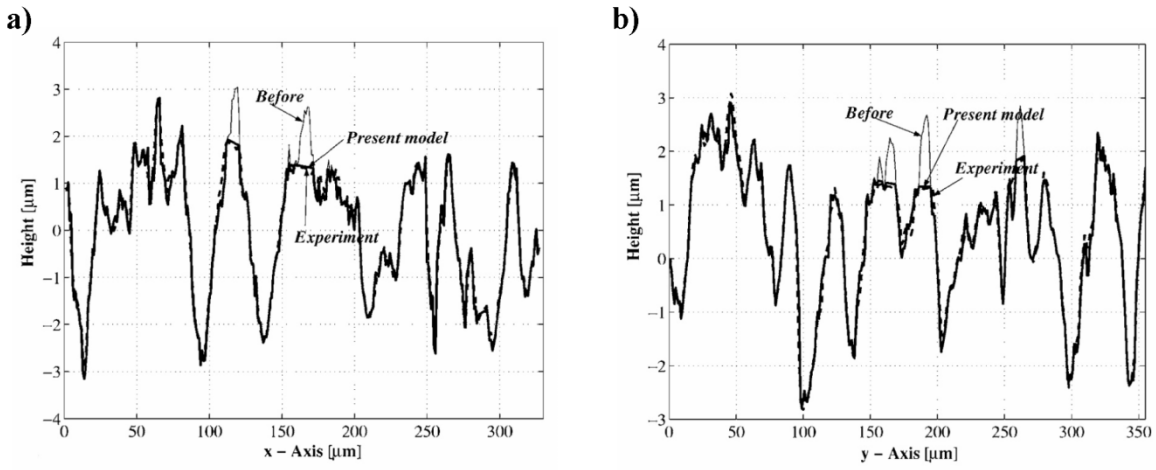

Figure 1.30 - Profile of the matched and stitched isotropic surface: a) x profile at y = 195 µm and b) y profile at x = 171 µm (Jamari *et al*. 2007).

Repeated stationary contact of rough surfaces was also considered (Jamari and Schipper 2008). As has been discussed already when considering other contact configurations, the majority of residual asperity deflection occurs in the first loading cycle. The rough surface is changed such that the developed contact area supports the applied load elastically. This can be seen in Figure 1.31, where the profiles for additional load cycles are essentially indistinguishable from the first.

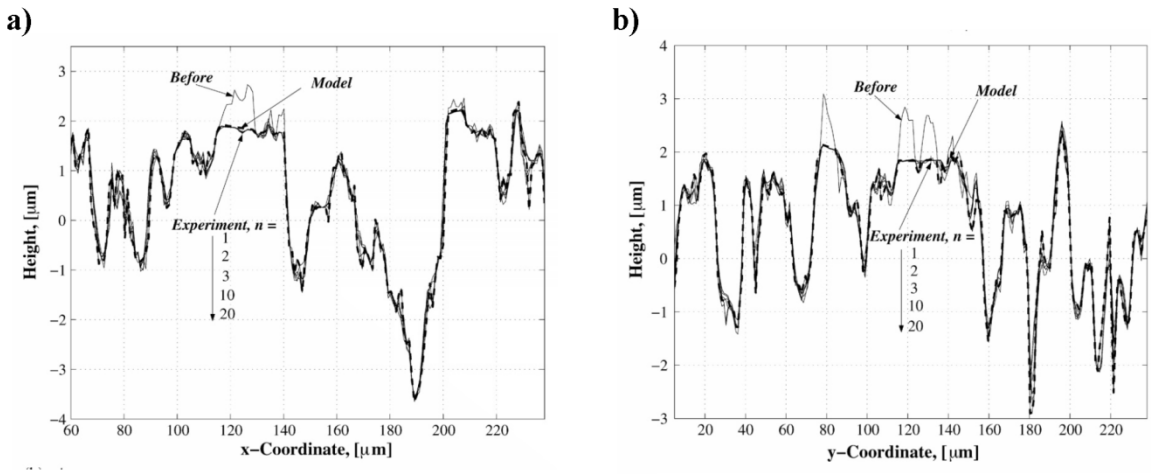

Figure 1.31 - Profile of the matched and stitched isotropic aluminium surface: a) x-profile at y = 120 μm and b) y-profile at x = 129 μm; n = number of load cycles (Jamari and Schipper 2008).

Wang *et al*. (2009) also used a development of their techniques used for single contacts to consider the contact of rough surfaces. Using an integration based on a multi-level contact model, the elastic-plastic contact of a smooth sphere and machined surface was investigated. It was found that during contact that the applied load was predominantly carried by the asperity tips, and that the mean contact pressure was highly dependent on the radius of the asperity peaks. In comparison with the stochastic models of Greenwood and Williamson (1966) and Chang *et al*. (1987), better agreement with the experimental results of Kucharski *et al*. (1994) was found to occur. The differences that did occur were attributed to the elastic-perfectly plastic behaviour assumed in the model by the authors.

As a result of the increasingly powerful computational resources available, some groups have attempted to model the contact of three dimensional real rough surfaces using finite element

analysis (Yastrebov *et al*. 2011; Olshevskiy *et al*. 2012). Each of these groups of authors focus on the intensive computational requirements of these models, with each model consisting of several hundreds of thousands of nodes and taking hundreds of hours to complete, even with modern computers. A special focus on mesh transition away from the contact surface can be seen in Figure 1.32, as well as von Mises stress distributions and displacements at the surface.

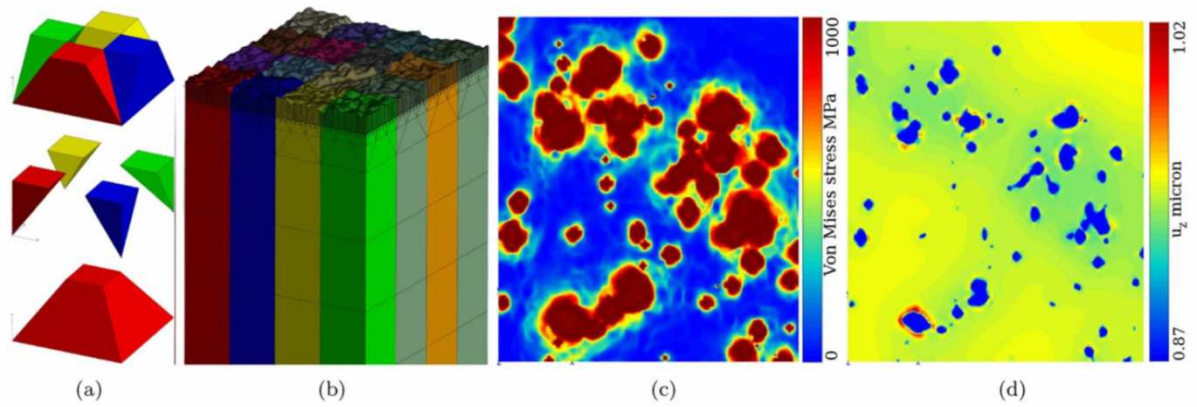

Figure 1.32 - Full finite element analysis: a) representation of the transition mesh allowing an efficient refinement from 1 to 9 elements; b) mesh of the rough surface 54 x 63 µm^2; c) distribution of the von Mises stress for a contact area of 6%; d) distribution of the vertical displacement for a contact area of 6% (blue regions correspond to contact area) (Yastrebov *et al*. 2011).

1.3.4. Lubricated contacts

In the previous sections, dry contacts have been the focus. In practice, the overwhelming majority of rolling/sliding engineering surfaces are lubricated in some shape or form. In general terms, three types of lubrication can be considered: boundary, mixed and hydrodynamic lubrication as shown in Figure 1.33. Boundary lubrication refers to situations where a lubricant is present between contacting surfaces, but does not act hydrodynamically in any way (BP 1969). In hydrodynamic lubrication, the geometry and motion of the surfaces combined with the lubricant viscosity combine to generate a lubricant film that completely separates the surfaces. In between these regions is mixed, or partial lubrication, where a lubricant film is present but is insufficient to separate the surfaces effectively, resulting in asperity contact (Teer and Arnell 1975b). This may be through

design or during starting up or shutting down, where the speed is insufficient to generate the required film thickness. Much research has been done investigating these lubrication regimes and the principles involved. However, much of the work on boundary and full film hydrodynamic lubrication is outside of the scope of this thesis. Therefore, the focus of this section will be predominantly on the mixed lubrication regime, the transition region between lubrication regimes, where both load carrying films and asperity contacts occur.

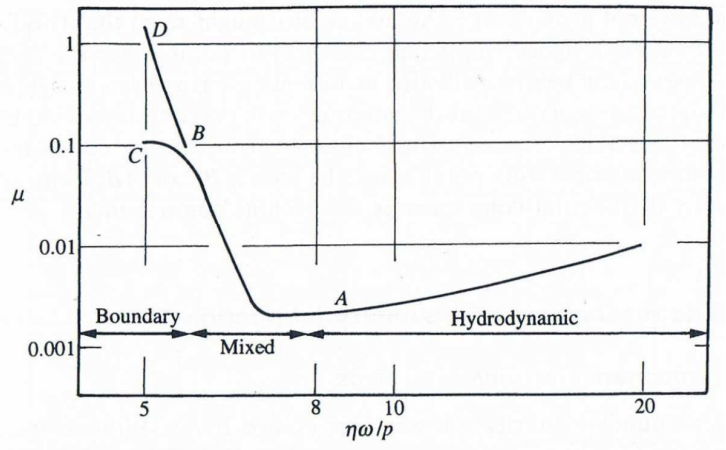

Figure 1.33 - The Stribeck diagram for a journal bearing. η is the lubricant viscosity, ω the rate of rotation, and p the nominal bearing pressure (Williams 1994).

In ideal conditions, the combination of load, speed, lubricant viscosity and surface roughness may allow surfaces to operate under full elastohydrodynamic films. The film thickness can be determined from the seminal work of Dowson and Higginson (1959). As previously stated however, in practice this is not always the case, and the scale of surface roughness features can be of the order of, or greater than, the predicted film thickness and asperity interaction can occur (Chow and Cheng 1976; Snidle *et al*. 1984). Furthermore, when analysis of EHL has taken place, it has been shown that "side-leakage" can result in thinner lubricant films than predicted (Karami *et al*. 1987; Barragan de Ling *et al*. 1989).

Some of the earliest work in tackling the mixed lubrication problem were studies by Zhu and Hu (1999; 2001a; 2001b) and Hu and Zhu (2000) who developed a numerical model for lubricated

contacts with thin films. Their results showed a considerable amount of direct contact occurring between the two surfaces. The model was later extended to consider the wear of surfaces operating under such lubrication regimes, assuming that wear took place at locations of direct contact as a form of running-in (Zhu *et al*. 2007). The modification of surface geometry was shown to reduce the subsurface elastic stresses. No material yielding behaviour was considered.

Jiang *et al*. (1999) created a numerical EHL model that considered the contact of asperities. Three dimensional roughness was taken from an as-manufactured surface and the contact behaviour of the lubricated contact investigated. A self-admitted crude form of elastic plastic behaviour was used for the asperity contacts, with contact pressures limited by the hardness. No asperity deformation was considered in the analysis. The amount of direct surface contact was found to vary dependent upon the contact conditions. This was expressed in terms of a non-dimensional velocity, U^*, a function of rolling speed, lubricant viscosity, elastic material properties and surface curvature. The variation of contact area ratio can be seen in Figure 1.34.

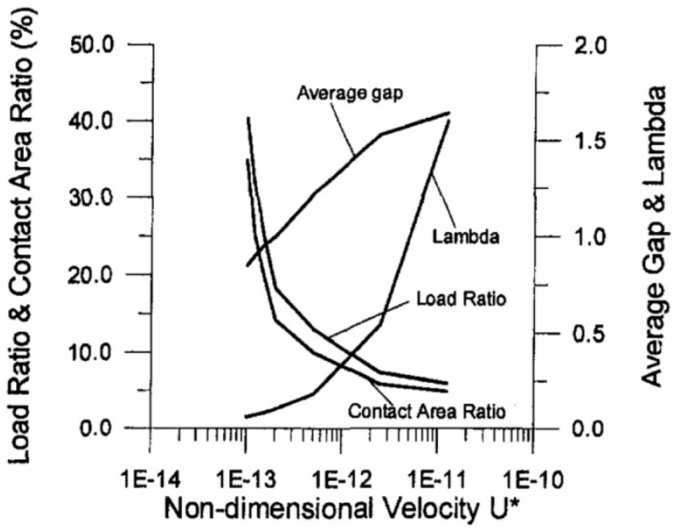

Figure 1.34 - Effects of non-dimensional velocity on performance characteristics of mixed lubrication with pure rolling mode (Jiang *et al*. 1999).

Tao *et al*. (2003) performed numerical analysis using roughness profiles taken from standard steel FZG (*Forshungsstelle für Zahnräder und Getriebebau* - The Gear Research Centre at the Technical

University of Munich) test gears. Profiles were taken from the gear surface at multiple load stages to investigate the lubrication behaviour as the surface geometry evolved. It was found that with increased running time and increased applied load, the roughness of the surface reduced, and also resulted in reduced instances of direct asperity contact. In the penultimate load stage, no instances of contact occurred. In the final load stage considered, evidence of micropitting was found on the portion of the surface recorded. As a result, the roughness of the surface increased once more, resulting in direct surface contact again. As well as surface contact, the possibility of lubrication cavitation was investigated. The authors speculate that this may be of significance to micropitting.

Holmes *et al*. (2005) also considered surfaces with various loading and running histories. Surfaces were subject to lubricated contact analysis with a range of slide/roll ratios, ξ. It was found that increased sliding velocities resulted in reduced counts of contact events, as shown in Figure 1.35a. This would suggest high sliding speeds are preferential for the reduction of direct surface contact, although the authors warn that the effect of this on other phenomenon was not considered. It was found that reduced surface roughness resulted in significantly less contact events also. It can be seen in Figure 1.35b that the regions where high frequency of direct surface contact has occurred correspond strikingly with the dark region of surface scuffing in the corresponding experiment. As lubricant passes through the contact, roughness features transverse to the entrainment direction cumulatively degrade the EHL film until complete breakdown, and localised dry surface contact occurs. This correlates with typically regions in where scuffing occurs, towards the end of the active contact (Snidle and Evans 2009).

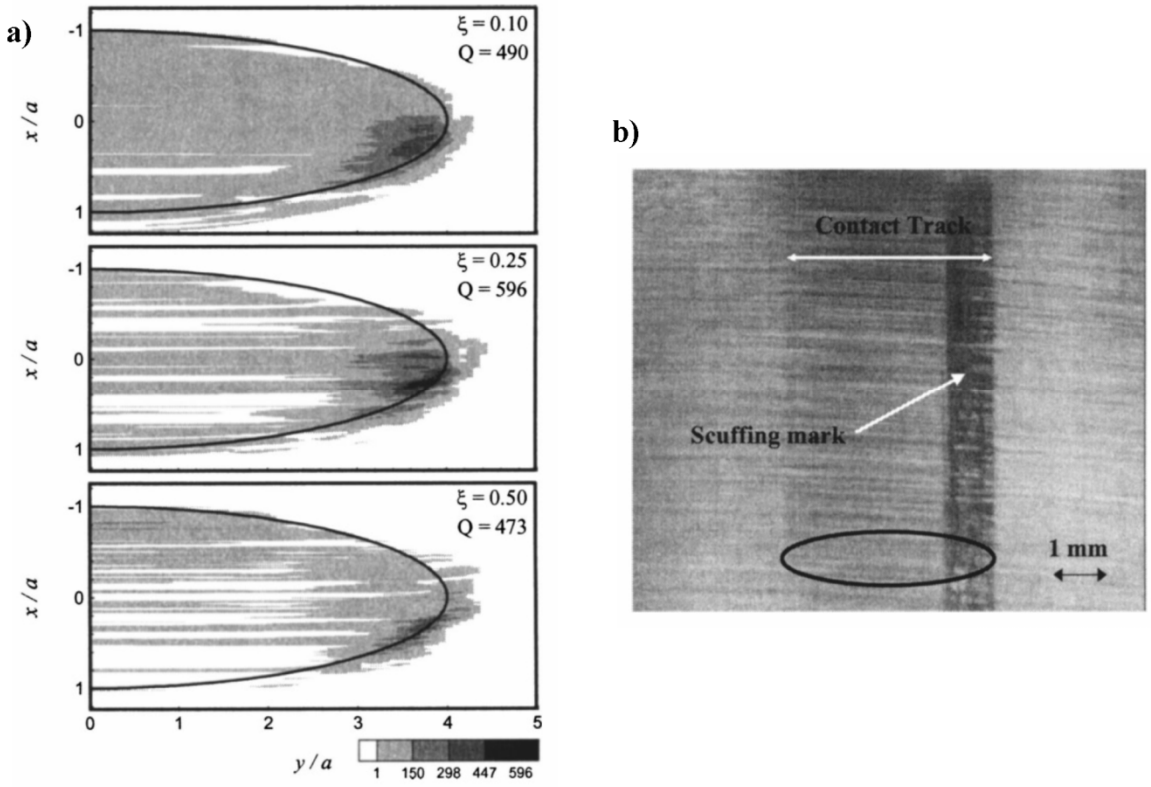

Figure 1.35 - a) Contours of contact count rate Q/ms for the transient analysis of two surface having Profile (C). The heavy curve indicates a Hertzian dry contact area. b) A photograph from the experimental scuffing program shown a track subject to scuffing damage. Also shown in the Hertzian contact ellipse for the operating load at which scuffing occurred (Holmes *et al*. 2005).

1.3.5. Implications for surface operating life

1.3.5.1. Running-in

Running-in is a process that most contacting surfaces undergo at the beginning of their operating life. The most prominent asperities are subject to combinations of normal and tractive loadings that exceed the elastic limit. This loading results in the modification of the surface by what is reported to be a combination of wear and plastic deformation (Teer and Arnell 1975; Johnson 1995; Hutchings 2003). The resulting finish has a significantly skewed height distribution, with valley features retained and asperity peaks less prominent and more rounded. Subsequent changes to the surface may occur as a result of mild wear processes that take place on a longer timescale. The interest in running-in for this project is the effect of the process on residual stresses at, or near, the surface

that could be a significant factor in fatigue damage calculations and thereby affect the life of the surfaces.

Barber *et al*. (1987) performed experimental testing aimed at investigating the running-in process as well as scuffing, on a number of surfaces, with a range of R_a values achieved using honing and polishing techniques. In the running-in tests, piston rings were contacted with cylinder liner materials under a constant nominal contact pressure for a period of two hours. It was found that the majority of the surface modification occurred within the first ten minutes of running, with the roughness reduced and increased skew of the surface height distributions. The progress of the R_a value can be seen in Figure 1.36. In these tests, the coefficient of friction between the surfaces was found to decrease alongside the reduction in roughness. Throughout the study, no reference to plastic deformation was made.

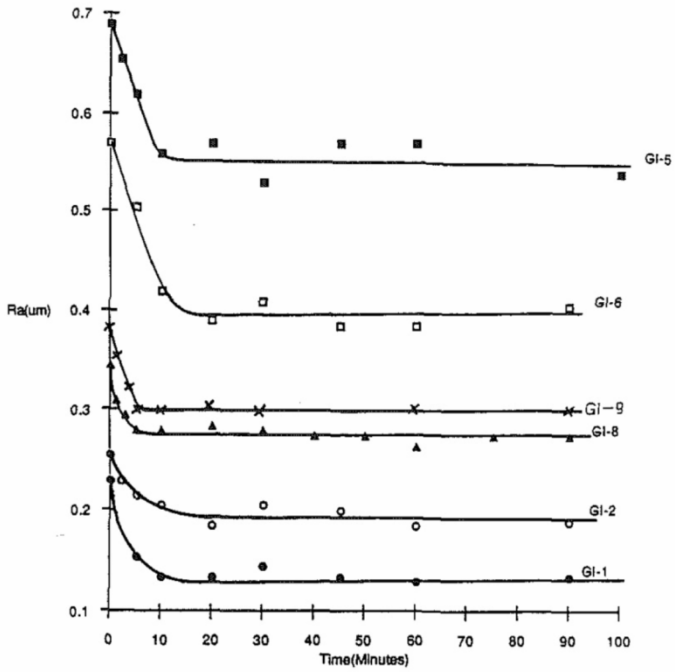

Figure 1.36 - R_a versus time of running in "normal" wear test for GI specimens (Barber *et al*. 1987).

Using a ring-on-flat test and a mathematical model, Liang *et al*. (1993) considered asperity plasticity in relation to the contact pressures. Plastic flow was considered to occur in an asperity if the contact

pressure exceeded $0.6H$ (Tabor 1951). The frequency of asperities with such contact pressures was found to decrease across the time period of five hours considered. As such, it was proposed that the proportion of the surface undergoing plastic behaviour reduced with running time. The largest reduction was found to occur quite early in the operating period.

Nonetheless, in recent work by Horng *et al*. (2002), running-in is still predominantly referred to as a wear process, with little reference to plastic deformation. Experimental disk on block tests were performed, using a range of loads and surface finishes. Figure 1.37 shows the effect of different loads on the same surface finish. It can be seen that a higher applied load results in a larger change in surface geometry, while also achieving a steady state after less operating time. The disk, or upper specimen, was finished to a significantly smaller average roughness and was found to undergo little to no change in surface geometry. With increased running time, the contact width and real contact area was found to increase, while at the same time the friction coefficient was found to decrease. Contact resistance was also found to increase, which alongside the reduction in friction coefficient, suggested improved lubrication between the surfaces.

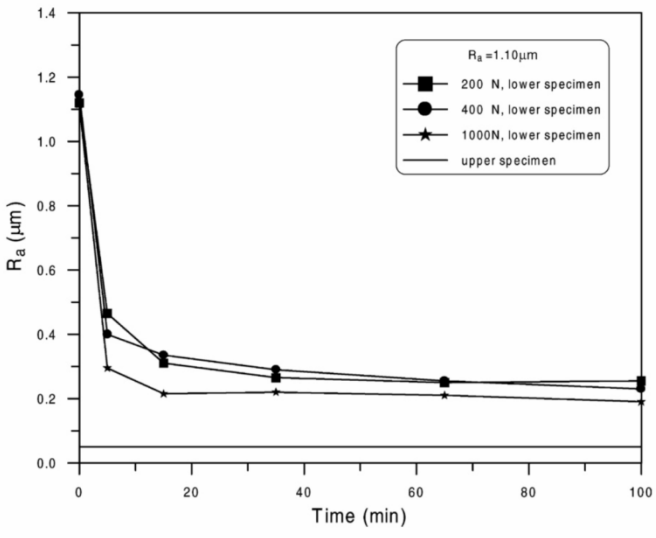

Figure 1.37 - Variation of average roughness value of both specimens at initial roughness of 1.10 μm with different applied loads (Horng *et al*. 2002).

Jeng *et al*. (2004) also offer little explanation of running-in as a result of plastic deformation. Figure 1.38 shows an SEM photograph of a worn engine bore. Jeng *et al*. (2004) suggest that as no smear phenomenon are evident and the honing manufacturing marks are still visible, no significant plastic deformation has occurred. However, these manufacturing marks are local valley features, while previous discussion of rough surface contact has shown most plastic deformation to occur at the asperity tips. The lack of smearing phenomenon means little tangential deflection of asperities has occurred. But this does not rule out normal deformation which would be expected to occur under lubricated conditions.

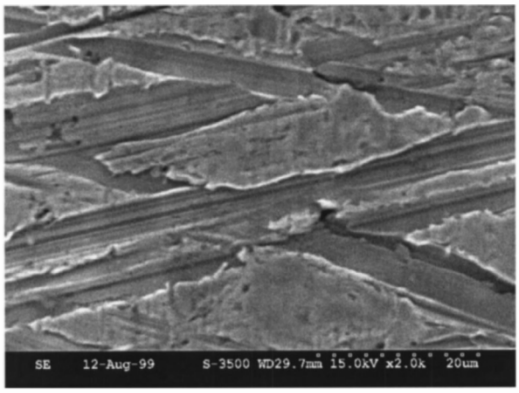

Figure 1.38 - SEM photo of worn engine bore, x2000 (Jeng *et al*. 2004).

Bosman *et al*. (2011) use both an elastic-plastic contact solver and a friction model in their semi-analytical method to describe the running-in process. However, the authors state how the model is based upon the assumption that the plastic deformations are small, and so the results of the semi-analytical method are unreliable for large plastic strains.

1.3.5.2. Surface failure

In discussing the running-in process, the early stages of the operating life of a contacting component have been covered. In this section, the end of the operating life will be considered by looking at work that investigates the causes of surface failures, such as surface fatigue, surface cracking, pitting

and micropitting. Relatively modern reviews that cover a wide range of these failure mechanisms can be found in work by Höhn and Michaelis (2004) and Olver (2005).

Early investigations of these types of surface failure mechanisms were performed by Way (1935), Dawson (1961; 1962; 1968) and later Onions and Archard (1974). One of the dominant themes in these studies was that lubricant film thickness and surface roughness affect the operating life of a surface. Thicker lubricant films, and thus reduced asperity contact, and smoother surface finishes were found to prolong surface life (Way 1935). Dawson (1962) showed that the number of cycles before pitting failure occurred was linked to a non-dimensional parameter, D, where:

$$D = \frac{combined\ surface\ roughness}{lubricant\ film\ thickness}$$

Onions and Archard (1974) evaluated the use of disk testing machines, as used in previous studies, to determine the life cycles of real gear surfaces. For this purpose, both a gear rig and disk rig were used to perform experiments on surface operating life. Each showed similar trends in behaviour to those previously found, that rougher surfaces and thinner lubricant film thicknesses adversely affect surface life, as illustrated in Figure 1.39. However, it was also found that the disk test rig was found to overestimate surface operating life, and that surfaces of gears were found to fail earlier than predicted. This difference was attributed to the dynamic loading experienced by gear tooth surfaces.

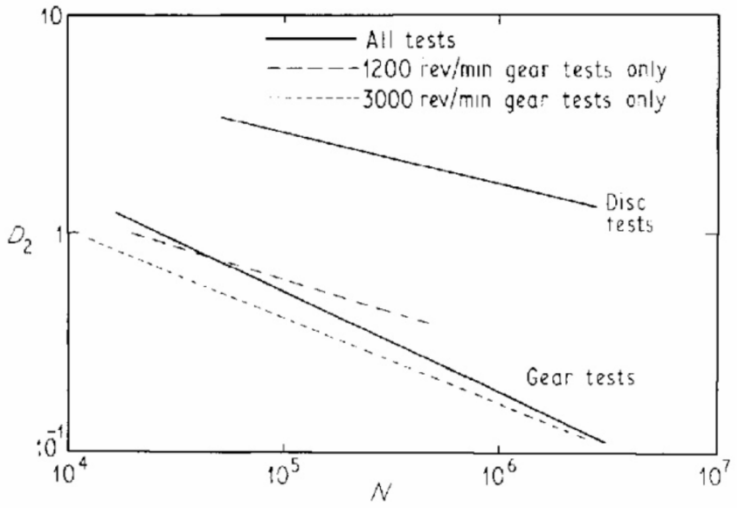

Figure 1.39 - Comparison of pitting tests on gears and on disks. The graph shows values of D_2 as a function of N. For clarity the experimental points have been omitted and the regression lines only plotted (Onions and Archard 1974).

Miller *et al*. (1985) used numerical and analytical methods to assess surface cracking from a fracture mechanics perspective. The authors highlight a number of simplifications in their analysis, choosing not to include such factors as material plasticity. Crack growth was found to occur in two phases, the slow propagation phase, followed by rapid growth to failure. Between the surface stresses and subsurface stresses, caused by asperity and Hertzian contact effects respectively, a "quiescent zone" was found. Failure was found to occur when this zone was bridged somehow, in this study by inclusions in the material, leading to accelerated crack growth and pit formation.

The progression of crack growth was investigated by Zhou *et al*. (1989) in rolling and sliding contacts. An analytical model was used to superimpose asperity contact stresses on Hertzian contact stresses, and crack initiation and propagation were investigated alongside fatigue life and micropitting. Increased contact pressure resulted in earlier crack initiation and swifter crack propagation, resulting in reduced operating life. This is illustrated in Figure 1.40. The effect on crack initiation is particularly pronounced, so much so that the propagation of the crack becomes the dominant factor in the fatigue life of the surface.

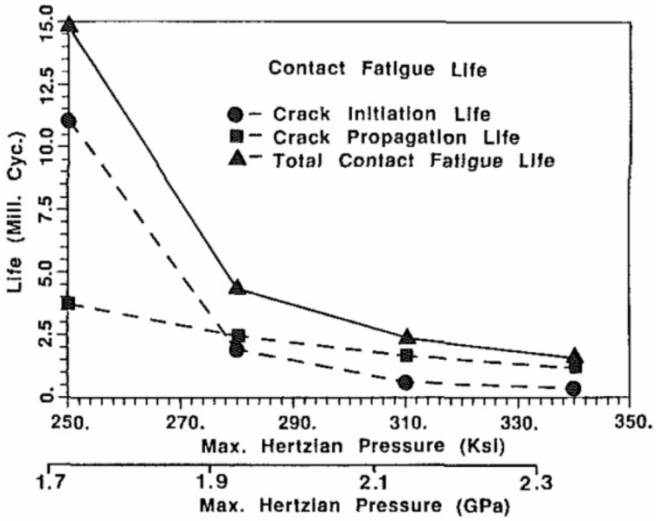

Figure 1.40 - Contact fatigue life from crack initiation to crack propagation (Zhou *et al*. 1989).

Beghini *et al*. (1992) used finite element analysis to determine the residual stresses in an elastic-plastic axisymmetric body, with an additional hemispherical "bump" at the centre of the contact to model a single asperity. The geometry of this asperity bump was altered in height and the residual stresses used in an elastic fatigue analysis based on that of Ioannides and Harris (1985). A range of different configurations were considered including the smooth and asperity geometry body with and without residual stress to determine the effects on fatigue life. The fatigue life was found to be most affected when the elastic stresses in the fatigue analysis interacted with the residual stresses from the elastic-plastic contact. Significantly smaller differences were found where little interaction occurred. Larger, sharper asperity features and increased contact pressures were found to reduce the fatigue life of the surface in comparison to the smooth surface.

Abudaia *et al*. (2005) also used finite element software to investigate the loaded and residual stresses of a spherical indentation. At the contact edge, the hoop stress under load was found to be compressive, and tensile once removed. Both the loaded and residual radial stress was found to be tensile. An experimental study of indentations was performed alongside this analysis to link these results to formation of surface cracks at the contact edge. Both ring and radial cracks were found to

occur, with the former occurring more frequently at lower loads. Both were commonplace at higher loads. This difference may be attributable to the cyclic nature of the hoop stress at the surface as load is applied and removed. Both types of cracks were found to be more severe in depth and length as a result of increased loads. The effect of shot peening on crack formation was investigated in this experimental study, with the induced compressive stresses thought to be protective. Shot peened surfaces were found to have fewer cracks.

The results of these studies have shown how surface cracks can initiate and propagate. Pitting and micropitting surface failures are associated with the growth of these cracks until small sections of the surface are detached. As the name of each failure suggests, the mechanisms are similar. Micropitting is generally limited to the surface region, of the order of up to 10 µm (Höhn *et al*. 1996), while pitting is typically of the order of the contact dimension (Olver 2005). Micropitting has come to forefront of modern gear research as a result of improvements in material production as well as gear manufacture. These developments have resulted in reduced frequency of stress raisers such as material inclusions that had previously resulted in gear failure. As these have been reduced so significantly, other forms of failure have become more prominent, in particular micropitting.

Oila and Bull (2005) performed a comprehensive experimental study of the contact of two disks, investigating the effect of a number of factors on micropitting. The factors considered were material, surface finish, lubricant, load, temperature, speed, and slide/roll ratio. The applied load was found to be the dominating factor on the initiation of micropitting. Speed and the slide/roll ratio were found to be the factors that most affected the propagation of micropitting failure. Also investigated was the effect of martensite decay (Swahn *et al*. 1976), where heat generated due to plastic deformation results in a phase transformation of material. This results in regions of stress concentrations and preferential sites for crack initiation and propagation. The steel which exhibited a greater degree of martensite decay in the experiments showed greater propensity to micropitting, suggesting a link between the two phenomena.

A factor that was not included in this study was the chemistry of the lubricant, rather than just the properties. Townsend *et al*. (1986) performed spur gear endurance tests that suggested that different types of additives used for the same purpose could affect the surface fatigue life in different ways. Phosphorous-type additives used to improve the load carrying ability of the lubricant were found to significantly improve the fatigue life of the surface. Sulphur-type additives also specified to increase the load carrying ability showed no effect. More modern work by Benyajati *et al*. (2003), Lainé *et al*. (2008) and Meheux *et al*. (2010) also considered the effects of additives the lubricants applied to such surfaces. It was found that additives that are included to reduce wear or reduce foaming in the lubricant can have a negative effect of the lubrication mechanism, and in turn promote micropitting. Micropitting can be seen as highly dependent on surface chemistry (O'Connor 2005).

Ahlroos *et al*. (2009) also performed a study of factors influencing micropitting and frictional performance, considering material, surface treatment and roughness, and lubricant types. Surface roughness was found to have a large effect on the amount of micropitting observed. Throughout the investigation, micropits did not occur on any of the polished surfaces (R_a ≈ 0.04 μm). Surface treatments were also found to affect micropitting performance. Three treatments were considered: carburising, carbonitriding as well as a diamond-like-carbon (DLC) coating. The DLC coated surfaces were found to have low coefficients of friction, and during the experiments effectively polished themselves, resulting in no micropits. Carbonitrided surfaces performed better than carburised surfaces, despite each being hardened to the same approximate hardness. The authors attribute this to the reduction of martensite decay of the surfaces subject to carbonitriding. The alloying nitrogen gives the material increased tempering resistance, resulting in reduced martensite decay and micropitting.

Bull *et al*. (1999) also found nitrided surfaces to improve micropitting performance. Carburised and nitrided gears were run against each other and the surface failure mechanism determined. The

contact fatigue strength of each type of gear can be seen in Figure 1.41. The carburised gears showed reduced life in comparison with nitrided gears. However, the failure mechanisms differed. Micropitting, leading to pitting was seen to occur in the carburised surfaces, while the nitrided surfaces failed by case crushing. This failure was at least partly attributed to the relatively shallow case depth of the nitriding process.

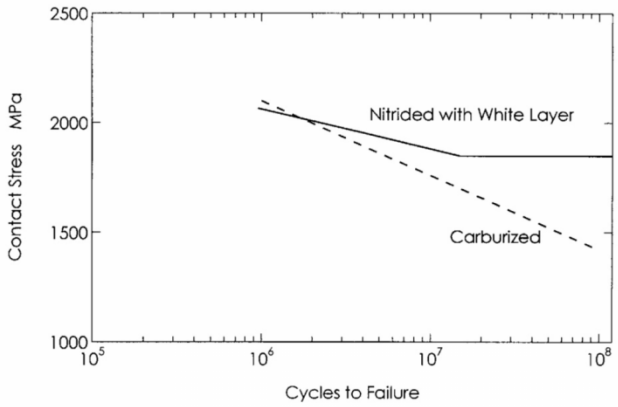

Figure 1.41 - Comparison of the surface contact fatigue strength of nitrided and carburised steel of 4.2 mm module gears. The nitrided steel contained a white layer and failed by case crushing. The carburised steel failed by pitting, believed to have developed from previously formed micropits (Bull *et al*. 1999).

D'Errico (2011) also studied the effect of different treatments on micropitting, looking at three different combinations of steel: hardened and tempered, nitrided, and carburised. Each material was tested to failure to determine characteristic mechanisms for each specification. The more ductile material, the hardened and tempered steel, exhibited micropitting. Cracks then extended deeper into the subsurface materials that the failure mechanism was classified as pitting. The carburised steel also showed micropits, with cracks initiating at oxides at grain boundaries, i.e. the most brittle regions. Cracks occurred in the surface layer, or white layer, of the nitrided material, but extended no further, resulting in only superficial cracks. This shows agreement with the previous study where the additional alloying nitrogen improves micropitting resistance.

Moorthy and Shaw (2013) performed gear tests and observed that the features of the rough surface can be a factor in micropitting. The occurrence of micropits was found to align with the location of

local valley features. These local valley features act as stress concentrations that can lead to the initiation of cracks and result in micropitting failure. The shape and orientation of the valleys in relation to the sliding direction can also be factor. Polishing of surfaces or surface coatings can reduce the severity of valley features, offering some protection against micropitting.

1.4. Summary

A thorough survey of the current literature has been performed. It has been show that in lubricated surfaces, asperity contact can still be remarkably common place, and that these contacts can significantly affect operating life. While a wide range of contact configurations has been considered, including single contacts and stochastic and idealised models of rough surfaces, the analysis of real rough surface contacts is, relatively, still in its infancy. The growing availability of computational resources is making finite element analysis of such problems increasingly viable.

The work in this thesis is part of ongoing research within the research group, investigating contacts operating in mixed lubrication regimes. The aims were to develop finite element analysis techniques, initially verified using single contact results available in the literature. These methods will be developed to allow modelling of rough surface contacts enabling the determination of residual stresses as a result of surface geometry changes due to asperity contact and deformation. These residual stresses are thought to be significant in the fatigue life of gear tooth surfaces, contributing to such failure mechanisms as micropitting.

The closest collection of work to these objectives has been published by Jamari and colleagues (Jamari and Schipper 2006a; 2006b; 2007a; 2007b; Jamari *et al*. 2007; Jamari and Schipper 2008). Using the contact of single hemispheres and experiments to verify their methods, the contact of rough surfaces was investigated. Good agreement was found between their analysis and experiment. However, to date no detailed discussion of residual stresses as a result of these changes has been discussed by the authors.

Finite element analysis of the contact of smooth surfaces

2.1. Introduction

This chapter describes the methods used for elastic-plastic contact modelling using the Abaqus Finite Element (FE) package. Initially, a purely elastic contact model was created for comparison with Hertzian theory as a check on modelling techniques. A review of the existing literature revealed multiple finite element studies of single point contacts (contact of a deformable hemisphere), with either rigid or deformable counter surfaces. Some of this work was used to verify the correct use of the software in the current project. The verification study was performed using an axisymmetric model of the nominal point contact between a deformable elastic-plastic hemisphere and a rigid flat for direct comparison with the work of Jackson and Green (2005). The study was then extended to a plane strain model of a line contact between a deformable elastic-plastic half cylinder and a rigid flat (Bryant *et al*. 2012). Early studies of elastic-plastic indentation of a deformable half-space using FE methods were reported by Hardy *et al*. (1971) and Lee *et al*. (1972) for the case of indentation by a rigid sphere, and by Dumas and Baronet (1971) for indentation by a rigid cylinder. More recently, the contact of deformable spheres and cylinders has also been subject to further scrutiny (Kogut and Etsion, 2002; Jackson *et al*, 2005; Green, 2005; Shankar and Mayuram, 2008), albeit with more focus on the axisymmetric problem. In contrast this research focuses upon two dimensional, line contacts. This approach to modelling contact is more relevant to ground gears where the surface finish is generally consistent with a two dimensional, plane strain simplification. A sinusoidal surface contact model was used as the first foray into simulating more complex contacts whereby neighbouring contacting features can give interacting stress distributions and deformations. The elastic sinusoidal surface contact was first verified by comparison with analytical solutions by Westergaard (1939) and Johnson (1985) before elastic-plastic material properties were introduced.

2.2. Introduction to Abaqus contact modelling

2.2.1. Using Abaqus/CAE (v6.10)

Figure 2.1 shows the graphical user interface of Abaqus/CAE version 6.10 upon initial start up of the software. Abaqus has a number of ways in which modelling and presentational tools can be utilised and these are explained in more detail in the Abaqus User's Manuals (Abaqus 2010a). As with the majority of Windows programs, across the top of the window is the tool bar. In Abaqus, this is content sensitive and the options presented change depending on the current task that the user is trying to achieve. This is dependent on which module is currently selected. The modules are listed in the drop-down menu in Figure 2.1, as well as in Table 2.1, which details the function and key features of each module. When a different module from this drop-down menu is selected, the options available on the tool bar change. However, most of the basic modelling options can be achieved by using the buttons directly alongside the modelling viewport. At the left of the screen is the model tree. This can be navigated by expanding the available options and clicking the relevant title to access the appropriate modelling tool menus.

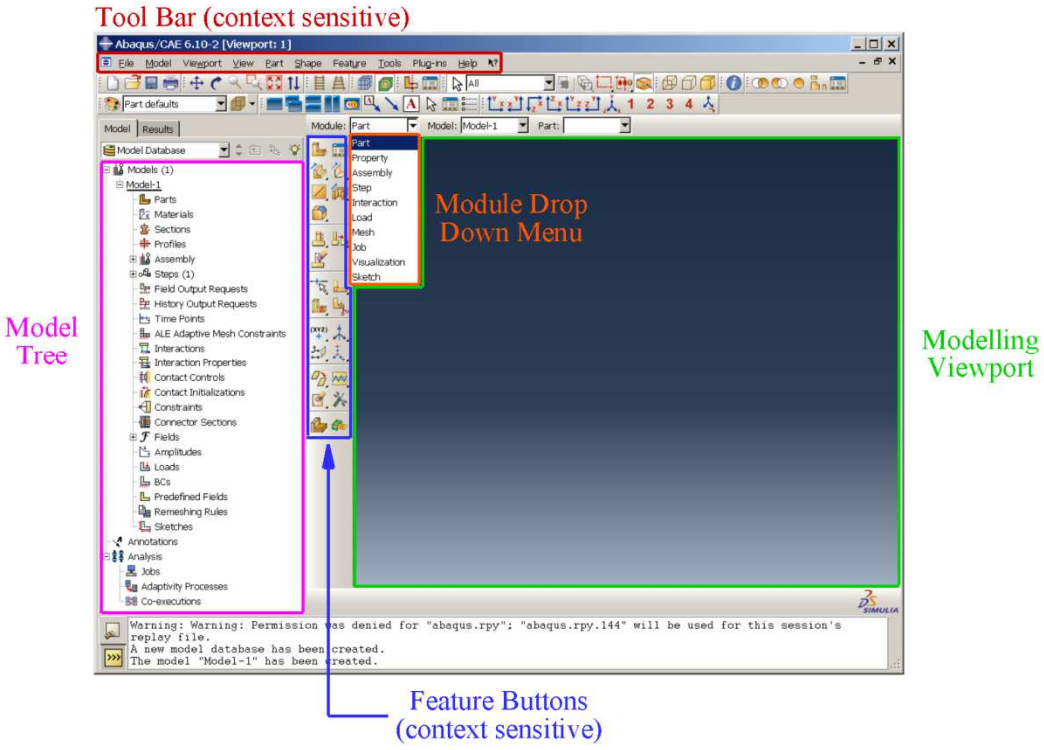

Figure 2.1 - Graphical user interface of Abaqus/CAE v6.10 upon start up.

Table 2.1 lists the modules available in Abaqus/CAE v6.10 and explains their basic functions and key features. There are significantly more tools and settings available within the program, and those used within the work of this thesis are detailed when their use is discussed.

Table 2.1 - Outline of Abaqus/CAE v6.10 modules.

Module	Description	Key Features	
Part	Used to define geometry of parts. Simple CAD functions are available, but files can be imported from more advanced CAD packages such as SolidWorks.	Create Part	Create deformable and rigid 2D and 3D parts.
		Regenerate Features	If changes are made to a part, assembly, etc, the features must be regenerated for the changes to take effect.
		Create Partition	Split created parts into regions which can make applying properties, loads, boundary conditions simpler, and give more control over meshing.
Property	Used to create materials and sections, and apply them to created parts.	Create Material	Define material properties.
		Create Section	Define cross sectional properties.
		Assign Section	Each part or region must have a section assigned to it.
Assembly	Insert parts into an assembly as "instances", which can then be manipulated individually.	Instance Part	Insert instances of created parts into the assembly.
		Translate/Rotate Instance	Position each instance as required within the assembly.
Step	Steps are essentially intermediate points within the simulation where parameters can be altered.	Create Step	Create intermediate steps within the simulation and define the way each one will be solved.
		Create Field Output	Choose which outputs are required in each step of the simulation.
Interaction	Define interactions between parts in the assembly, such as contact interactions.	Create Interaction	Select potentially interacting surfaces and define how the simulation will treat them.
		Create Interaction Property	Define the details of the interactions of part surfaces.
		Contact Controls	Advanced contact settings.
Load	Used to create loads and boundary conditions.	Create Load	Define type of loading and application region.
		Create Boundary Condition	Define type of boundary condition and application region.
Mesh	Create finite element meshes on parts.	Seed Part Instance	Sets a global mesh seed that is applied to all edges on the selected part.
		Seed Edge	Define a mesh seed on a selected edge.
		Mesh Part Instance/Region	Create mesh based on currently applied mesh seeds.
		Assign Mesh Controls	Select element shape and meshing technique for selected part or region.

Mesh (continued)	Create finite element meshes on parts.	Assign Element Type	Choose type of elements to be used in selected part or region.
		Verify Mesh	Assess mesh quality based on element shape and size. Check for potential analysis problems.
Job	Create jobs for submission, write input files and monitor running simulations.	Create Job	Create jobs for analysis.
		Monitor	Check progress of currently running job.
Visualization	Show requested field outputs after (or during) a simulation.	Plot Contours on Deformed Shape	Quickest and simplest way of viewing results of a simulation.
Sketch	Similar to the part module, but just the CAD drawing tool.	Create Sketch	Opens the CAD drawing tool, without subsequently creating a part. Sketches can be opened in the Part module.

2.3. Hertzian single point contact

2.3.1. Material elasticity and elastic contact

Elasticity is concerned with the determination of stresses and strains in bodies as a result of applied loads, such that the body reverts to its original state upon load removal (Barber 2002). Hooke's Law provides a general description of elasticity where stress is proportional to strain.

$$\sigma \propto \varepsilon \qquad \text{Eq. 2.1}$$

The constant of proportionality in this equation is the elastic modulus, or Young's modulus, E.

$$\sigma = E\,\varepsilon \qquad \text{Eq. 2.2}$$

This equation describes the relationship between direct stresses and strains. The relationship between shear stresses and strains is expressed using a similar constant of proportionality, the shear modulus, G (Ford 1963).

$$\tau = G\,\gamma \qquad \text{Eq. 2.3}$$

Both the elastic modulus and shear modulus are inherent material properties, and, in isotropic materials, are related by Poisson's ratio, ν (Callister 2003).

$$E = 2\,G(1+\nu)$$ **Eq. 2.4**

Poisson's ratio is defined as the ratio between strains in the transverse and axial directions. For example, in a simple uniaxial tensile test, a positive strain is observed in the axial (z) direction; the direction of the applied load. Simultaneously, strains proportional to the axial strain are produced in the directions normal to the applied load (Ford 1963).

$$\nu\,\varepsilon_{zz} = -\varepsilon_{xx} = -\varepsilon_{yy}$$ **Eq. 2.5**

$$\nu = -\frac{\varepsilon_{xx}}{\varepsilon_{zz}} = -\frac{\varepsilon_{yy}}{\varepsilon_{zz}}$$ **Eq. 2.6**

Contact of purely elastically behaving bodies was comprehensively studied by Hertz (1882). While much of this work focussed upon elliptical contacts, solutions for line contacts have also been found (Johnson 1985). A summary of the formula to calculate key contact details for both point and line contacts are shown in Table 2.2.

Table 2.2 - Elastic contact formula for point and line contacts.

	Point Contacts	**Line Contacts**
Contact Dimension, a	$a = \sqrt[3]{\frac{3}{2}\frac{R\,w}{E'}}$	$a = \sqrt{\frac{8}{\pi}\frac{R\,w'}{E'}}$
Max. Contact Pressure, p_0	$p_0 = \frac{3\,w}{2\,\pi\,a^2}$	$p_0 = \frac{2\,w'}{\pi\,a}$
Elastic Approach Distance / Interference, ω	$\omega = \frac{a^2}{R}$ $\omega \cong 1.31\sqrt[3]{\left(\frac{w^2}{R\,E'^2}\right)}$	N/A
Where	$\frac{2}{E'} = \frac{1-\nu_1^2}{E_1} + \frac{1-\nu_2^2}{E_2}$	$\frac{1}{R} = \frac{1}{R_1} + \frac{1}{R_2}$

2.3.2. Modelling details

Familiarity with the basic tools and functions of Abaqus was gained by performing some basic contact modelling. In the Abaqus Benchmarks Manual (Abaqus 2010b), a Hertzian contact problem is available (Section 1.1.11). It provides a guide to creating and running simple contact problems. Using the benchmark problem as a reference, a study was performed to assess two properties crucial to creating accurate contact models. The suitability of linear and quadratic elements for contact problems and the choice of node-to-surface and surface-to-surface surface discretisation were also assessed. While both linear elements and surface-to-surface contact are recommended by the Users Manuals, the study was performed to provide a greater appreciation of these recommendations. The results of each of the simulations were compared with the Hertzian theory for the defined geometry and material properties.

Figure 2.2 shows a representation of two dimensional linear and quadratic elements, with nodes depicted by black circles. The linear element has nodes located at the corners, while the quadratic elements have corner nodes and nodes at the midpoint between corners. Linear elements approximate variables over the element linearly, whereas quadratic elements use a quadratic approximation, allowing a nonlinear variation of output variables across a single element. In general applications, quadratic elements are recommended as they provide a higher accuracy than linear elements (Abaqus 2010a). Geometric features are better represented, and stress concentrations more effectively analysed using quadratic elements. However, for more complex problems, such as those than consider contact, impacts, or severe element distortions, linear elements are recommended. Quad4 (linear) and Quad8 (quadratic) elements will both be used in the analysis to determine the effect of choice of element.

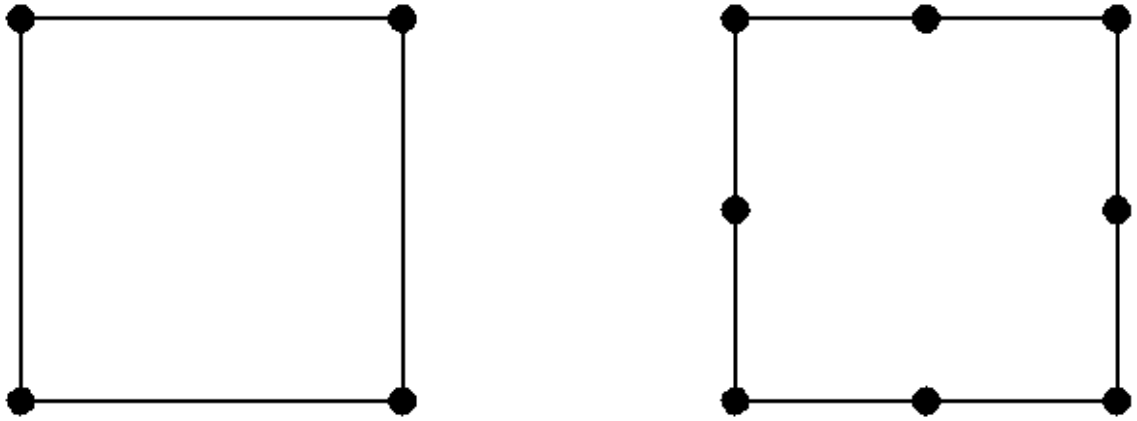

Figure 2.2 - Two dimensional linear (left) and quadratic (right) elements.

The contact discretisation method determines how Abaqus applies constraints at surface locations to effectively simulate contact between surfaces. Two options exist for contact discretisation; node-to-surface and surface-to-surface. Each method requires the definition of the two contacting surfaces to be defined as either the master or slave surface. Contact in Abaqus is based upon the interactions and constraints applied to master and slave surfaces and unreasoned designation can give incorrect results. While further reference should be sought from the Abaqus User's Manual (Abaqus 2010a) , in general it is recommended that the master surface be assigned to the larger body, the stiffer surface (including structural considerations, not only material) or the surface that consists of the coarser mesh.

Node-to-surface contact is where an individual node on the slave surface interacts with a point of projection on a nearby facet on the master surface. The contact direction is determined only by the normal of the master surface, and the shape and normal of the slave surface are not relevant to the contact formulation. Slave nodes are restricted from penetrating into the master surface, while master nodes are not explicitly restricted from penetrating the slave surface. This can be mitigated to some extent by ensuring that the slave surface mesh density is sufficiently fine, preventing larger magnitude penetration.

Surface-to-surface contact takes into account the shape of both the master and slave surfaces in the contact formulation. The contact conditions are enforced in an average sense over regions of the contact. Contact at an individual node is still predominantly focused on the node in question, but also considers neighbouring slave nodes. Small penetration is still possible, but the likelihood of large localised penetrations is reduced as penetration is resisted in an average sense across a region of the surface.

Table 2.3 summarises the specifications of the Hertzian point contact model. The model consisted of a deformable 50 mm radius half hemisphere, created using an axisymmetric model, loaded against a rigid flat plane. Typical elastic properties of steel were applied to the half hemisphere; E = 200 GPa and ν = 0.3. Boundary conditions were applied in the "Initial" analysis step required by the software. This step is reserved for applying boundary conditions only; no loads can be applied during set up of the model. In this step the rigid flat plane was restrained in all directions. No boundary conditions were required for the hemisphere. By defining the part as axisymmetric, Abaqus implements appropriate restraints to the part corresponding to the defined rotational axis of symmetry. In the subsequent analysis step, contact was initiated by applying a pressure to the top free edge of the deformable hemisphere.

Table 2.3 - Hertzian point contact model summary.

Part	Axisymmetric 2D Quarter Circle; Radius, r = 50 mm → Half Hemisphere
	Line Segment → Rigid Flat Plane
Property	E = 200 GPa, ν = 0.3
Assembly	Lines of axisymmetry aligned. Parts on the verge of contact
Step	Initial (required), Contact
Interaction	Frictionless
	Small Sliding
	Node-to-Surface and Surface-to-Surface
Load	1 MPa pressure acting on top edge of hemisphere
Boundary Conditions	Rigid Flat Plane - Encastre ($U_x = U_y = U_z = UR_x = UR_y = UR_z = 0$)
Mesh	Partitioned around contact area
	Axisymmetric Stress Elements
	Linear and Quadratic Elements

2.3.3. Loaded result comparisons

Table 2.4 shows the results of the initial elastic study, comparing the contact area, a, and maximum contact pressure, p_0, obtained using the two different element types and surface discretisation methods. The contact dimension and maximum contact pressure calculated by using Hertzian theory are also shown. The contact pressure profiles for each combination are shown in Figure 2.3.

Table 2.4 - Summary of results comparing element type and surface discretisation methods.

		Contact Dimension, a / mm	**Contact Dimension Difference**	**Maximum Contact Pressure, p_0 / GPa**	**Maximum Contact Pressure Difference**
Hertzian Theory		1.103	-	3.090	-
Node-to-surface	Quad4	1.194	8.3%	4.112	33.1%
	Quad8	1.180	7.0%	0.051	98.3%
Surface-to-surface	Quad4	1.194	8.3%	3.035	1.8%
	Quad8	1.180	7.0%	25887.2	837673.5%

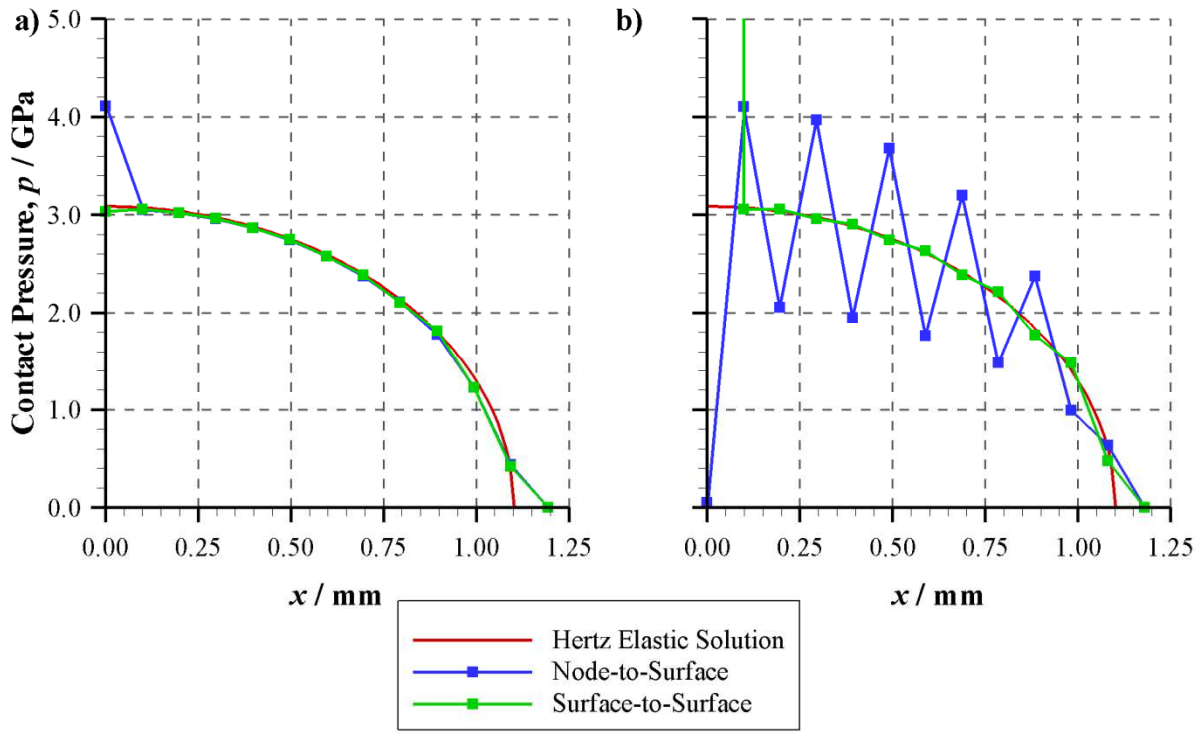

Figure 2.3 - Contact pressure plots for node-to-surface and surface-to-surface contact discretisation methods for a) Quad4 elements, and b) Quad8 elements.

The contact dimension was determined as the first node in which the contact pressure was found to be zero. The maximum potential error in determining the contact dimension is therefore the distance between the nodes at the contact edge. The mesh seedings were manipulated such that the same number of nodes was in contact for each simulation regardless of element type. It can be seen that the choice of surface discretisation method has little effect on determining the contact dimension. The result given for each method is identical when the same element type is selected.

The element type and surface discretisation method both have a significant effect on determining the contact pressure. In Figure 2.3 it can be seen that the node at the centre of the contact causes problems for each simulation except surface-to-surface contact using Quad4 elements, which accurately predicts the maximum contact pressure. It also matches the theoretical contact pressure distribution across the contact very well. Node-to-surface contact using Quad8 elements

overestimates the contact pressure at the contact centre. However, away from the centre, the pressure distribution closely follows the surface-to-surface contact results.

Similar behaviour is seen when combining surface-to-surface contact and Quad8 elements, although the contact pressure spike at the contact centre is several orders of magnitude greater, exceeding the scale plotted in Figure 2.3b. Aside from this node however, the contact pressure profile matches the theory reasonably well. The simulation combining node-to-surface contact with Quad4 elements underestimates the contact pressure at the contact centre. Unlike other simulations however, the contact pressure profile does not agree well across the contact. The profile alternates between over- and underestimating the contact pressure at the mid and corner nodes, respectively.

As a result of this study, it became clear why both surface-to-surface surface discretisation and Quad4 elements are recommended for contact problems, and as such, each of these was carried forward into the subsequent contact modelling.

2.4. Elastic-plastic single point contact

2.4.1. Material plasticity and plastic contact

In Section 2.3.1, Hooke's Law and elastic material properties were discussed, as well as contact theory based on purely elastic bodies. However, in practice, considering bodies as purely elastic is rarely sufficient. For most metals, elastic deformation continues only to strains of approximately 0.5% (Callister 2003).

Further loading results in strain that is no longer proportional to stress and is permanent. This nonrecoverable strain is known as plastic deformation. The point at which deformation changes from elastic to plastic deformation in a uniaxial test is known as the yield strength, σ_y.

While the yield strength of a material can be determined relatively simply using a uniaxial tensile test, and plotting the results on a graph of stress against strain, in more complex problems, the

states of stress are generally complicated (bi-axial or tri-axial). This has resulted in the development of several different yield criterion to determine the state of a material (Ford 1963). For isotropic plasticity, two of the most commonly used yield criteria are the Tresca (1864), and von Mises (1913) criterion.

The Tresca criterion is also known as the maximum shear theory, and it assumes that material yield will occur when the maximum shear stress reaches the value of maximum shear stress at yield under simple tension (Mendelson 1968). The maximum shear stress is given by half of the greatest difference between the principal stresses and as $\sigma_2 = \sigma_3 = 0$, the maximum shear stress is given by half the yield strength. The Tresca yield criterion can be stated as shown in Equation 2.7.

$$\frac{1}{2}\max(|\sigma_1 - \sigma_2|, |\sigma_2 - \sigma_3|, |\sigma_3 - \sigma_1|) = \tau_y = \frac{1}{2}\sigma_y \qquad \textbf{Eq. 2.7}$$

The von Mises yield criterion is also known as the distortion energy theory, and predicts that material yield will occur when the distortion energy reaches the distortion energy at yield in simple tension (Mendelson 1968). The von Mises yield criterion can be expressed in terms of direct stresses or principal stresses as shown in Equations 2.8 and 2.9 respectively.

$$\sqrt{\frac{1}{2}\left[\left(\sigma_{xx} - \sigma_{yy}\right)^2 + \left(\sigma_{yy} - \sigma_{zz}\right)^2 + (\sigma_{zz} - \sigma_{xx})^2 + 6\left(\tau_{xy}^2 + \tau_{yz}^2 + \tau_{zx}^2\right)\right]} = \sigma_y \qquad \textbf{Eq. 2.8}$$

$$\sqrt{\frac{1}{2}\left[(\sigma_1 - \sigma_2)^2 + (\sigma_2 - \sigma_3)^2 + (\sigma_3 - \sigma_1)^2\right]} = \sigma_y \qquad \textbf{Eq. 2.9}$$

Experimental studies have found that the von Mises yield criterion gave more accurate results for a range of materials, under a combined loading of tension and torsion, (Lode, 1926; Ros and Eichinger, 1929; Taylor and Quinney, 1931) and so the von Mises yield criterion is widely used today and is the basis for isotropic plastic material behaviour in Abaqus.

The von Mises yield criterion can be used to determine when material yield first occurs in point and line contacts. The maximum shear stress occurs at a depth of $z = 0.48a$ and $z = 0.70a$ for point and line contacts, respectively, with magnitudes of $0.62p_0$ and $0.56p_{0,}$ respectively (Johnson, 1985). By

setting the maximum stress to be equal to the yield strength, σ_y, the maximum contact pressure at yield can be determined to be $1.60\sigma_y$ and $1.79\sigma_y$ for point and line contacts. By rearranging the elastic contact equations in Table 2.2, the load required to cause material yield can be found. Each of these equations can be found in Table 2.5.

Table 2.5 - Plastic contact formula for point and line contacts using the von Mises yield criterion.

	Point Contacts	Line Contacts
Maximum Stress	$0.62p_0 \ @ \ z = 0.48a$	$0.56p_0 \ @ \ z = 0.70a$
Max. Contact Pressure at Yield, $(p_0)_y$	$(p_0)_y = 1.60\sigma_y$	$(p_0)_y = 1.79\sigma_y$
Load at Yield, w_c, w'_c	$w_c = \frac{2\,\pi\,a^2}{3}(p_0)_y \cong 3.75\,a^2\,\sigma_y$ $w_c = \frac{2\,\pi^3\,R^2}{3\,E'}(p_0)_y^3 \cong 118.6\,\frac{R^2}{E'}\,\sigma_y^3$	$w'_c = \frac{\pi\,a}{2}(p_0)_y \cong 2.81\,a\,\sigma_y$ $w'_c = \frac{2\,\pi\,R}{E'}(p_0)_y^2 \cong 20.1\,\frac{R}{E'}\,\sigma_y^2$
Where	$\frac{2}{E'} = \frac{1-\nu_1^2}{E_1} + \frac{1-\nu_2^2}{E_2}$	$\frac{1}{R} = \frac{1}{R_1} + \frac{1}{R_2}$

2.4.2. Modelling details

Having verified that basic modelling techniques were in place and that the model using elastic only material properties gave results in line with Hertzian theory, the next step was to introduce material plasticity. Jackson and Green (2005) performed a finite element study of contact of a deformable elastic-plastic hemisphere with a rigid flat plane, investigating the contact loads and dimensions, as well as the transitional behaviour from elastic to plastic material behaviour. Jackson and Green primarily used ANSYS for finite element modelling, although it is stated that it was found that Abaqus produced the same results. In the finite element software, contact was initiated by applying a displacement to the free edge of the deformable hemisphere towards the contact plane. This was defined as the interference. An interference of zero corresponds to the initial contact of the undeformed hemisphere at zero load. This study was used as a benchmark in order to test whether

the modelling techniques being used could generate results comparable with those already published.

In a single point contact, the approach distance, or critical interference can be calculated as in Equation 2.10.

$$\omega_c = \left(\frac{\pi\, C\, \sigma_y}{2\, E'}\right)^2 R \qquad \textbf{Eq. 2.10}$$

Where:

$$C = 1.295^{(0.736\,\nu)} \qquad \textbf{Eq. 2.11}$$

By substitution of the elastic contact formula, it can therefore be shown that the critical load and contact area are given respectively Equations 2.12 and 2.13.

$$w_c = \frac{4}{3}\left(\frac{R}{E'}\right)^2 \left(\frac{C}{2}\,\pi\,\sigma_y\right)^3 \qquad \textbf{Eq. 2.12}$$

$$A_c = \pi^3 \left(\frac{C\,\sigma_y\,R}{2\,E'}\right)^2 \qquad \textbf{Eq. 2.13}$$

Following Jackson and Green, these critical values were then used to normalise the results for comparison. The normalised parameters are defined as:

$$\omega^* = \frac{\omega}{\omega_c} \qquad \textbf{Eq. 2.14}$$

$$w^* = \frac{w}{w_c} \qquad \textbf{Eq. 2.15}$$

$$A^* = \frac{A}{A_c} \qquad \textbf{Eq. 2.16}$$

The model itself was set up to replicate the conditions used by Jackson and Green, subject to differences in the two programs, including boundary conditions, material properties, and the range of interferences applied. However, rather than the hemisphere radius of 1 µm, the radius modelled was 50mm. This was primarily to avoid scaling issues through creating such a small model. In the study by Jackson and Green, a range of plastic behaviours were examined by performing analyses

using five different values for the yield strength; ranging from 0.210 GPa to 1.619 GPa. This verification model only compared one of the yield strengths; σ_y = 1.265 GPa. Table 2.6 summarises the specifications of the elastic-plastic point contact model.

Table 2.6 - Elastic-plastic single point contact model summary.

Part	Axisymmetric 2D Quarter Circle; Radius, r = 50 mm → Half Hemisphere
	Line Segment → Rigid Flat Plane
Property	E = 200 GPa, ν = 0.3, σ_y = 1.265 GPa (perfectly plastic)
Assembly	Lines of axisymmetry aligned. Parts on the verge of contact
Step	Initial (required), Contact
Interaction	Frictionless
	Small Sliding
	Surface-to-Surface
Load	None applied
Boundary Conditions	Vertical displacement applied to top edge of hemisphere
	Rigid Flat Plane - Encastre ($U_x = U_y = U_z = UR_x = UR_y = UR_z = 0$)
Mesh	Partitioned around contact area
	Axisymmetric Stress Elements
	Linear Elements

2.4.3. Loaded results

As can be seen from Figure 2.4, Figure 2.5 and Figure 2.6, excellent agreement can be seen between the results achieved by Jackson and Green and the verification model. Figure 2.4 shows the relationship between dimensionless interference, ω^*, and dimensionless contact area, A^*. At low loads, where material behaviour is elastic, a linear relationship on the logarithmic scale is shown, agreeing with the theoretical solution that $A^*/\omega^* = 1$. This relationship develops through the elastic-plastic region, transitioning beyond a relationship of $A^*/\omega^* = 2$ for plastic contact, as predicted by Abbott and Firestone (1933). Jackson and Green (2005) report that this is not unreasonable to expect, as the Abbott and Firestone model considers the truncation of asperities, and does not take into account asperity deformation.

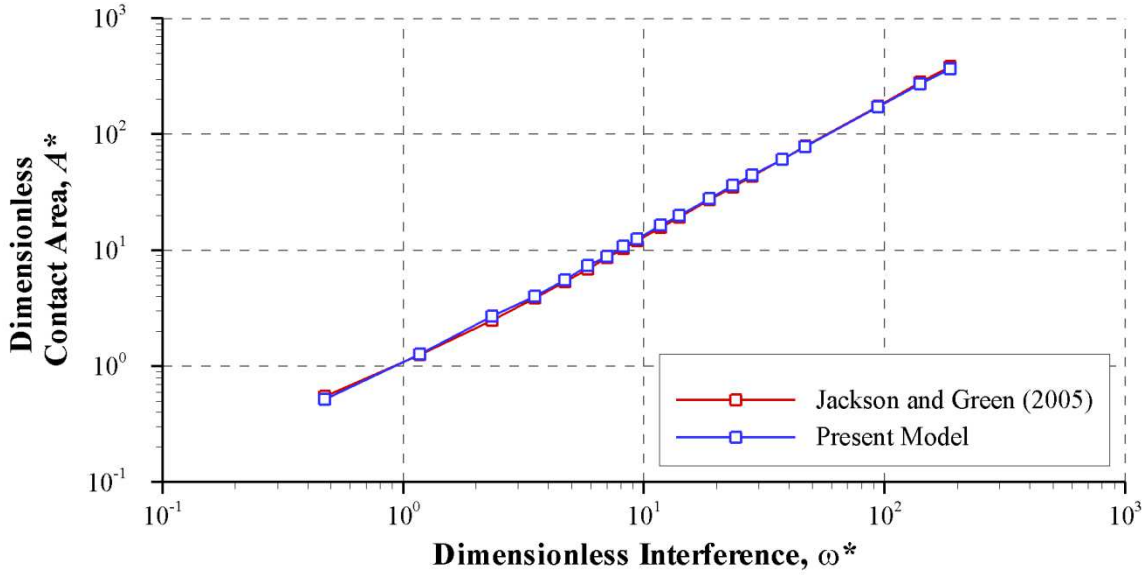

Figure 2.4 - Dimensionless contact area versus dimensionless interference.

Figure 2.5 shows the relationship between dimensionless interference, ω^*, and dimensionless load, w^*. Good agreement between the theoretical behaviour and the analysis are again seen at low loads with elastic material behaviour. From the figure, it can be found that $w^*/(\omega^{*3/2}) = 1$ as can be derived from the equations in Table 2.2. As Jackson and Green (2005) report, as the contact becomes more dominated by plastic behaviour, the behaviour tends towards the model proposed by Abbott and Firestone (1933).

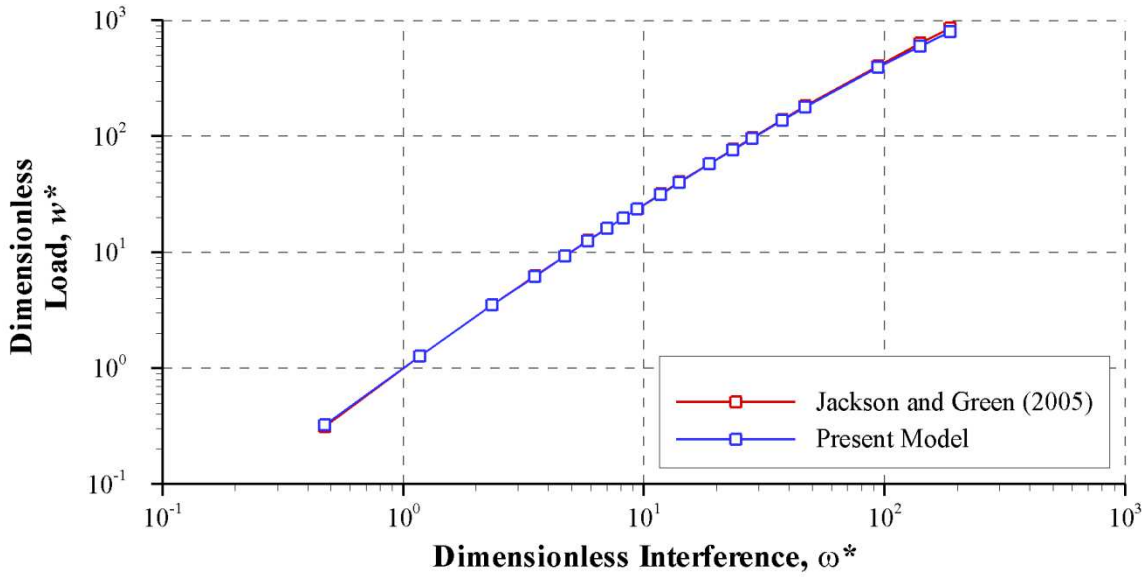

Figure 2.5 - Dimensionless load versus dimensionless interference.

Figure 2.6 shows the relationship between dimensionless load, w^*, and dimensionless contact area, A^*. As would be expected from the discussion of the results from Figure 2.4 and Figure 2.5, good agreement between the results of the analysis and theoretical elastic behaviour is seen at low loads, $A \propto w^{2/3}$. Beyond the point of initial yield, elastic-plastic behaviour begins. Initially, elastic behaviour dominates, with the gradient of the line staying close to 2/3. As the load is increased, plasticity becomes more of a factor as the relationship tends towards $A^*/w^* = 1$, and a gradient of unity.

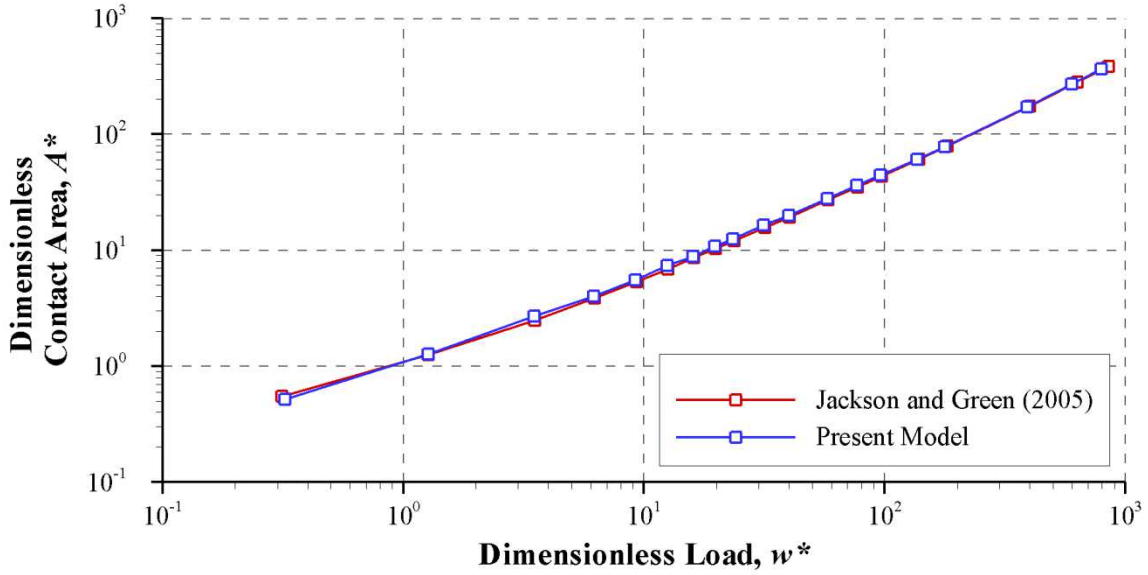

Figure 2.6 - Dimensionless contact area versus dimensionless load.

2.5. Elastic-plastic single line contact

2.5.1. Modelling details

Once the modelling techniques had been verified using a single point contact model, a new single line contact model was created. The model consisted of a 50 mm radius quarter cylinder, loaded against a rigid flat plane. The model used the same elastic material properties as before: E = 200 GPa and ν = 0.32, whilst two different yield strengths were investigated; σ_y = 210 MPa and σ_y = 1.619 GPa, the lowest and highest yield strengths used in the study by Jackson and Green (2005). Unlike the single point contact, the interference could not be calculated theoretically. Instead, critical parameter values were calculated by considering the maximum von Mises stress and contact pressure in a Hertzian line contact. The maximum von Mises stress occurs at a depth of $z = 0.70a$, of magnitude $0.56p_0$. Sub-surface yielding in a line contact first occurs when the maximum contact pressure is $p_0 = 1.79\sigma_y$. These values assume contact of a semi-infinite body, whereas the model considered is of finite size and is a finite element approximation. Through experimentation, it was found that the first sub-surface yielding occurred at a maximum contact pressure of $p_0 = 1.82\sigma_y$. The parameter values at this load case were taken as the critical conditions. The maximum contact

pressure in elastic contact theory can be given by Equation 2.17. By rearranging, the load can be found in terms of the maximum contact pressure as shown in Equation 2.18.

$$p_0 = \sqrt{\frac{E' w'}{2 \pi R}} \qquad \text{Eq. 2.17}$$

$$w' = \frac{2 \pi R p_0^2}{E'} \qquad \text{Eq. 2.18}$$

By substituting the maximum contact pressure at the initiation of sub-surface yielding, $p_0 = 1.82\sigma_y$, the critical load can be shown to be:

$$w'_c = 20.8 \frac{R}{E'} \sigma_y \qquad \text{Eq. 2.19}$$

Similarly, the contact dimension as given by elastic contact theory can be given by Equation 2.20. By substitution of the load, the critical contact dimension can be found as in Equation 2.21.

$$a = \frac{2 w'}{\pi p_0} \qquad \text{Eq. 2.20}$$

$$a_c = 7.28 \frac{R \sigma_y}{E'} \qquad \text{Eq. 2.21}$$

The normalised parameters were calculated as previously stated in Section 2.3.

Where possible, the quarter cylinder was meshed using linear quadrilateral plane strain elements. Use of these elements alone resulted in undesirable corner angles in some elements as highlighted by the mesh verification tool within Abaqus. As a result, a small number of compatible linear triangular elements were used in order to ensure a valid mesh. Abaqus documentation (Abaqus 2010a) recommends that the stiffer of two contact bodies be defined as the master surface, and so the rigid flat plane was defined as such. The rigid flat plane was meshed using elements sized slightly larger than on the corresponding slave contact surface on the quarter cylinder, again as recommended by Abaqus documentation.

The tangential behaviour at the contact interface was defined as frictionless, while the normal behaviour used the augmented Lagrange constraint enforcement method as opposed to the default

Penalty method used before. The Penalty method is the default method for "hard" contact, whereby contact pressure is proportional to overclosure, or penetration. The alternative, "softened" contact, also permits overclosure, but also allows contact pressure to occur at small surfaces clearances too (i.e. when surfaces are not yet in contact). The augmented Lagrange method alters the sequence that occurs in each increment as follows:

1. Abaqus uses the Penalty method to find a converged solution.
2. If a slave node penetrates the master surface by more than the penetration tolerance, the contact pressure is "augmented" (increased) and further iterations are performed to find convergence.
3. The contact pressure is further augmented and the solution iterated until the actual penetration is less than the penetration tolerance.

Choosing this method allows the more advanced contact controls to be used in Abaqus, such as controlling the penetration tolerance. The default setting for penetration tolerance is proportional to element size; 0.1% of the characteristic element length. As is later discussed, the mesh at the contact surface was modified throughout the study, ensuring a consistent number of elements across the contact as the load was increased. By setting an absolute penetration tolerance of 10^{-15}m, consistency of the contact interaction could be assured throughout the study.

The constraint enforcement method can be defined by the user in the **Interaction** Module. When defining the normal behaviour in the **Interaction Properties**, a drop down menu allows the user to specify the constraint enforcement method. To alter the penetration tolerance, the user can select **Contact Controls**, either from the model tree or the task bar. Under the **Augmented Lagrange** tab, either an absolute or relative penetration tolerance can be selected and specified. The final step to introduce the new contact controls is in the **Edit Interaction** menu. At the bottom of the window, two drop down menus allow the selection of created interaction properties and contact controls.

The load was defined by applying a constant displacement in the z-direction to the flat rigid plane. The displacement applied corresponded to the specified interference. Each load case was achieved by increasing the interference in a number of small increments. The size of each increment was governed by the need to maintain numerical convergence of the iterative solution process embodied in the software to solve the non-linear contact with elastic-plastic material properties. The unloading process was performed in a similar manner.

For each simulated interference, the model was remeshed to suit the deformation expected. These meshes were created using an iterative process, whereby more generalised meshes were initially tested across the range of interferences to obtain the approximate contact dimension. With this information, the mesh could be tailored for each interference, without incurring an excessive computational penalty associated with increasing the number of elements in the model. Examples of two of the meshes used within the study are shown in Figure 2.7.

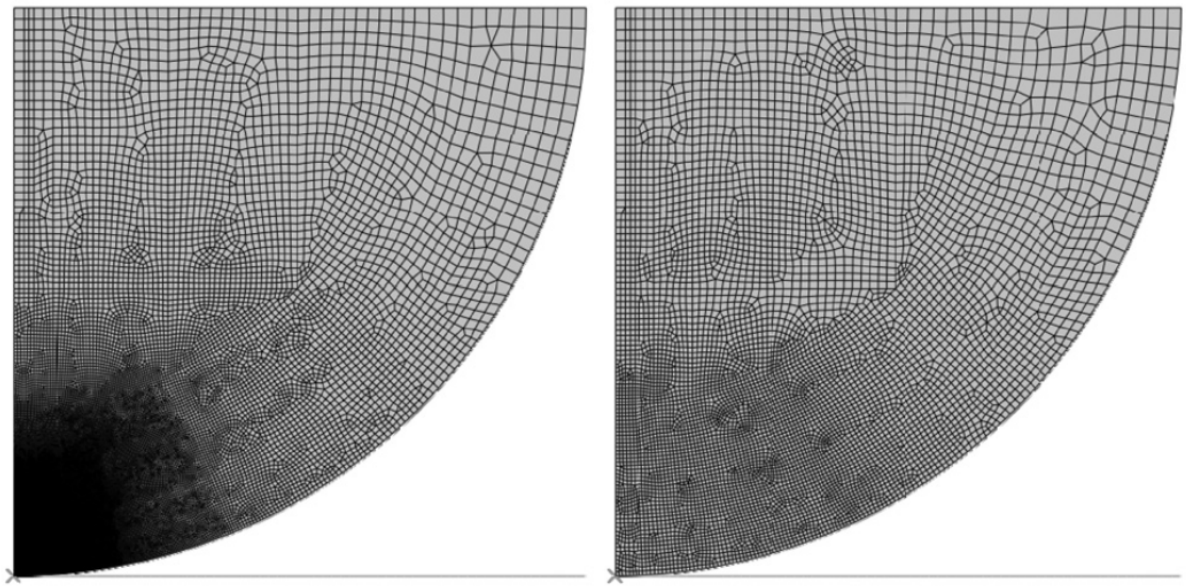

Figure 2.7 - Example of fine mesh used for smaller interferences (left), and coarser mesh used for larger interferences (right).

For similar reasons, the quarter cylinder model was divided using the partitioning tool. This allowed different mesh densities to be more effectively implemented in various regions of the model. For

example, a finer mesh was implemented around the contact area, whilst a coarser mesh was used in areas remote from it. The transition between these different regions was kept smooth in order to avoid discontinuity in results from occurring at partition boundaries. The total number of elements in the deformable quarter cylinder ranged from 7003 to 80360. The number of elements in the contact region was kept within a relatively narrow range. From the smallest contact to the largest, the number of elements in actual contact ranged from 33 to 71, giving a contact dimension precision of from 0.73% to 1.47%, with an average of 0.91%. The precision values were calculated by dividing half the element size at the contact edge by the nominal contact dimension. Table 2.7 summarises the specifications of the elastic-plastic single line contact model.

Table 2.7 - Elastic-plastic single line contact model summary.

Part	2D Quarter Circle; Radius, r = 50mm → Half Cylinder
	Line Segment → Rigid Flat Plane
Property	E = 200 GPa, v = 0.32, σ_y = 210 MPa and σ_y = 1.619 GPa
Assembly	Lines of symmetry aligned. Parts on the verge of contact
Step	Initial (required), Contact, Removal
Interaction	Frictionless
	Augmented Lagrange Constraint Enforcement Method
	Small Sliding
	Surface-to-Surface
	Absolute Penetration Tolerance = 10^{-15}m
Load	None applied
Boundary Conditions	Vertical displacement applied to rigid flat plane
	Top edge of quarter cylinder: Restrained ($U_x = U_y = 0$)
	Side edge of quarter cylinder: Symmetry in y-axis ($U_x = 0$)
Mesh	Partitioned around contact area
	Plane Strain Elements
	Linear Elements

2.5.2. Loaded results

The results given in Table 2.8 show the non-dimensional parameters obtained for each of the finite element analysis simulations performed using the smooth quarter cylinder contact model.

Table 2.8 - Elastic-plastic single line contact results.

Case	Dimensionless Interference, ω^*	Dimensionless contact dim., a^*	Dimensionless contact load, w'^*	a/R
1	0.23	0.46	0.19	0.012
2	0.47	0.66	0.42	0.017
3	0.70	0.82	0.66	0.021
4	0.93	0.96	0.91	0.025
5	1.40	1.23	1.42	0.032
6	1.86	1.53	1.92	0.040
7	2.33	1.82	2.41	0.047
8	3.26	2.38	3.33	0.062
9	4.66	3.17	4.57	0.082
10	6.99	4.30	6.34	0.112
11	9.32	5.25	7.83	0.137
12	14.0	6.82	10.35	0.177
13	21.9	9.05	13.82	0.235
14	32.6	11.29	16.61	0.293
15	50.3	14.31	19.40	0.372

Figure 2.8 shows both the dimensionless contact dimension, a^*, and dimensionless contact load, w'^*, plotted as functions of dimensionless interference, ω^*. It can be seen that both contact dimension and contact load increase linearly until the onset of material plasticity at $\omega^* = 1$. While no exact theoretical solution exists for the relationship of the interference and load or contact dimension, this behaviour agrees with the approximation as reported by Hamrock *et al*. (2005). Little deviation from this linear behaviour is seen to occur until the amount of subsurface yielding increases. Significant departure from the elastic behaviour becomes apparent for a^* at $\omega^* \approx 2$ and for $w'^* \approx 3$.

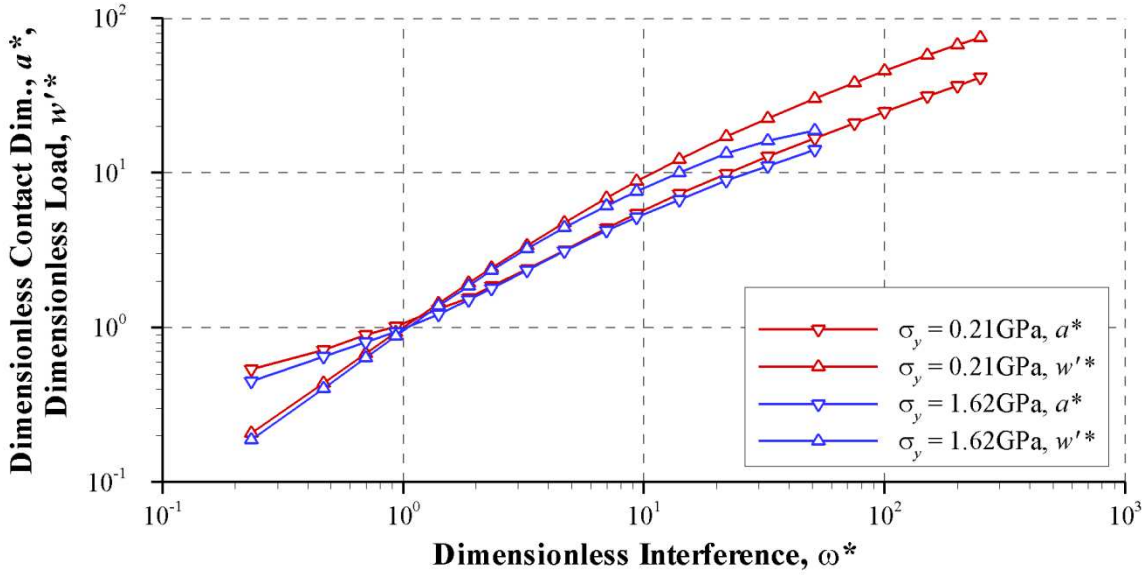

Figure 2.8 - Dimensionless contact dimension and contact load versus interference.

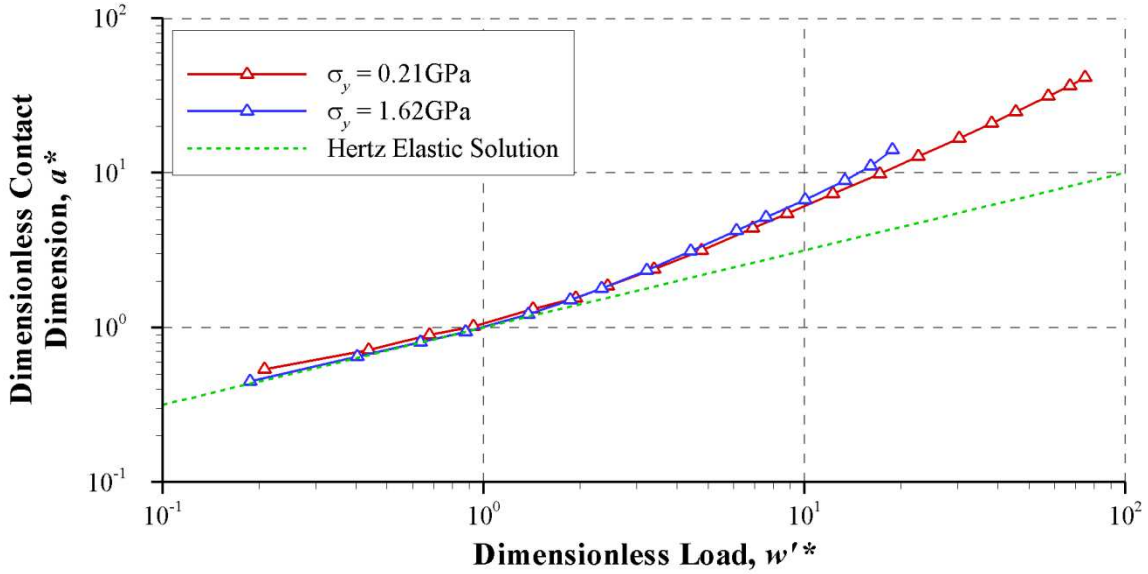

Figure 2.9 - Dimensionless contact dimensions versus dimensionless load.

Figure 2.9 shows a^* plotted as a function of w'^* together with the equivalent result for an elastic Hertzian contact, which is a straight line with a gradient of 0.5. As before, the expected linear behaviour is exhibited, in the case of both yield strength values, before yielding occurs. Deviation from the dashed elastic Hertzian results is not seen to occur immediately as w'^* becomes greater

than unity. Divergence begins to become significant once $w'^* \approx 2$. As w'^* increases further, the gradient of the line changes from 0.5 to 1 on the logarithmic plot as the material behaviour transforms from elastic to fully plastic behaviour. Under very heavy loads, the gradient tends to exceed unity. For contact of a semi-infinite body, this behaviour would be unexpected. In the current model, this behaviour occurs in simulated load cases where the leading edge of the yielding material approaches the boundaries of the finite-size model. This progression of the boundary, or "plastic front", is demonstrated in Figure 2.10. Each contour line shows the boundary between elastic and plastic material for a particular labelled interference. By considering the proximity of the contours to the model boundaries, it is clearly questionable as to whether the semi-infinite assumption holds up once the dimensionless interference exceeds much beyond 10.

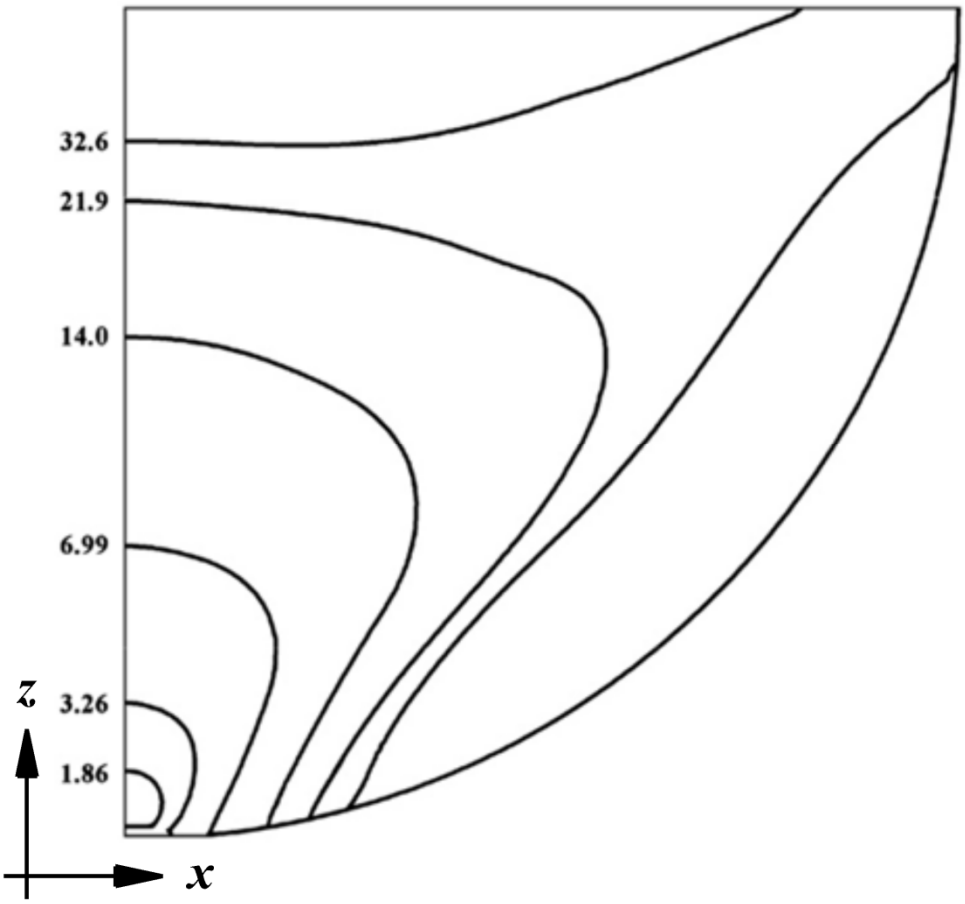

Figure 2.10 - Progression of "plastic front" with increased interference (leading edge of plastic zone only shown for clarity)

Figure 2.11 shows the average contact pressure to yield strength ratio ($w'/2\ a\ \sigma_y$), calculated from the finite element results. For relatively lightly loaded contacts where a/R is small, this value is expected to approach a constant value similar to the flow pressure as the contact becomes fully plastic. Williams (1994) uses an approximate upper bound method to calculate this value to be 2.83 for a line contact. It is also stated that despite variation for different geometric configurations and frictional conditions that this value is "always close to the value 3". The σ_y = 0.21 GPa, results achieved by Jackson and Green (2005) for small a/R (approximately 0.05) in a single point contact agree with this theoretical value, while results for the higher yield strength of σ_y = 1.619 GPa approached a maximum value of around 2.4. Results from this single line contact model gave maximum values of approximately 2.6 and 2.2 for the lower and higher yield strength materials, respectively. The distinct reduction in the average contact pressure at the two largest interferences shown in Figure 2.11 is believed to be due to the finite nature of the model. The two load cases in question have ω^* = 32.6, a/R = 0.29 and ω^* = 51.3, a/R = 0.37 respectively. In each of these cases, the yielded material extends towards the boundary of the quarter cylinder model, as previously shown in Figure 2.10. This invalidates the semi-infinite assumption that is applied to calculate the theoretical maximum value. Jackson and Green (2005) have provided an explanation of this phenomenon in terms of the behaviour in the limiting case where $a/R \rightarrow 1$.

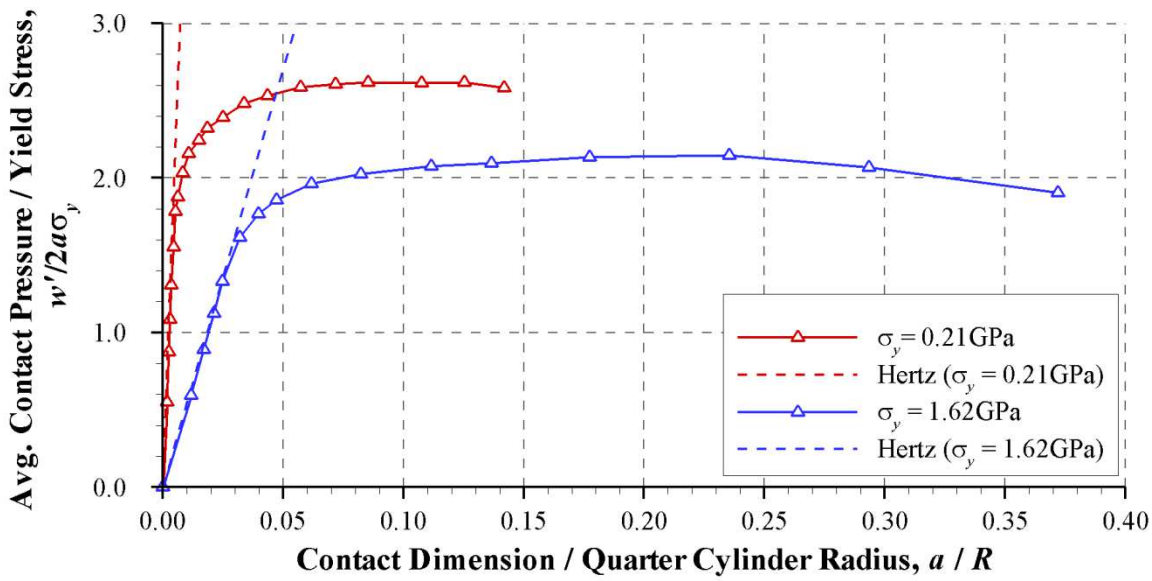

Figure 2.11 - Variation of mean contact pressure / yield strength with contact dimension / quarter cylinder radius.

2.5.3. Loaded stress distributions

As the contact load is increased beyond the elastic limit, the stress distributions deviate from those predicted using purely elastic Hertzian theory and the area of peak von Mises stress and this results in localised material yield. This region of yielding material grows with increasing interference, but initially remains beneath the surface as previously shown in Figure 2.10. As the interference is increased, this area of yielding material grows and expands towards the contact surface. This is illustrated in Figure 2.12 which shows the normalised von Mises stress distribution for four load cases, ω^* = 3.26, 6.99, 14.0 and 32.6. Plastic behaviour is first seen at the surface at a dimensionless interference of 3.26. At the same time, the von Mises stress at the centre of the contact increases until surface yielding occurs at ω^* = 6.99. Further loading causes the surface plastic zone at the contact centre to grow, while the plastic zone located at the edge of the contact remains constant in size relative to the contact area. The two zones meet at an interference of around 50, where the entire contact is plastic at the surface. It should be noted that as the geometry is normalised by the loaded contact dimension, which increases with applied load, that the curvature outside of the

contact (x / a > 1.00) differs greatly between each of the load cases shown. This phenomenon is also seen i Figure 2.14Figure 2.15, Figure 2.16.

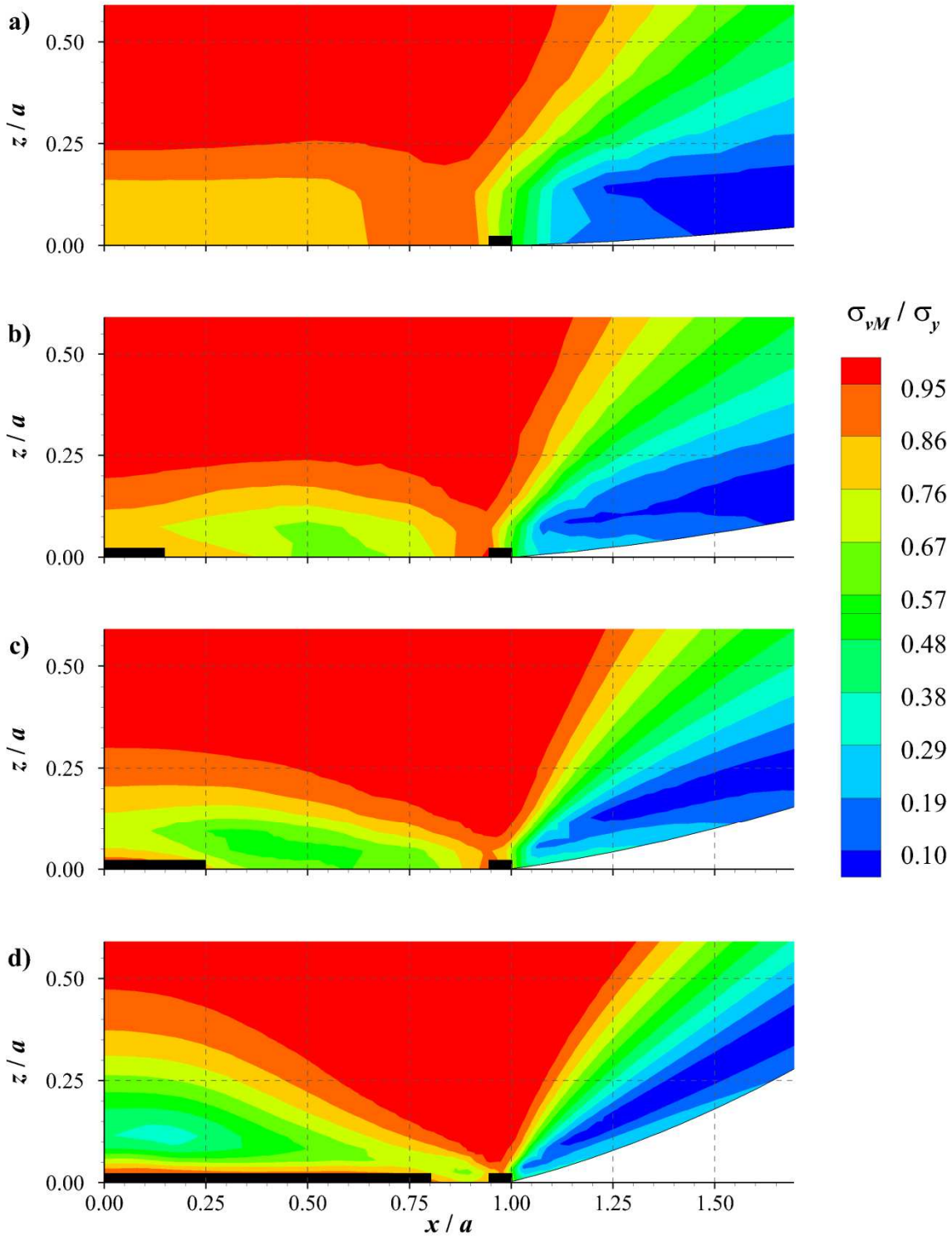

Figure 2.12 - Contours of normalised von Mises stress for interference values, a) ω^* = 3.26, b) ω^* = 6.99, c) ω^* = 14.0, d) ω^* = 32.6.

The normalised von Mises stress distributions in Figure 2.12 were produced using nodal output values from Abaqus. The nodal values are produced by averaging the neighbouring element values at each node. An element experiencing plastic behaviour will have a normalised von Mises stress of 1, but when averaged with the neighbouring element's value, the nodal value will be less than unity. Consequently, in order for the normalised von Mises stress contours to show plastic behaviour, three adjacent surface elements must be in the plastic state. Yielding at the contact surface is typically found to occur in one or two elements and as such, the normalised von Mises stress contours cannot clearly illustrate the behaviour. The additional heavy lines in the figure indicate which surface elements are yielding.

The way in which the von Mises stress grows, and the surface material at the contact centre line begins to yield is shown in Figure 2.13. Four load cases are shown, ω^* = 0.23, 1.40, 3.26 and 14.0, as well as the theoretical result for the critical elastic condition where the material is on the verge of yielding. For ω^* = 1.40 and, the plastic zone is confined to the subsurface material, as can also be seen in Figure 2.10 for ω^* = 1.86. For increasing heavy load cases, the stress found at the contact centre line increases, approaching the yield stress. For the load case ω^* = 14.0, the contact surface at the centre line is plastic. However, in this case a subsurface elastic zone is encapsulated by yielding material. The phenomenon can also be seen in Figure 2.12.

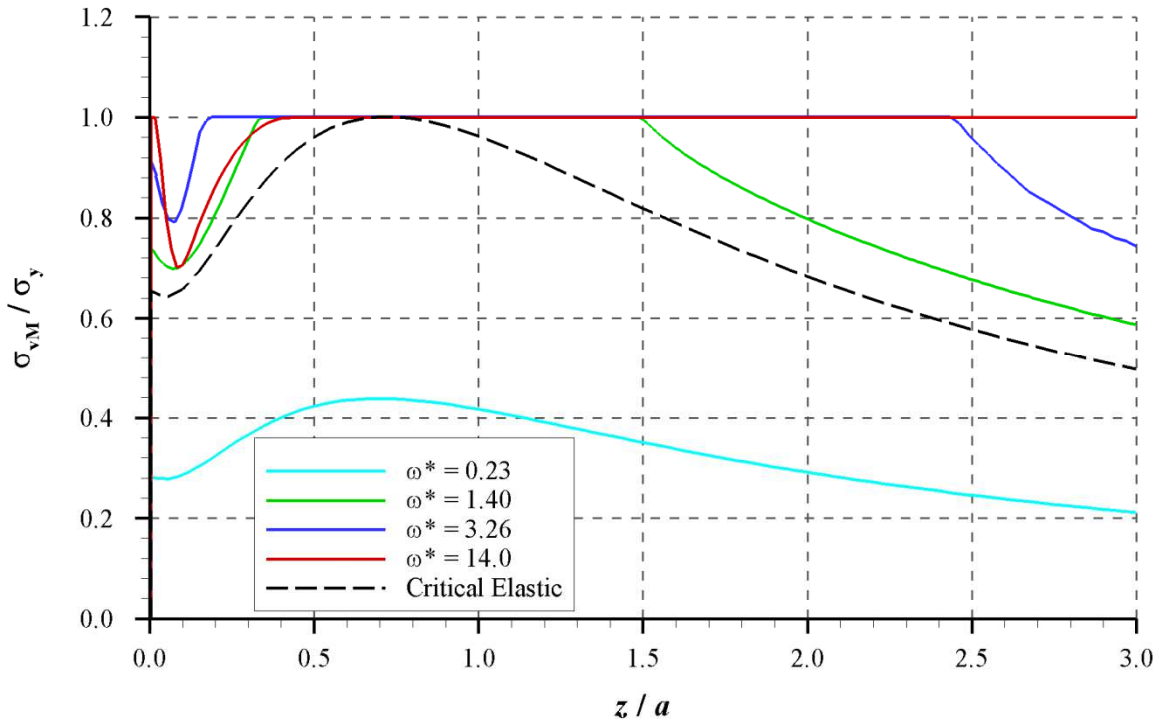

Figure 2.13 - Normalised von Mises stress as a function of z / a on the contact centre line, x = 0. Theoretical critical elastic behaviour illustrated by a dashed line.

Contours of the direct stress component in the tangential direction, σ_{xx}, normalised by σ_y, are shown in Figure 2.14 for the four load cases ω* = 3.26, 6.99, 14.0, 32.6. Tensile values of σ_{xx} can be significant in consideration of surface cracking under fatigue conditions. At the lowest load shown (ω* = 3.26) σ_{xx} is tensile at the surface immediately outside the contact with a maximum value of around 0.1σ_y. This stress pattern continues as the interference increases, with the magnitude rising to 0.25σ_y for ω* = 14.0. The magnitude then decreases for the highest interference shown, ω* = 32.6, as a result of the increased plastic flow at the surface. This reduction may also partly be due to the direction of the stress component σ_{xx} becoming progressively less aligned with the surface tangential direction as more deformation occurs.

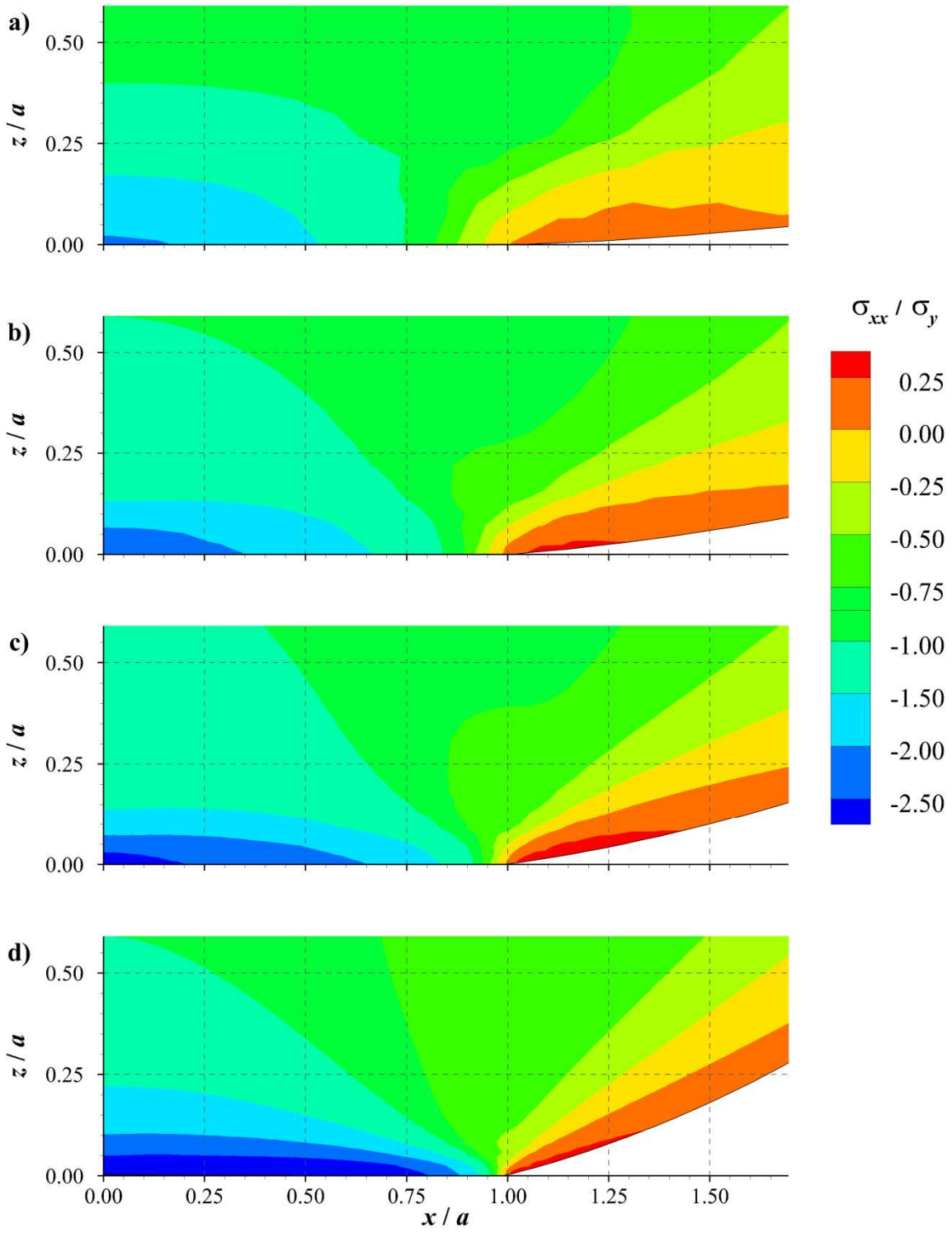

Figure 2.14 - Contours of normalised direct stress in tangential direction under load, σ_{xx} / σ_y for interference values, a) ω^* = 3.26, b) ω^* = 6.99, c) ω^* = 14.0, d) ω^* = 32.6.

2.5.4. Residual stress distributions and deformations

As a result of material yielding at interferences greater than ω_c, significant residual stresses remained following unloading of the model. Contours of the normalised direct stress components in the tangential and normal direction are shown in Figure 2.15 and Figure 2.16, respectively. The load cases shown are the same as in Figure 2.12 and Figure 2.14, illustrating the residual effects of the stress under load shown. High tensile values of σ_{xx}, the tangential component of direct stress, are generally seen at and near the contact boundary. The highest of these stresses is seen at the lowest of the displayed interferences, ω^* = 3.26, at a magnitude of over $0.5\sigma_y$. As the amount of residual plastic deformation at the surface increases with interference, the magnitude of this tensile stress falls, until σ_{xx} is generally compressive for ω^* = 32.6. The magnitude of the normal component of direct stress, σ_{zz}, is lower for all the load cases shown. For ω^* = 3.26, tensile values can be seen in the contact zone, while compressive values exist below the surface at the contact edge. The highest observed surface stresses of $\pm 0.02\sigma_y$ are seen for the ω^* = 14.0 load case, with significant compressive stress in the plastic zone beneath the surface. A further increase of the interference to 32.6 results in a reduction of the residual normal stress. The same colours are used to represent the magnitudes of stress for each load case. The load case shown Figure 2.15d, ω^* = 32.6, appears different to the remaining load cases due to the nature of the stresses found. For ω^* = 32.6, the magnitude of tensile stress found is reduced, while compressive stresses are more commonplace.

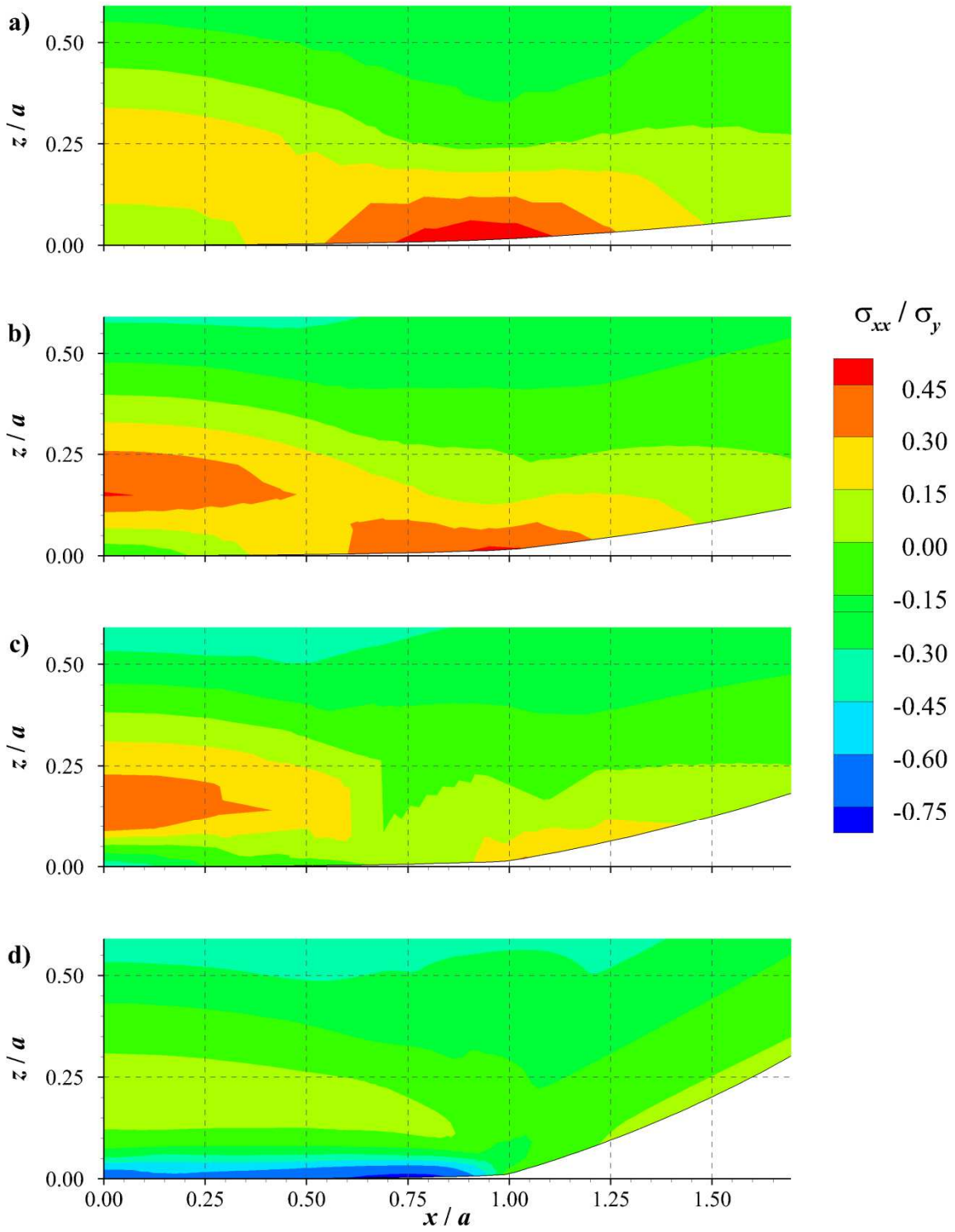

Figure 2.15 - Contours of normalised residual direct stress in tangential direction, σ_{xx} / σ_y for interference values, a) ω^* = 3.26, b) ω^* = 6.99, c) ω^* = 14.0, d) ω^* = 32.6.

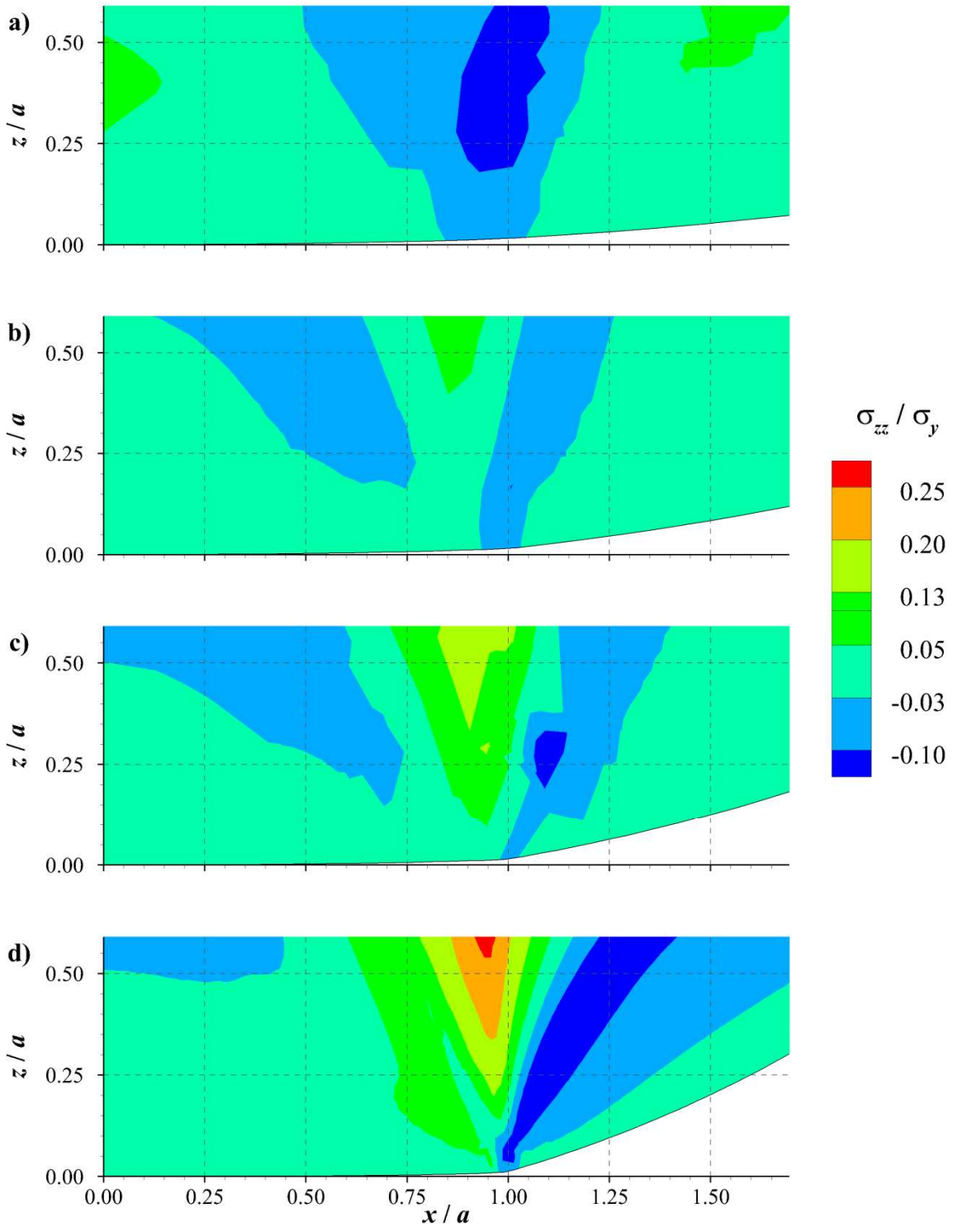

Figure 2.16 - Contours of normalised direct stress in normal direction under load, σ_{zz} / σ_y for interference values, a) ω^* = 3.26, b) ω^* = 6.99, c) ω^* = 14.0, d) ω^* = 32.6.

Figure 2.17 presents the residual normal deformations, U_z, normalised against the critical interference, ω_c, for a range of load cases from ω^* = 1.40 to 21.9. This deformation corresponds to the change in asperity height when considering a rough surface contact. Additionally, each curve is normalised in the tangential direction against its own contact dimension to allow for easier comparison. The figure shows how the deformation increases in the contact zone as the load is increased. It also shows how build up occurs at the edge of the contact as material is pushed away from the contact. It should be noted that for the larger shown values of ω^*, the deformations in the z-direction, as shown, are no longer normal to the surface because of the high a/R value for these load cases.

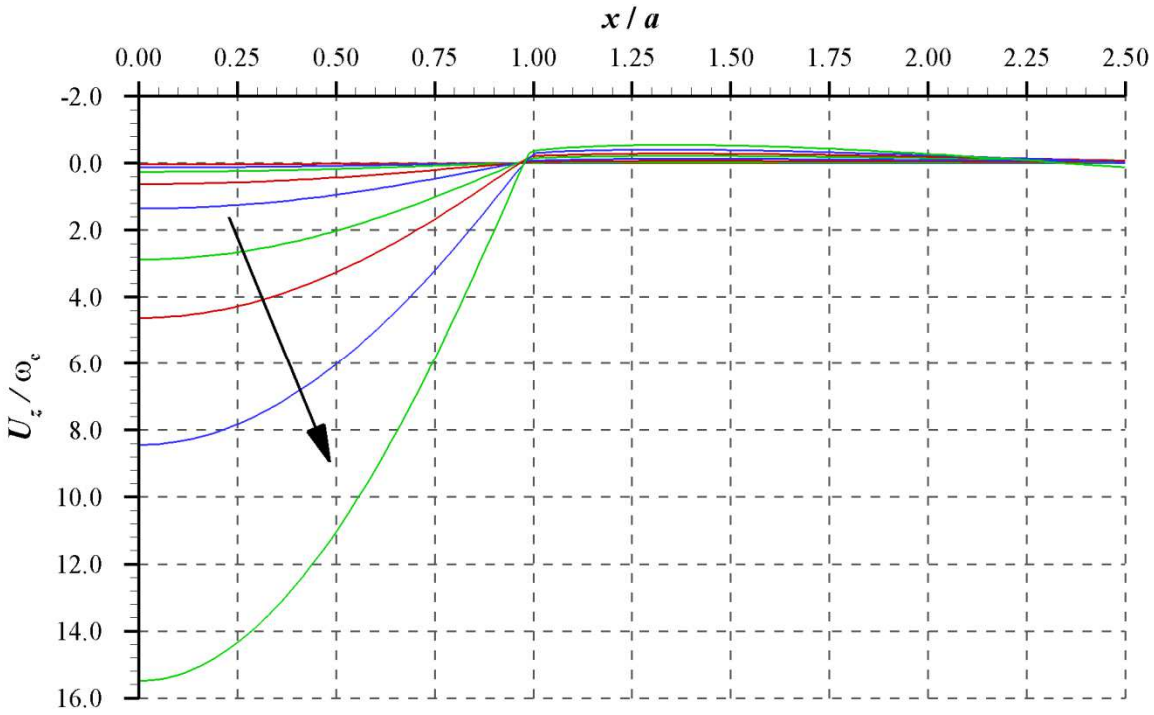

Figure 2.17 - Residual normal deformations at normalised interferences, ω^*, from 1.40 to 21.9. Arrow indicates sense of increasing ω^*.

2.6. Sinusoidal contact

2.6.1. Modelling details

Having modelled single point and line contacts, the first step in modelling a multiple contact problem was the case of elastic-plastic contact between a deformable sinusoidal surface and a rigid flat plane. The behaviour of this configuration differs from that of a single contact because of the possibility of interaction of the deformation and stress fields of adjacent features. Theoretical solutions for the elastic only sinusoidal surface contact have been given by Westergaard (1939) and Johnson (1985). The model was therefore run in both elastic only and elastic-plastic material definitions to allow comparison. The sinusoidal contact model is illustrated in Figure 2.18.

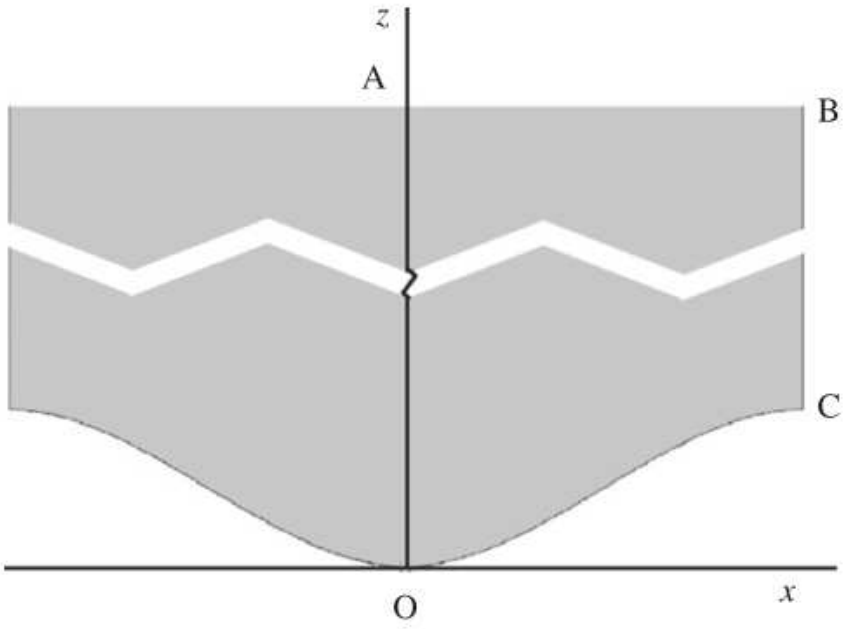

Figure 2.18 - Sinusoidal surface contact model (*z*-axis magnified 20:1).

The amplitude and wavelength chosen for the sinusoidal surface were 0.2 µm and 20 µm, respectively. In Figure 2.18, the *z*-axis has been scaled in the ratio 20:1 to the *x*-axis for clarity. The theoretical solutions use a semi-infinite body assumption, and so to approximate this, the model was extended 100 µm from the contact surface to the upper boundary AB. For a simple cyclic sinusoid, both the *z*-axis and the line BC are lines of symmetry, and as such, only the positive sector was

modelled to reduce computational requirements. The model was created and set up in a similar way to the previous smooth point and line contact models. The sinusoidal surface was defined either as an elastic or elastic-perfectly plastic deformable body, with mechanical properties of E = 200GPa, ν = 0.32 and, where appropriate, σ_y = 1.619GPa. This deformable body was brought into contact with a rigid flat plane, coincident with the x-axis in Figure 2.18. In order to replicate the lines of symmetry, the boundaries at OA and CB were restrained in the x-direction, while the upper boundary AB was restrained in both the x- and z-directions. The model was loaded by applying a constant displacement in the z-direction, δ, to the rigid flat plane. Table 2.9 summarises the specifications of the sinusoidal surface contact model.

Table 2.9 - Sinusoidal contact model summary.

Part	2D Sinusoidal Surface; A = 0.2 µm, λ = 20 µm
	Line Segment → Rigid Flat Plane
Property	E = 200 GPa, ν = 0.32, σ_y = 1.619 GPa
Assembly	Lines of symmetry aligned. Parts on the verge of contact
Step	Initial (required), Contact, Removal
Interaction	Frictionless
	Augmented Lagrange Constraint Enforcement Method
	Small Sliding
	Surface-to-Surface
	Absolute Penetration Tolerance = 10^{-15}m
Load	None applied
Boundary Conditions	Vertical displacement applied to rigid flat plane
	Top edge of sinusoidal part: Restrained ($U_x = U_y = 0$)
	Side edges or sinusoidal part: Symmetry in y-axis ($U_x = 0$)
Mesh	Partitioned around contact area
	Plane Strain Elements
	Linear Elements

2.6.2. Elastic results

In order to validate the application of the single contact modelling techniques to multiple contacts, results were obtained for the sinusoidal surface contact model using elastic only material properties. These results were then compared to the corresponding analytical solution of Westergaard (1939). The displacement of the rigid flat plane was specified such that contact between the two bodies occurred, and the contact pressure distribution at increasing degrees of contact, including complete contact, was compared to the Westergaard result. The left side of Figure 2.19 shows the comparison of contact pressure distributions from the finite element simulation to the analytical solution, showing good agreement between the two.

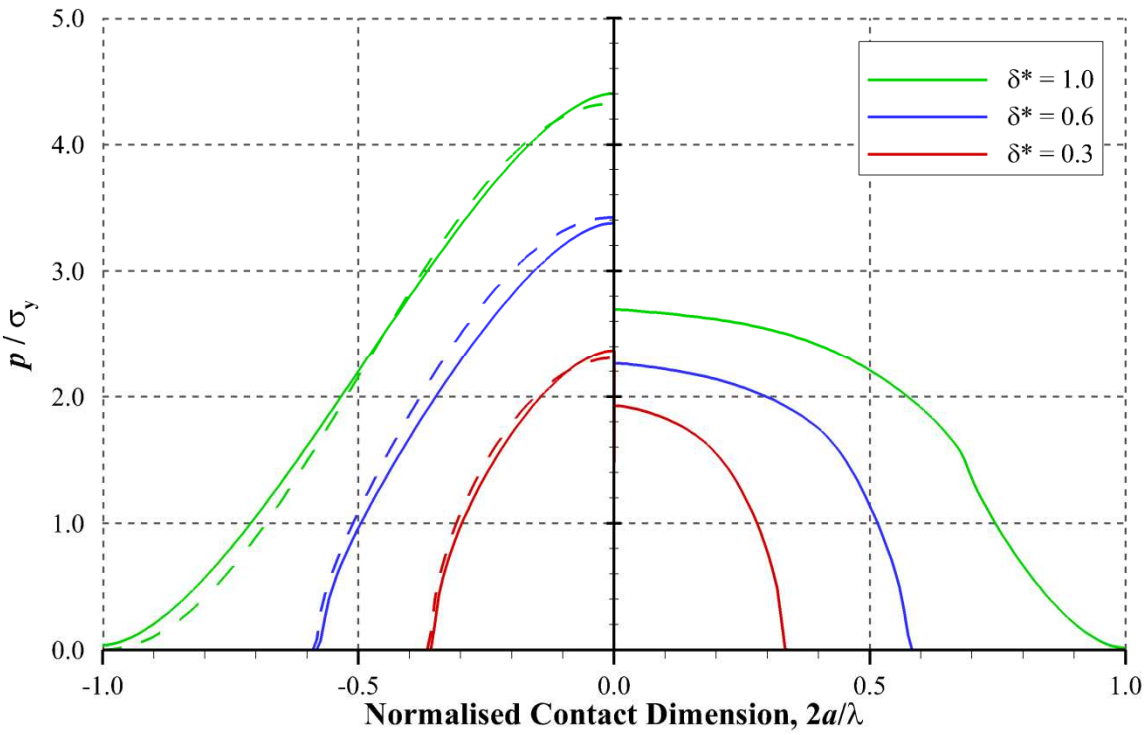

Figure 2.19 - Contact pressure plots for elastic solution (left) and equivalent elastic-plastic (right) at different stages of contact. Westergaard pressure distribution shown as dashed lines.

In the Westergaard theory the contact pressure distribution which is required to completely "flatten" the sinusoidal surface is itself sinusoidal. The smallest amplitude of pressure distribution to cause complete contact therefore has a minimum value of zero in each of the valleys of the sinusoid.

The mean pressure in this state is denoted as p^*, and the displacement applied to achieve this pressure distribution at complete surface flattening is defined as δ_c. The ratio of the applied displacement to the critical displacement is defined in Equation 2.22.

$$\delta^* = \frac{\delta}{\delta_c} \qquad \textbf{Eq. 2.22}$$

Figure 2.19 shows three pressure distributions for three different load cases, δ^* = 0.3, 0.6 and 1.0. Agreement is generally good between the simulated and analytical results, although the best agreement occurs at the lower value of δ^* = 0.3.

Further comparisons can be made with work by Johnson (1985) as shown in Figure 2.20. This figure shows the variation of the real area of contact, $2a$, with the mean pressure, $\overline{p}$. The real contact area is normalised by the apparent area of contact, or wavelength, λ, while the mean pressure is normalised by p^*. Again, good agreement generally occurs throughout, although it is best at smaller loads as previously seen in Figure 2.19. Gao *et al*. (2006) suggested that in their 2D sinusoidal contact study that as contact tended towards being complete, that the non-dimensional contact pressure could exceed the limit previously discussed by Williams (1994). This phenomenon was not observed in these simulations.

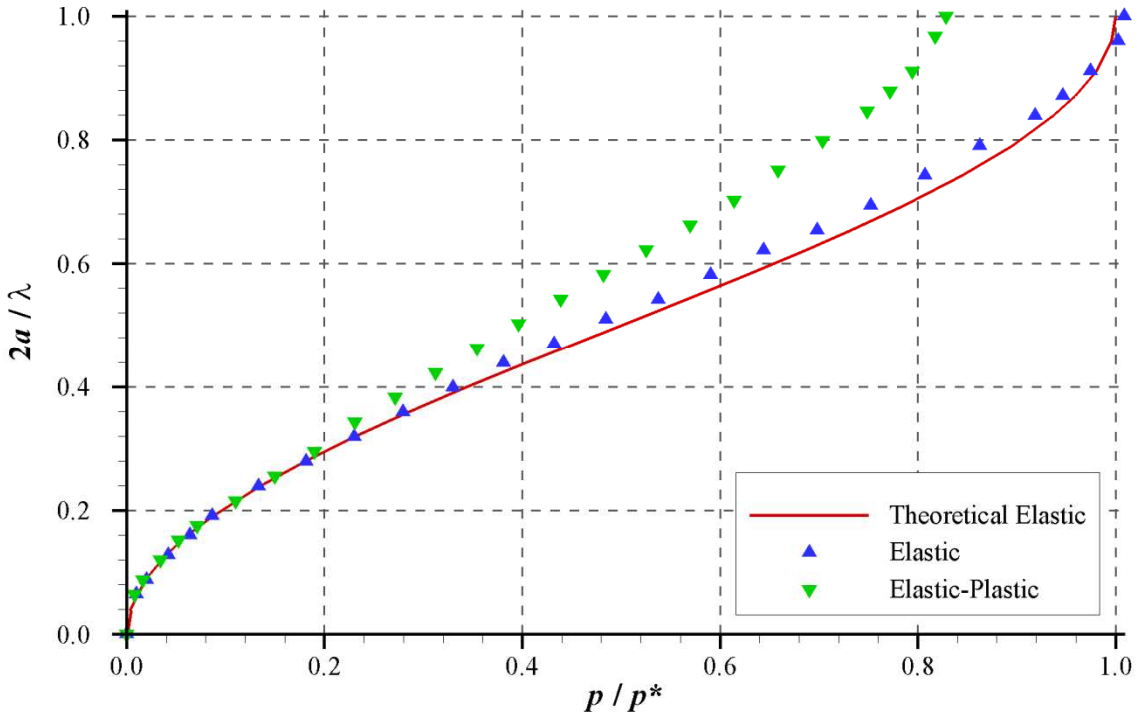

Figure 2.20 - Real / apparent contact area ratio versus non-dimensional pressure amplitude.

2.6.3. Elastic-plastic results

The material properties were then altered from purely elastic to elastic-perfectly plastic, with a yield strength of 1.619 GPa. The same range of load cases was simulated and the contact pressure plots can be seen on the right side of Figure 2.19. Each of the three load cases shown resulted in some plastic deformation occurring. As expected, the introduction of plasticity resulted in lower peak contact pressures than in the corresponding elastic analysis. The elastic-plastic pressure is generally lower than the elastic pressure across the contact. However, in the complete contact case, the elastic-plastic pressure exceeds the elastic pressure in the valley features, indicating interaction between adjacent sinusoidal "asperity" features. For low δ*, the plastic effects are limited to the contact zone. As δ* is increased, the degree of interaction increases, causing the rise in contact pressure.

2.7. Conclusions

This chapter has shown the development of contact modelling using Abaqus. Initially, modelling techniques were verified using an elastic only point contact model, using Hertzian theory for comparison. Material plasticity was introduced and results verified by using existing published work (Jackson and Green 2005). A plane strain line contact model was then created. The directionality of common gear finishing techniques makes a two dimensional assumption for surface features applicable. It was found that areas of significant residual tensile stress occurred at the surface following contact loading sufficient to give material yielding (Bryant *et al*. 2012). A sinusoidal surface contact model showed how idealised asperity features affect stress fields of adjacent features, and as such cannot be considered as isolated independent contacts.

Development of modelling techniques suitable for real rough surface contacts

3.1. Introduction

This chapter describes the techniques employed and the results obtained in the simulation of elastic-plastic contact between rough surfaces using profile measurements taken from the surfaces of ground gears. The surfaces of gear teeth tend to have a random distribution of surface heights, and when such surfaces are loaded together multiple asperity contacts that are at varying stages of localised elastic-plastic behaviour occur. Complex interactions between the stress fields of adjacent local contacts can occur, and this affects the resulting loaded and residual local displacement and stress behaviour. Rough surface profile information was obtained from both run and unrun gear teeth measured using a Talysurf profilometer. The gears were of helical form used in micropitting tests at the Design Unit, Newcastle University. The raw Talysurf profiles were digitally filtered (using a standard Gaussian filter) to remove wavelengths in excess of 0.25 mm and imported into Abaqus to create contact models. For the initial modelling attempt, profiles taken from gears which had been loaded together and run were superimposed on flat surfaces. Subsequently both the run and unrun (i.e. freshly-prepared) profiles were superimposed onto a smooth roller to simulate the contact of a pair of disks with one surface superfinished and the other having the gear roughness profile. In elastic-plastic contact of such un-run surfaces it was found that local contact pressures well in excess of the hardness of the material were predicted, and clearly indicating the need for a detailed consideration of plastic behaviour, particularly as this may determine the residual effects of the initial “running in” process undergone by gears. As a result, a study of further advanced contact modelling techniques was performed to evaluate their effect on such complex contact simulations.

3.2. Flat rough surface contact modelling

3.2.1. Profilometry

Profiles were taken from both the run and unrun tooth surfaces, from root to tip, parallel to the gear face, at the midpoint of the face width, as shown by the red line from point A to point B in Figure 3.1. These profiles were taken in the transverse direction, rather than the lead direction, in order to take advantage of the directionality of the grinding process. While grinding occurs in a circular form, the radius of the grinding wheel is large compared to the gear. The recorded profiles were approximately perpendicular to the grinding direction. This allows the approximation of a plane strain module to represent the rough surface in the finite element analysis. The raw profiles were then filtered using a Gaussian filter with a cut off of 0.25 mm, which removed the involute form of the gear but retained the surface roughness profile.

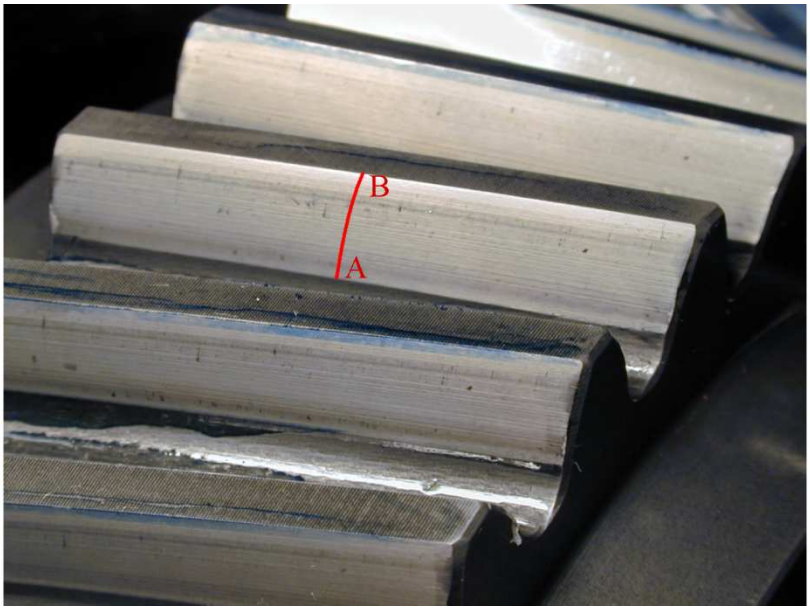

Figure 3.1 - Gear tooth profile location.

The run and unrun profiles were clearly distinguishable by the shape of the asperity peaks; those of the run surface exhibited wider, flatter peaks due to plastic deformation, resulting in a more negative skew in the surface height distribution in comparison to the unrun surface. Sections of the surface roughness profiles of the run and unrun surfaces can be seen in Figure 3.2. For each surface, a number of surface roughness parameters are also displayed; R_a, R_z and R_{sk}. In industry, surfaces are typically specified using a R_a, or roughness average, value, at least partly due to its ease of measurement. In this case, the surfaces have a R_a of between approximately 0.30 µm and 0.37 µm. These are appropriate surfaces to consider, as ground gears used in aerospace typically have a R_a of up to 0.4 µm. In some cases, R_z is the average height difference between the five highest peaks, and five lowest valleys, and may be used to restrict any extreme behaviour in the surface profile after finishing. It can be seen for the unrun and run surfaces that while each of these parameters differs, that they are still somewhat similar. By considering the skewness of the surface, R_{sk}, a more pronounced difference can be seen as the run surface is significantly negatively skewed as a result of running, resulting in multiple flat lands where the surface has been deformed or worn.

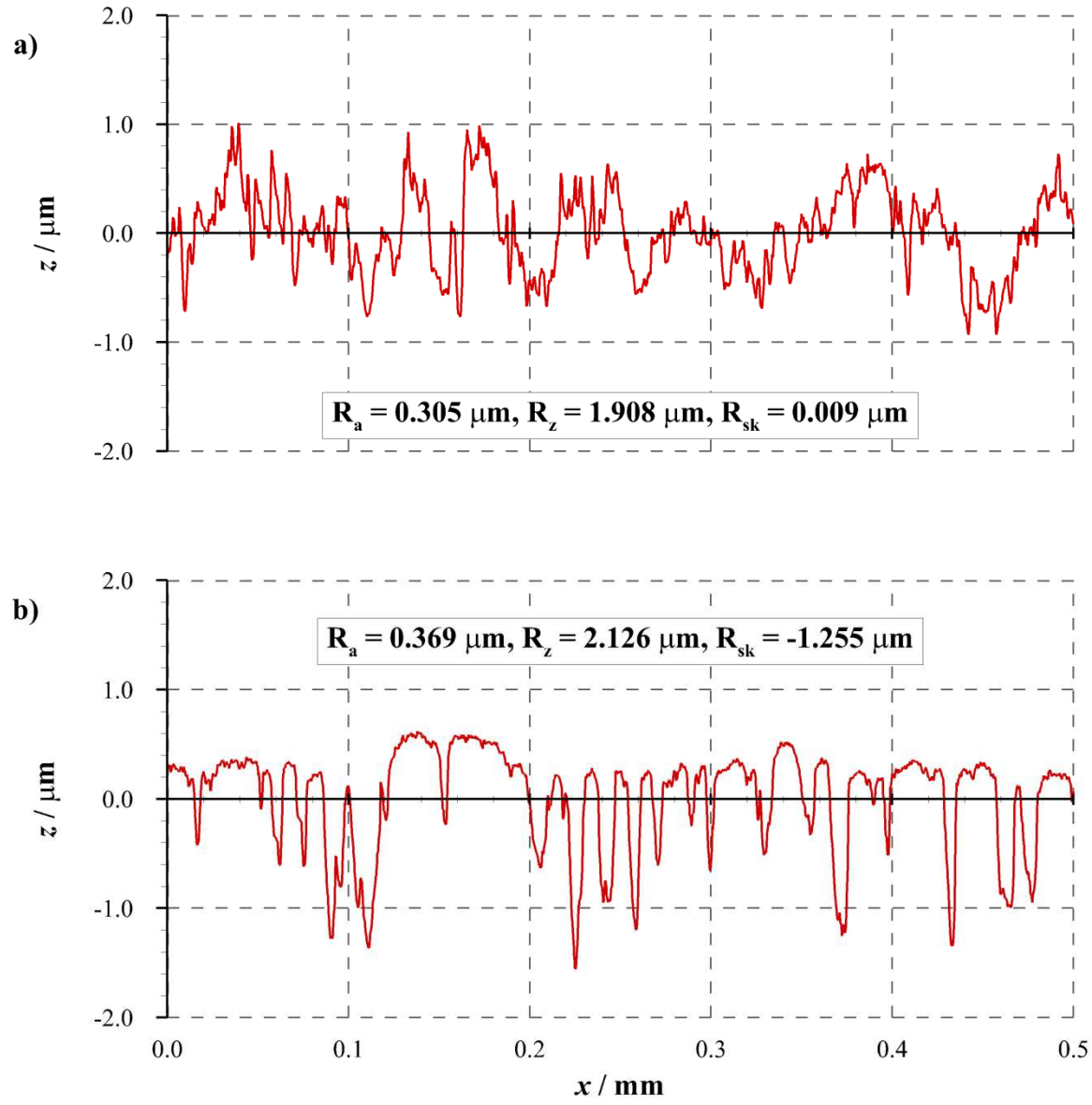

Figure 3.2 - Filtered unrun (top) and run (bottom) surface roughness profiles from gear teeth.

3.2.2. Run surface contact modelling details

Having taken roughness profiles from the gear teeth, 100 µm sections of the filtered run gear surface profile were imported to Abaqus using a Python script, to create a 2D deformable part. The model used for the sinusoidal surface contact discussed in Chapter 2 was modified. The sinusoidal surface was replaced with sections of the filtered run roughness profile, creating five models in total, each corresponding to a different section of the (run) roughness profile. The boundary conditions were defined such that the rough surface was effectively infinitely repeated, as illustrated in Figure

3.3. The vertical edges of each rough surface part, as shown by the dashed lines AB and CD, were restrained in the x-direction, producing lines of symmetry in which the rough surface was reflected. This ensured that edge effects did not distort the results of the simulations. The depth of the model was found to be appropriate through experimentation. Plasticity was found to be limited to less than 20 µm from the surface, while stresses at the boundary AC were found to be less than 1 MPa.

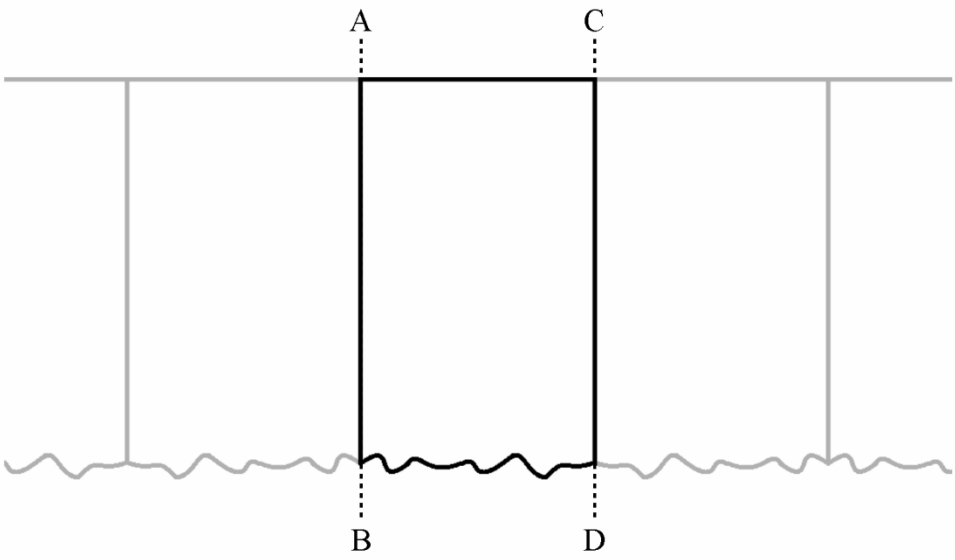

Figure 3.3 - Infinitely reflected boundary condition.

The material properties of the sinusoidal surface contact model were maintained, while improvements to the modelling details which were necessary in the case of the more complex and finely detailed nature of real roughness were made. In the earlier models described in the previous chapter, contact loading was performed by applying a specified displacement, or interference, to one of the contacting bodies. This technique was adopted because the simulations failed when distributed loads were applied. For the rough surface contact models this approach was modified. A small initial displacement was applied, initiating the contact. This displacement was small enough to result in only very low elastic stresses in the material. It was found that once the contact had been established distributed loads could then be applied in the following step without encountering numerical difficulties. In the subsequent step, this displacement was removed while simultaneously

applying a distributed load. Over the duration of the analysis step, the distributed load was increased to 900 N/mm, resulting in material plasticity for multiple asperity contacts. In the final step, the distributed load was removed to obtain the residual results. Details of the run surface contact model are given in Table 3.1.

Table 3.1 – Run Surface Contact Model Summary.

Part	2D Roughness – Imported Run Gear Surface Profiles
	Line Segment → Rigid Flat Plane
Property	E = 200 GPa, ν = 0.32, σ_y = 1.619 GPa
Assembly	Lines of symmetry aligned. Parts on the verge of contact
Step	Initial (required), Contact, Load, Removal
Interaction	Frictionless
	Augmented Lagrange Constraint Enforcement Method
	Small Sliding
	Surface-to-Surface
	Absolute Penetration Tolerance = $1x10^{-15}$m
Load	Up to 900 N/mm distributed load acting on top edge of rough surface parts
Boundary Conditions	Small vertical displacement applied to top edge of rough surface to initiate contact
	Reference point of rigid flat plane restrained ($U_x = U_y = UR_z = 0$)
	Side edges of rough surface parts: Symmetry in y-axis ($U_x = 0$)
Mesh	Partitioned around contact area
	Plane Strain Elements
	Linear Elements

3.2.3. Run surface contact model results

Figure 3.4 shows the von Mises stress distributions for one of the run surface contact model simulations. Figure 3.4a shows the stress contours for the loaded state, with the maximum applied distributed load of 900 kN/m. This load was applied in incremental stages, and as such the development of the contact could be observed. As the load was increased, interaction between neighbouring asperities became more apparent as each individual feature became more heavily loaded. New asperity contacts were created with increasing load, existing contacts grew in size, and some merged with neighbouring contacts.

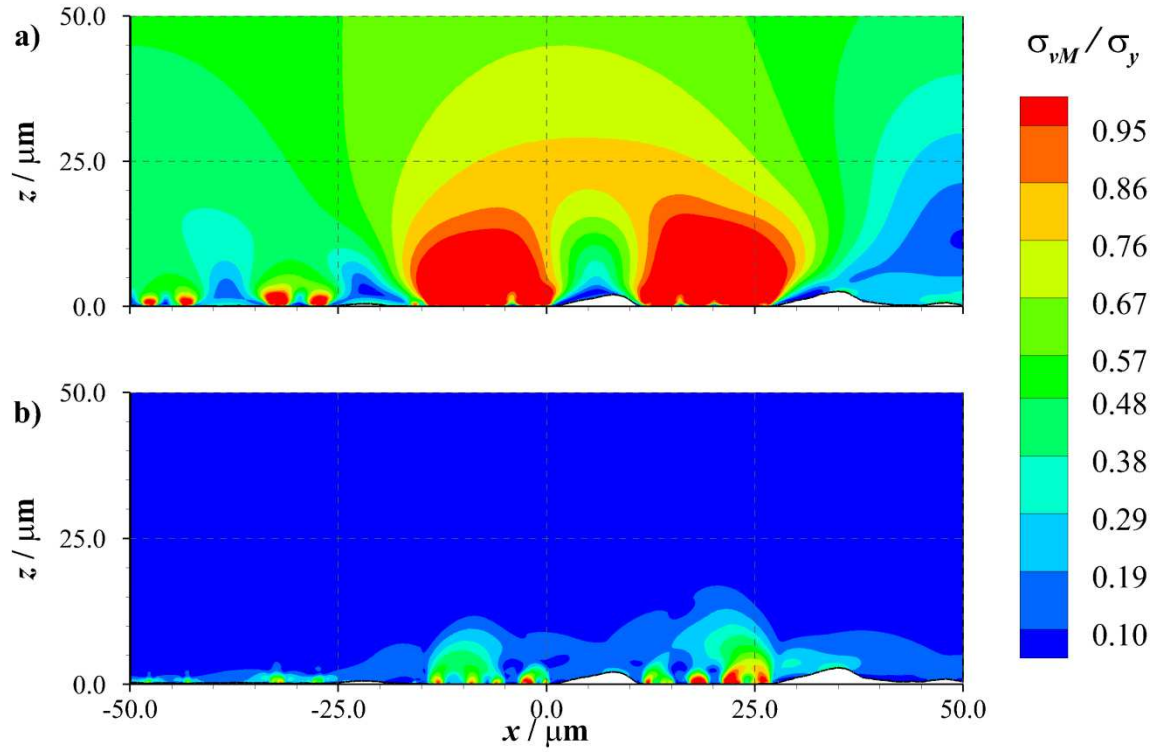

Figure 3.4 - Run surface contact normalised von Mises stress distributions; a) loaded, b) residual.

Figure 3.4b shows the residual von Mises stress distributions of the same run surface contact simulation following removal of the 900 kN/m load. The areas of highest stress were found to occur where the surface has been most heavily loaded. The region between x = 12 µm and 27 µm has three individual contacts when the surface is lightly loaded. These contacts develop to create a single large contact at the final load, but these three regions, corresponding to the earlier contact stage, can be observed in the residual stress fields. Figure 3.5 shows the residual deformation that occurred due to the applied loading in this region, showing both the initial and residual profiles. It can be seen that in this case, the shape change of the asperity is limited to the contact itself and does not noticeably extend to the neighbouring valley features. As has been stated, the roughness profile adopted in these simulations was taken from an already run gear surface and as such the asperities had already undergone some plastic deformation.

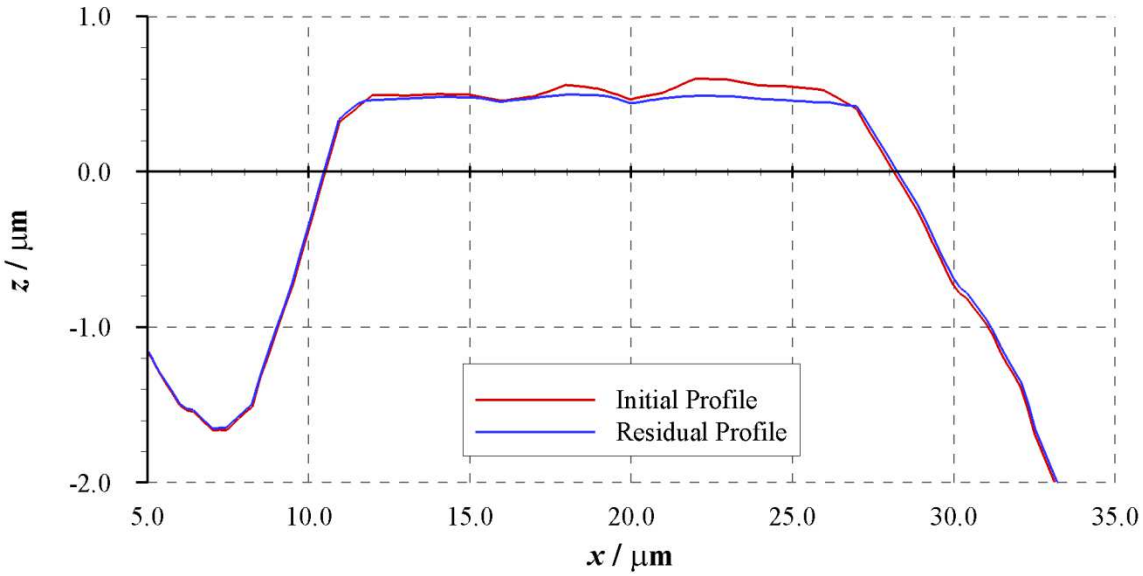

Figure 3.5 - Comparison of surface profiles before and after loading.

3.3. Rough roller contact modelling

Having tested the model creation techniques for rough surface contact models, the surface roughness profiles were superimposed onto smooth rollers to include a curvature of the surface in the simulations that would be found in gear contacts. Both run and unrun profiles were superimposed onto a profile of a smooth roller of radius 38.1 mm, as shown in Figure 3.6. This specific radius was chosen as it matches the size of the specimens used in a two-disc test rig that was to be used subsequently to compare real life measured deformations with those obtained using finite element simulation techniques, as described in Chapter 5.

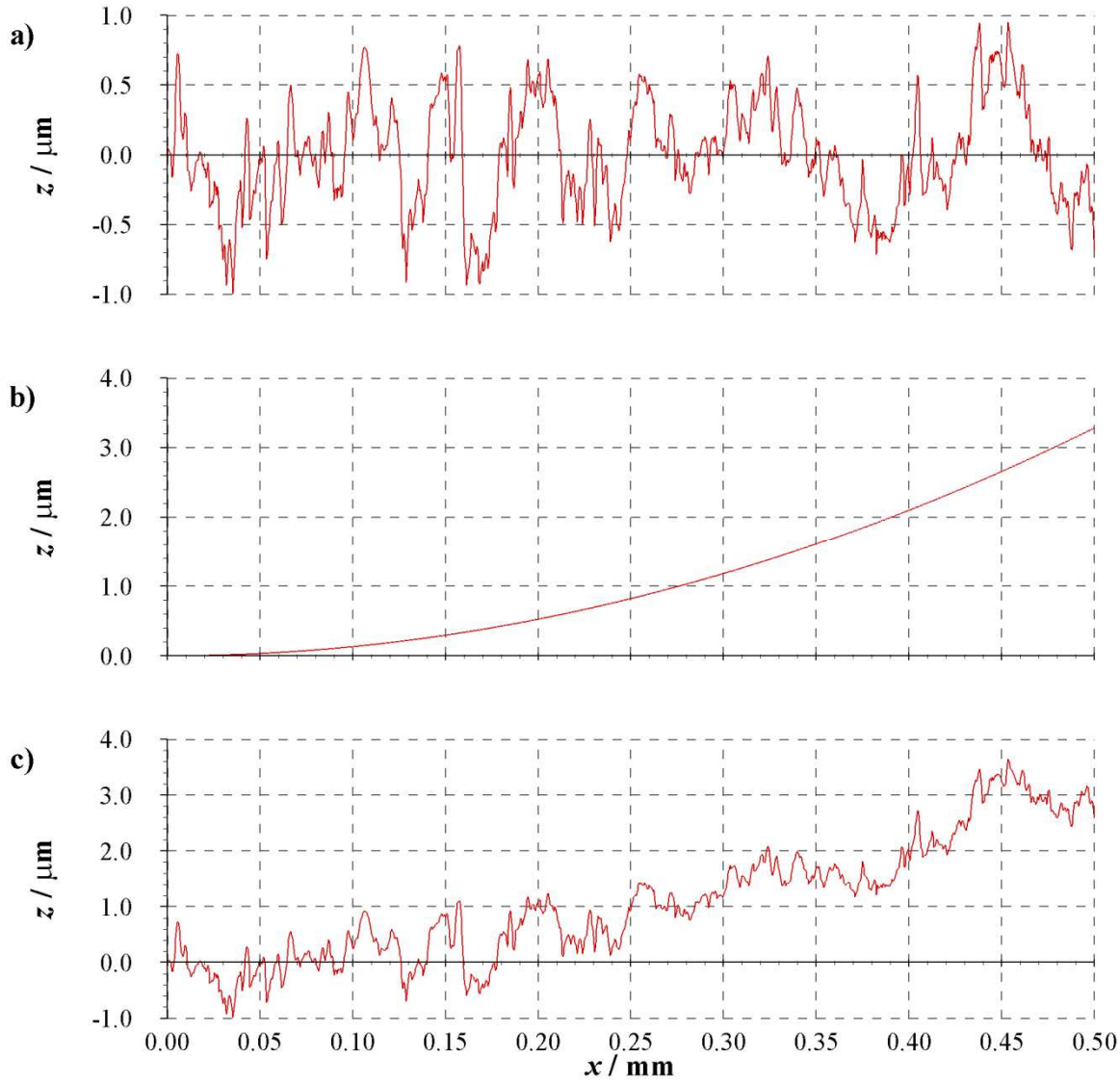

Figure 3.6 - Rough roller model construction method; a) Unrun surface roughness profile, b) smooth roller profile, c) rough roller profile.

3.3.1. Rough roller contact modelling details

The run and unrun rough roller profiles were imported to Abaqus using a Python script, and used to create 2D deformable parts. These parts were assigned the same elastic-plastic material properties as previous models. In some cases, the rough rollers were assigned elastic only material properties for comparison. The models were developed to simulate the interaction of two contacting bodies. The other contacting body in each of the simulations was a deformable, elastic only, smooth roller of the same radius. These were the first simulations undertaken in which the opposing contact surface

was allowed to deform as well as the surface of interest. A distributed load of 75 N/mm was applied to the bottom edge of the smooth surface roller, having initiated contact with a small vertical displacement. The applied load was subsequently removed in order to obtain residual deformation and stress fields. Hertzian contact theory was used to estimate the nominal contact dimension, and each roller was assigned a finer mesh in this predicted contact region. The details of the rough roller contact models can be seen in Table 3.2.

Table 3.2 - Rough Roller Contact Model Summary.

Part	2D rough roller – Imported run and unrun gear surface profiles
	2D smooth roller
Property	Rough: E = 200 GPa, ν = 0.32, σ_y = 1.619 GPa (for elastic-plastic simulations only)
	Smooth: E = 200 GPa, ν = 0.32
Assembly	Model boundaries aligned. Parts on the verge of contact
Step	Initial (required), Contact, Load
Interaction	Frictionless
	Augmented Lagrange Constraint Enforcement Method
	Small Sliding
	Surface-to-Surface
	Absolute Penetration Tolerance = $1\text{x}10^{-15}$ m
Load	75 N/mm distributed load acting on bottom edge of smooth roller
Boundary Conditions	Small vertical displacement applied to bottom edge of smooth surface to initiate contact
	Top edge of rough roller restrained ($U_x = U_y = 0$)
	Side edges of rough and smooth roller restrained in y-axis ($U_x = 0$)
Mesh	Partitioned around contact area
	Plane Strain Elements
	Linear Elements

3.3.2. Rough roller contact model results

Figure 3.7 shows the contact pressure distributions for the run and unrun rough roller simulations respectively, for rough surface elastic and elastic-plastic material properties loaded against a smooth counterface which was assumed to remain elastic. Also plotted is the theoretical Hertzian contact pressure distribution for the same geometrical, material and loading specifications. The contact pressure plots have been normalised against the yield strength, σ_y, of the elastic-plastic material model. It can be seen that the introduction of roughness to the contact surface results in significantly higher contact pressures. In a smooth contact, the load applied is insufficient to cause subsurface plasticity, whereas multiple asperities deformed plastically in rough roller contact models for both the run and unrun surface roughness profiles. In the elastic simulations, the von Mises stress has no limit, and as such neither does the contact pressure. This is particularly pronounced in the unrun rough roller model shown in Figure 3.7b, where contact pressures approach $7.5\sigma_y$ at several asperities. This phenomenon is not seen in the run surface rough roller simulation, as the loading history of the surface has resulted in modifications to the surface that allow it to distribute the applied load more effectively, resulting in lower peak contact pressures.

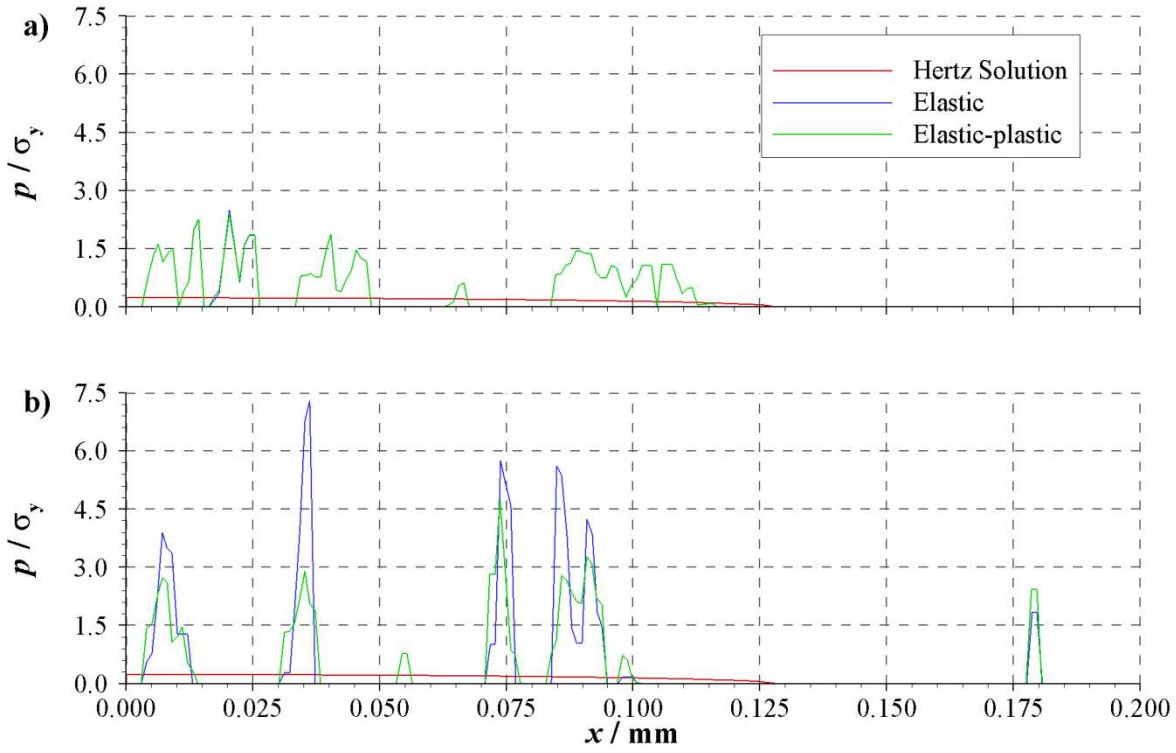

Figure 3.7 - Contact pressure distribution for elastic and elastic-plastic rough roller simulations. a) Run surface, b) Unrun surface (Hertzian smooth contact pressure distribution also shown).

For the elastic-plastic simulation results, the von Mises stress is limited by the specified yield strength and it is then expected that the contact pressure is limited to approximately three times the yield strength (Williams 1994). In the unrun surface model shown in Figure 3.7b, this limit is exceeded. The observed maximum contact pressure is $4.8\sigma_y$ at approximately x = 0.074 mm, but the limit is also exceeded at x = 0.092 mm. As the aim of the research was to investigate the residual deformations and stresses as a result of contact in as-manufactured surfaces, it was decided that the results obtained were open to doubt and that the modelling techniques required further development to provide reliable solutions for such contacts with the maximum contact pressures conforming more closely to the expected maximum value of approximately $3\sigma_y$.

3.4. Advanced modelling techniques

The rough roller contact models were examined at the locations where the normalised contact pressure exceeded the theoretical limit. It was found that the slave surfaces were penetrating the master surfaces more than the user defined limit in the model and that elements were distorting significantly due to the relatively large local deformations occurring at the asperity level. It was thought these surface penetrations were linked to the element distortion, and that if this could be reduced then the model would produce more reliable results. A number of modelling techniques and options aimed at reducing the element distortion were tested using a flat, unrun surface model. A flat surface model was chosen as opposed to a roller for simplicity and reduced computational time, an important factor when testing a wide range of different techniques.

3.4.1. Techniques

Each of the techniques tested in order to reduce element distortion and improve the accuracy of the unrun surface rough roller simulations are summarised below. It should be noted that greater detail is available in the Abaqus Users Documentation (Abaqus 2010a), and it is recommended that these are consulted before implementation of any advanced options.

3.4.1.1. Hourglass Control

Abaqus uses a numerical technique called Gaussian quadrature to integrate quantities over each element. Each element has a number of internal points, known as integration points, or Gauss points, where the reactions to the applied conditions are calculated. Fully integrated elements consist of sufficient integration points to exactly solve each of the terms, assuming that the element is undistorted. Reduced integration uses less integration points, reducing the accuracy, but also reducing computational requirements at the same time. Each of these element types are illustrated in Figure 3.8.

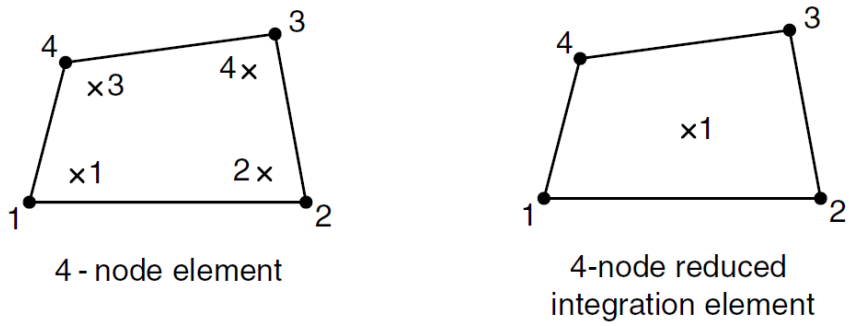

Figure 3.8 - Full and reduced integration, first order, quadrilateral elements (Abaqus 2010a).

By default, Abaqus utilises reduced integration when quadrilateral elements are selected. Under bending loads, reduced integration elements can allow deformations to occur that cause no strain to occur at the integration point. This is illustrated in Figure 3.9 which shows that despite the change in shape, the horizontal and vertical broken lines have remained unchanged. As a result, no stresses or strains can be seen to occur at the integration point at the element centre. This is known as a zero energy mode, and in this case results in a phenomenon called “hourglassing”. Hourglassing is particularly severe in first order quadrilateral elements (Abaqus 2010c). By default, Abaqus combats this by introducing an additional artificial stiffness to the element. However, it is suggested that caution be used in particularly nonlinear problems, as the default hourglass controls are not always effective. An enhanced control option is also available, which is suggested as mitigation in these circumstances. This enhanced hourglass control option is activated in the **Mesh** module, by choosing the **Element Type** menu. From here, the hourglass control can be switched from the default to an enhanced setting.

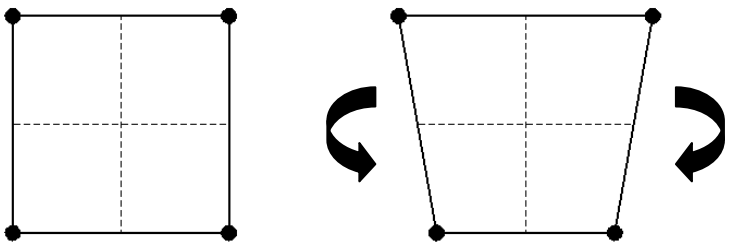

Figure 3.9 - Deflection of a first order, reduced integration quadrilateral element subject to bending.

3.4.1.2. Element integration scheme

Fully integrated elements are not without issues however. Figure 3.10 shows the ideal deflection of an element subject to bending, while Figure 3.11 shows the deflection of a fully integrated element. In ideal bending, the intersections of the dashed lines remain perpendicular to one another. These angles change in fully integrated elements, resulting in shear strains and stresses observed and evaluated at the integration points. This behaviour is known as “shear locking”. This severity of this behaviour can be reduced by refining the mesh; smaller elements can more closely approximate ideal behaviour.

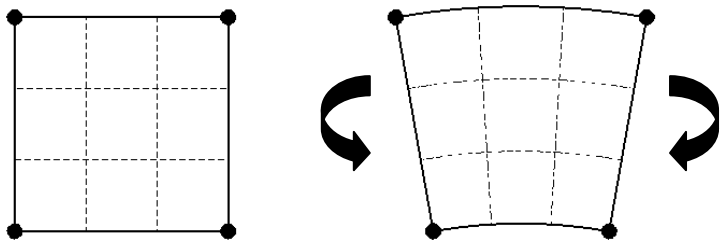

Figure 3.10 - Ideal deflection of a quadrilateral element subject to bending.

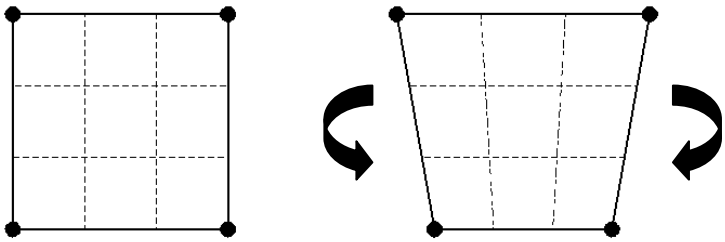

Figure 3.11 - Deflection of a first order, fully integrated quadrilateral element subject to bending.

Another locking phenomenon associated with fully integrated elements is volumetric locking. This occurs in incompressible materials, or materials tending towards incompressibility, such as perfectly plastic materials. The values of strain at each integration point cannot combine effectively to conserve the volume of the element, causing the element to lock. This can be combated by utilising reduced integration, and Abaqus does this automatically. Fully integrated first order elements

actually utilise a selectively reduced integration whereby the integration point volume changes are replaced by the average volume change of the element (Abaqus 2010c). The element integration type can be chosen within the **Mesh** module, in the **Element Type** menu. The relevant tick box can then be chosen. Reduced integration is the default selection.

3.4.1.3. Arbitrary Lagrangian-Eulerian (ALE) adaptive meshing

ALE Meshing is an adaptive meshing technique that is detailed in the Abaqus Users Manual in Section 12 – Adaptivity Techniques (Abaqus 2010a), and illustrated in Figure 3.12. It provides a method to control mesh distortion by allowing the mesh to move independently of the underlying material. In purely Lagrangian formulations, the finite element mesh is "attached" to the underlying material, while in a purely Eulerian analysis, the mesh is fixed in space, and the underlying material can move freely relative to it. ALE adaptive meshing is a combination of these two formulations. The nodes at the edge of the defined regions are fixed to the material, allowing accurate tracking of the region boundaries. The nodes inside the region are free to move relative to the material to ensure element shapes are maintained.

In Abaqus, ALE adaptive meshing is only available when using fully integrated elements. It is activated within the **Step** module, by selecting **Other** from the tool bar. The regions in which the ALE adaptive meshing is applied are chosen by selecting **ALE Adaptive Mesh Domain** and then **Edit**. The regions can then be chosen from the viewport. After selecting the regions in which ALE adaptive meshing is applied, the least number of parameter settings that must be defined are the **frequency** and **sweeps**. The frequency defines, in terms of solution increments, how often the mesh smoothing will take place. The default setting is for mesh smoothing operations to take place every ten increments. The number of sweeps determines the number of mesh sweepings the ALE adaptive mesh region will be subject to. Each mesh sweep allows nodes to be relocated to reduce element distortion. Further options are available and information can be found in the Abaqus Users Manual.

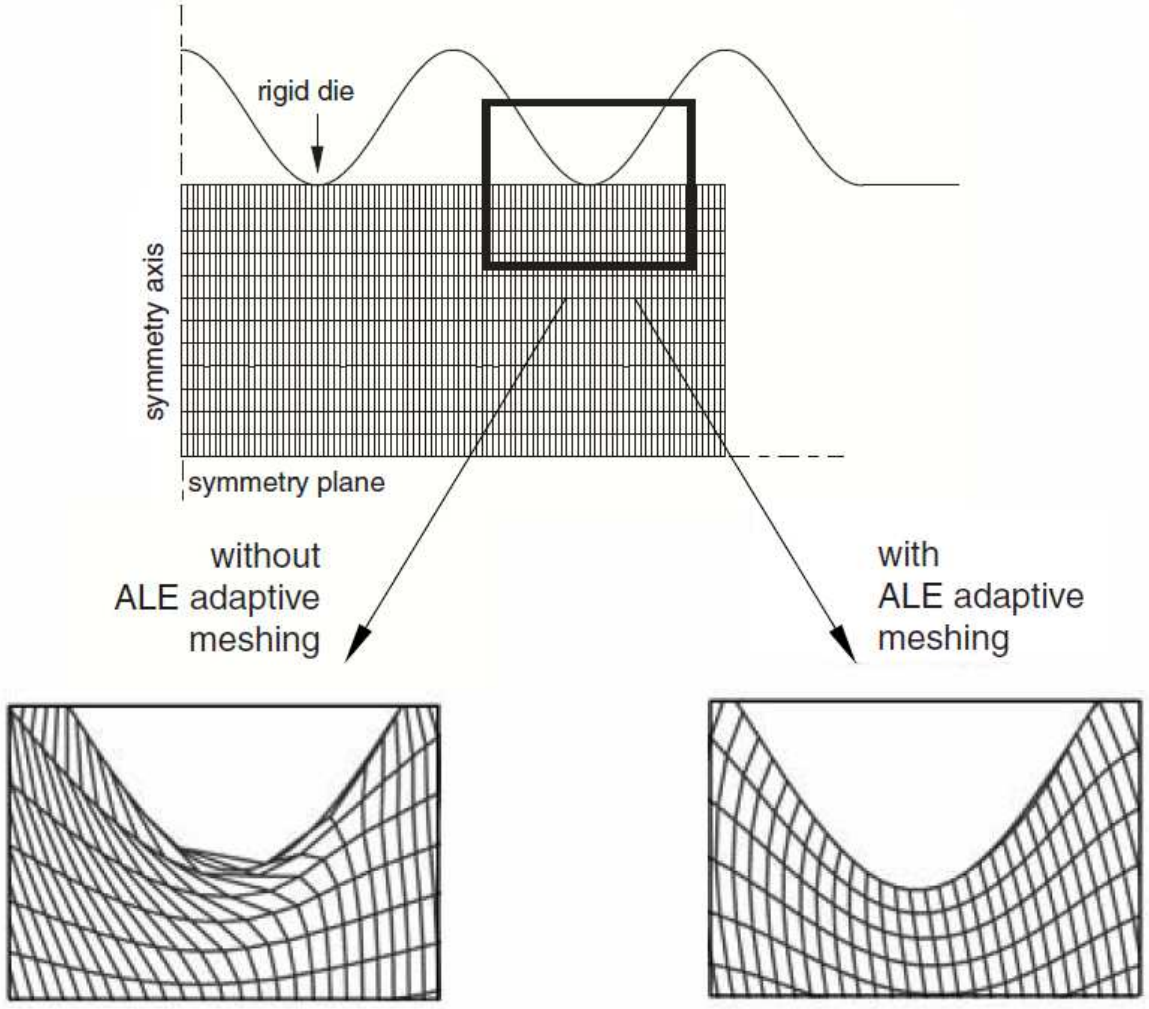

Figure 3.12 - Use of ALE adaptive meshing to control element distortion (Abaqus 2010a).

3.4.2. Modelling details

The model used for the investigation was similar to the flat run rough surface simulations discussed in Section 3.2. Unrun rough surface profiles were imported using a Python script. The rough surface part was given elastic-plastic material properties, with a yield strength, σ_y, of 1.619 GPa. The contacting body was a smooth flat surface of the same width, with elastic only material properties. The parts were arranged to be on the verge of touching and then a small vertical displacement was applied to initiate the contact. This small displacement was then replaced by a distributed load, before being removed again to identify residual shape and stress results. The interaction properties were defined as before, except where detailed in italics in Table 3.3. These were the subject of the

investigation and as such were varied across a number of simulations. These are listed in Table 3.4 where the settings for each of the tested techniques are shown.

Table 3.3 - Modelling Techniques Model Summary.

Part	2D flat rough surface – Imported unrun gear surface profiles
	2D flat smooth surface
Property	E = 200 GPa, ν = 0.32, σ_y = 1.619 GPa
Assembly	Model boundaries aligned. Parts on the verge of contact
Step	Initial (required), Contact, Load, Removal
	ALE adaptive meshing
Interaction	Frictionless
	Augmented Lagrange Constraint Enforcement Method
	Small Sliding
	Surface-to-Surface
	Range of penetration tolerances
Load	750 N/mm distributed load acting on bottom edge of smooth surface part
Boundary Conditions	Small vertical displacement applied to bottom edge of smooth surface to initiate contact
	Top edge of flat rough surface restrained ($U_x = U_y = 0$)
	Side edges of rough and smooth parts restrained in y-axis ($U_x = 0$)
Mesh	Partitioned around contact area
	Plane Strain Elements
	Linear Elements
	Enhanced hourglass control
	Reduced and fully integrated elements

Table 3.4 - Jobs Summary.

Job Name	Integration Scheme	Hourglass Control	Penetration Tolerance	ALE meshing	
				Frequency	Sweeps
Standard	Reduced	Default	Default (Rel. = 0.001 equiv. to Abs. = 2.5×10^{-7})	-	-
ContactControl	Reduced	Default	Abs. = 2.5×10^{-10}	-	-
ContactControl1	Reduced	Default	Abs. = 2.5×10^{-15}	-	-
HourControl	Reduced	Enhanced	Abs. = 2.5×10^{-10}	-	-
HourControl1	Reduced	Enhanced	Abs. = 2.5×10^{-15}	-	-
FullInteg	Full	-	Abs. = 2.5×10^{-10}	-	-
FullInteg1	Full	-	Abs. = 2.5×10^{-15}	-	-
ALE	Full	-	Abs. = 2.5×10^{-10}	10	1
ALE1	Full	-	Abs. = 2.5×10^{-15}	10	1
ALE1_Freq	Full	-	Abs. = 2.5×10^{-15}	1	1
ALE1_Freq_Sweep	Full	-	Abs. = 2.5×10^{-15}	1	10

3.4.3. Investigation results

Table 3.5 shows the maximum contact pressures found in each of the jobs simulated. The contact pressures were then normalised against the yield strength, and compared against the theoretical maximum proposed by Williams (1994). It should be emphasised that the contact pressures shown are the maximum observed contact pressures across the entire contact, and that not all asperity features are found to have such contact pressures. These regions of excessively high contact pressure are relatively infrequent.

Table 3.5 - Contact pressure results from modelling techniques investigation.

Job Name	Max. Contact Pressure, p_0 / GPa	Max. Normalised Contact Pressure	Percentage *over* 'expected' max. contact pressure ($3\sigma_y$) of worst asperity feature
Standard	5.441	3.361	12.0%
ContactControl	5.418	3.347	11.6%
ContactControl1	5.381	3.324	10.8%
HourControl	6.660	4.114	37.1%
HourControl1	6.447	3.982	32.7%
FullInteg	5.480	3.385	12.8%
FullInteg1	5.475	3.382	12.7%
ALE	5.432	3.355	11.8%
ALE1	5.364	3.313	10.4%
ALE1_Freq	5.246	3.240	8.0%
ALE1_Freq_Sweep	5.230	3.230	7.7%

It can be seen that employing tighter control over the penetration tolerance reduces the observed "overpressures". This behaviour was found using each of the techniques tested. However, when the penetration tolerance was reduced further still, the simulations either failed to complete, or resulted in a larger overpressure. These jobs were discarded and are not included in the results shown. Jobs utilising the default hourglass controls (Standard, ContactControl and ContactControl1) each exhibited deformed elements in heavily loaded regions, as shown in Figure 3.13. These were found to occur both at the surface and subsurface. It appears that in the regions where contact overpressures are observed, the elements at the surface are distorted and penetrate the opposing master surface. Using the enhanced hourglass control resulted in better element shape in the contact areas, removing the hourglassing seen to occur in the subsurface region, and reduced the amount of surface penetration. Conversely, not only were significantly higher overpressures found to occur but the number of asperity contacts that resulted in overpressures increased when enhanced hourglass control was implemented. Changing from reduced integration elements, to fully integrated elements also resulted in a reduction in element distortion, but still gave slightly larger

overpressures compared with more default settings. However, selecting fully integrated elements allows ALE adaptive meshing to be utilised, and development of this technique resulted in the contact pressures being the closest to the theoretical limit. ALE adaptive meshing also significantly improved element shape in areas where the most distortion was originally seen to occur. Increasing both the frequency and number of sweeps was found to give the most satisfactory results as can be seen from Figure 3.13.

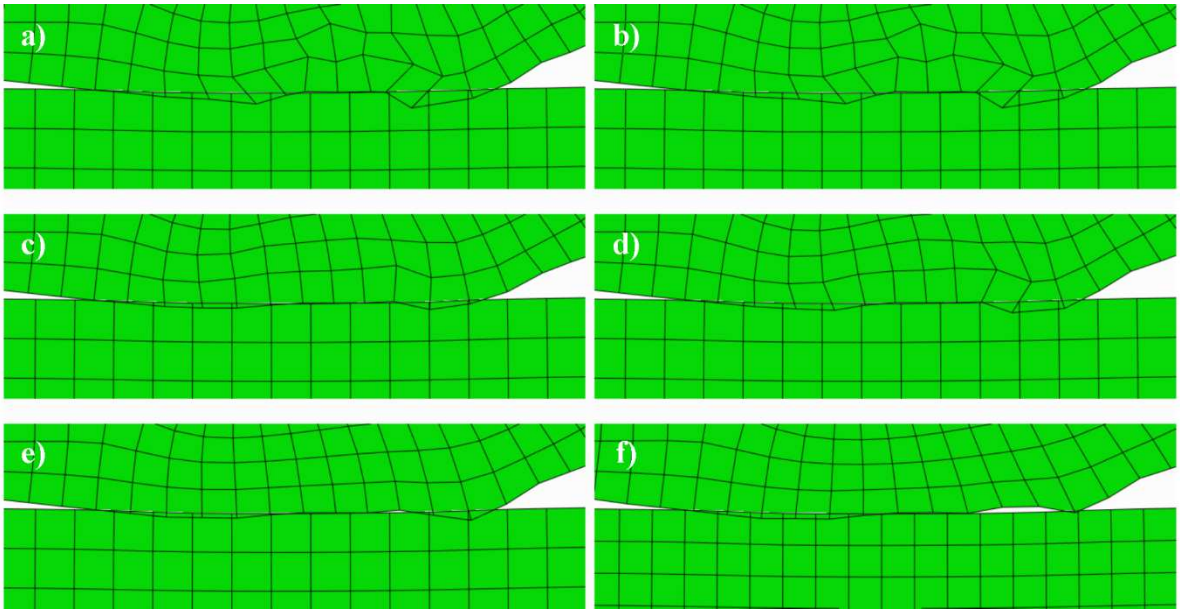

Figure 3.13 - Element shape at surface contact; a) Standard, b) ContactControl1, c) HourControl1, d) FullInteg1, e) ALE1, f) ALE1_Freq_Sweep.

Contact pressures from three of the tested modelling techniques can be seen in Figure 3.14. These three simulations were the jobs named Standard, HourControl1 and ALE1_Freq_Sweep from Table 3.4 and Table 3.5. While the contact pressures for the job Standard did not reach the magnitudes on the unrun rough roller shown in Figure 3.7, the limit of $3\sigma_y$ proposed by Williams (1994) is still slightly exceeded in a number of locations as seen in Figure 3.14a. This behaviour is shown in more detail for one asperity feature in Figure 3.14b. This shows that while the introduction of hourglass control resulted in less distorted elements in Figure 3.13c, this resulted in a higher frequency of pressures exceeding $3\sigma_y$, as well as increasing the magnitude by which is was exceeded. However,

the introduction of ALE adaptive meshing both reduced the amount of element distortion as shown by Figure 3.13f, but also reduced the frequency and magnitude of contact pressures exceeding the limit of $3\sigma_{y.}$

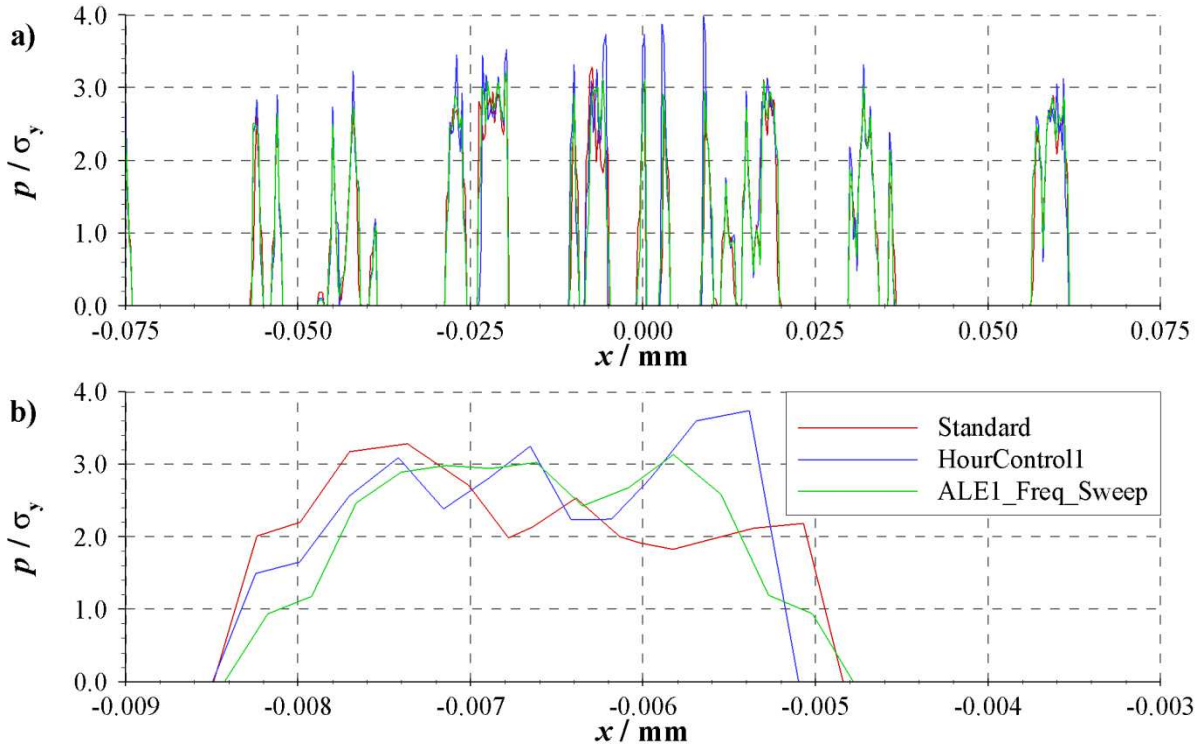

Figure 3.14 - Contact pressure distribution for elastic-plastic unrun rough surface roller simulations; a) Whole surface, b) Between x = –0.009 and x = –0.003.

3.4.4. Unrun rough roller contact model

In order to check the validity of the new modelling techniques for application to other rough surface contact models, the new modelling techniques used for ALE1_Freq_Sweep were applied to the unrun rough roller contact model as previously described in Section 3.3. Figure 3.15 shows the normalised contact pressures for the unrun rough roller contact model as in Figure 3.7. It can be seen that the contact pressures exceeding the limit of $3\sigma_y$ (Williams 1994) using the old techniques have been significantly reduced. The maximum contact pressure has been reduced from $4.75\sigma_y$ to $3.25\sigma_y$, or from 58.4% over the proposed limit, to 8.5%, for this particular surface and associated features. It is therefore recommended that the use of fully integrated elements and ALE adaptive

meshing be used to reduce the degree of element distortion and to reduce the contact pressures to the accepted physical limits.

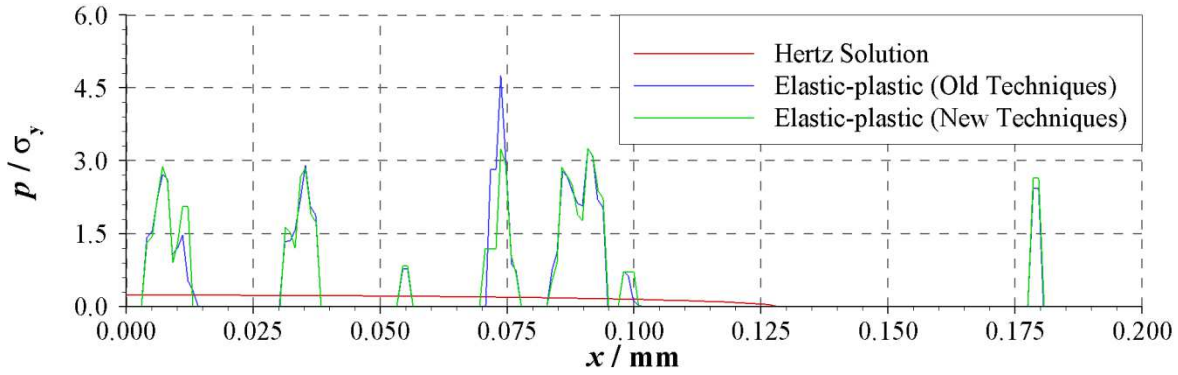

Figure 3.15 - Comparison of old and new modelling techniques on unrun rough roller contact model, as previously shown in Figure 3.7.

3.5. Conclusions

During initial attempts at simulating rough surface contact using unrun gear surface profiles, it was found that the contact pressures significantly exceeded the accepted limit proposed by Williams (1994) of approximately $3\sigma_y$. Upon examination of the strained FE meshes, it was found that noticeable element distortion and surface penetration was found to occur. This surface penetration was seen in regions where elements were distorting at the surface. A number of alternative modelling techniques were therefore investigated to assess their effectiveness in reducing this erroneous behaviour. ALE adaptive meshing emerged as the most effective way of reducing the element distortion, both below and at the surface. This resulted in the reduction of the penetration of the slave surface into the master surface and the degree of overpressure observed in the contact simulation. The method was found to be most effective when the FE package settings were altered from the default, increasing both the frequency and number of sweeps performed in the adaptive meshing smoothing process.

Repeated load contact modelling of real rough surfaces and the effect of tangential loading

4.1. Introduction

The previous chapter described the FE modelling methods which were specially developed for simulating the contact of rough surfaces. This chapter describes the application of these methods in a study of rough surface contact including the effect of multiple loadings and different linear strain hardening material properties. Tangential loading is also considered for a series of defined friction coefficients. The simulation of multiple loadings of the same surface was specified to approximate the running-in process which takes place when new surfaces are first brought into contact and put to work in gears, for example. Numerical comparisons were performed using multiple applications of the same loads, and the order in which different loads were applied. Strain hardening was also introduced in these simulations to assess its effect. It was found that at a given load the majority of the plastic deformation occurred in the first loading cycle. Subsequent applications of the same load resulted in insignificant additional plastic deformation. It was also found that the final residual profile depended only upon the largest load applied to the surface. Little difference was seen when a lower load was applied prior to a larger load when compared to the application of the larger load alone. Additionally, when strain hardening was introduced, the only effect seen was in the magnitude of the plastic deformation. As the material behaviour deviated further from elastic-perfectly plastic, the amount of residual deformation observed decreased. However, the majority of this deformation was still found to occur in the first loading, with little further deformation after subsequent repeat applications of the same load.

In the tangential loading simulations, a series of friction coefficients were defined, and once the normal load was in place, a tangential load was applied simultaneously. For each model considered

the surface was loaded tangentially in both the positive and negative x-direction for comparison. The tangential load varied in proportion to the normal load, with the maximum tangential load taking the surface to the verge of slipping (F/R = 0.95μ). It was found that, even for high practical coefficients of the friction, the tangential loading had only a small effect on the residual shape of the surface and the residual stresses in the material. In order to observe significant effects, the coefficient of friction had to be increased to an unrealistic level.

4.2. Introduction of new modelling components

4.2.1. Strain hardening

In the models described in Chapters 2 and 3, the elastic-plastic behaviour was defined as elastic-perfectly plastic and the von Mises stress did not exceed the yield strength. This model assumes a constant plastic flow stress, whereby any strain can then be achieved. In practice, no materials exhibit elastic-perfectly plastic properties. The simplest extension of elastic-plastic behaviour in the FE model is to introduce linear strain hardening. In this approach, elastic behaviour is assumed up to the yield strength as before and the tangent modulus, E_T, characterises the stress-strain relationship post-yield as illustrated in Figure 4.1, where the elastic and elastic-perfectly plastic limits are shown, together with three intermediate linear strain hardening behaviours. Kogut and Etsion (2002) state that most practical materials have a tangent modulus of less than 0.05E, and so the characteristics illustrated in this figure exaggerate the range to be implemented in the simulations where a lower value of E_T is specified. The stress-strain relationship for a real alloy steel is shown in Figure 4.2 (Callister 2003). This highlights the differences between the elastic-perfectly plastic behaviour assumed and real life behaviour, which exhibits a more complex relationship.

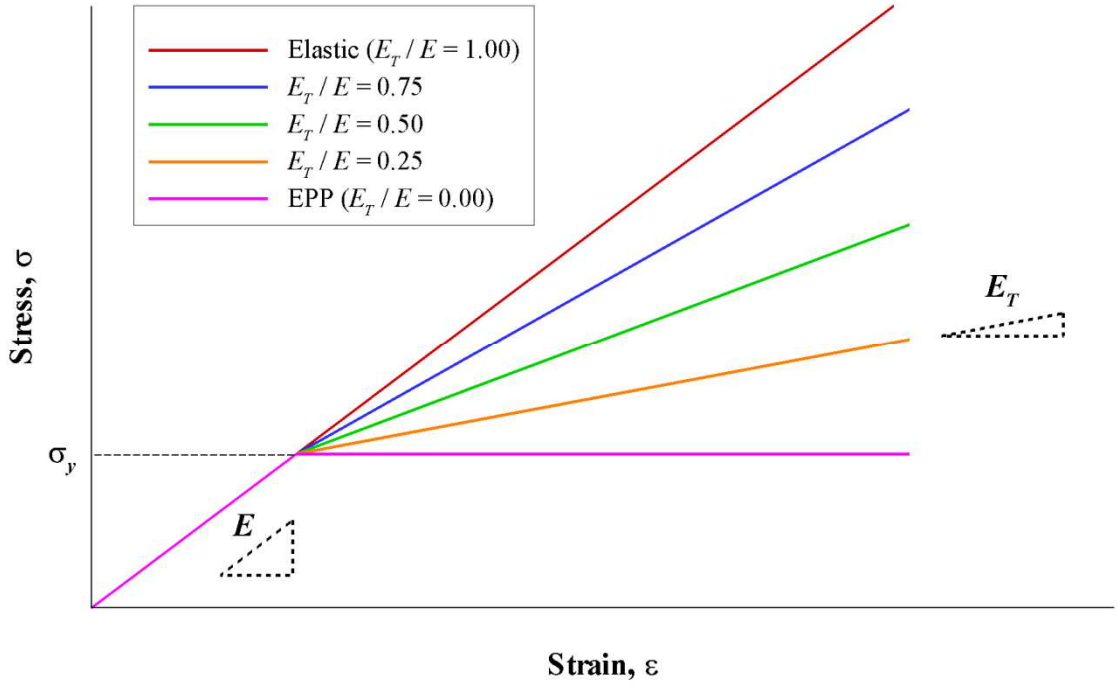

Figure 4.1 - Stress-strain relationship for a range of elastic-plastic materials.

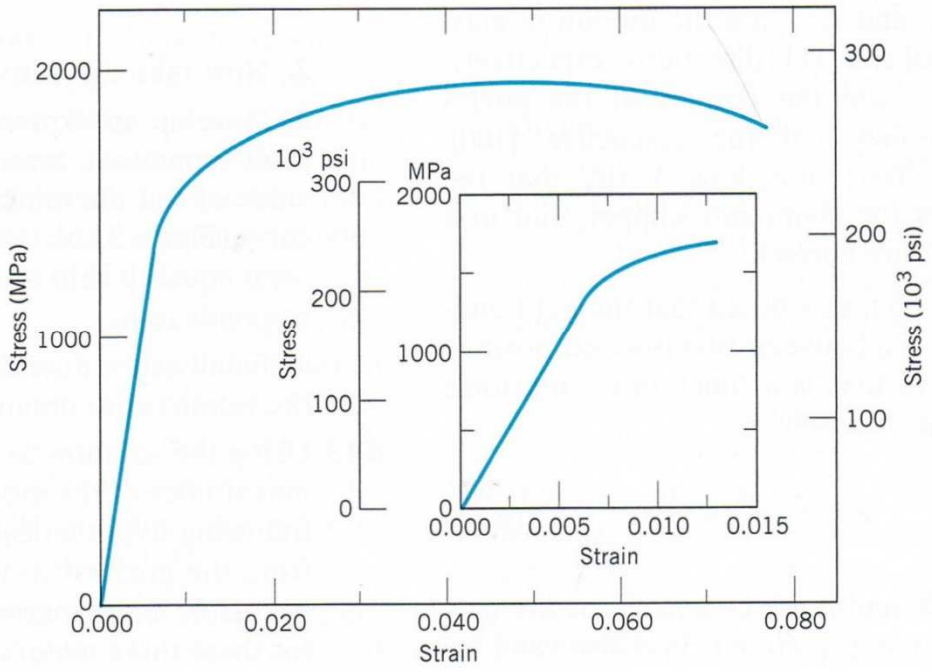

Figure 4.2 - Tensile stress-strain behaviour for an alloy steel (Callister 2003).

Strain hardening behaviour is defined in Abaqus by using the **Property** module, and is specified in the **Edit Materials** menu in almost the same way as the yield strength value is specified for elastic-perfectly plastic behaviour. A further option is obtained by "right clicking" on the existing plastic properties. Here the stress and strain behaviour can be defined, as shown in Figure 4.3. Figure 4.3a shows the input properties for elastic-perfectly plastic material, while Figure 4.3b shows the properties for an elastic-plastic material with linear strain hardening behaviour of E_T / E = 0.250. The corresponding stress-strain relationships for each material are shown in Figure 4.3c and Figure 4.3d, respectively.

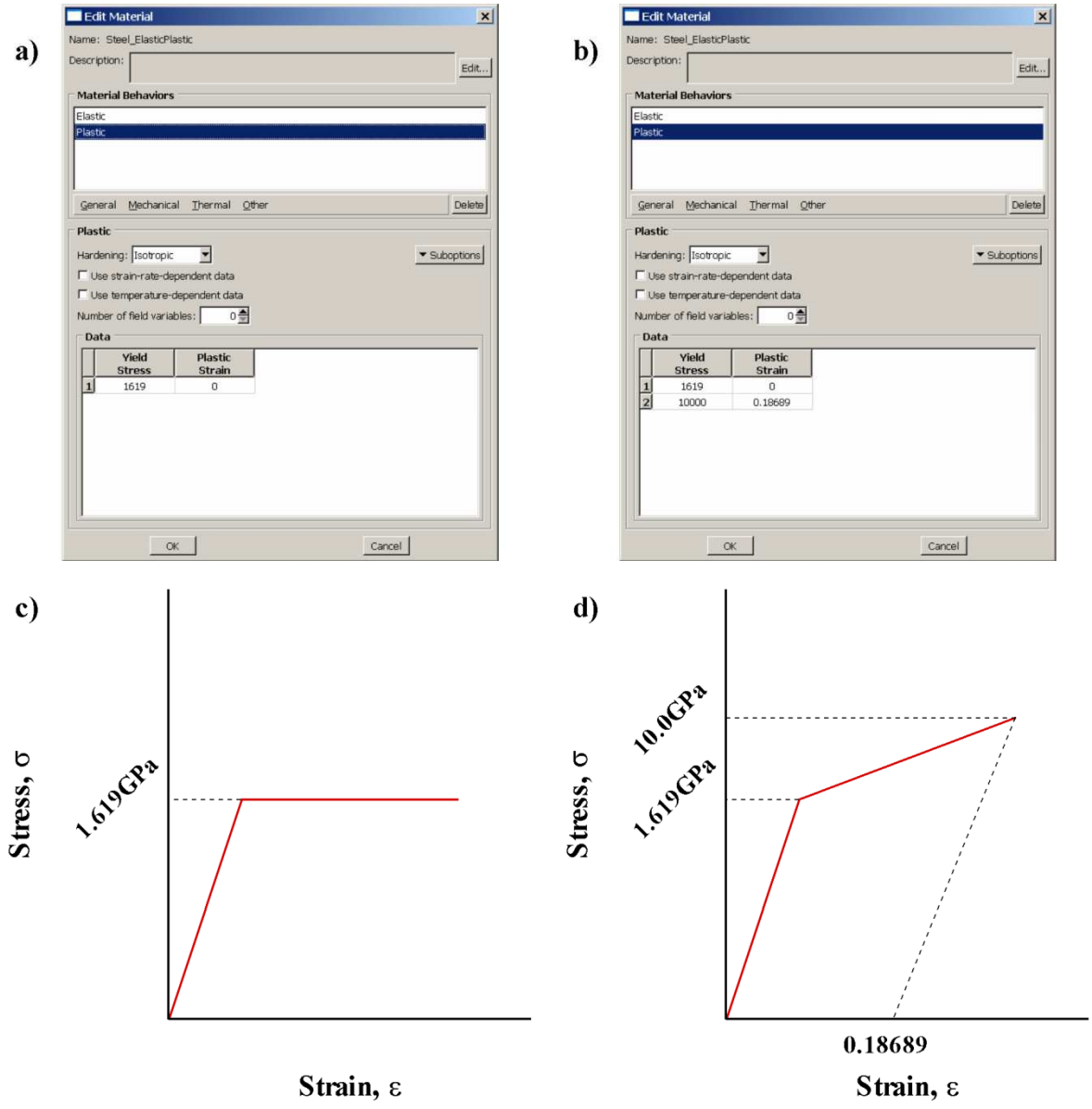

Figure 4.3 - Abaqus/CAE 6.10 "Edit Materials" menu for a) elastic-perfectly plastic, b) linear strain hardening (E_T / E = 0.250), and stress-strain relationships for c) elastic-perfectly plastic, d) linear strain hardening (E_T / E = 0.250).

Abaqus requires the true stress and strain to be defined rather than the nominal stress and strain, which is particularly important if, for example, the user is importing stress-strain data from a uniaxial test. True stress and strain are required to more accurately represent the material response to load as a result of evolving geometry. Using nominal stress uses an approximation that will be fairly accurate under small strains. However, by defining plastic behaviour, large strains are expected to occur, and geometry is expected to change to relatively large extent. Therefore true stress and strain

are required. In the table, the amount of plastic strain that occurs at a specific stress is inserted in the right and left columns, respectively. This is illustrated in Figure 4.3b, where a strain of 0.18689 will be achieved when the von Mises stress is 10.0 GPa. Until the yield strength is achieved, no plastic strain occurs. Abaqus interpolates the stress-strain relationship between these two states. In previous simulations, the plastic behaviour table consisted of the yield strength in the left column and zero strain in the right. Abaqus assumes elastic-perfectly plastic behaviour when no additional information has been given, and so previous simulations have required no further data. In order to define the plastic behaviour the user must therefore calculate the stress-strain relationship for the required tangent modulus subsequent to initial material yield. It is recommended to choose a particularly high stress value that the loading conditions of the simulation are unlikely to exceed in order to ensure the required plastic behaviour is observed throughout. The required strain input can then be calculated given the following relationship.

$$\varepsilon = E\,\sigma \qquad \textbf{Eq. 4.1}$$

However, these stress and strain values cannot immediately be input to the left and right columns respectively. Abaqus uses the true stress and strain, rather than the nominal stress and strain. The true stress and strain can be calculated as follows.

$$\sigma_{true} = \sigma_{nom}\,(1 + \varepsilon_{nom}) \qquad \textbf{Eq. 4.2}$$

$$\varepsilon_{true} = \ln\,(1 + \varepsilon_{nom}) \qquad \textbf{Eq. 4.3}$$

The true strain must then be converted into the true plastic strain.

$$\varepsilon_{true}^{pl} = \varepsilon_{true} - \frac{\sigma_{true}}{E} \qquad \textbf{Eq. 4.4}$$

The true stress and true plastic strain are then input into the plastic properties table in the left and right columns, respectively. Abaqus interpolates between zero and defined strain for any stress between the yield and maximum stresses. Upon completion of the simulation a check is made to

ensure that the proposed maximum stress has not been exceeded, as perfectly plastic behaviour will be exhibited beyond it.

4.2.2. Friction and tangential loading

In previous simulations, the contact was defined as frictionless, i.e. the surfaces were allowed to slide relative to one another with no resistance. In practice friction resists relative tangential motion between the two surfaces. According to Amontons' classical laws of friction, the tangential force required to overcome friction is proportional to the applied normal force.

$$F = \mu R \qquad \text{Eq. 4.5}$$

In dry, metal on metal contact, the coefficient of friction can range from μ = 0.5-1.0 (Bowden and Tabor 1964). In lubricated surfaces, the coefficient of friction where surfaces come into contact can typically range from $\mu \approx 0.1$ in boundary lubrication, to as low as $\mu \approx 0.005$ in hydrodynamic or mixed lubrication conditions (Williams 1994).

Friction is implemented in Abaqus using the **Interaction** module. When creating the interaction properties, the normal and tangential behaviour are defined. In previous simulations, the tangential properties were defined as frictionless. The most basic form of friction behaviour which can be specified is the "penalty" method. Upon selecting this option, the user can then enter the required friction coefficient.

A tangential force can be applied to the model in the same way as a normal force. Normal forces in the previous simulations were applied as pressures, i.e. as a force per unit area. As a plane strain assumption has been made throughout, this is effectively a force per unit length perpendicular to the model acting on the edge to which it has been applied. In the **Load** module, a mechanical category load is created and the surface traction option selected. The application region and magnitude of the tangential force per unit area can then be defined in the same manner as the normal load has been applied previously. A difference between the normal loading and tangential

loading is the requirement to specify a vector which defines the direction of the tangential force. This is created by clicking the edit button next to "vector" in the **Edit Load** menu. The first and second point of the desired vector can then be selected in the viewport to specify the friction force direction.

4.3. Multiple load contact modelling

4.3.1. Modelling details

Two 0.1 mm sections of un-run surface roughness were imported to Abaqus using a Python script and used to create 2D deformable parts. The node spacing at the surface for each part was specified to be 1.0 µm. This spacing was chosen to provide results at a similar resolution to that used by the research group at Cardiff in EHL analysis. Additional discussion of the effect of element sizing can be found in Chapter 5, in Section 5.4.2.1.

The parts extended 0.5 mm (five times the width of the surface) above the rough surface to provide an approximation to a semi-infinite body. The opposing contacting body for each rough part was an identical 2D deformable part, except that the rough surface was replaced by a smooth one. The elastic material properties were defined as before for each contacting body. The rough part was also given plastic properties, with a yield strength, σ_y, of 1.619 GPa. The effect of introducing strain hardening behaviour was to be assessed and so two different characteristics were simulated for comparison with the typical elastic-perfectly plastic model. Tangent modulus, E_T, values of 25 GPa and 50 GPa were chosen for evaluation, giving E_T / E ratios of 0.125 and 0.250 respectively. While practical materials typically have E_T / E ≤ 0.05 (Kogut and Etsion 2002), the aim of implementing a more pronounced strain hardening behaviour was to judge its effects, thus providing more information for an assessment of the suitability of the assumption of elastic-perfectly plastic behaviour.

Previously three steps had been created in each simulation; one to initiate contact with a small displacement, one to apply the required load, and one to remove it. In the series of analyses described here, these steps were then duplicated a further five times, creating a simulation with six independent loading stages. These steps could then be suppressed if fewer loadings were required. Two different loads were applied in the form of a pressure to the top free edge of the rough part. Given the 2D simplification of the contact, these were effectively distributed line loads of 350 N/mm and 700 N/mm respectively. Each surface was subject to two load schemes defined as follows. Load scheme 1 was a simulation with three applications of the lower load, followed by three applications of the higher load. Load scheme 2 was a separate simulation with just three applications of the higher load. This procedure was used to test the effects of the loading history of a surface. Boundary conditions were applied at the sides of each part to simulate an infinitely repeated mirrored surface, while the bottom free edge of the smooth part was restrained against vertical and horizontal displacement. The remaining modelling details were specified in accordance with the contact modelling developments for rough surface contact described in Chapter 3 and can be seen in Table 4.1.

Table 4.1 - Multiple loading contact model summary.

Part	2D rough surface – Imported unrun gear surface profiles
	2D smooth surface
Property	Rough: E = 200 GPa, ν = 0.32, σ_y = 1.619 GPa, E_T / E = 0 (elastic-perfectly plastic), 0.125, 0.250
	Smooth: E = 200 GPa, ν = 0.32
Assembly	Model boundaries aligned. Parts on the verge of contact
Step	Initial (required), Contact, Load, Removal (repeated for number of loadings)
	ALE Adaptive Meshing – Frequency = 1, Re-meshing sweeps = 10
Interaction	Frictionless
	Augmented Lagrange Constraint Enforcement Method
	Finite Sliding
	Surface-to-Surface
	Absolute Penetration Tolerance = $1x10^{-15}$m
Load	300 N/mm or 700 N/mm distributed load acting on top edge of rough surface part
Boundary Conditions	Small vertical displacement applied to top edge of rough surface to initiate contact
	Bottom edge of smooth surface part restrained ($U_x = U_y = 0$)
	Side edges of rough and smooth surface parts restrained in y-axis ($U_x = 0$)
Mesh	Partitioned around contact area
	Plane Strain Elements
	Linear Elements
	Fully integrated elements

4.3.2. Loaded results

Figure 4.4 shows the contact pressure distribution obtained at the final loading application of 700 N/mm for both of the simulated load schemes. Figure 4.4a, Figure 4.4b and Figure 4.4c show the results obtained for the different material models assumed. It can be see that the two distributions in each figure are essentially the same for the two different loading schemes but significant differences are seen to occur in some locations. These differences occur at the edge of asperity contacts, where slight differences in asperity contact areas may result in a node being outside of the contact in one load scheme, and in contact in the other. The first scenario results in zero contact pressure, while the latter results in a finite contact pressure. In plastic contacts, contact pressure increases rapidly at the contact edges further highlighting the differences. Across the remainder of

the contacts, excellent agreement is seen to occur. Including the previously described larger differences, the average difference in contact pressures between load schemes for each set of material properties was approximately 16 MPa, or one percent of the yield strength. This strongly suggests that only the highest load to which a surface is subjected is important when considering the behaviour of a surface under load.

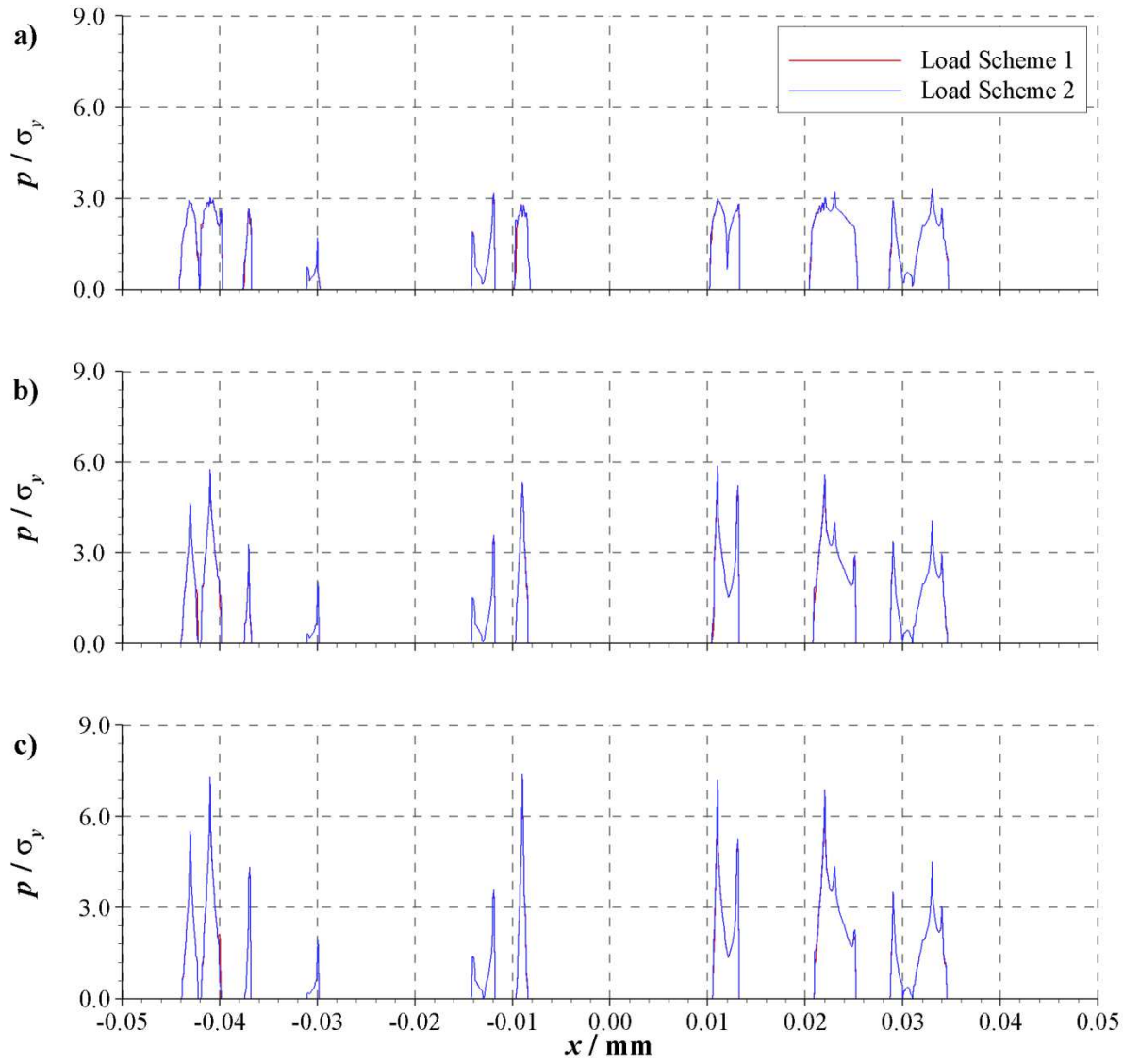

Figure 4.4 - Contact pressure distributions for final 700 N/mm loading for loading schemes 1 and 2; a) elastic-perfectly plastic, b) E_T / E = 0.125, c) E_T / E = 0.250.

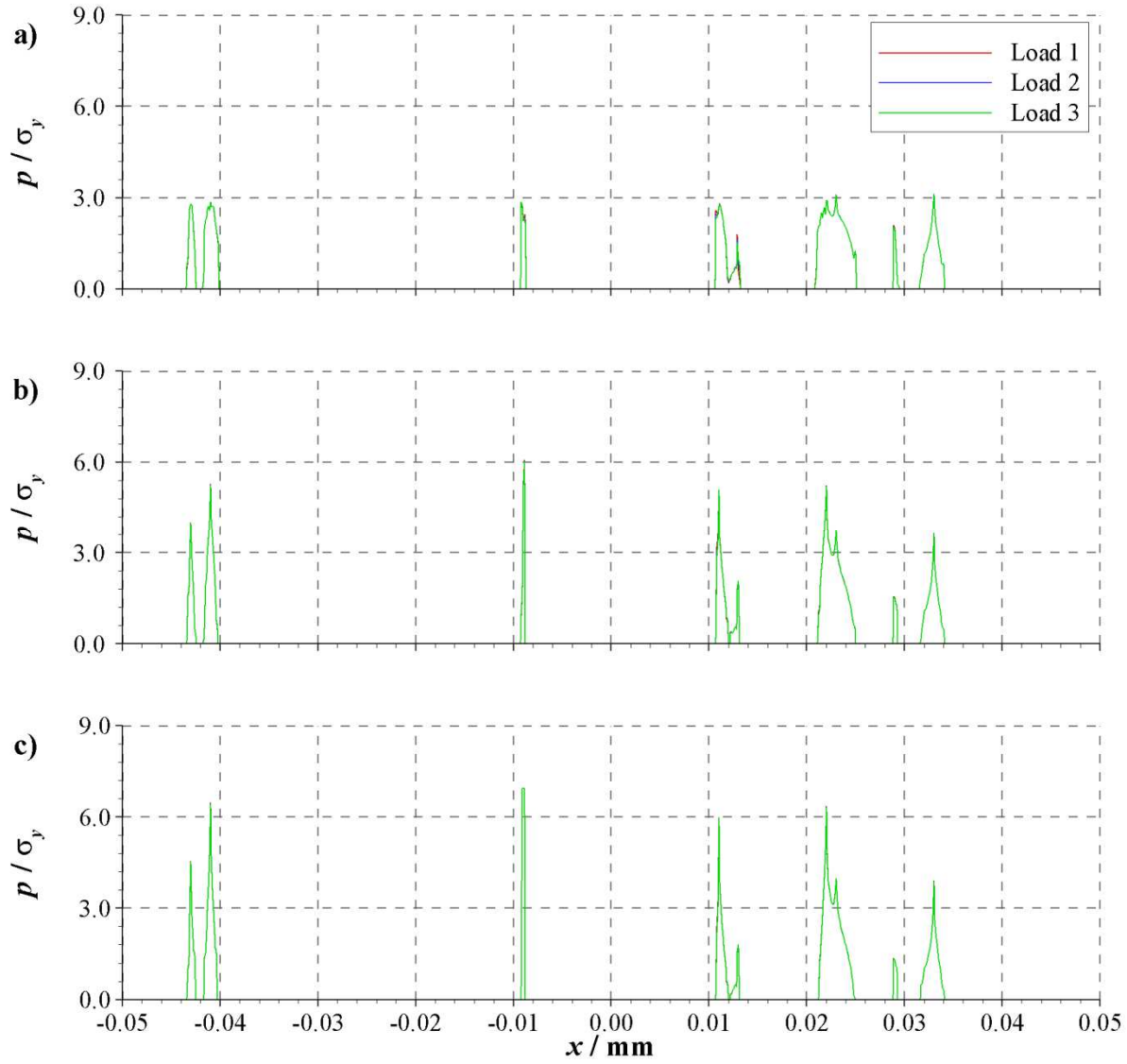

Figure 4.5 - Contact pressure profiles for each 350 N/mm load application; a) elastic-perfectly plastic, b) E_T / E = 0.125, c) E_T / E = 0.250.

Figure 4.5 shows the contact pressure profiles for each 350 N/mm load application in load scheme 1. Each figure shows three pressure profiles, and Figure 4.5a, Figure 4.5b and Figure 4.5c show results for the different material models. Figure 4.6 shows the contact pressure profiles for each 700 N/mm load application in load scheme 2, with Figure 4.6a, Figure 4.6b and Figure 4.6c again showing the results for different material models. For each material model it is clear that there is no significant difference in the contact pressure obtained for repeated applications of the same load. However, comparing them against one another, clear differences can be seen. In Figure 4.5a and Figure 4.6a it

can be seen that the elastic-perfectly plastic behaviour limits the contact pressure to approximately three times the yield strength. Upon introducing strain hardening however, the limit is exceeded, and the contact pressure can be seen to exceed this value in numerous locations. The maximum contact pressure observed increases as E_T / E increases from 0.125 to 0.250 as the material properties allow the surface to carry more of the load in smaller, more concentrated regions.

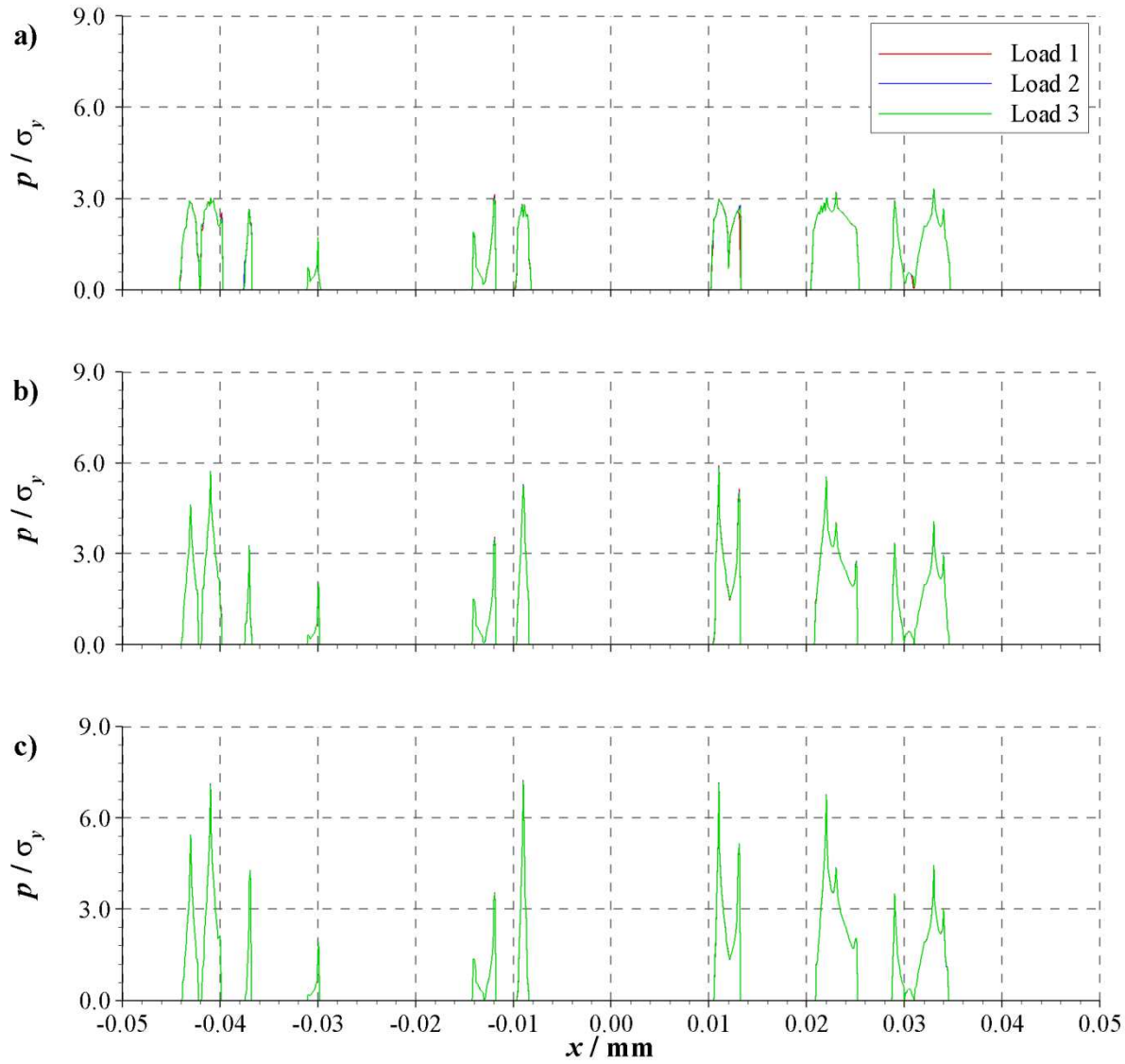

Figure 4.6 - Contact pressure profiles for each 700 N/mm load application; a) elastic-perfectly plastic, b) E_T / E = 0.125, c) E_T / E = 0.250.

Figure 4.7 and Figure 4.8 show detailed contact pressure plots for two asperity features, at loads of 350 N/mm and 700 N/mm, respectively. With elastic-perfectly plastic material properties, it can be

seen that the contact pressures do not exceed three times the yield strength, as previously discussed, and that a higher E_T / E ratio results in increasingly higher contact pressures. It can also be seen that this increase in contact pressure is associated with a reduction in the contact area.

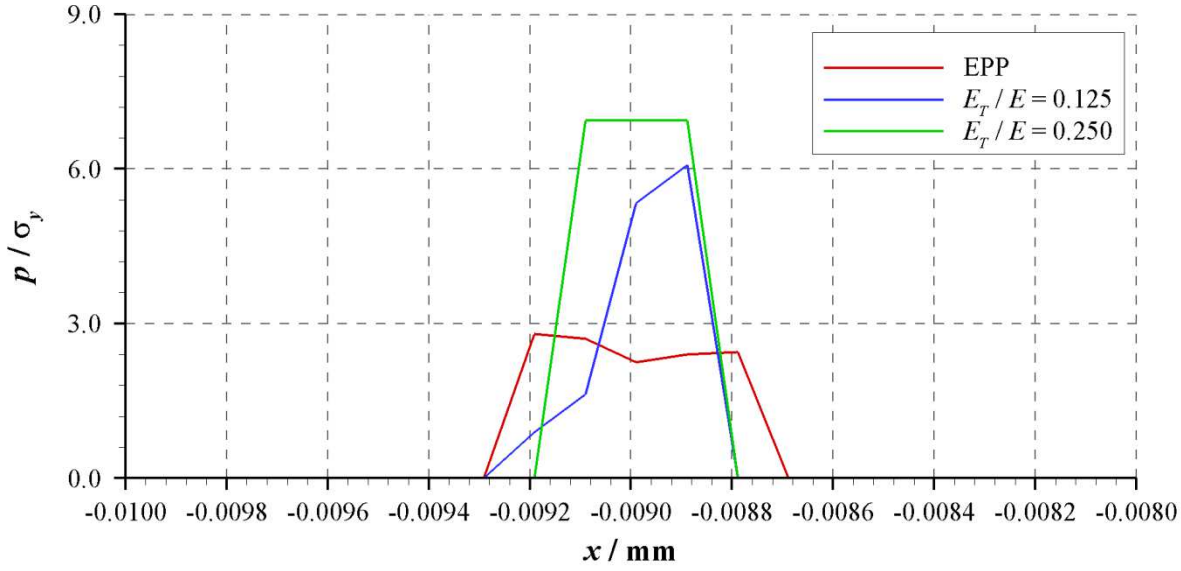

Figure 4.7 - Contact pressure plot for first load application of 350 N/mm.

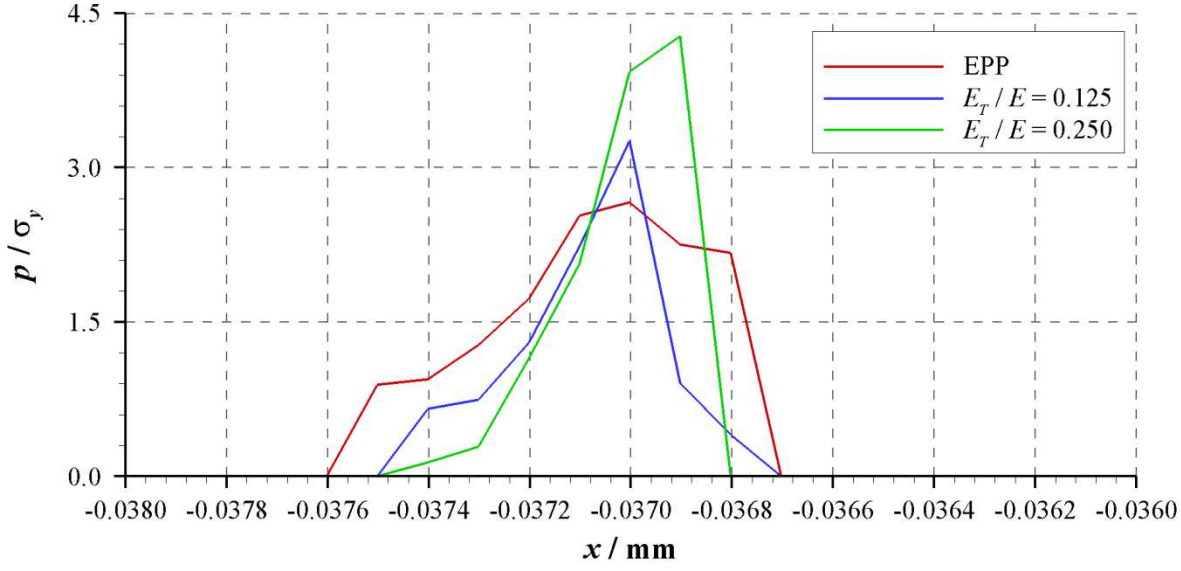

Figure 4.8 - Contact pressure plot for first load application of 700 N/mm.

Figure 4.9 shows contours of the normalised von Mises stress for each of the materials when subject to the final loading of 700 N/mm for a 40 µm section of the rough surface. The von Mises stress was normalised against the assumed material yield strength of 1.619 GPa. Three large contact regions can be seen, between x = 0.010 mm and x = 0.013 mm, x = 0.021 mm and x = 0.025 mm and x = 0.032 mm and x = 0.034 mm, with a smaller contact region at x = 0.029 mm, each resulting in significant subsurface stresses. It can be seen that the stresses in the bulk material are consistent across each of the materials simulated; it is in the heavily loaded asperity regions that differences become apparent. In the elastic-perfectly plastic material in Figure 4.9a, the von Mises stress is limited by the yield strength. In the materials exhibiting linear strain hardening behaviour in Figure 4.9b and Figure 4.9c, this limit is removed, and so regions of higher stress are apparent, particularly around x = 0.011 mm, and x = 0.022 mm. This illustrates the way in which the load is carried by the rough surface in each case. As the stress is limited in the elastic-perfectly plastic material, the contact is slightly larger, as more material is required to carry the asperity load. Without the limit of perfectly plastic behaviour, the surface carries the load in smaller, more concentrated regions. In comparing the two materials with linear strain hardening, it can be seen that a higher peak von Mises stress is found to occur in the material where E_T / E = 0.250.

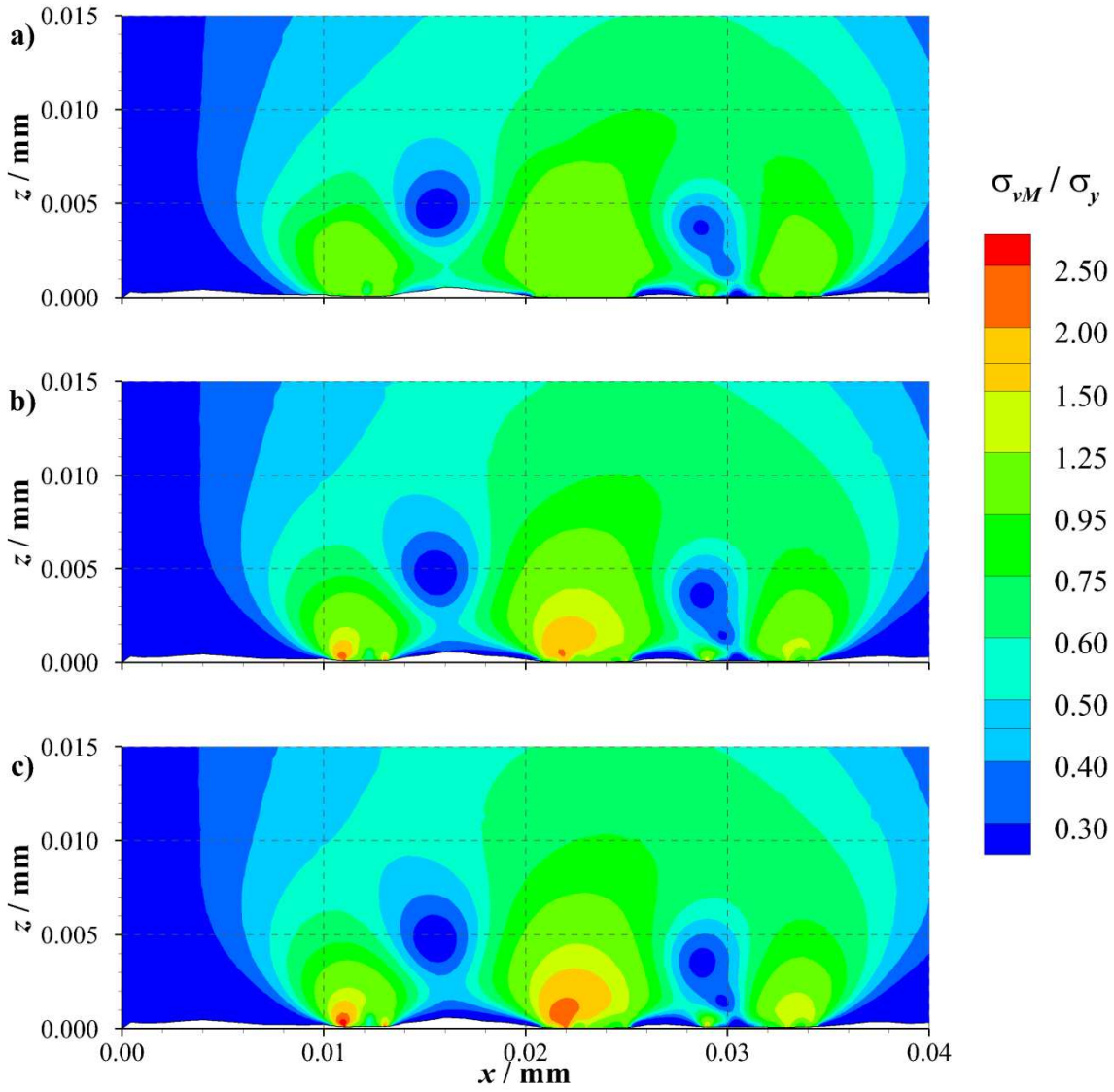

Figure 4.9 - Contours of normalised von Mises stress for final 700 N/mm loading; a) elastic-perfectly plastic, b) E_T / E = 0.125, c) E_T / E = 0.250.

Figure 4.10 shows contours of normalised direct stress in the tangential (x) direction for each of the materials when subject to the final loading of 700 N/mm for a 40 µm section of the rough surface. It can be seen that the majority of the material is in a compressive state of stress. The same three large contact regions are highlighted by larger magnitude stresses. These can be found between x = 0.010mm and x = 0.013 mm, x = 0.021 mm and x = 0.025 mm and x = 0.032 mm and x = 0.034 mm, with a smaller contact region at x = 0.029 mm. As with the von Mises stress contours, the general forms of the distributions are similar between each of the materials, albeit with small differences. In

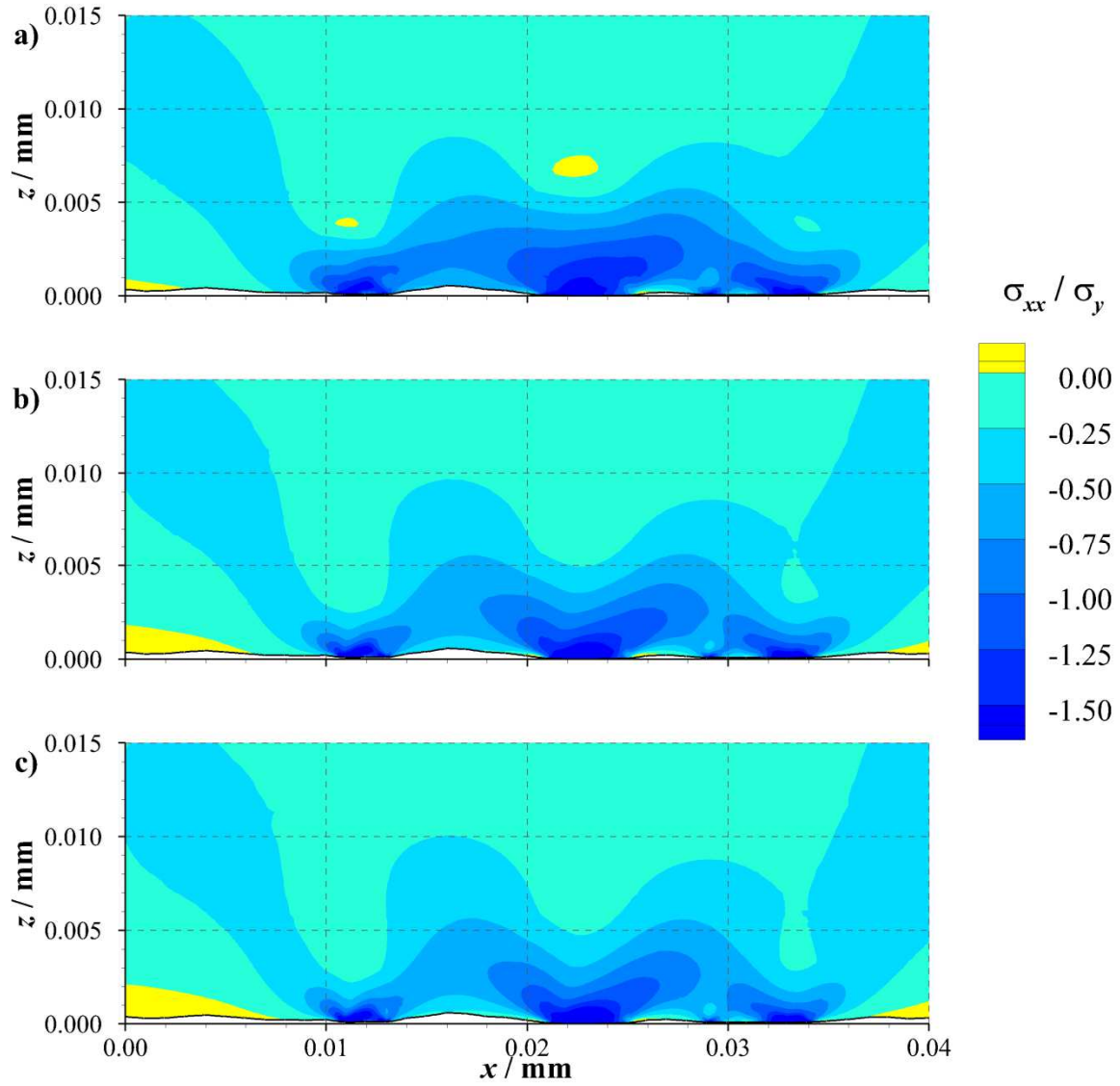

Figure 4.10 - Contours of normalised direct stress in the tangential direction for final 700 N/mm loading; a) elastic-perfectly plastic, b) E_T / E = 0.125, c) E_T / E = 0.250.

comparison with the elastic-perfectly plastic material, increasing E_T / E results in the higher magnitude stress regions being smaller and more concentrated around the asperity contacts. Small regions of tensile stress can be found outside of the contact regions, in the local valley features, for each of the materials. These stresses may be contributing factors to micropitting failures, as it has been found that micro-cracks can initiate in local valleys, depending on the orientation of the valley relative to the sliding direction. (Moorthy and Shaw 2013). These can be seen at the edges of the plotted section, increasing in size as E_T / E is increased. In the elastic-perfectly plastic material, some

subsurface tensile stresses can be seen at x = 0.011 mm, z = 0.004 mm and at x = 0.022 mm, z = 0.007 mm. This is possibly due to the incompressibility of the material after yielding resulting in material being forced from beneath the asperity contacts to the surrounding areas to the sides.

4.3.3. Residual results

Figure 4.11 shows the residual profiles following the final loading application for load scheme 1 and load scheme 2 which are indistinguishable. Each figure includes results for each set of material properties. Results for elastic-perfectly plastic, E_T / E = 0.125 and E_T / E = 0.250 materials are shown in Figure 4.11a, Figure 4.11b and Figure 4.11c, respectively. It can be seen that for each material definition, very little difference can be seen between the residual profiles resulting from the two loading schemes; that is, the order of loading is unimportant. These differences can be quantified by comparing the co-ordinates of the surface nodes following each load scheme. The maximum and mean differences calculated are given in Table 4.2. Also shown are the maximum and mean differences expressed as a percentage of the maximum deflection of the surface. For each material model, the maximum deflection occurred for the asperity located at x = 0.022 mm.

For each material model, the profile deformation is limited to the tips of the asperities. Across the whole 0.1 mm profile, five contact regions occur, at approximately x = −0.042, −0.009, 0.012, 0.023 and 0.033 mm. The different material models lead to different results for the residual profiles in the vicinity of the loaded asperities, with the magnitude of deformations decreasing as the strain hardening behaviour is increased. As with the contact pressure results previously discussed in Section 4.3.2, this suggests that little difference is seen in the surface subsequent to the initial application of a given load, further suggesting that the running-in process is limited to the very early life of a surface when initial contact occurs. Further changes would be expected to occur in the event of an increased load being applied to the surface. Increasing loads may occur as part of the start up process of a machine, extending the running-in process to the time it takes for the largest load to be applied. Subsequently, the running-in process could be expected to occur very quickly.

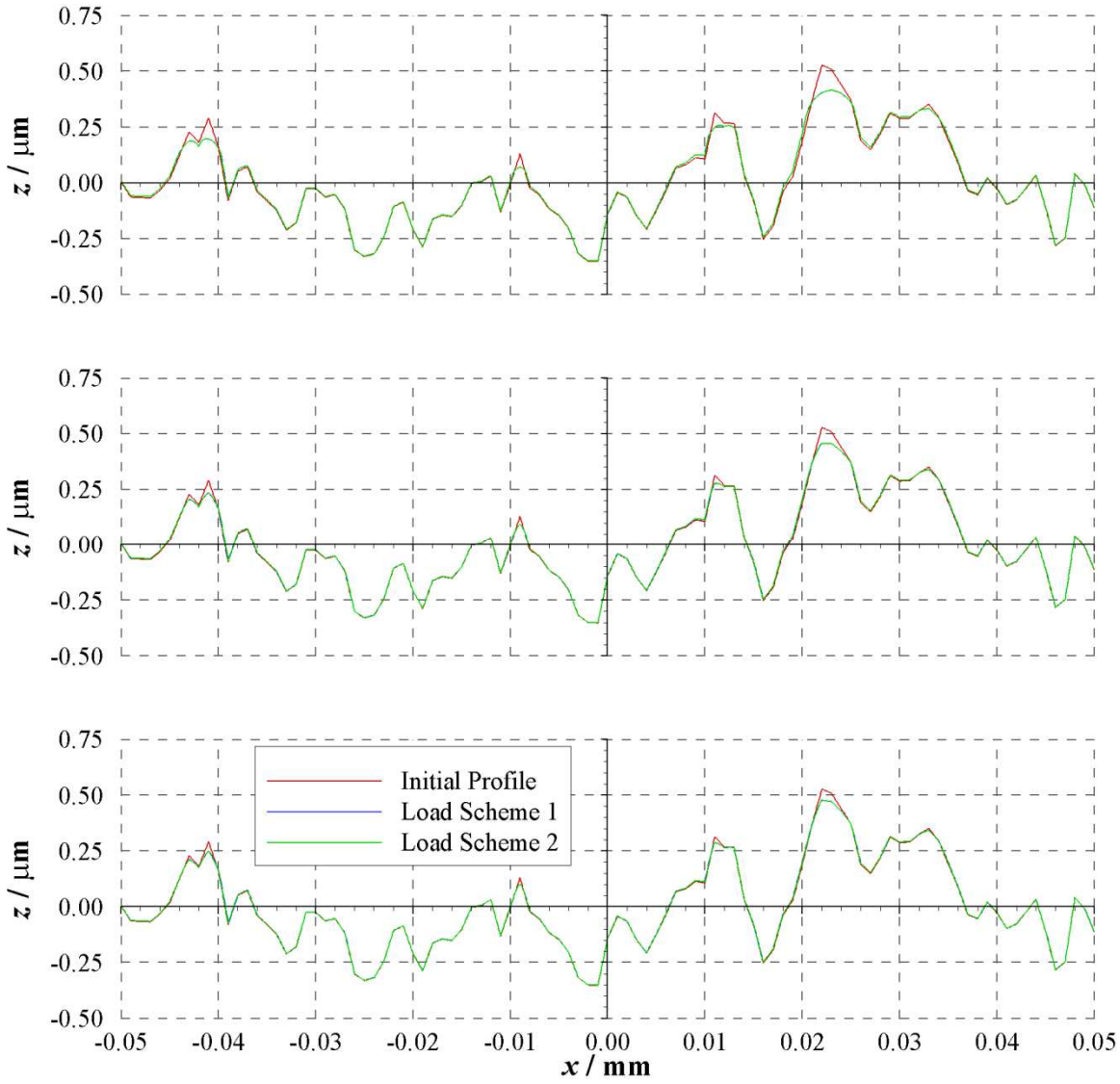

Figure 4.11 - Residual profiles following load schemes 1 and 2; a) elastic-perfectly plastic, b) E_T / E = 0.125, c) E_T / E = 0.250.

Table 4.2 - Maximum and mean differences in surface node locations between load schemes 1 and 2.

Material Properties	Maximum difference / nm	Max. difference as percentage of max. deflection	Mean difference / nm	Mean difference as percentage of max. deflection
Elastic-perfectly plastic	3.05	2.72%	0.25	0.22%
E_T / E = 0.125	3.29	4.62%	0.24	0.34%
E_T / E = 0.250	3.23	6.30%	0.24	0.47%

Figure 4.12a shows the residual shape change for each of the sets of material properties tested, as well as the initial roughness profile. The location where deformation has occurred is consistent across each of the materials tested, while the magnitude decreases as the ratio of E_T / E increases. It can be seen that the largest residual deformations occur in the elastic-perfectly plastic material, and the least in the E_T / E = 0.250 model. This can be seen in more detail in Figure 4.12b, which shows the residual deformation of one asperity. This figure also shows how the elastic-perfectly

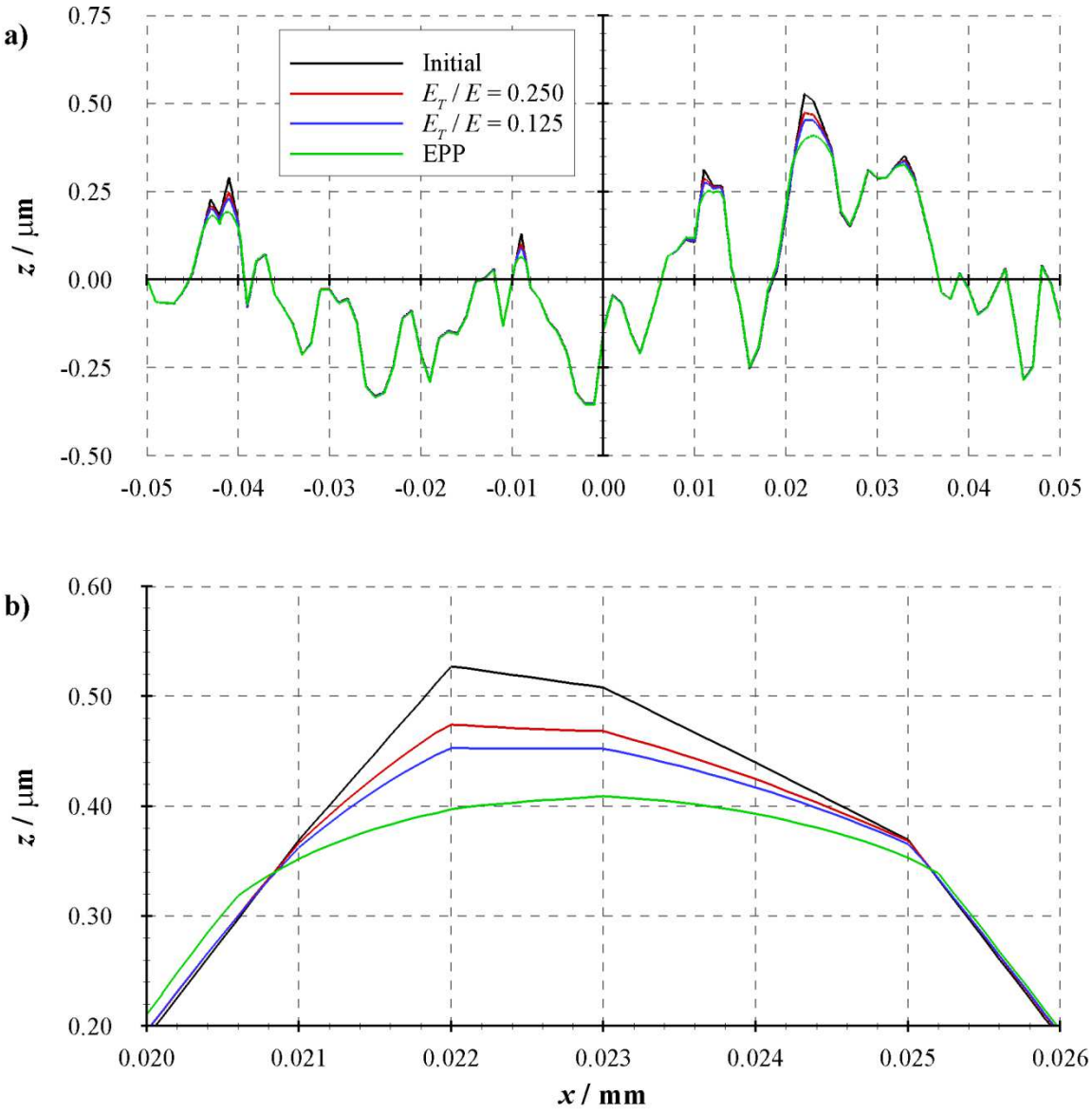

Figure 4.12 - Initial and residual profiles after final 700 N/mm loading; a) Whole profile, b) Larger scale view of the asperity at x ≈ 0.0225 mm.

plastic material behaviour also results in more positive residual deformation outside the contact. As elastic-perfectly plastic materials are incompressible once the yield strength has been reached, when a compressive load, and therefore strain, is applied in the z-direction, to conserve volume, the region must expand in the x-direction, as a plane strain assumption has been used. Therefore material is pushed towards the sides of an asperity feature, or towards neighbouring valley features. This results in some positive deformation in the z-direction outside of the contact region. This can be seen in Figure 4.13a and particularly in Figure 4.14a. The additional plastic strain after yielding is permanent, and so the plastically deformed material maintains its shape, unless elastic recovery of surrounding material applies sufficient load to deform the material.

Figure 4.13 and Figure 4.14 show the residual changes in shape between three individual load applications. Figure 4.13 shows the results after three applications of 350 N/mm, while Figure 4.14 shows results for three applications of 700 N/mm. Each figure shows the change in shape for elastic-perfectly plastic material properties, E_T / E = 0.125, and E_T / E = 0.250. Each plotted curve shows the difference in shape after each load; the red curve shows the difference between the initial profile and the residual profile after the first load, the blue curve shows the difference between the residual profiles after the first and second loadings, and the green curve is the difference between the residual profiles after the second and third loadings. It can be seen that for each magnitude of loading, and for each set of material properties, the overwhelming majority of residual shape changes occur after just one load application. The additional shape change during the subsequent load applications is significantly less. As a result, only the red curve is visible in each of the figures. The blue and green curves effectively lie on the x-axis at the scale plotted and the additional deflection after the second and third load applications are so small relative to the first. This is particularly pertinent when considering elastohydrodynamic lubrication of the contact of two rough surfaces. EHL performance depends on the gap between the two contacting surfaces, which is turn is related to the shape of each surface. If a surface runs-in, i.e. be subject to no further surface plastic deformation, after only a few load applications of the maximum operating load, then the predictive

analysis of EHL can assume purely elastic contact behaviour subsequently, and the maximum contact pressure that can be developed on plastically deformed asperities will be given by the yield strength which may be enhanced by strain hardening effects.

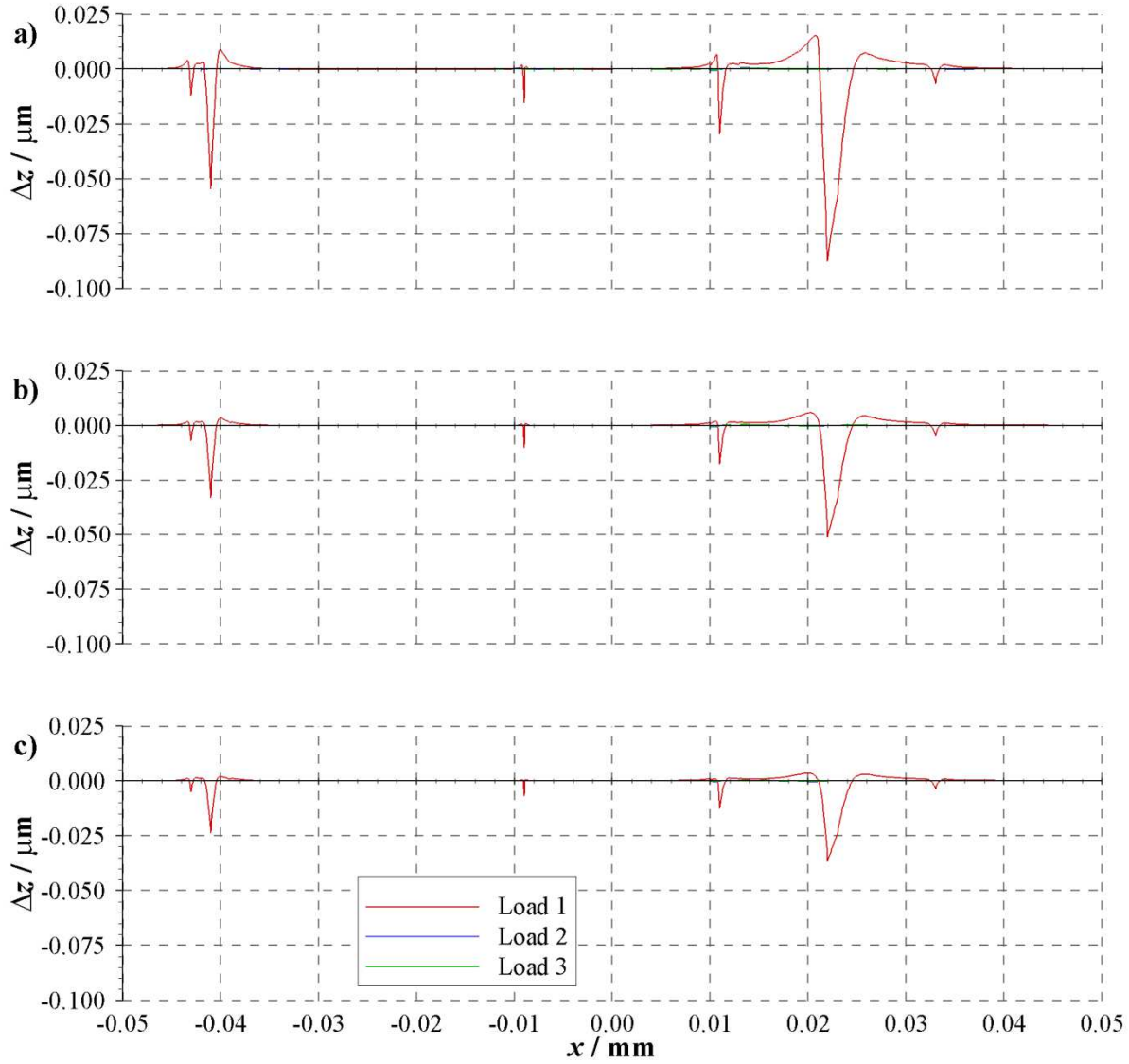

Figure 4.13 - Change in height of rough surface after three repeated loadings of 350 N/mm. a) elastic-perfectly plastic, b) E_T / E = 0.125, c) E_T / E = 0.250.

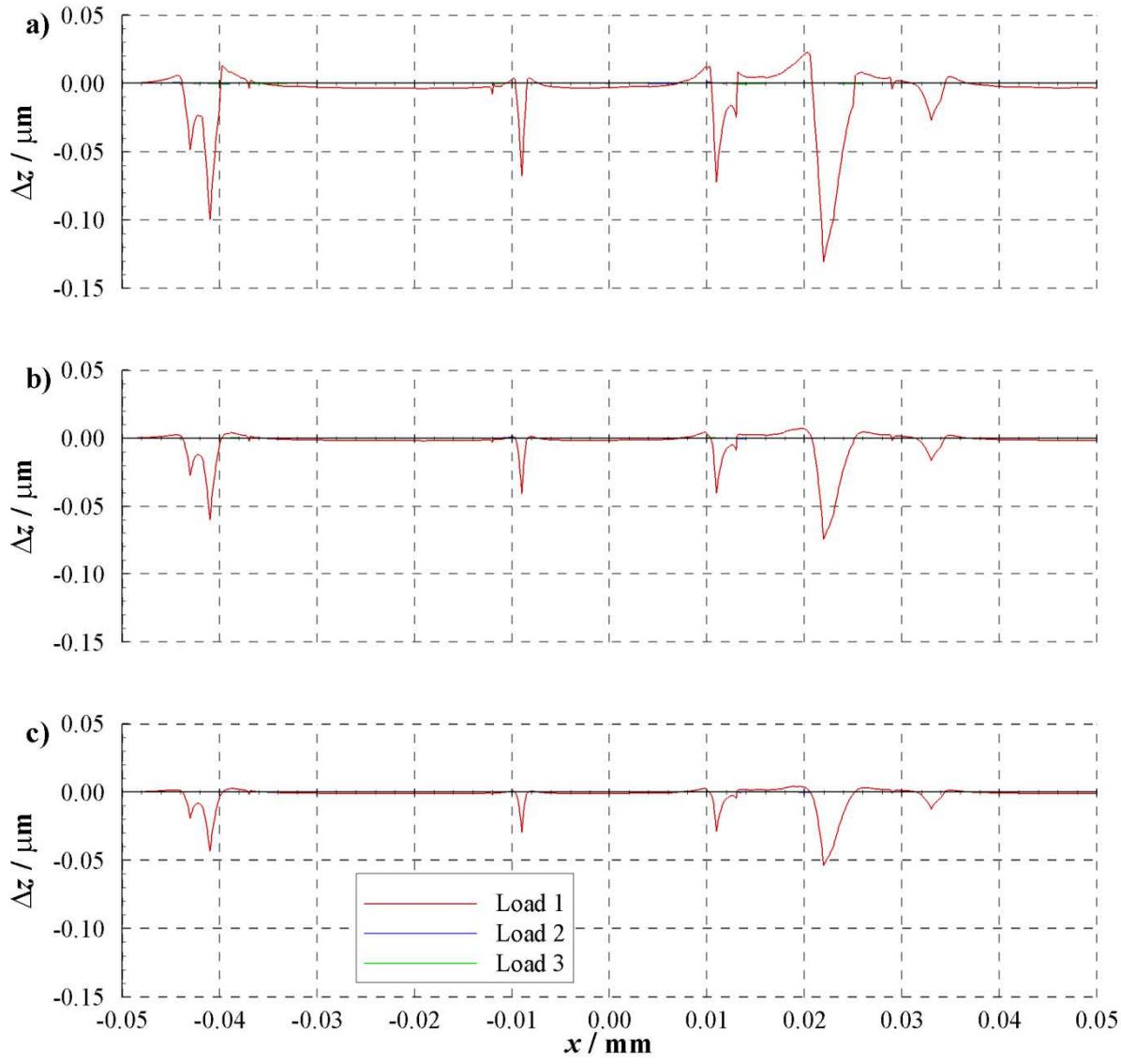

Figure 4.14 - Change in height of rough surface after three repeated loadings of 700 N/mm. a) elastic-perfectly plastic, b) E_T / E = 0.125, c) E_T / E = 0.250.

The difference between the material properties specified is seen in the magnitude of residual deformation which occurs. The greatest amount of deformation occurred with elastic-perfectly plastic materials. As the E_T / E ratio was increased the magnitude of residual deformation reduced. The general form of the residual displacements was consistent throughout. Locally, the largest magnitude displacements occurred where each individual contact first occurred under loading. These displacements were negative in nature. Outside of the immediate contact region, positive displacements, or "pile up" occurred, as the loading of the contact forced material to flow away

from the loaded region. The displacements are consistent with the descriptions of pile up by Tabor (1951) and Johnson (1985), who also indicates that materials with properties closer to an "ideal" plastic material will exhibit more extensive pile up, as shown here. The form of the residual deformations are also comparable to those found experimentally by Johnson (1968) and by others using finite element analysis, albeit in spherical contacts (Beghini *et al*. 1992; Kral *et al*. 1993; Taljat and Pharr 2004; Jackson *et al*. 2005). The work in each of these studies considers contacts of single symmetrical bodies, whereas in the example shown here neighbouring contacts can interact with each other. This can be seen in particular between x = 0.012 mm and 0.020 mm where significant positive deformation can be seen to occur.

Figure 4.15 shows the residual von Mises stress distributions for the same 40 µm section of the rough surface as previously shown in Figure 4.9 after the final loading of 700 N/mm had been removed. Residual stresses occur when the material tries to recover elastically to its original shape, but is prevented from doing so by plastically deformed material. Higher magnitude peak values of stress as well as a larger stress-affected region can be seen to occur in the elastic-perfectly plastic material. In an elastic-perfectly plastic material, once the yield strength is reached, the additional plastic strain that can be achieved is, in theory, limitless. As previously discussed, as the von Mises stress is limited by the yield strength, neighbouring material is forced to carry more of the load, leading to further material yield. As more plastic strain is allowed to occur in the elastic-perfectly plastic material for a specific stress compared to the materials with linear strain hardening, larger and more widespread residual stress is observed.

Knowledge of residual stresses in run-in surfaces could be particularly useful as an aid to the prediction of fatigue in mixed EHL modelling (Evans *et al*. 2012). The techniques outlined by Holmes *et al*. (2003a; 2003b) use the time dependent Reynolds equation and elastic deflection equation to determine the film thickness and pressures applied to a surface operating under EHL. In turn, equivalent loading cycles and fatigue damage can then be calculated using a rainfall counting

method (Amzallag *et al*. 1994) and a shear strain-life model (Fatemi and Darrell 1988). In previous fatigue prediction work it has been assumed that the unloaded surfaces were stress-free. Results of the present work can allow the inclusion of initial residual stress effects which will influence fatigue behaviour. In this way the effect of the running-in process on subsequent fatigue life can be better understood.

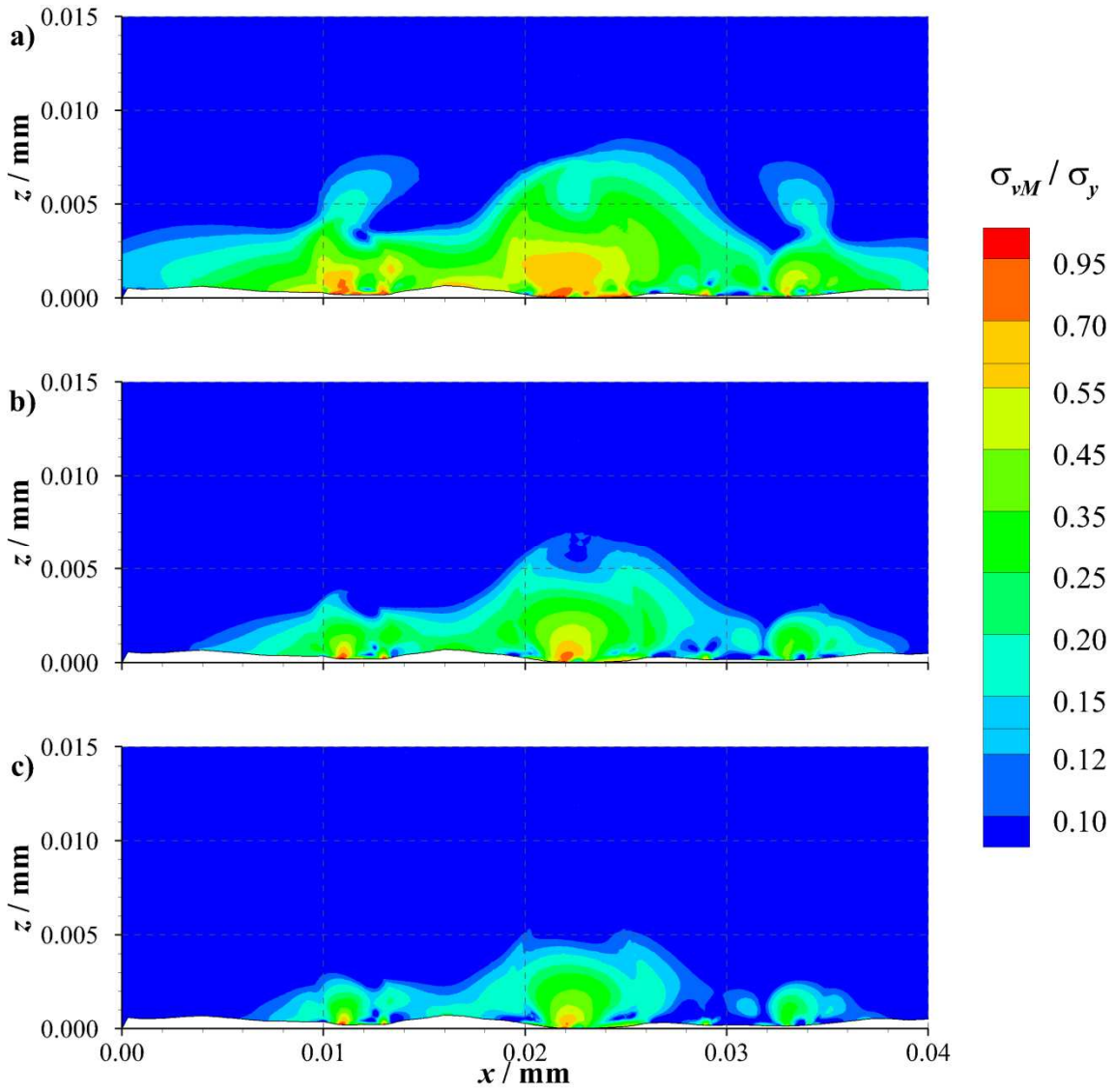

Figure 4.15 - Contours of normalised residual von Mises stress after final 700 N/mm loading; a) elastic-perfectly plastic, b) E_T / E = 0.125, c) E_T / E = 0.250.

Figure 4.16 shows contours of normalised residual direct stress in the tangential direction for each of the materials after the final loading of 700 N/mm for a 40 µm section of the rough surface. As

previously seen in Figure 4.15 with the von Mises stress, the general stress distributions are similar across each of the tested materials. The difference between the materials is in the magnitude of the stress observed, with the elastic-perfectly plastic material typically exhibiting the highest stresses, and materials with E_T / E = 0.250 giving the lowest stresses. It can be seen that for each asperity contact region tensile stresses occur both at the surface and subsurface. These two regions are separated by a region of compressive stress.

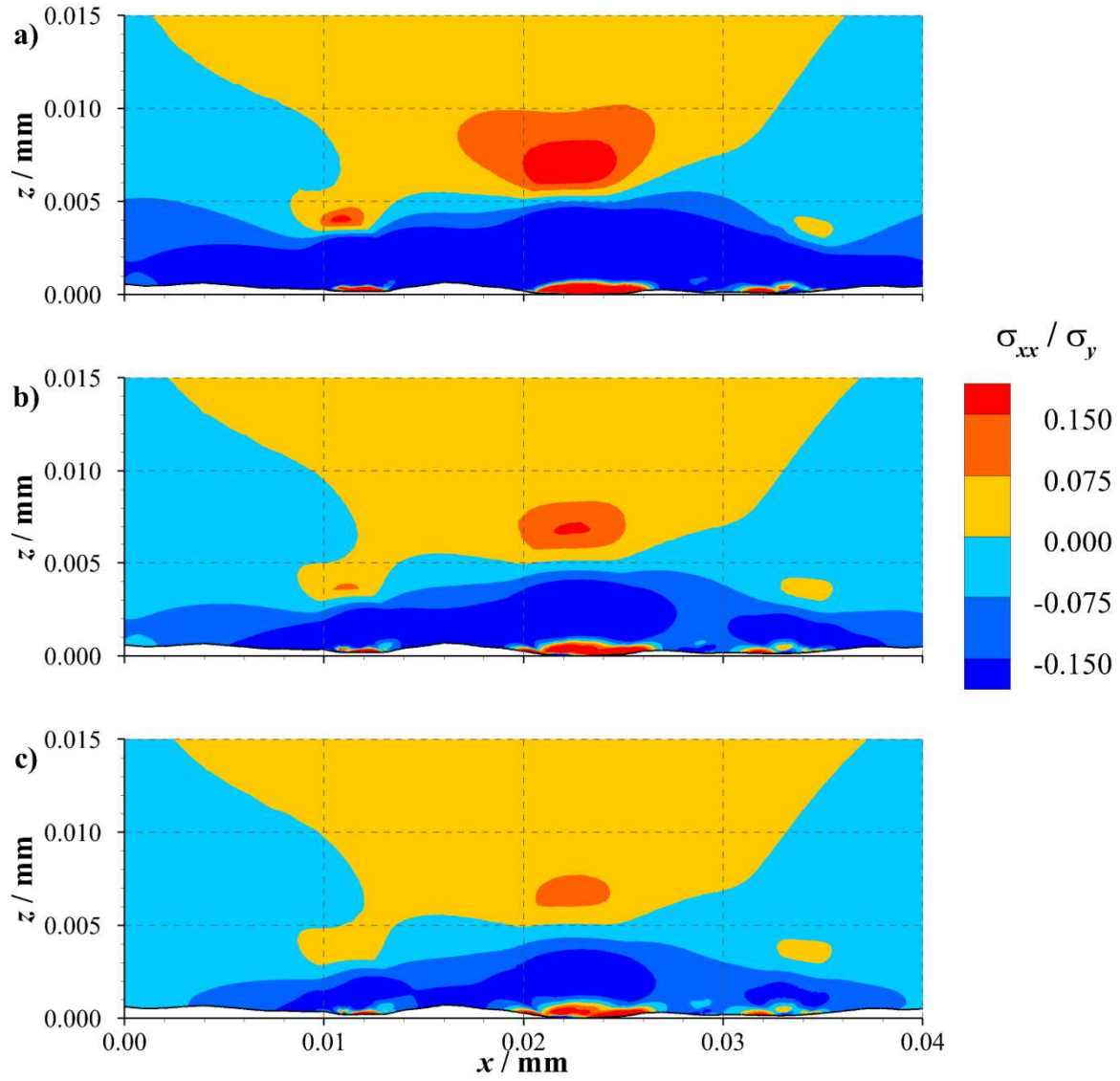

Figure 4.16 - Contours of normalised residual direct stress in the tangential direction after final 700 N/mm loading; a) elastic-perfectly plastic, b) E_T / E = 0.125, c) E_T / E = 0.250.

By considering the loaded and residual direct stresses shown in Figure 4.10 and Figure 4.16 respectively, it can be seen that the surface undergoes cyclic loading whereby the tangential stress varies between compression and tension. At the surface, this may lead to the initiation and propagation of cracks. Subsurface, the region of maximum tensile stress occurs at a depth between 5.0 µm and 10.0 µm, which is the characteristic depth of micropits (Höhn *et al*. 1996).

4.4. Tangential loading with frictional contact modelling

4.4.1. Modelling details

The assemblies of the two 0.1 mm sections of unrun surface roughness used in the multiple loadings contact modelling were also used in the study of friction effects. The multiple load stages were suppressed and a new intermediate step between the load application and removal was created during which the tangential load was applied. The tangential load was applied as a surface traction, which is analogous to an applied pressure in the normal direction. The units of are therefore typically a force per unit area. However, as previously described, because a 2D simplification is being utilised, this effectively becomes a distributed line load in the tangential direction. This was applied to the same top, free edge of the rough surface part; the same application region as the applied pressure. The magnitude of the tangential load applied was dependent upon the coefficient of friction, μ, specified in each simulation. By definition, the coefficient of friction defines the maximum tangential load that can be applied before the surfaces move relative to one another. For each of the simulations, the applied normal load was 700 N/mm. The friction coefficients used were 0.15, 0.25, 0.50, 0.75 and 1.00. For lubricated steel on steel contacts, even μ = 0.15 is somewhat high. More realistic coefficients of friction range from $\mu \approx 0.1$ to $\mu \approx 0.005$ for effective boundary and mixed lubrication regimes respectively. However, the aim of this study is to investigate the effect of introducing significant friction into the simulations, and so the exaggerated behaviour can be useful for analysis and comparison. The limiting tangential load for each friction coefficient, F_{max}, was 105

N/mm, 175 N/mm, 350 N/mm, 525 N/mm and 700 N/mm, respectively. A series of tangential loads was applied for each coefficient of friction to assess the behaviour as the surfaces came closer to slipping. These were a proportion of the maximum tangential load, denoted as F/F_{max}, and each load cases in summarised in Table 4.3.

Table 4.3 - Series of tangential loads /Nmm^{-1} applied.

Friction coefficient, μ	F_{max} / N/mm	F/F_{max} = 0.25	F/F_{max} = 0.50	F/F_{max} = 0.75	F/F_{max} = 0.95
0.15	105.00	26.25	52.50	78.75	99.75
0.25	175.00	43.75	87.50	131.25	166.25
0.50	350.00	87.50	175.00	262.50	332.50
0.75	525.00	131.25	262.50	393.75	498.75
1.00	700.00	175.00	350.00	525.00	665.00

Previous models have utilised boundary conditions that simulate an infinitely reflected surface, in which the part edges are the axes of symmetry. When applying a tangential loading, this configuration is no longer acceptable, as the direction of the force would also be mirrored, resulting in the situation illustrated in Figure 4.17a. In order to combat this, the boundary conditions at the sides were removed, and a new modelling technique was introduced known as surface ties. As is the case when defining surface contact, surface ties require the selection of a master and slave surface. Applying a surface tie allows the two surfaces to be tied together for the duration of the simulation, constraining each of the nodes of the assigned slave surface to have the same variable values as the equivalent node on the assigned master surface. In the tangential loading model, this replaced the infinitely reflected simulation, with a more appropriate infinitely tiled simulation, as shown in Figure 4.17b.

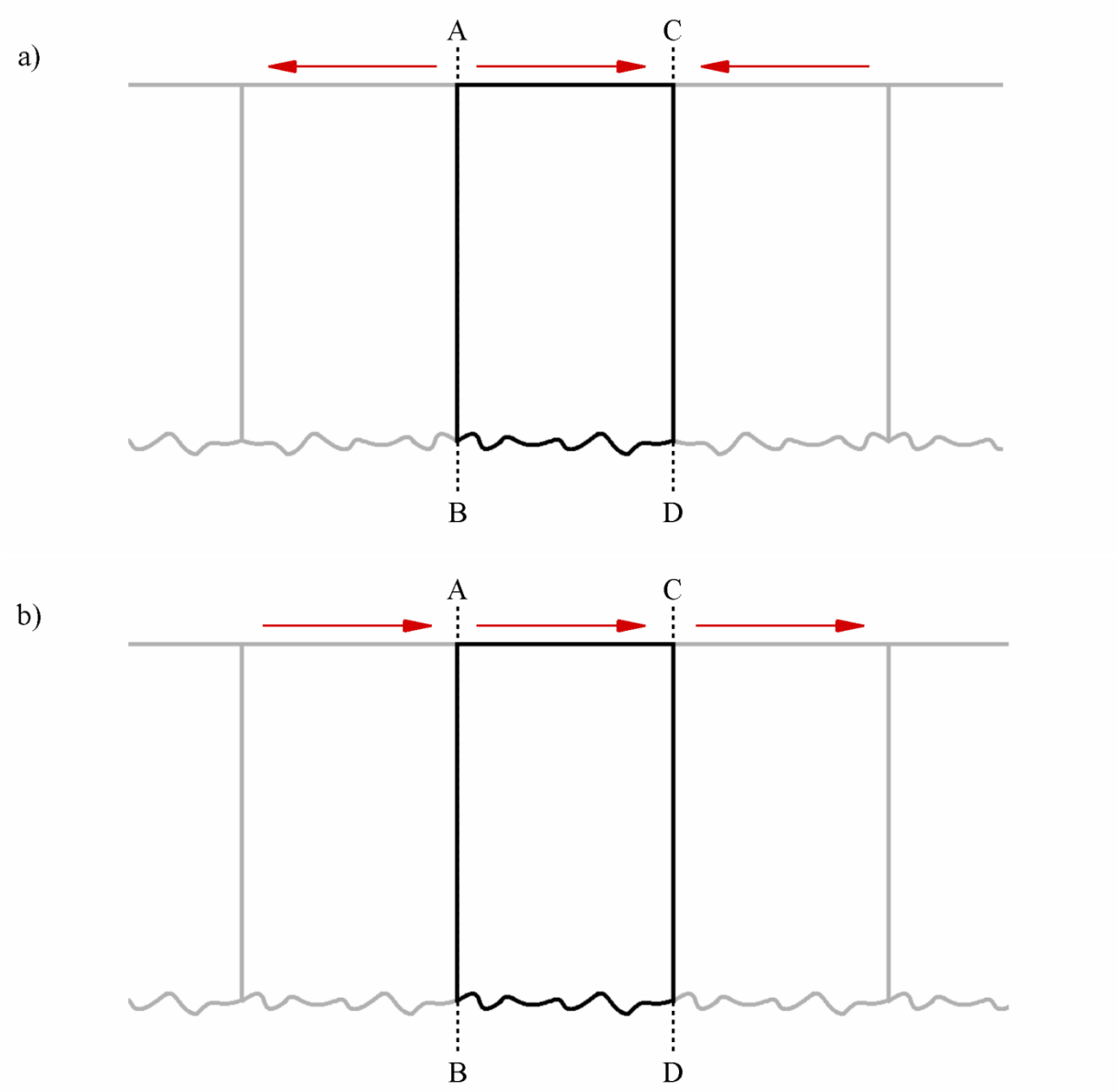

Figure 4.17 – Rough surface contact boundary conditions; a) infinitely reflected boundary condition, b) infinitely tiled surface tie boundary condition.

Surface ties are defined in Abaqus using the **Interaction** module, either by selecting **Constraint** from the taskbar or model tree. Abaqus presents a list of options, from which the user must select **Tie**. The master and slave surfaces are then selected using the modelling viewport as when defining contact interactions. Once the surfaces are defined, Abaqus provides the user with a list of options for the surface tie. For the infinitely repeated boundary condition, a number of changes to the default settings were performed. The position tolerance was specified to be the horizontal distance

between the two surfaces to be tied together. The tick box to **Adjust slave surface initial position** was unchecked, and the surface tie restraint completed.

For the purpose of comparison, the majority of the simulations were performed using a single material, namely elastic-perfectly plastic steel, with E = 200 GPa, ν = 0.3 and σ_y = 1.619 GPa. However, in order to assess the effect of tangential loading on materials with strain hardening properties, a small number of load cases were tested with strain hardening behaviour implemented. Unlike the multiple loadings study, a more practical range of materials were tested (Kogut and Etsion 2002). Elastic-perfectly plastic properties were compared with strain hardening properties of E_T / E = 0.01 and E_T / E = 0.05. The effects of tangential loading were only tested using the lowest of the friction coefficients, μ = 0.15, the closest value to that found to occur in boundary or mixed lubrication regimes.

The remainder of the model details are summarised in Table 4.4.

Table 4.4 - Summary of tangential loading and frictional contact model.

Part	2D rough surface – Imported unrun gear surface profiles
	2D smooth surface
Property	Rough: E = 200 GPa, ν = 0.32, σ_y = 1.619 GPa, E_T / E = 0 (elastic-perfectly plastic), E_T / E = 0.01, E_T / E = 0.05 (for μ = 0.15 only)
	Smooth: E = 200 GPa, ν = 0.32
Assembly	Model boundaries aligned. Parts on the verge of contact
Step	Initial (required), Contact, Load, Traction, Traction Removal, Removal
	ALE Adaptive Meshing – Frequency = 1, Remeshing sweeps = 10
Interaction	Range of friction coefficients - μ = 0.15, 0.25, 0.50, 0.75, 1.00.
	Augmented Lagrange Constraint Enforcement Method
	Finite Sliding
	Surface-to-Surface
	Absolute Penetration Tolerance = 1x10^{-15}m
	Surface ties applied to vertical sides of parts – tiled boundary condition
Load	700 N/mm distributed normal load acting on top edge of rough surface part
	Range of distributed tangential loads, proportional to friction coefficient, acting on top edge of rough surface part
Boundary Conditions	Small vertical displacement applied to top edge of rough surface to initiate contact
	Bottom edge of smooth surface part restrained (U_x = U_y = 0)
Mesh	Partitioned around contact area
	Plane Strain Elements
	Fully integrated elements

4.4.2. Results

4.4.2.1. Loaded results

Figure 4.18 shows the roughness profiles when under both normal and tangential loading, for three different coefficients of friction, μ = 0.15, μ = 0.25 and μ = 0.50. In each case the load was 700 N/mm in the normal direction, and 0.95 times F_{max} in the tangential direction, and so the surfaces were close to complete slip, i.e. the surfaces sliding across one another. The corresponding simulations for μ = 0.75 and μ = 1.00 could not be completed. The magnitude of the tangential load resulted in severe element distortion at the contact surface, before errors resulted in job failure. This loading combination was chosen to highlight the effect the tangential loading had upon the surface in

comparison with the purely normal loading. The difference found to occur for smaller proportions of F_{max} was smaller than those shown.

Each figure shows results for a profile subject to a purely normal load, in blue. Results for a combination of the normal load plus a tangential load applied in the positive and negative x-directions are shown in red and green, respectively. It can be seen that for μ = 0.15, the effect of the tangential load is small, even when the contact is on the verge of slipping. As the coefficient of friction was increased, the maximum allowable tangential load, F_{max}, before complete slip occurred increased proportionally, and as a result, more deformation was seen to occur. It can also be seen that the tangential load direction can produce significantly different results at higher coefficients of friction. In Figure 4.18a, the directionality results in asperities being slightly deflected in the positive or negative x-direction. However, Figure 4.18c shows how neighbouring asperities can interact with one another if the frictional force is high. When tangentially loaded in the negative x-direction, the two asperities at x = 0.020-0.025 mm and x = 0.029-0.035 mm remain separate from one another, although the local valley between them is greatly reduced in width and depth in comparison with a purely normal load. When tangentially loaded in the positive x-direction, the two asperities are effectively merged into one wide and flat asperity via plastic deformation. This is marked in Figure 4.18c.

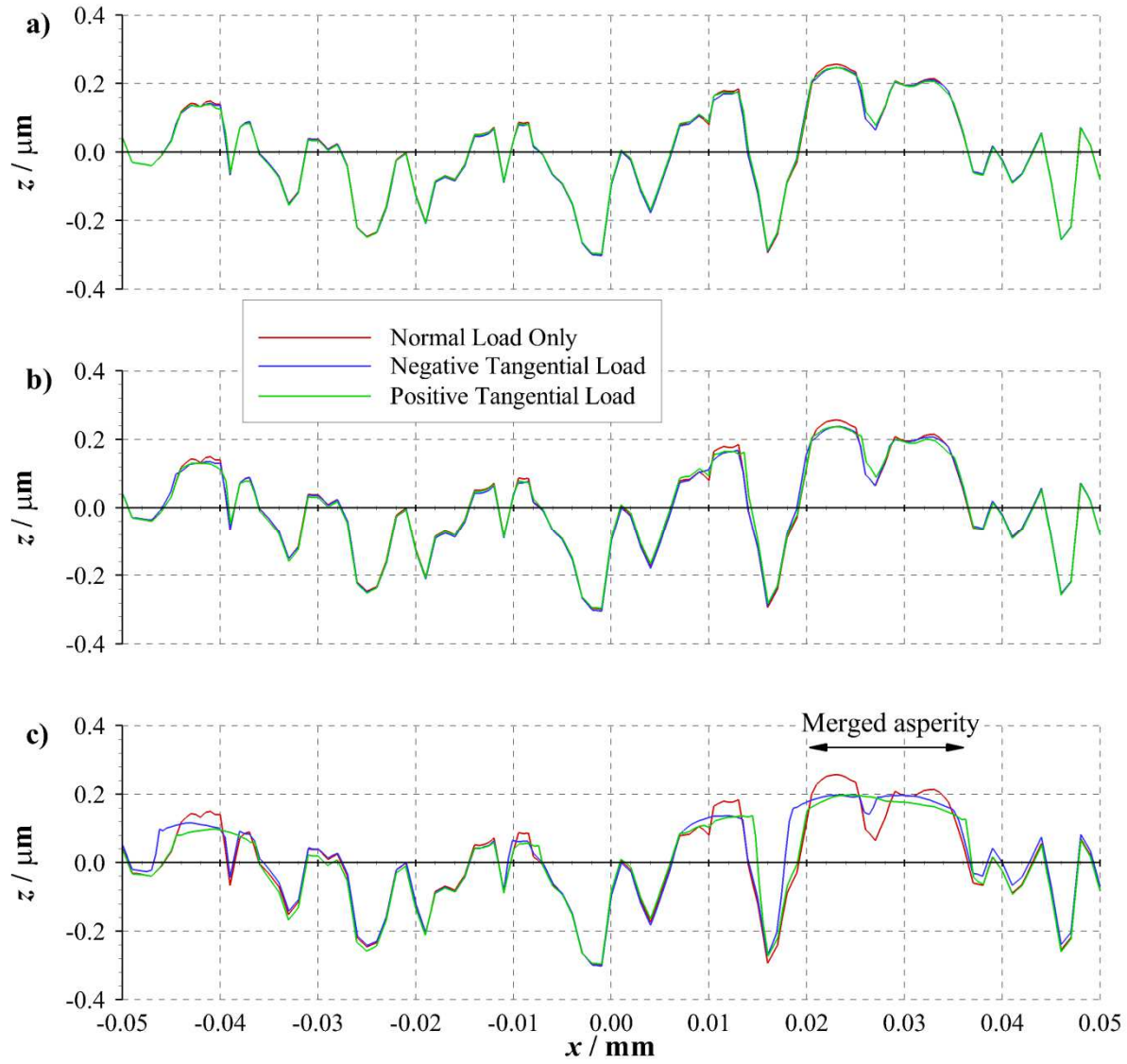

Figure 4.18 - Loaded roughness profiles for surfaces on the verge of complete slip (F/F_{max} = 0.95); a) μ = 0.15, b) μ = 0.25, c) μ = 0.50. Elastic-perfectly plastic material was used in each load case.

Figure 4.19 and Figure 4.20 show the contours of normalised von Mises stress for the combined normal and tangential loading. The normal load was 700 N/mm, and the tangential load was 0.95 times the maximum tangential force before complete slip would occur, F_{max}. For each of the friction coefficients shown, μ = 0.15, μ = 0.25 and μ = 0.50, this corresponded to 99.75 N/mm, 166.25 N/mm and 332.50 N/mm, respectively. In Figure 4.19 the tangential loading is in the negative x-direction, while Figure 4.20 shows the results for tangential loading in the positive x-direction. Also shown in each figure are the von Mises stress distributions for purely normal loading of the surface.

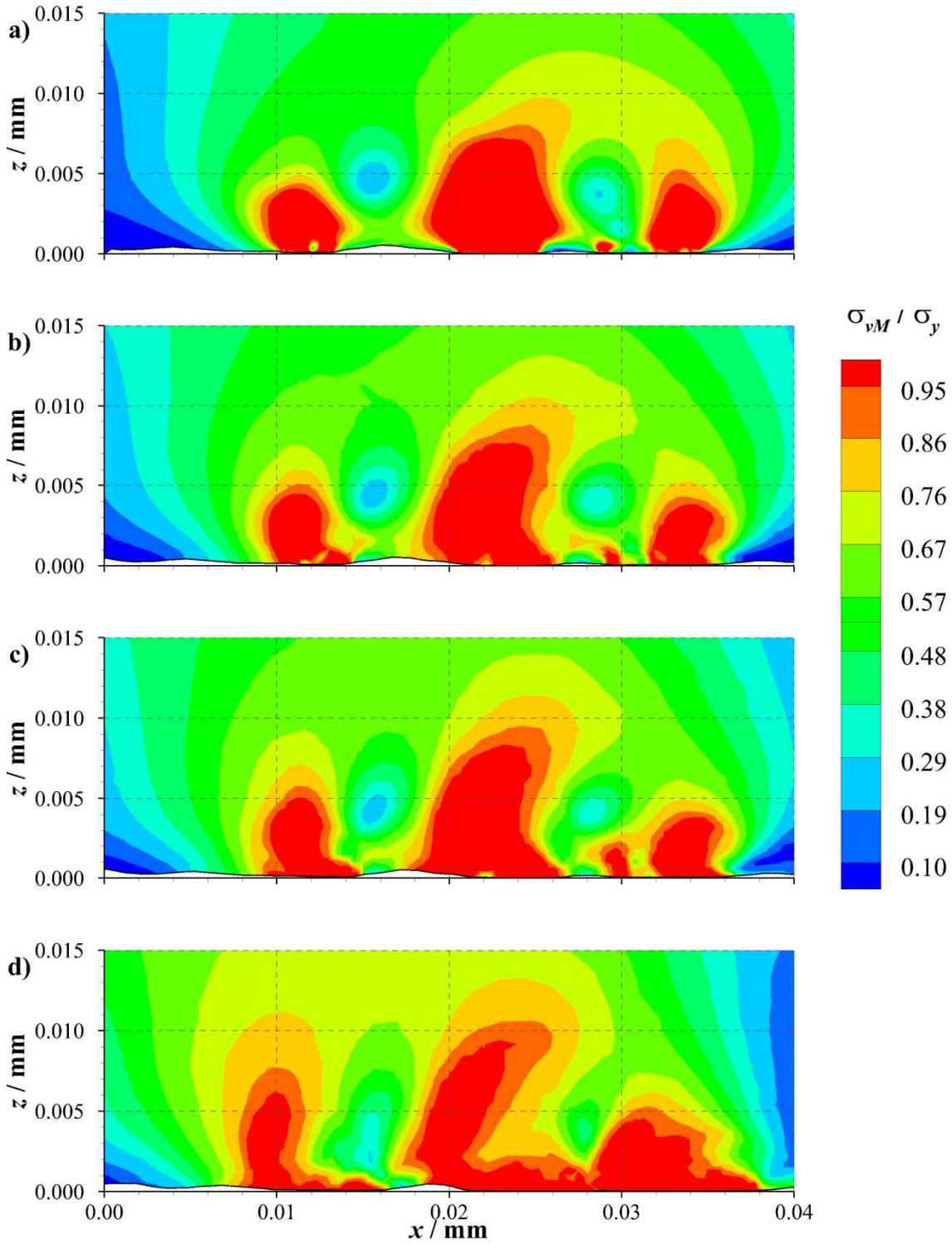

Figure 4.19 - Contours of normalised von Mises stress under a) normal loading only, and combined normal and negative x-direction tangential loading, F/F_{max} = 0.95; b) μ = 0.15, c) μ = 0.25, d) μ = 0.50. Elastic-perfectly plastic material was used in each load case.

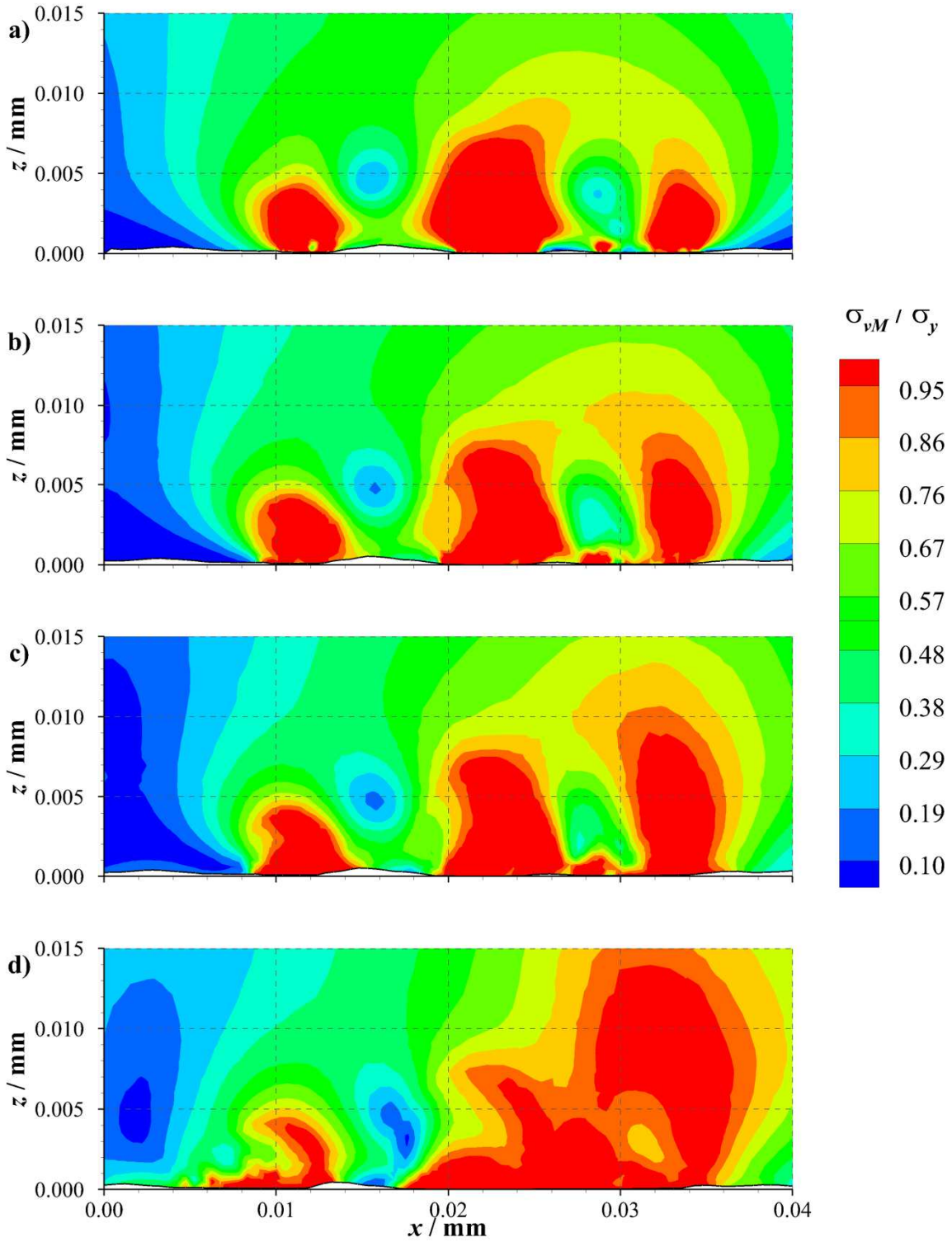

Figure 4.20 - Contours of normalised von Mises stress under a) normal loading only, and combined normal and positive x-direction tangential loading, F/F_{max} = 0.95; b) μ = 0.15, c) μ = 0.25, d) μ = 0.50. Elastic-perfectly plastic material was used in each load case.

In comparison with a purely normal loading the regions in which the highest magnitudes of stress are seen to occur are similar. These regions are located beneath the surface of the heavily loaded asperity contacts. As the friction coefficient, and applied tangential load, is increased, the highest levels of stress migrate closer to the surface and towards the direction of the tangential load, as reported by Johnson (1985) and Williams (1994). Additionally, these regions appear more elongated and deeper in the subsurface material. Outside these highly stressed regions, the stress observed in the bulk material is generally of higher magnitude. At the top of each figure, at z = 0.015 mm, more of the material is within a higher contour band, and thus closer to plastic behaviour.

The direction of the tangential loading can be seen to make a significant difference even at the lowest friction coefficient shown, μ = 0.15, with the stress being "dragged" in the direction of the tangential loading at the surface. These regions of high stress are then orientated in similar way to the way surface cracks are found to initiate (Olver *et al*. 2004; Oila *et al*. 2005) A larger effect is seen to occur at the two asperity contacts at the edges; at approximately x = 0.011 mm and especially at x = 0.034 mm, while the effect at the central contact at x = 0.022 mm is less pronounced. The difference between these asperity contacts is due to the neighbouring features. At x = 0.022 mm, the contact is locally neighboured by contacts to either side, while no local contact occurs to the left of x = 0.011 mm or to the right of x = 0.034 mm, which illustrates how surface features can interact.

Figure 4.21 and Figure 4.22 show the contours of normalised direct stress in the tangential direction for the combined normal and tangential loading. The load cases shown are the same as previously discussed in Figure 4.19 and Figure 4.20, with F/F_{max} = 0.95 for friction coefficients of μ = 0.15, μ = 0.25 and μ = 0.50. Figure 4.21 shows the stress contours for a negative tangential load while those for a positive tangential load are shown in Figure 4.22. Each figure also shows the stress contours under normal loading only for comparison.

The figures show that the direct stress in the tangential direction remains predominantly compressive as the friction coefficient and magnitude of tangential load is increased. The regions in

which the largest compressive stresses are found remain at the surface of contacting asperity features. In the application of a normal load only, a small zone of tensile stress occurs in the local valley feature between x = 0 mm and x = 0.002 mm. When a negative tangential load is applied to the surface as in Figure 4.21, this tensile stress disappears, but another region of tensile stress develops between x = 0.036 mm and x = 0.04 mm, which increases in magnitude with the tangential load applied. For the largest tangential load shown in Figure 4.21d, another region of tensile stress occurs at x = 0.016 mm. Furthermore, for the normal load application, two small regions of subsurface tensile stress occur. When a tangential load is applied, this tensile stress no longer occurs.

In Figure 4.22, the tangential load is applied in the positive x-direction. As the friction coefficient and the magnitude of the tangential are increased, the region of tensile stress between x = 0 mm and x = 0.002 mm grows, both in size and magnitude of stress. As with the negative tangential load application, for the largest magnitude tangential load, an additional region of tensile stress occurs at the surface at x = 0.017 mm, on the opposite side of the same local valley feature, highlighting the difference in the surface response as a result of the direction of load application. The subsurface tensile stresses do not immediately disappear upon the application of a positive tangential load. Each grows slightly in size in Figure 4.22b and Figure 4.22c, although each stays within the same stress contour band. In Figure 4.22d, one of these regions no longer occurs, while the other merges with the growing surface tensile stress between x = 0 mm and x = 0.002 mm.

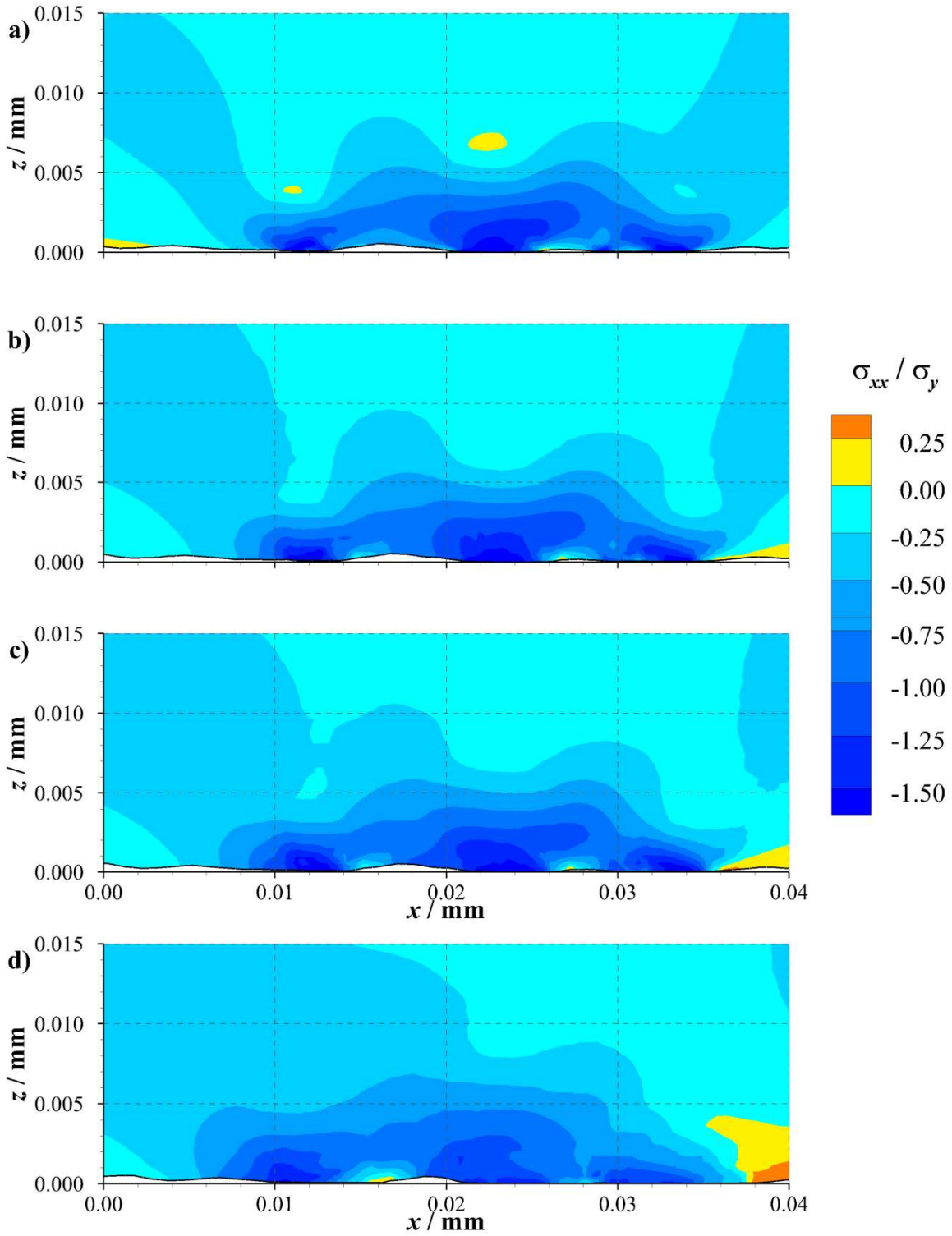

Figure 4.21 - Contours of normalised direct stress in the tangential direction for a) normal loading only, and combined normal and negative x-direction tangential loading, F/F_{max} = 0.95; b) μ = 0.15, c) μ = 0.25, d) μ = 0.50. Elastic-perfectly plastic material was used in each load case.

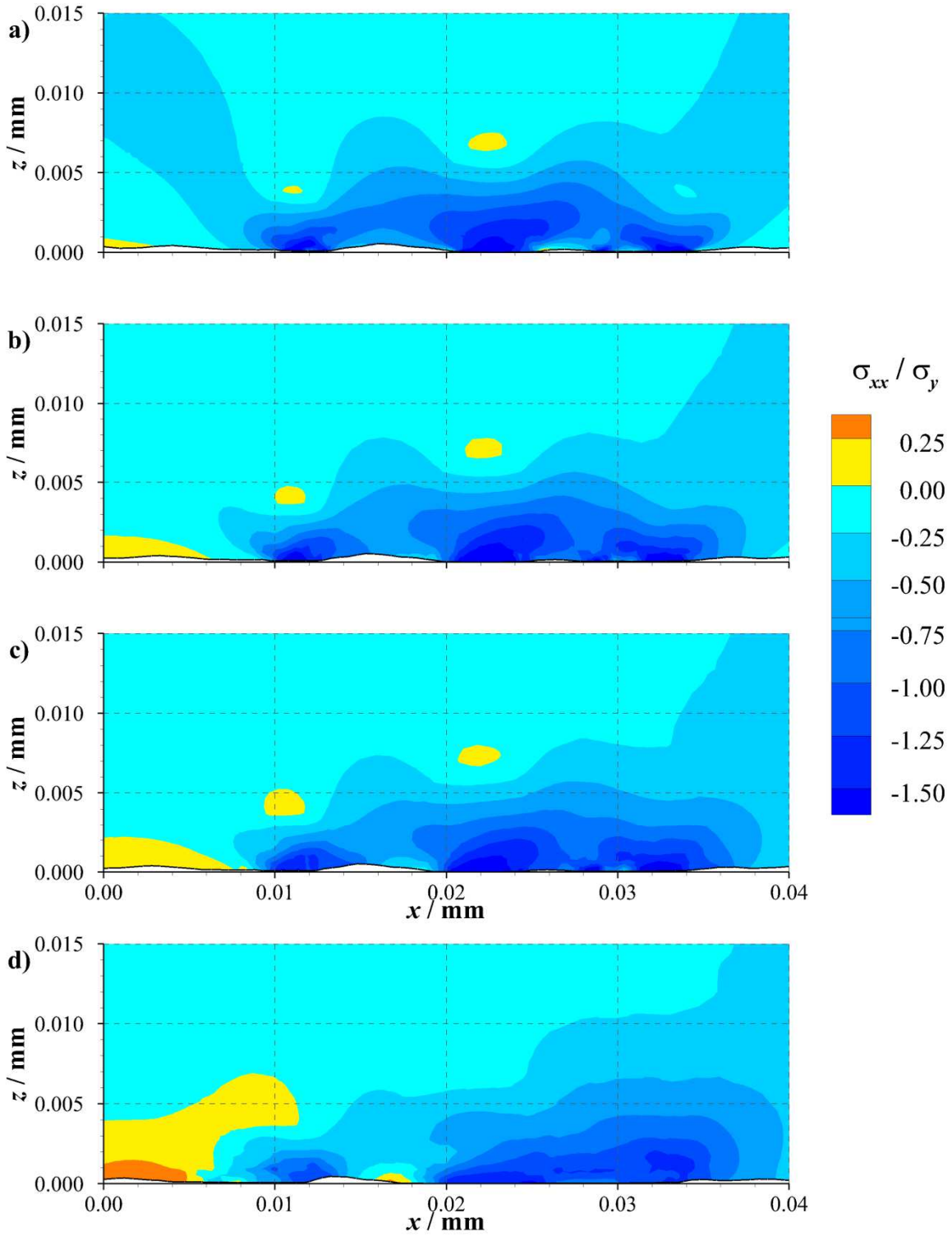

Figure 4.22 - Contours of normalised direct stress in the tangential direction for a) normal loading only, and combined normal and positive x-direction tangential loading, F/F_{max} = 0.95; b) μ = 0.15, c) μ = 0.25, d) μ = 0.50. Elastic-perfectly plastic material was used in each load case.

4.4.2.2. Residual results

Figure 4.23 shows the residual roughness profiles following loading with normal and tangential loads. The profiles are shown for a range of friction coefficients; μ = 0.15, μ = 0.25 and μ = 0.50. Also shown for comparison are the initial roughness profile in black and the residual profile after normal loading only in blue. The red and green lines show the residual surface as a result of the normal load in combination with a tangential load in the positive and negative x-directions respectively. As with the loaded results shown, the applied normal load was 700 N/mm and the tangential load applied was 0.95 times F_{max}. This fraction of the limiting tangential load was chosen to highlight the effect of the tangential load. At lower levels of tangential loading, differences were more difficult to distinguish.

As with the loaded profiles previously shown, only small differences between the normal only and combined loadings can be seen when μ = 0.15; small deflections occur in the direction of the tractive force at asperity features. The magnitude of this deflection is larger when μ = 0.25. In both cases, the magnitude of the vertical deflection remains almost identical to that found when subject to purely normal loading. When μ = 0.50, significant deflection in the direction of the tractive force can be seen to occur. Furthermore, the vertical deflection of the asperity features has significantly increased. Interaction between asperities can also be seen to occur, and this depends on the direction of the tractive force. For a tractive force in the positive x-direction, separate asperity features between x = 0.070 mm and x = 0.084 mm are merged into single features. For a tractive force in the negative x-direction, these features remain separated by a local valley feature.

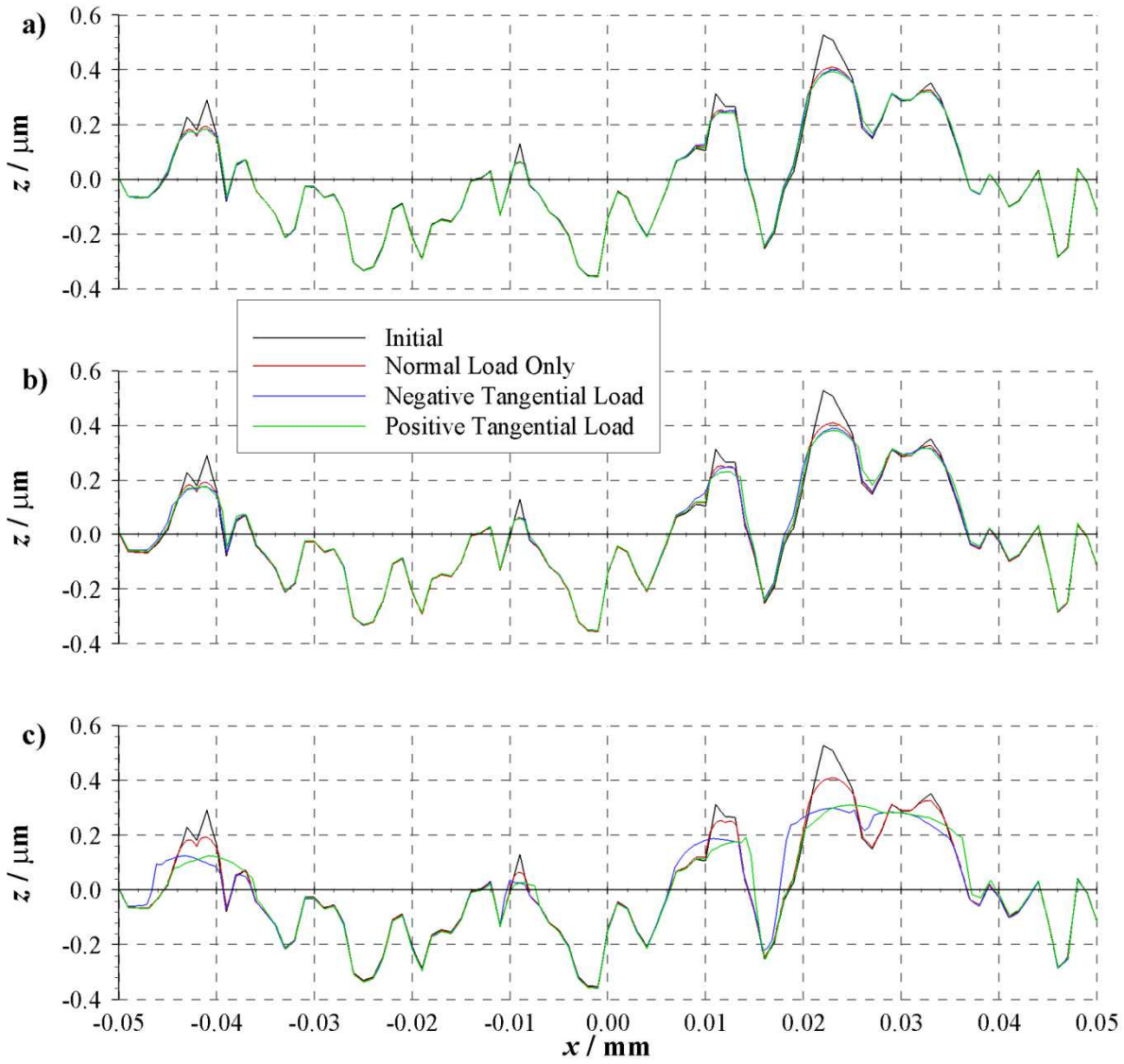

Figure 4.23 - Initial and residual roughness profiles for surfaces on the verge of complete slip (F/F_{max} = 0.95); a) μ = 0.15, b) μ = 0.25, c) μ = 0.50. Elastic-perfectly plastic material was used in each load case.

Figure 4.24 and Figure 4.25 show the contours of normalised residual von Mises stress following combined normal and tangential loading. The results shown are those corresponding to the loaded cases shown in Figure 4.19 and Figure 4.20, and so have the same friction coefficients and loading combinations as previously discussed. Figure 4.24a and Figure 4.25a show the results for the application of the normal load only for comparison.

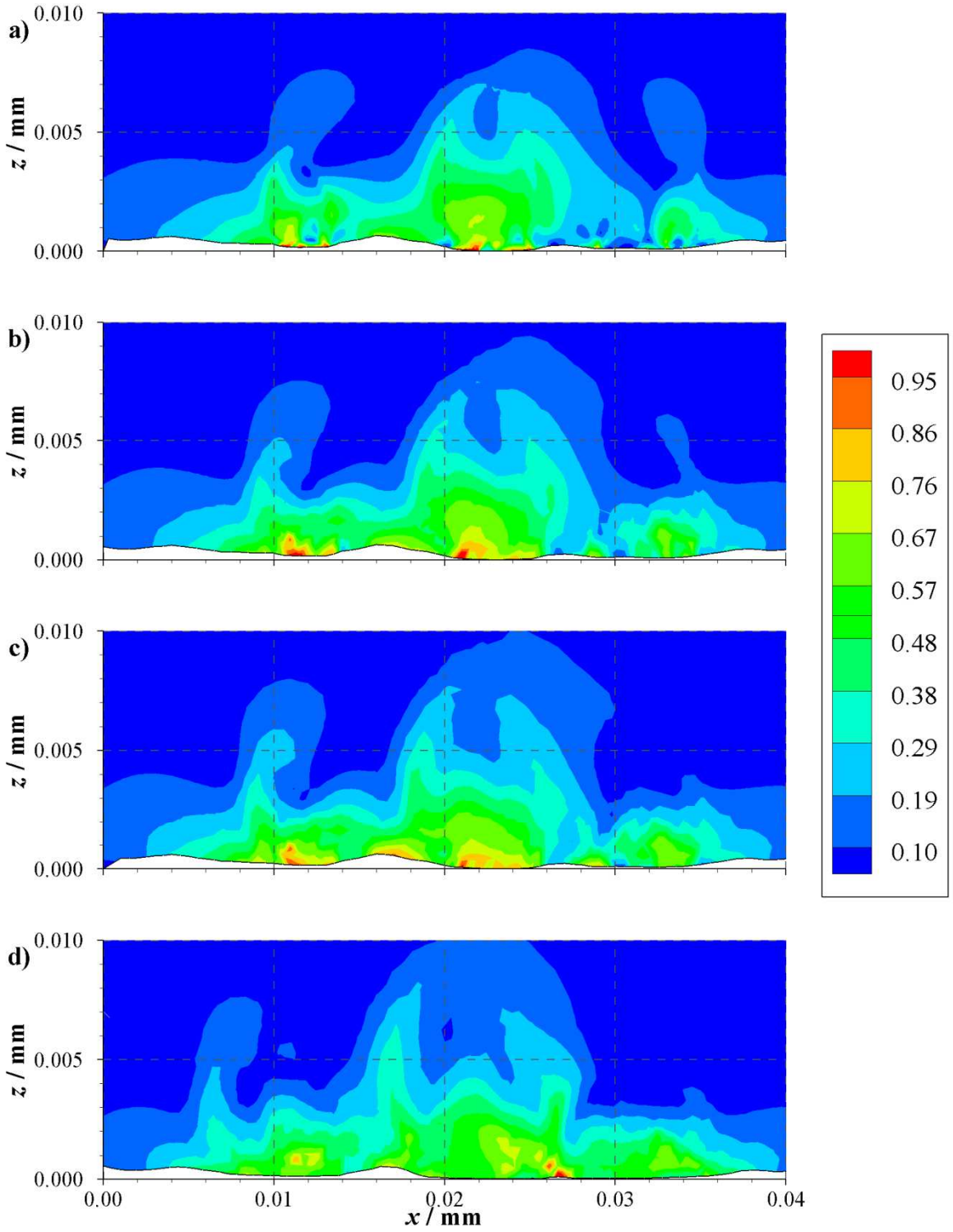

Figure 4.24 - Contours of normalised residual von Mises stress after a) normal loading only, and combined normal and negative x-direction tangential loading, F/F_{max} = 0.95; b) μ = 0.15, c) μ = 0.25, d) μ = 0.50. Elastic-perfectly plastic material was used in each load case.

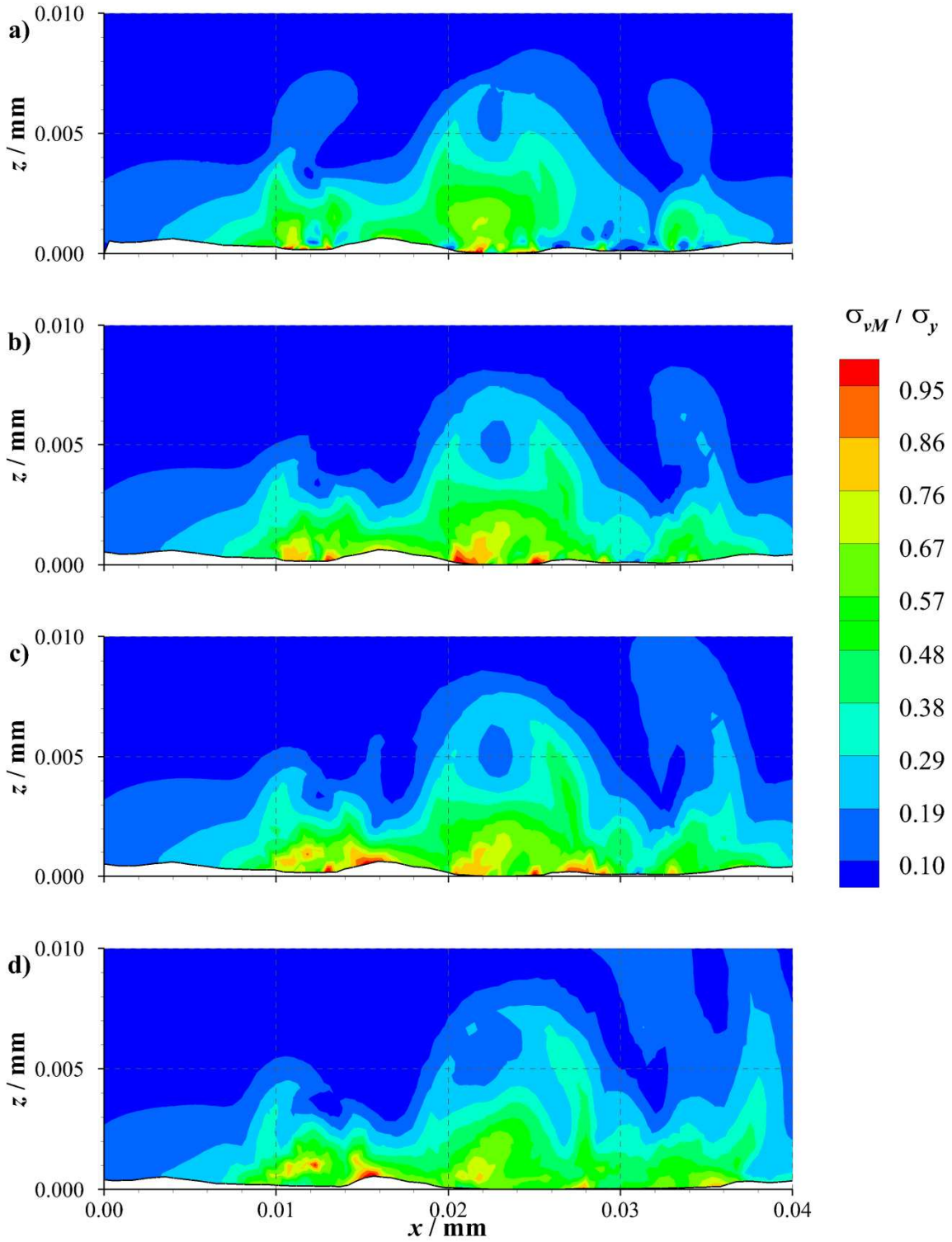

Figure 4.25 - Contours of normalised residual von Mises stress after a) normal loading only, and combined normal and positive x-direction tangential loading, F/F_{max} = 0.95; b) μ = 0.15, c) μ = 0.25, d) μ = 0.50. Elastic-perfectly plastic material was used in each load case.

Comparing the residual stresses for purely normal loading to the combined load, similar distributions can be seen, especially for the lowest friction coefficient, μ = 0.15. This was not unexpected as it has previously been shown that little difference occurs in the residual roughness profile between the normal loading and combined loadings. With higher friction coefficients and tangential loads, more prominent effects of the combined loading again occurred at the asperities at x = 0.011 mm and 0.032 mm without contacting features to the left and right respectively. It can also be seen that the number of zones of high von Mises stress at the surface is reduced with higher friction coefficient and tangential load. This has also been reported by Vijaywargiya and Green (2007) who compared sliding contacts with and without friction. In normal only loading, and for low friction combined loading, regions of this kind often exist where the asperity feature has been deformed as a result of direct contact with the counterface. In results obtained using higher coefficients of friction, the regions of peak von Mises stress occur in the valley features between loaded asperities. A typical example of this phenomenon can be seen in Figure 4.25d, at x = 0.0155 mm.

Figure 4.26 and Figure 4.27 show the contours of normalised residual direct stress in the tangential direction for the same 40 μm section of the rough surface as previously discussed. Figure 4.26 shows the residual stress after the negative tangential load application, while contours for the positive tangential load application are shown in Figure 4.27. In each figure, the results for three different friction coefficients are shown, μ = 0.15, μ = 0.25 and μ = 0.50, and in each case, F/F_{max} = 0.95. Additionally, the stress contours for a normal only load application are shown for comparison.

Similar behaviour is seen to occur in the material as a result of the tangential load in either direction. As previously discussed, residual tensile stresses occur both at the surface and subsurface. These are separated by a band of compressive residual stress. As the friction coefficient and magnitude of applied tangential load is increased, the surface tensile stress moves along the surface in the direction of the tangential load. The tensile stress migrates towards the edge of each asperity contact, towards the neighbouring local valley feature. In Figure 4.26 this can be seen as the peak

surface tensile stress moves from approximately x = 0.021 mm to x = 0.026 mm in Figure 4.26a, to x = 0.018 mm to x = 0.024 mm. In Figure 4.27d, the asperity features at x = 0.021-0.025 mm and x = 0.029-0.034 mm have merged as previously shown in Figure 4.23, and so the two regions of surface tensile stress at x = 0.021 mm to x = 0.026 mm and approximately x = 0.032 mm merge on the asperity-valley "boundary" between x = 0.03 mm to x = 0.036 mm.

The subsurface regions of tensile stress remain across the range of tangential loads applied, in either direction, although the magnitude of the stress reduces slightly, as does the area of the peak subsurface tensile stress. In both Figure 4.26d and Figure 4.27d, the band of compressive stress separating the surface and subsurface tensile stress regions is narrowed at approximately x = 0.027 mm, z = 0.003 mm and x = 0.03 mm, z = 0.003 mm, respectively. These regions are at an angle of approximately 30-45° to the surface, against the tangential loading direction, which is, interestingly, in line with experimental observations of the initiation and propagation of surface cracks in the formation of micropitting by Moorthy and Shaw (2013). It was also found that cracks tend to initiate from valleys orientated against the sliding direction. This also correlates well with the behaviour of the valley feature between x = 0.014 mm and x = 0.019 mm, where significantly larger von Mises stress is found to occur when orientated against the sliding direction than with it. This high stress could have connotations for the fatigue life of this section of the surface once cyclic loading is applied.

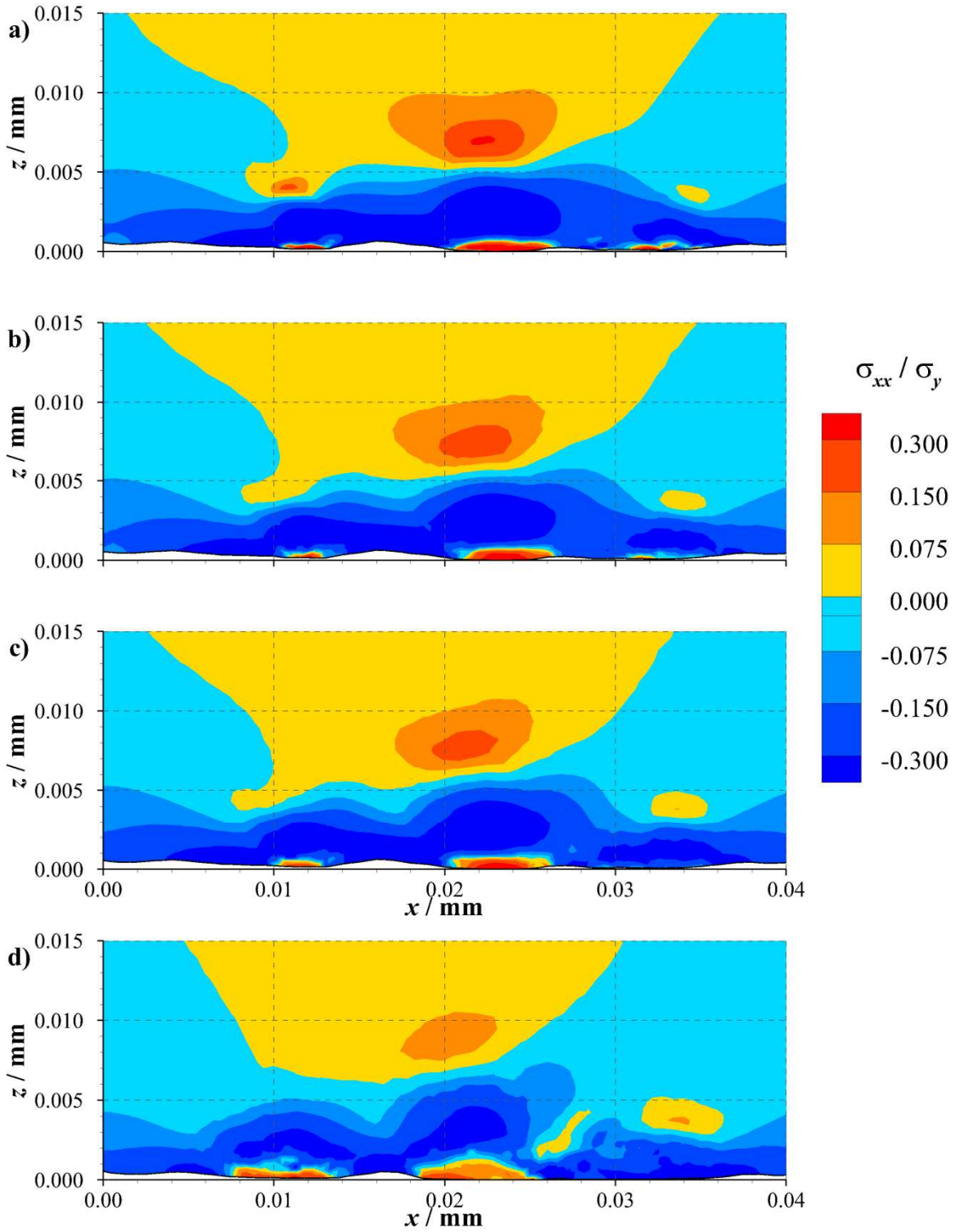

Figure 4.26 - Contours of normalised residual direct stress in the tangential direction after a) normal loading only, and combined normal and negative x-direction tangential loading, F/F_{max} = 0.95; b) μ = 0.15, c) μ = 0.25, d) μ = 0.50. Elastic-perfectly plastic material was used in each load case.

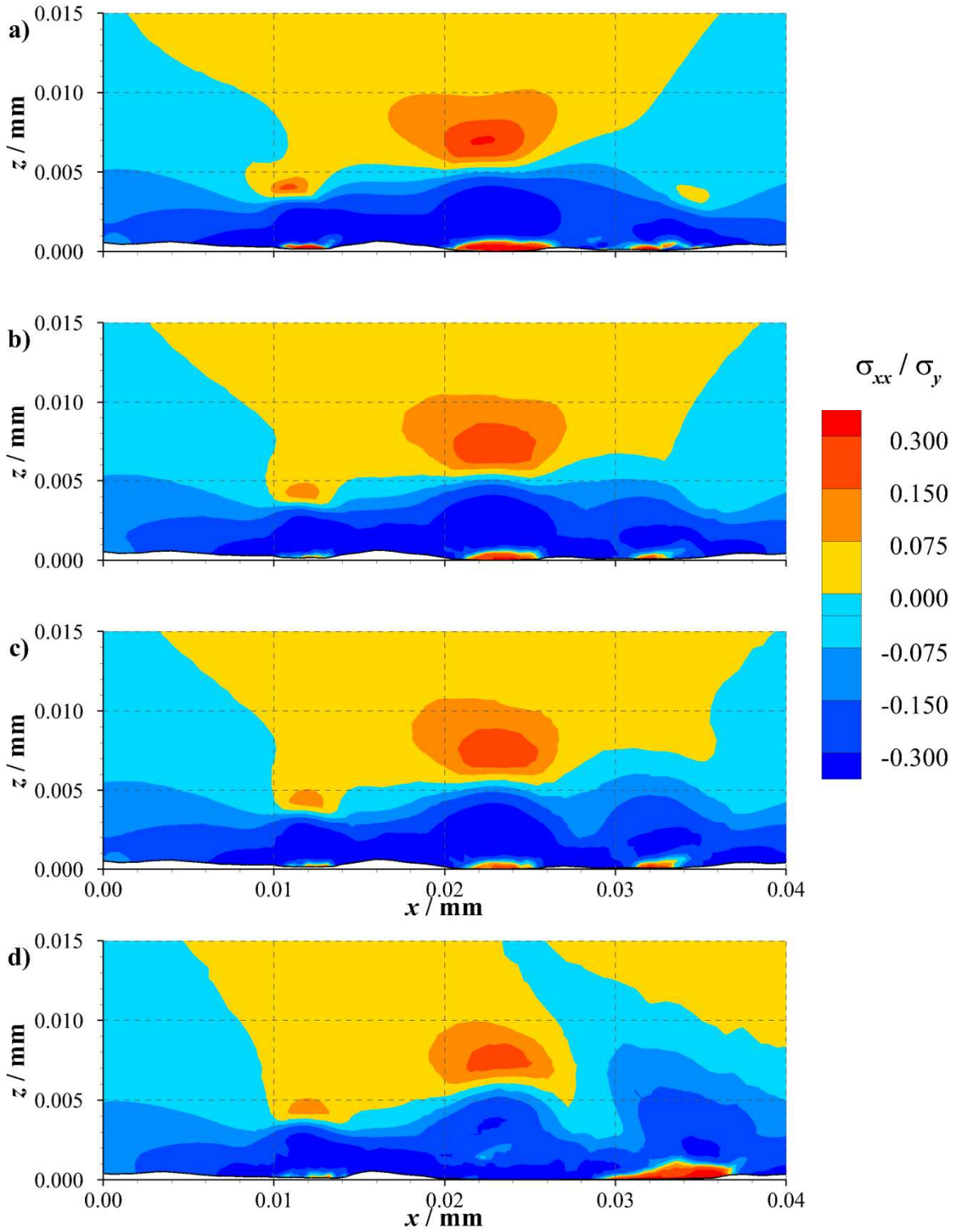

Figure 4.27 - Contours of normalised residual direct stress in the tangential direction after a) normal loading only, and combined normal and positive x-direction tangential loading, F/F_{max} = 0.95; b) μ = 0.15, c) μ = 0.25, d) μ = 0.50. Elastic-perfectly plastic material was used in each load case.

4.4.3. Effect of strain hardening

4.4.3.1. Loaded results

Figure 4.28 shows the contours of normalised von Mises stress under load. Figure 4.28a shows the stress under normal load application only, while Figure 4.28b shows the stress under combined normal and tangential load in the negative x-direction for the elastic-perfectly plastic material previously shown in Figure 4.24b. Figure 4.28c and Figure 4.28d show the stresses as a result of combined normal and tangential loading for the E_T / E = 0.01 and E_T / E = 0.05 materials, respectively. The difference between the normal load only and combined load applications has already been discussed, and the introduction of strain hardening follows the same pattern as previously found in the multiple load applications study. In the bulk subsurface material, the stress distributions are similar for each of the combined loading material simulations. However, as the limit in the von Mises stress no longer restricts the stress in the material, the magnitudes of the stress in heavily loaded regions is higher in the materials with strain hardening behaviour. Examples of this behaviour can be seen at approximately x = 0.0118 mm and x = 0.0222 mm. As previously discussed in Section 4.3.2, the introduction of strain hardening results in the surface carrying the load in smaller, more concentrated regions.

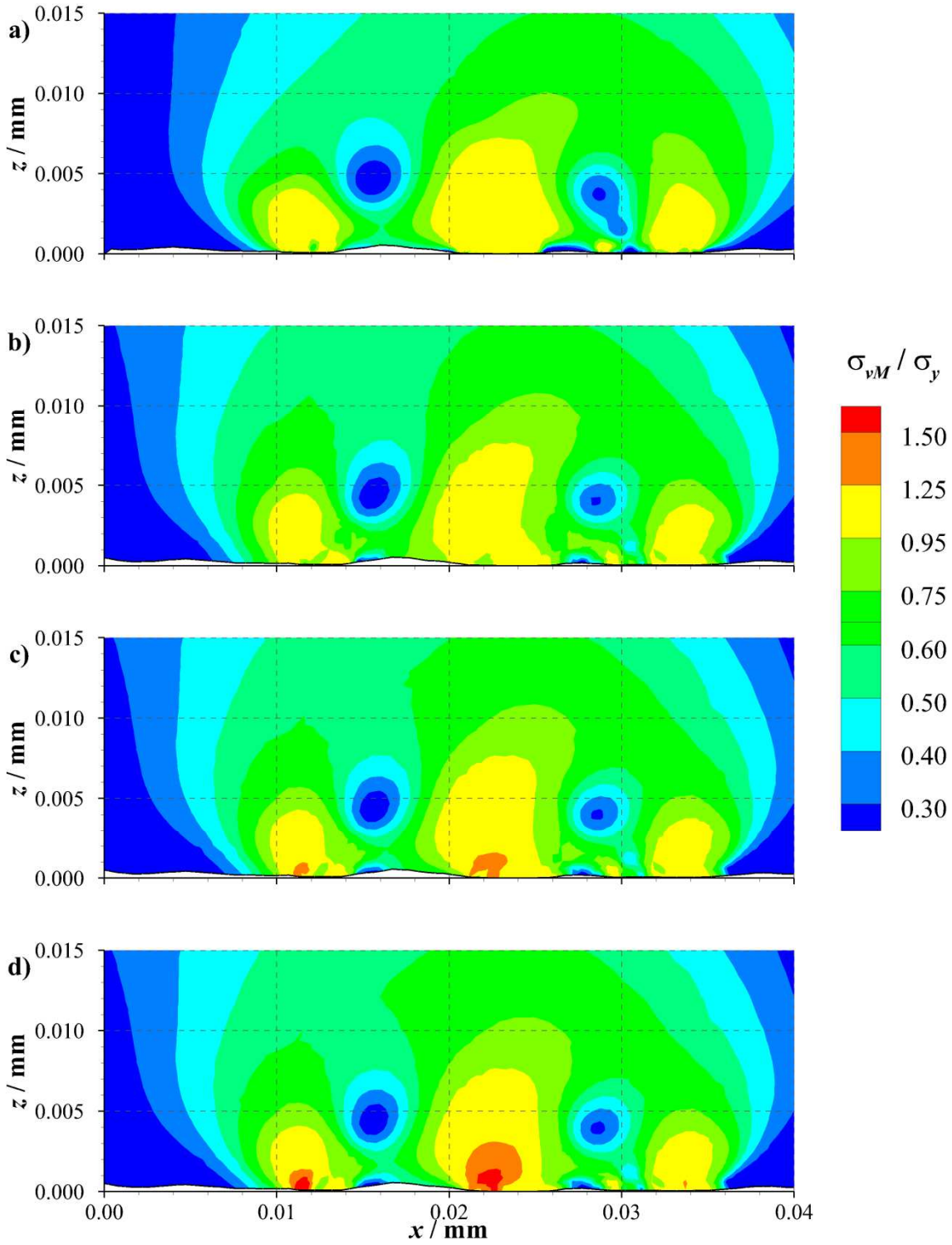

Figure 4.28 - Contours of normalised von Mises stress under a) normal loading only, and combined normal and negative x-direction tangential loading, μ = 0.15, F/F_{max} = 0.95; b) elastic-perfectly plastic, c) E_T / E = 0.01, d) E_T / E = 0.05.

Figure 4.29 shows the contours of the direct stress in the tangential direction for each of the load applications and material properties as discussed previously in relation to Figure 4.28. As E_T / E is increased, a similar progression as previously observed in Figure 4.10 is obtained, with the general distribution remaining similar, but with some reduction in the magnitude of subsurface stresses. However, with strain hardening introduced, some characteristics of the normal load application only can be observed, for example, the slightly larger magnitude compressive stress in the subsurface region from x = 0 to x = 0.01 mm, for z > 0.005 mm. In comparison with elastic-perfectly plastic material under combined loading, the high magnitude compressive stresses regions at the surface are smaller than previously seen. The main difference is seen in the regions of surface tensile stress found to occur in the valley feature at x = 0.027 mm. This tensile stress occurred under the normal loading for elastic-perfectly plastic material, but was not found under the combined loading. Introducing strain hardening behaviour resulted in the surface tensile stress returning, and increasing in extent and magnitude from E_T / E = 0.01 to E_T / E = 0.05. The subsurface tensile stress regions found at x = 0.0105 mm, z = 0.004 mm and x = 0.022 mm, z = 0.007 mm for the each of the elastic-perfectly plastic simulations are no longer found to occur in either strain hardening material simulation.

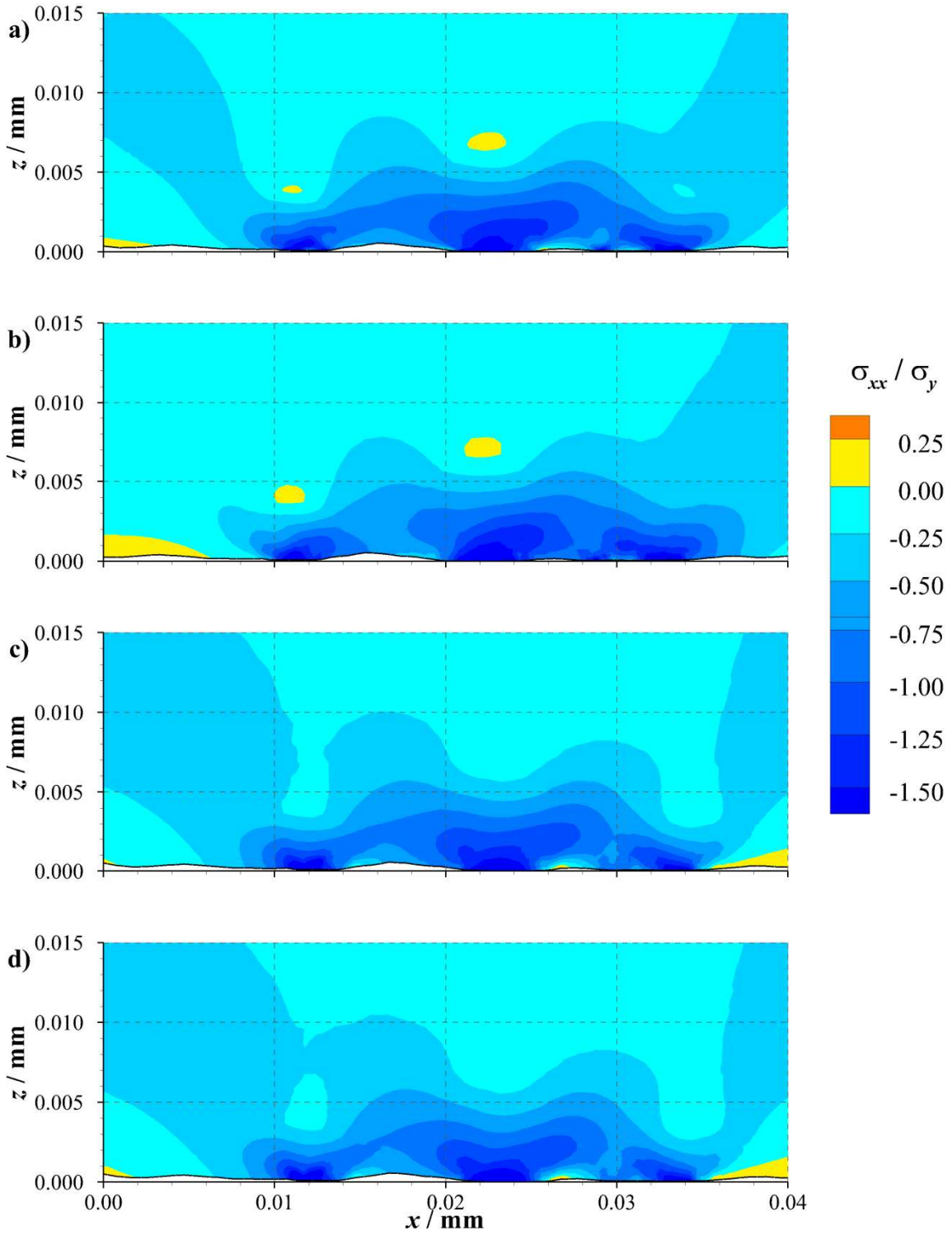

Figure 4.29 - Contours of normalised direct stress in the tangential direction under a) normal loading only, and combined normal and negative x-direction tangential loading, μ = 0.15, F/F_{max} = 0.95; b) elastic-perfectly plastic, c) E_T / E = 0.01, d) E_T / E = 0.05.

4.4.3.2. Residual results

Figure 4.30 shows a close up on an individual asperity feature between x = 0.015 mm to x = 0.030 mm after loading. The initial profile and the residual shape of the surface is shown for a normal load application, as well as combined normal and tangential load application for each of the material properties considered. Figure 4.30a shows the loaded profile under negative x-direction tangential loading, while Figure 4.30b shows the loaded profile under positive x-direction tangential loading.

As previously shown in Figure 4.12, introducing strain hardening behaviour results in less residual deflection at the asperity tips. Introducing the tangential loading to the elastic-perfectly plastic model results in larger residual deflections, as was previously shown in Figure 4.23. The introduction of strain hardening behaviour results in less residual deflection, both at the asperity tips and the neighbouring valleys.

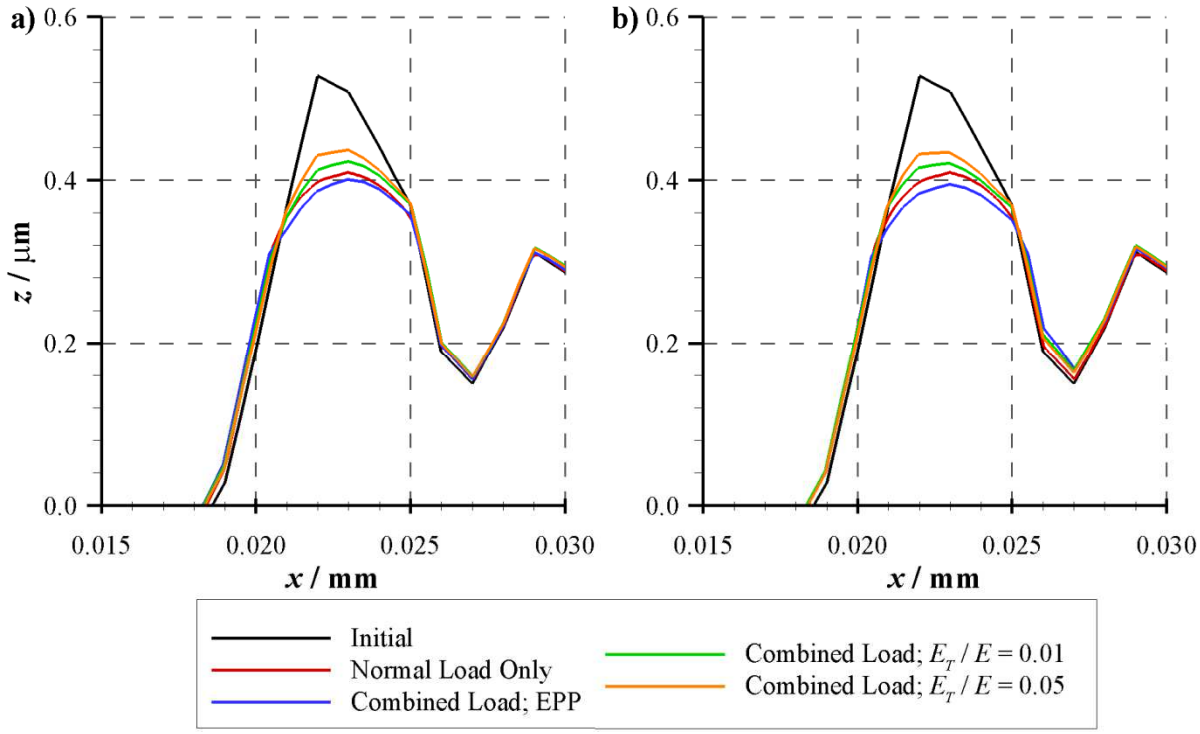

Figure 4.30 - Initial and residual profiles after normal loading only, and combined normal and tangential loading, μ = 0.15, F/F_{max} = 0.95; a) negative x-direction, b) positive x-direction.

Figure 4.31 shows contours of the normalised residual direct stress in the tangential direction for each of the load cases and material properties as previously shown in Figure 4.28 and Figure 4.29. As previously shown in Figure 4.15, the residual von Mises stress becomes more concentrated in smaller regions at the surface as E_T / E is increased. This can be seen in particular for the region between x = 0.010 and x = 0.013 mm in Figure 4.31b, which becomes more concentrated at approximately x = 0.0116 mm in Figure 4.31d. In the local valley features at the surface, the von Mises stress is also seen to decrease in magnitude. An example of this behaviour can be seen at x = 0.026 mm. In the bulk of the subsurface material, the residual von Mises stress can be seen to reduce in magnitude as strain hardening is introduced and as E_T / E increases. This can be seen at x = 0.034 mm, z = 0.005 mm where a region of elevated von Mises stress is present for elastic-perfectly plastic behaviour, but not for either of strain hardening materials.

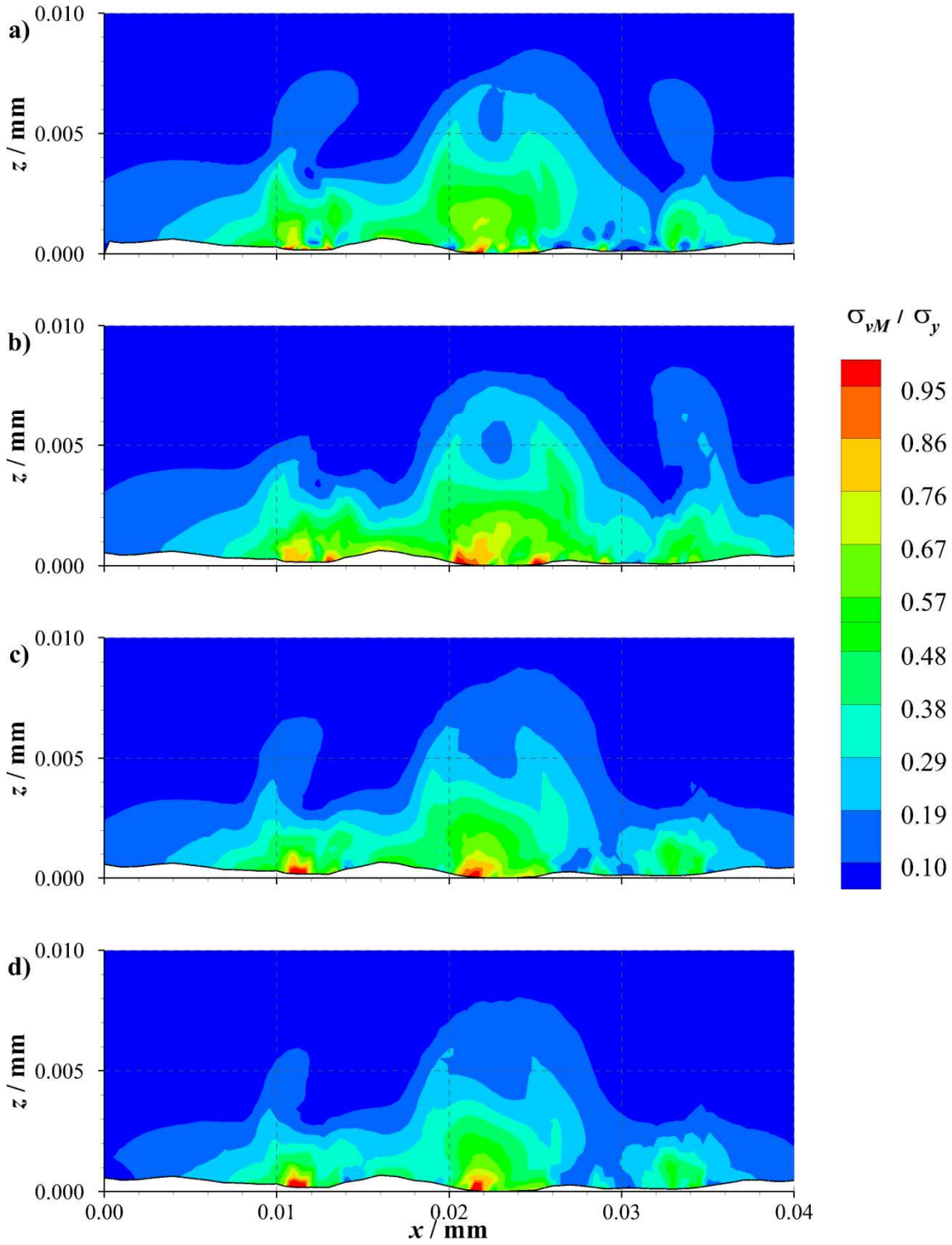

Figure 4.31 - Contours of normalised residual von Mises stress after a) normal loading only, and combined normal and negative x-direction tangential loading, μ = 0.15, F/F_{max} = 0.95; b) elastic-perfectly plastic, c) E_T / E = 0.01, d) E_T / E = 0.05.

Figure 4.32 shows the contours of residual direct stress in the tangential direction for the load cases shown in Figure 4.31. As shown in Figure 4.16, increasing E_T / E results in a reduction in the magnitude of the residual stress. This occurs in both the regions of subsurface tension, and in the band of compressive stress separating the subsurface and surface tensile stresses. The addition of the tangential load resulted in the surface tensile stresses, which occur as a result of the normal load only, to reduce. However, when strain hardening is introduced, these surface tensile stress regions increased in extent. As E_T / E is increased from 0.01 to 0.05, this trend continues. This can be seen in particular between x = 0.021 mm and x = 0.026 mm in Figure 4.32b, which then grows both in width and depth in Figure 4.32d. The compressive stresses surrounding this tensile region at the surface also reduce in magnitude as is E_T / E increased. From a fatigue life perspective, this maybe suggest that as cyclic loading is applied, that a surface of a material with a higher E_T / E is more susceptible to micropitting. Larger, higher magnitude regions of tensile stress at the surface potentially makes surface cracking more likely. With reduced compressive stress beneath the surface, these cracks are not prevented from propagating as effectively as in material with lower E_T / E.

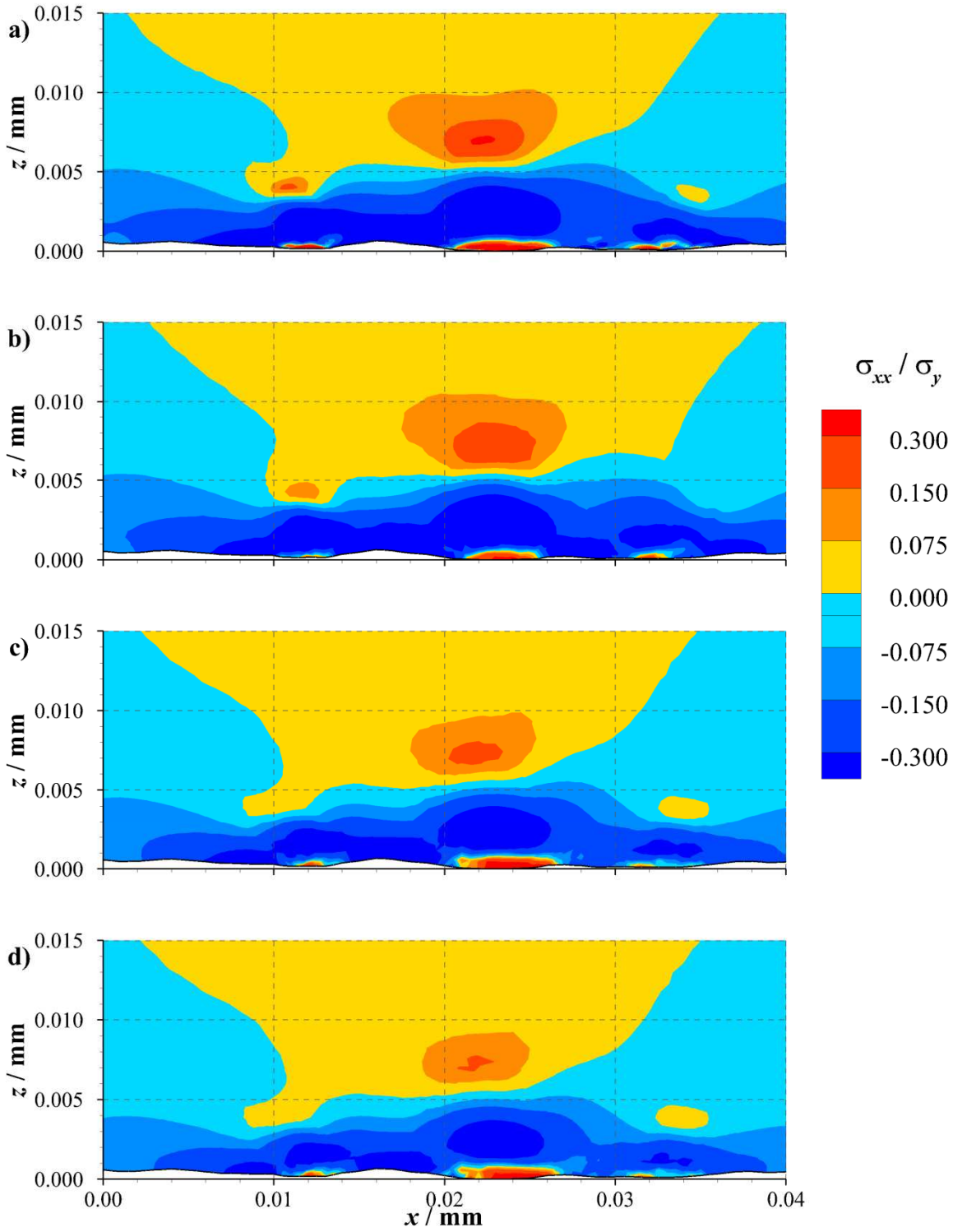

Figure 4.32 - Contours of normalised residual direct stress in the tangential direction under a) normal loading only, and combined normal and negative x-direction tangential loading, μ = 0.15, F/F_{max} = 0.95; b) elastic-perfectly plastic, c) E_T / E = 0.01, d) E_T / E = 0.05.

4.5. Conclusions

This chapter has applied the techniques developed and discussed previously to model an unrun rough surface contact. Three variables have been examined in two simulation studies; multiple load applications incorporating strain hardening and tangential loading with a user specified friction coefficient. It was found that the loaded and residual characteristics of a loaded surface depend primarily upon the largest magnitude load to which it has been subjected. Contact pressures and subsurface stresses under load, and residual deformations and subsurface stresses were found to be almost identical in spite of different loading history. This was the case for both elastic-perfectly plastic and strain hardening materials. The difference between materials lay in the magnitude of the quantities measured. Peak contact pressures and loaded stresses were found to rise as the ratio E_T / E increased. As the restrictions of elastic-perfectly plastic behaviour were removed, the surface carried the applied load in smaller, more concentrated regions. Conversely, in the residual results, the deformations and residual stresses were found to decrease as E_T / E increased, due to less plasticity. A smaller proportion of the strain in the material under load was plastic. More elastic recovery took place and the surface returned closer to the initial state after the load was removed.

In the tangential loading study, sufficient load was applied such that the surfaces were on the verge of slipping. The tangential load applied was 0.95 times the maximum tangential force, F_{max}, for a range of friction coefficients. The friction coefficients assumed were rather high bearing in mind the observed net friction in boundary or fluid film lubrication, but were chosen to illustrate some measureable effects of friction. Under load, it was found that the combined normal and tangential loading, moved the region of highest von Mises stress closer to the surface, and also in the direction of the tractive force. This behaviour was more pronounced as the friction coefficient and applied tangential load were increased. For friction coefficients more typical of lubricated contacts only small differences were found between the normal loading and combined loading results. Upon

raising the friction coefficient further, larger differences were seen to occur, with significant residual deformations taking place.

When realistic levels of strain hardening behaviour were introduced into the tangential loading model, the differences in the surface under and after loading were found to be similar to those following the application of purely normal loading. Under load, the individual asperity contact areas were smaller, and more heavily loaded. This was due to the limit of the yield strength under elastic-perfectly plastic behaviour being removed. This was also reflected in the contours of von Mises stress, with less difference seen in the direct stress in the tangential direction. Upon removal of the combined loading, the magnitude of the residual deflections was seen to decrease as E_T / E increased, as more of the deflection under load was able to recover elastically. The residual stresses were distributed in a similar way, albeit peak magnitudes of stress were generally found to be reduced. However, the possibly troublesome regions of tensile stress at the surface remained with increasing E_T / E, even increasing slightly in size and this may have important implications for the development of micropitting cracks.

Experimental validation of finite element analysis of real rough surface contacts

5.1. Introduction

This chapter describes the experimental work performed in parallel with the finite element analysis discussed in previous chapters. The primary aim was to provide experimental verification of the residual deformations obtained using the modelling techniques developed. The rig used was a twin-disk testing machine, originally designed at the Cardiff University School of Engineering by Dr. M. Alanou (2006) to investigate micropitting. The test rig was developed using similar principles as in a pre-existing machine at the university, designed by Dr. M. Patching (1994) to investigate elastohydrodynamic lubrication and scuffing in aerospace gear contacts. The micropitting rig was subsequently modified by Dr C. Davies (2005) for research into the running-in process. This rig was used to perform static, loaded contacts of a ground and a superfinished disk, each of which were crowned, at three different circumferential positions, at nominal Hertzian contact pressures of 1.0 GPa, 1.5 GPa and 2.0 GPa, respectively. An array of surface roughness profiles was taken at each contact position before and after loading. To correlate the initial and residual profiles, a Vickers hardness indentation was created on the circumferential surface of the ground disk, outside of the contact region. This allowed nominal relocation of profiles, before identifiable local valley features were then used to accurately correlate profiles, allowing assessment of the residual deformation as a result of the applied load. A finite element 2D plane strain model incorporating the geometric and material properties was created, and appropriate loading parameters applied. Residual profiles from both the experimental and finite element analysis could then be compared. Excellent correlation was found, providing confidence in the results. Subsequently, further in-depth analysis of the residual stresses caused by the contact was performed.

5.2. Twin-disk test rig

5.2.1. Rig details

The design of the twin-disk machine was based upon the principles outlined by Merritt (1935), and was initially designed by Alanou (2006) to study contact fatigue and micropitting in aerospace gear contacts. The disks are mounted on hardened steel test shafts which are flexibly coupled to driven input shafts. The input shafts are connected by spur gears that can be changed in order to alter the relative speeds of the shafts. This functionality was not necessary as the current investigation using static loading so the couplings between the test and input shafts were removed. The shafts previously described in work by Alanou (2006) and Davies (2005) as the "fast" and "slow" shafts will therefore be referred to as Shafts A and B, respectively. Shafts A and B were mounted with a test disk, with different material properties and surface finishes. Mounted to Shaft A was a disk that had been nitrided and superfinished, resulting a relatively hard and smooth contact surface. Shaft B had a carburised and ground disk, providing a slightly softer and rougher surface. Each of these disks is labelled in Figure 5.1.

In the micropitting experiments, the test shafts were mounted in the rig using rolling element bearings, restrained by bolted split housings. In the static load tests, these bearings were replaced with solid steel collars, which prevented rotation of the shafts once inserted into the test rig. Careful alignment of the desired contact regions was required, before the shafts were secured into place. The bearing housings for Shaft A were mounted directly to the base of the test rig, while the bearing housings for Shaft B were mounted to a swinging yoke. This allowed the shaft to move in an arc about the pivot located on the test rig base. This is labelled as a rotating bearing housing in Figure 5.1. Load was applied by a hydraulic ram and push rod, which loaded the ground disk mounted on Shaft B against the superfinished disk mounted on Shaft A. This arrangement ensured that the load was transferred through the disks alone, and was applied in a smooth manner. The maximum force that could be applied to the contact between the disks was 8.0 kN.

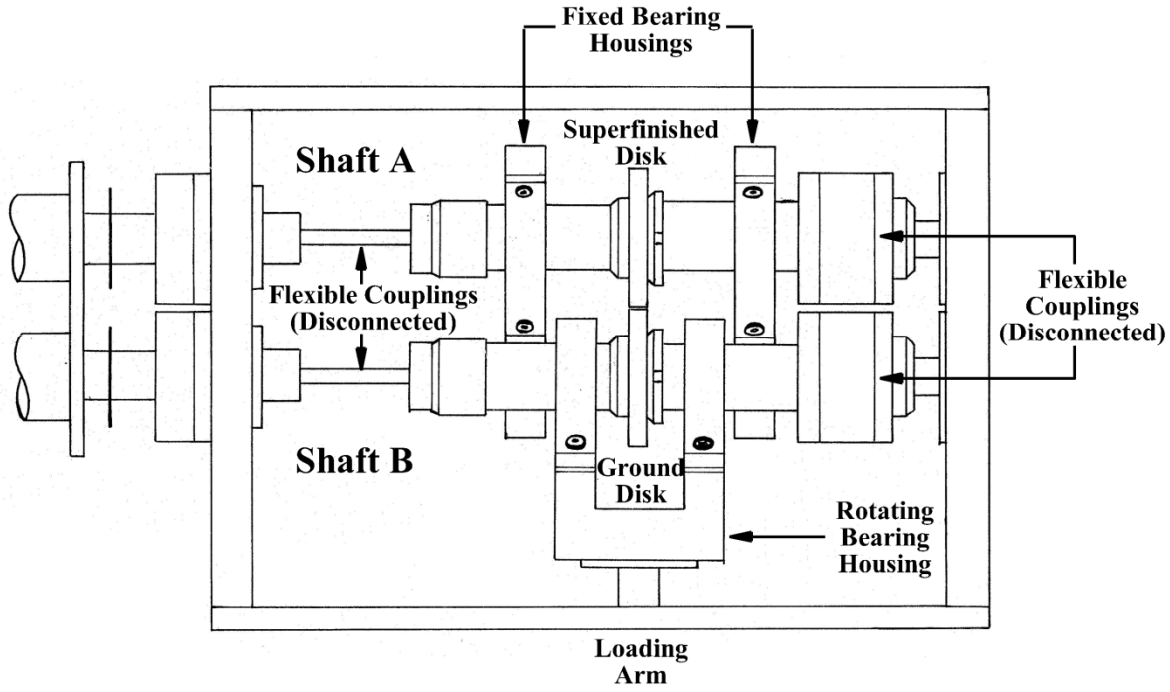

Figure 5.1 - Isometric view of test head, showing the disks, shafts and bearing housings.

5.2.2. Disk specification

5.2.2.1. Disk geometry

The disks used in the static contact loadings were of a standard geometry used within the research group at Cardiff for scuffing and running-in research. The disks have a diameter of 76.2 mm (3 inches), and have a crown radius of 304.8 mm (12 inches). When loaded elastically, this gives a Hertzian elliptical contact with an axis ratio of 3.91. The major axis of the contact, a, is in the axial direction of the disk, while the minor axis of the contact, b, is in the circumferential direction. The geometry of the disks is shown in Figure 5.2.

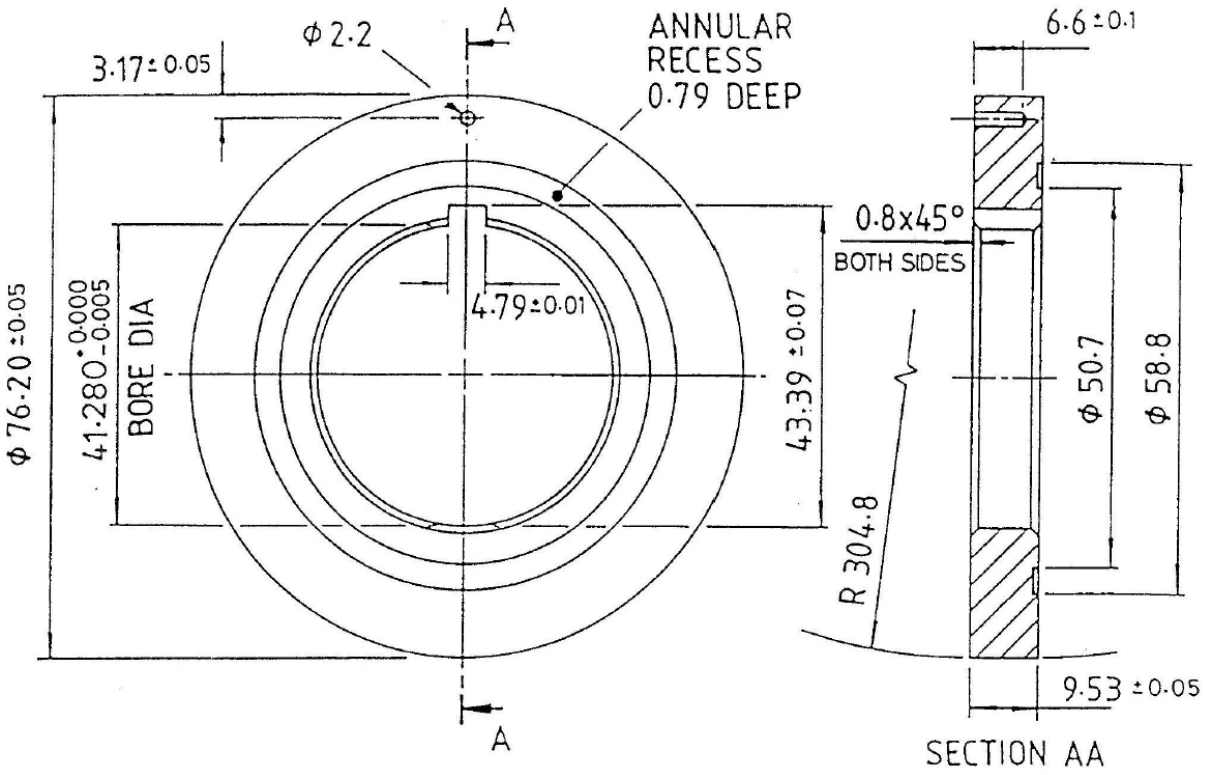

Figure 5.2 - Drawing of test disk (all dimensions in mm).

5.2.2.2. Disk material

The disks were manufactured from case-carburising Nickel-Chromium alloy steel previously supplied by Rolls-Royce, to their specification RR6010, for previous work in the research group at Cardiff University. The composition of RR6010 steel is given in Table 5.1.

Table 5.1 - Composition of RR6010 steel (% mass).

Element	C	Si	Mn	P	S	Ni	Cr	Mo
Max.	0.18	0.35	0.55	0.015	0.012	4.30	1.40	0.30
Min.	0.14	0.10	0.25	0.0	0.0	3.80	1.00	0.20

The disks were heat treated to a typical aerospace gears specification, the details of which are shown in Table 5.2.

Table 5.2 - Heat treatment specification.

• Normalise @ 930°C ± 10°C for 3 hours ± 15 minutes
• Harden @ 850°C ± 10°C for 3 hours ± 15 minutes
• Temper @ 530°C ± 10°C for 3 hours ± 15 minutes
• Carburise @ 927°C ± 10°C to yield a carburised case depth (Rc 50) of 0.036" to 0.042", with a surface carbon (second 0.002" cut) of 0.65% to 0.95% carbon
• Cool to room temperature after carburising
• Stress relieve @ 566°C to 621°C for 4 hours ± 15 minutes, then air cool
• Harden @ 788°C to 829°C for 30 minutes, then oil quench (24°C to 60°C)
• Subzero treat, within 60 minutes of quenching, for 3 hours minimum at -79°C or lower
• Temper @ 160°C ±5°C for 3 hours ± 15 minutes
• Final carburised surface hardness to be HRC 60 to 63
• Case depth (HRC 50) to be 0.036" to 0.042"
• HRC 60 depth to be 45% of 0.036" (0.016" of case)
• Core hardness to be HRC 36 to 41

This ended the treatment of the carburised disks, which were subsequently ground to an R_a of approximately 0.4 µm. The radius of the grinding wheel was large in comparison to the size of the circumferential face of the disks, and so the grinding lay was assumed to consist of purely axial features. The opposing disk was nitrided before being superfinished in house using the Abral process, whereby the disk was immersed in a bed of small zinc chips, water and aluminium oxide powder. The container is then vibrating for several hours, while the fineness of the aluminium oxide powder is increased in several stages, ultimately producing a superfinished component with an R_a of approximately 0.05 µm. As this surface finish was so smooth relative to the ground surface, it was assumed to be perfectly smooth in the finite element analysis.

In order to test and verify the yield strength of the disk material, two ground, carburised disks and a superfinished nitrided disk were subject to Vickers hardness testing. The results of the hardness tests are shown in Table 5.3, Table 5.4 and

Table 5.5. Each disk was tested in three different locations. At each location, each diagonal dimension of the diamond indentation was measured and recorded. The Vickers hardness was then

found from the appropriate chart. Also shown in the tables is the equivalent Rockwell hardness, for comparison against the specification previously shown in Table 5.2. It can be seen that each of the disks show hardness values exceeding the specification in some locations. The variation was not deemed significant enough to affect the results. The approximate yield strength was calculated by multiplying the Vickers hardness values by standard gravity, g, and dividing by 3 (Meyers and Chawla 2009). Upon averaging the results across each of the ground, carburised disks, this gave an approximate yield strength of the disk material of 2.55 GPa, which was subsequently used in the finite element analysis. The superfinished, nitrided disk showed a yield strength of approximately 2.86 GPa, greater than that of the ground, carburised disks. The superfinished disk was assumed to act purely elastically in the finite element analysis.

Table 5.3 - Vickers hardness testing of disk RR6010B-26.

Location	Dimension / mm	Vickers Hardness / kgf / mm^2	Rockwell Hardness	Yield Strength / GPa
1	0.272	752	62.1	2.46
	0.265	792	63.7	2.59
2	0.276	730	61.5	2.39
	0.263	804	64.2	2.63
3	0.274	741	61.8	2.42
	0.277	725	61.2	2.37
Average	*0.271*	*757*	*62.4*	*2.48*

Table 5.4 - Vickers hardness testing of disk RR6010B-51.

Location	Dimension / mm	Vickers Hardness / kgf / mm^2	Rockwell Hardness	Yield Strength / GPa
1	0.257	842	65.3	2.75
	0.265	792	63.7	2.59
2	0.265	792	63.7	2.59
	0.262	810	64.4	2.65
3	0.260	823	64.8	2.69
	0.271	757	62.3	2.48

Average	*0.263*	*803*	*64.0*	*2.62*

Table 5.5 - Vickers hardness testing of disk EN40BAB.

Location	Dimension / mm	Vickers Hardness / kgf / mm^2	Yield Strength / GPa
1	0.256	849	2.78
	0.252	876	2.86
2	0.254	862	2.82
	0.252	876	2.86
3	0.252	876	2.86
	0.247	912	2.98
Average	*0.252*	*875*	*2.86*

5.2.3. Load calibration

The load cell in the test rig was first calibrated against a known load. The rig was designed with an attachable lever arm to which known masses could be attached, applying a known force in turn to the load cell. The magnitude of the force at the load could be calculated by the ratio of the lever arm dimensions between the mass and the pivot, and the pivot and the load cell. These were 500 mm and 47 mm respectively. Mass was added in 5 kg increments and the reading from the load cell was allowed to settle before being recorded. This was repeated until a final mass of 70 kg was attached, corresponding to a force on the load cell of 7303 N. This force applied to the disks would result in a nominal Hertzian contact pressure of just over 2.0 GPa. The mass was removed in 5 kg increments in a similar manner. The recorded load cell results can be seen in Table 5.6.

Table 5.6 - Load cell calibration results.

Mass / kg	Force / N	Theoretical Force at Load Cell / N	Loading		Unloading		Loading x 0.9		Unloading x 0.9	
			Force / N	Error	Force / N	Error	Force / N	Error	Force / N	Error
5	49.0	521.6	568	8.9%	586	12.3%	511.2	-2.0%	527.4	1.1%
10	98.1	1043.3	1120	7.4%	1137	9.0%	1008.0	-3.4%	1023.3	-1.9%
15	147.1	1564.9	1677	7.2%	1688	7.9%	1509.3	-3.6%	1519.2	-3.0%
20	196.1	2086.5	2247	7.7%	2258	8.2%	2022.3	-3.1%	2032.2	-2.6%
25	245.2	2608.2	2823	8.2%	2826	8.4%	2540.7	-2.6%	2543.4	-2.5%
30	294.2	3129.8	3398	8.6%	3395	8.5%	3058.2	-2.3%	3055.5	-2.4%
35	343.2	3651.4	3993	9.4%	3994	9.4%	3593.7	-1.6%	3594.6	-1.6%
40	392.3	4173.0	4593	10.1%	4598	10.2%	4133.7	-0.9%	4138.2	-0.8%
45	441.3	4694.7	5190	10.6%	5198	10.7%	4671.0	-0.5%	4678.2	-0.4%
50	490.3	5216.3	5791	11.0%	5800	11.2%	5211.9	-0.1%	5220.0	0.1%
55	539.4	5737.9	6408	11.7%	6408	11.7%	5767.2	0.5%	5767.2	0.5%
60	588.4	6259.6	6992	11.7%	6996	11.8%	6292.8	0.5%	6296.4	0.6%
65	637.4	6781.2	7580	11.8%	7590	11.9%	6822.0	0.6%	6831.0	0.7%
70	686.5	7302.8	8162	11.8%			7345.8	0.6%		

Mean	9.7%	**Mean**	10.1%	**Mean**	-1.3%	**Mean**	-0.9%
Max.	11.8%	**Max.**	12.3%	**Max.**	0.6%	**Max.**	1.1%
Min.	7.2%	**Min.**	7.9%	**Min.**	-3.6%	**Min.**	-3.0%

It can be seen from the table that the readings taking directly from the load cell overestimate the load being applied to the disks, with an average error of around 10% in both the loading and unloading phase. To counter this, the measured force from the load was multiplied by a factor of 0.9, which significantly reduces the error across the range tested, reducing the average error to around 1% in the loading and unloading phases. The force read from the load cell, and the factorised force are shown in Figure 5.3, showing the reduction in error. This allowed the applied load to be more accurately controlled, which was important for comparisons with the finite element analysis.

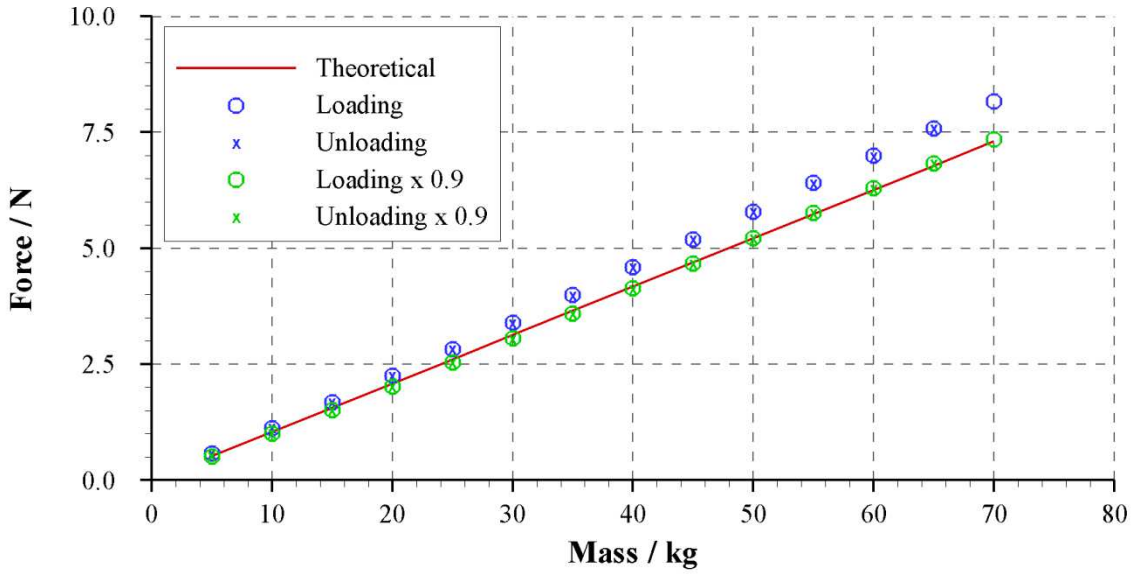

Figure 5.3 - Applied mass versus force at load cell and calibrated force.

5.3. Experimental

5.3.1. Profile measurement

In order to compare experimental results with the finite element analysis, the surface roughness profiles before and after loading were required. Profiles were taken using a standard stylus profilometer made by Taylor-Hobson, with the Talysurf probe highlighted in green in Figure 5.4. Profiles were recorded by moving the probe in the x-direction, as shown by the blue arrow. A moveable stage was utilised, that allowed movement perpendicular to the probe measurement direction, in the transverse, or y-direction. This allowed measurement of an array of surface roughness profiles across the contacting edge of the ground disk. The disk was mounted upon a test shaft, and a bespoke jig was made using v-blocks to fix the disk and shaft to the moveable stage.

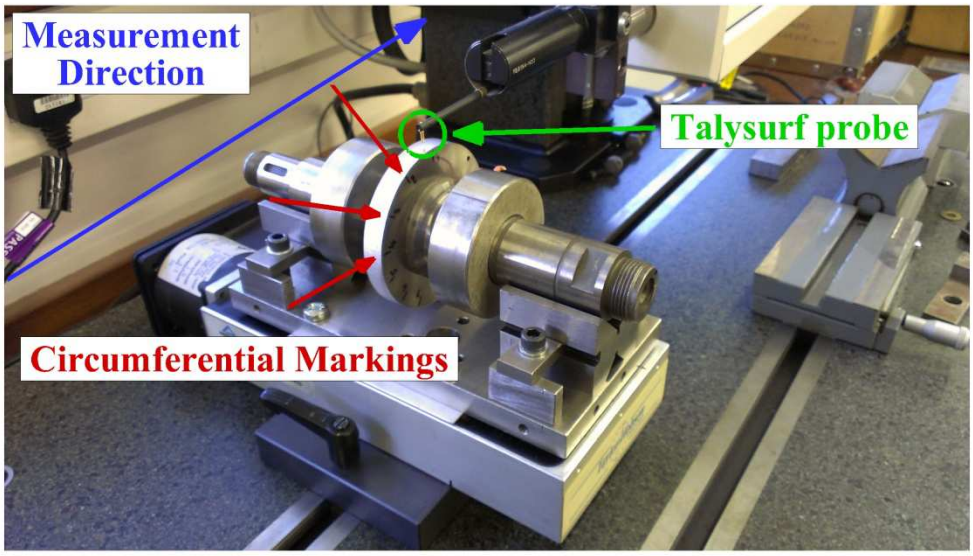

Figure 5.4 - Talysurf and moveable stage with ground disk mounted on test shaft with solid bearing replacements. Circumferential location markings are indicated by red arrows.

An array of profiles ensured that the entire contact was detected and that profiles from outside the contact region (axially) could be used to relocate the initial and residual profiles in the circumferential direction. To simplify this process, each disk had a number of circumferential positions marked on the face of the disk, as seen in Figure 5.4, indicated by the red arrows. These

marked locations would be lined up to contact in the test rig so the approximate circumferential location is known. On the contacting edge, a Vickers hardness test indentation was made outside of the contact area lined up with the face markings, as shown in Figure 5.5. The Vickers indentation allowed a greater level of accuracy in the relocation than the circumferential markings. The circumferential offset to relocate the profile with the Vickers indentation could then be applied to the profiles within the contact region, before local valley features unaffected by the contact loading were used to fine tune the profile relocation.

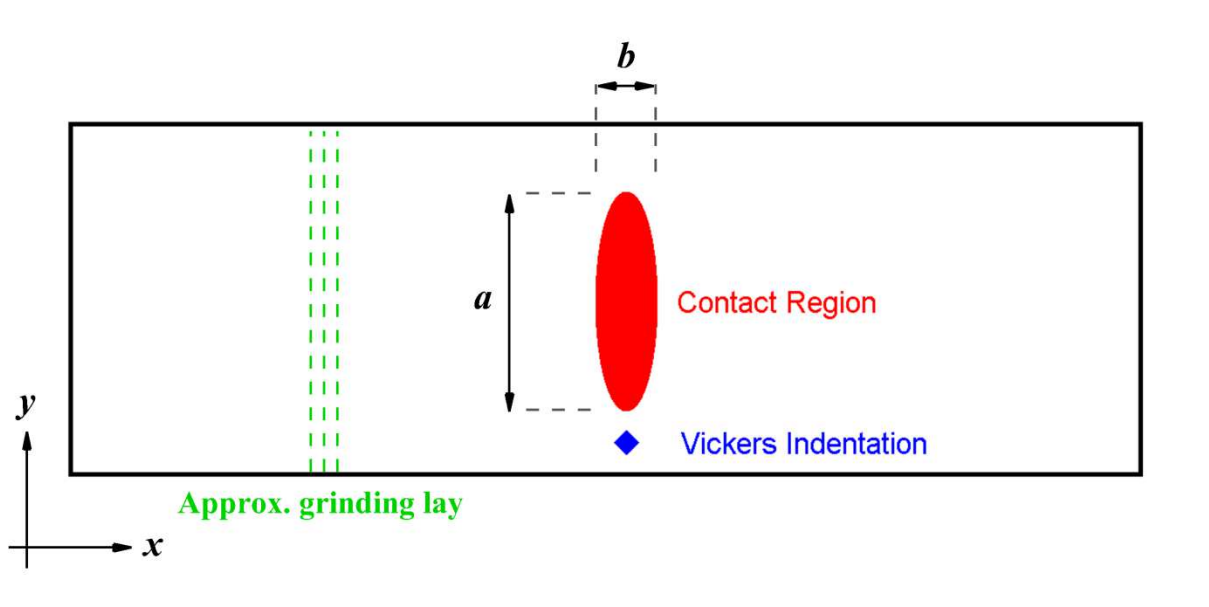

Figure 5.5 - Illustration of Vickers indentation location used for profile relocation.

The crown of the disk was found in both the x- and y-directions (circumferential and axial) using the appropriate function within the Taylor Hobson Talysurf Ultra software. The stylus was then offset 5 mm in the x-direction and 4.75 mm in the y-direction. An array of 10 mm long profiles in the x-direction was then taken, spaced 0.5 mm apart in the y-direction. The array of profiles is shown in Figure 5.6, as presented in the TalyMap presentational software. The Vickers indentation used for profile relocation can be clearly seen between y = 8.0 mm and y = 8.5mm at approximately x = 4.5mm, and is circled for clarity.

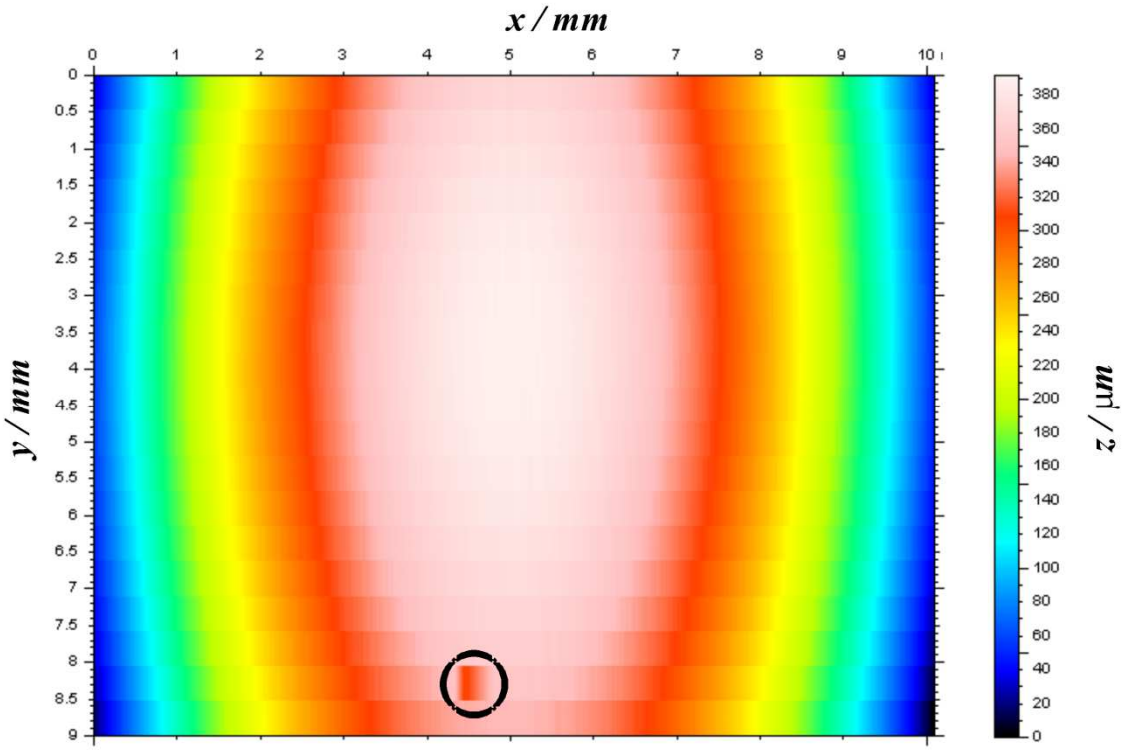

Figure 5.6 - 3D representation of the array of surface roughness profiles taken from ground disk. Vickers indentation used for profile relocation is circled.

5.3.2. Loading of disks

Once the array of initial surface roughness profiles had been measured using the Talysurf, the shaft mounted disks were secured in the test rig, with the required circumferential locations aligned for contact. For a nominal Hertzian contact pressure of 1.0 GPa, a load of approximately 900 N was required. The load was increased slowly until the specified load was achieved, and was maintained while the gauge readout was allowed to settle. The load was then slowly reduced to zero, before the disks were separated from contact and the shafts removed from the test rig. The ground disk was then returned to the Talysurf and another array of surface roughness profiles was measured. For nominal Hertzian contact pressures of 1.5 GPa and 2.0 GPa, loads of approximately 3.0 kN and 7.2 kN were required, respectively.

5.3.3. Profile relocation

Following loading, the raw profiles were filtered using a Gaussian filter with a cut-off of 0.25 mm. This removed the underlying form of the disks. To relocate the profiles such that the surface roughness was aligned, the profile with the Vickers hardness indentation was first used to provide a general relocation offset in the x-direction. The unfiltered and filtered profiles with the Vickers hardness indentation can be seen in Figure 5.7a and b, where the red and blue curves give the surface profile measurement before and after loading respectively. Also shown in Figure 5.7b are the roughness parameters R_a, R_z and R_{sk} for the measured profile before and after loading. Due to the presence of the Vickers indentation, the parameters were calculated for two sections of the profile; up to 4.5 mm and after 6.0 mm. This ensured that the Vickers indentation did not distort the calculations. The R_a value found of between 0.357 µm and 0.394 µm is similar to that of the measured gear teeth profiles from Chapter 3, showing that the techniques used are appropriate for recreating such components. What can also be seen in these parameters is the similarity of the parameters for each section before and after loading, showing that the surfaces have not undergone any significant surface deformation between measurements.

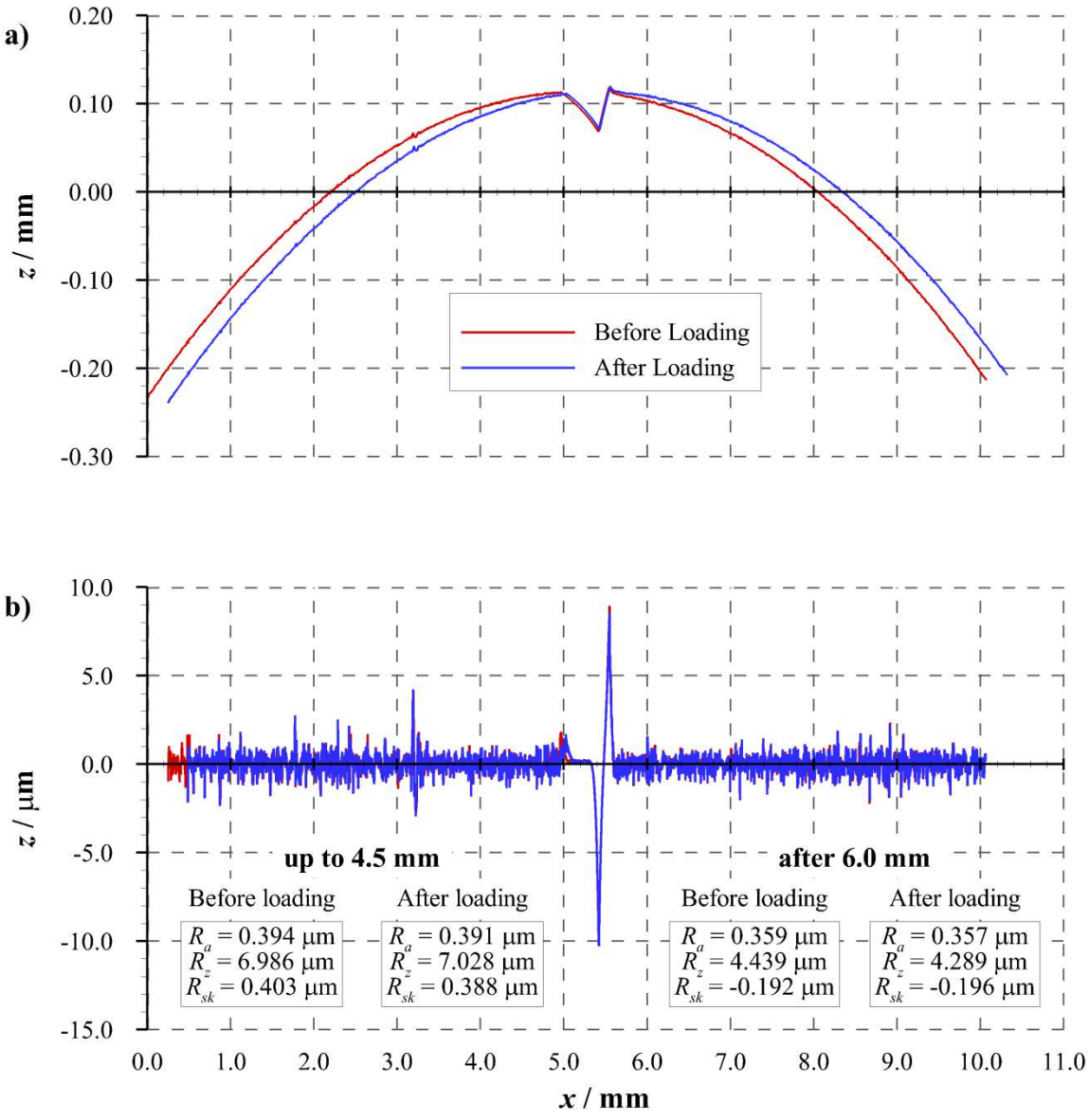

Figure 5.7 - Surface roughness profile including Vickers hardness indentation; a) raw, b) filtered.

The arrays of profiles before and after loading were then assessed to find the profiles in which plastic deformation had occurred. Those profiles with residual shape change were deemed to have been within the contact region, while those without were discarded. This gave an approximate size of the contact in the y-direction, determining the major axis length of the contact, a. The contact size in the x-direction, the minor axis length of the contact, b, could be estimated by measuring the distance between the first and last deformed asperities in the x-direction using the profile whose y-coordinate was in the centre of the contact. This gave a contact with approximate dimensions of a =

1.250 mm and b = 0.591 mm. For an elliptical contact with a nominal Hertzian contact pressure of 1.0 GPa, the approximate contact dimensions are a = 1.349 mm and b = 0.337 mm, while for a line contact with the same pressure the approximate contact dimension is given by a = 0.342 mm (equivalent to b in an elliptical contact). It can be seen by comparing the theoretical results that approximate an elliptical contact with a line contact results in an overestimate of the contact pressure. However, the approximate contact dimensions predicted by the finite element analysis still differ from theory fairly noticeably. In the y-direction, considering the major contact dimension a, profiles were taken every 0.50 mm, and could therefore only measure the overall contact size, 2a, to a precision of 1.0 mm. Therefore the precision of a is 0.5 mm, and so the difference between the finite element analysis and theory is within the expected margin of error. For the minor contact dimension, b, the uncertainty is a result of the difference in geometry and material properties in comparing the finite element analysis and theory. The rough surface results in asperity features far above the smooth surface in Hertzian theory. The precision of measurement of the minor contact dimension is proportional to the distance between prominent asperity features that result in residual deflection, which is unique to each rough surface.

Figure 5.8a shows the relocated initial and residual profiles from the approximate centre line of the contact region. The 2.0 mm length of surface roughness shown, from x = –1.0 mm to x = 1.0 mm, was the surface roughness imported into Abaqus for analysis. For the 1.5 GPa and 2.0 GPa models, widths of 2.5 mm and 3.0 mm were imported to allow for the increased contact size. Figure 5.8b shows a magnified view of the surface roughness, which illustrates the profile relocation and plastic asperity deformation more clearly.

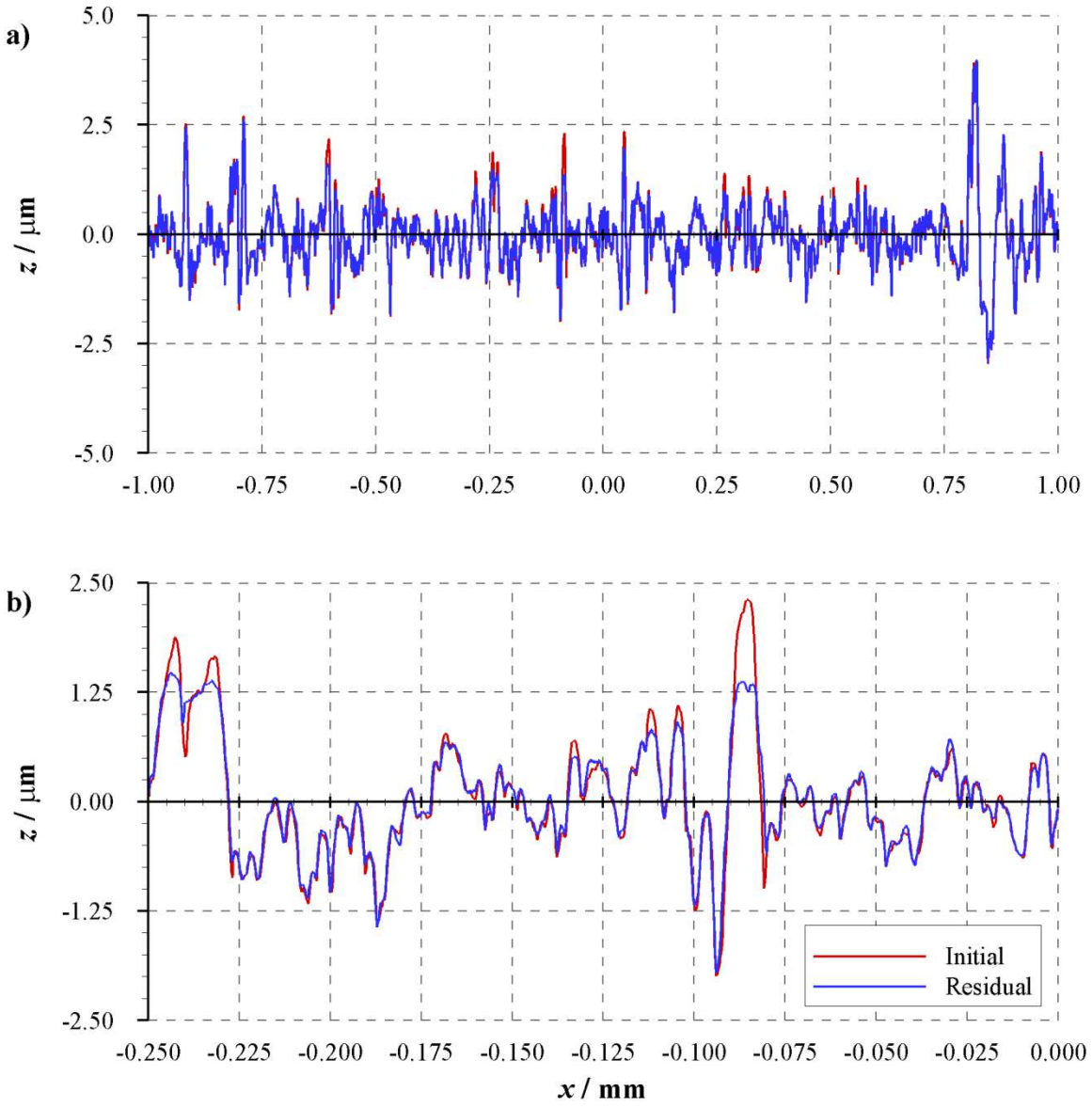

Figure 5.8 - Initial and residual profiles after relocation; a) complete profile, b) magnified view showing asperity deflection.

5.4. Finite element modelling

5.4.1. Model details

For the nominal Hertzian contact pressure of the 1.0 GPa model, the 2.0 mm length of surface roughness from the carburised, ground disk previously shown in Figure 5.8 was superimposed onto a smooth surfaced roller of radius 38.1 mm (the radius of the test disks) as illustrated in Figure 5.9. This rough surfaced roller data was then imported into Abaqus using a Python script, and a 2D

deformable part created. For the 1.5 GPa and 2.0 GPa nominal Hertzian contact pressure models, the length of roughness imported was 2.5 mm and 3.0 mm, respectively to allow for the increase in expected contact size, whilst maintaining distance between the contact and the model boundaries. The counter surface was assumed to be a smooth, purely elastic body, due to the relative roughness and hardness of the surface of the superfinished, nitrided disk as previously described in Section 5.2.2.2.

In contrast to previous models, each contacting body consisted of three separate parts that were assembled to create each contacting roller. Each constituent part was the same width, and the side boundaries aligned within the **Assembly** module. Where each part contacted another, the surfaces were joined using surfaces ties. This can be seen in Figure 5.10. Figure 5.10a shows the constituent parts before final assembly with surfaces to be tied highlighted in red. Once the surface ties had been applied, the parts were then assembled as in Figure 5.10b to create the final rough roller parts. The reason behind this choice was to reduce the overall number of elements within the relatively large model, thus reducing computational time, without compromising the number of elements at the contact surface, and affecting the accuracy of the simulation. In previous modelling, biased mesh seeds had been used to increase element size remote from the contact surface; the use of surface ties allows for more rapid transitions. The Abaqus User's Manual (Abaqus 2010) specifically recommends surface ties for this purpose. Given the relatively large size of the contact and associated model, a large number of elements are required to solve the problem with a sufficient degree of accuracy. The number of elements at the surface is particularly important as this defines the accuracy at each asperity contact and the stresses in the surrounding material. However, the stresses within the bulk material remote from the immediate subsurface material are of relatively little interest, and so a much lower mesh density in these regions is desirable to reduce computation time. It was found that by utilising separate parts with tied surface constraints, a smaller number of elements could be used in the model compared to smooth transitioning of element sizes away from the contact. The discontinuous mesh used for the nominal Hertzian contact pressure of 1.0 GPa

model can be seen in Figure 5.10, with three separate sections of height 0.05 mm, 0.75 mm and 1.2 mm shown in Figure 5.10a. These dimensions were determined as a resulting of experimentation. For the load cases considered, the highest stresses and material plasticity was limited to the surface layer of 0.05 mm. Stresses in the remaining layers were significantly less, significantly below the yield strength. The middle layer had some stress variation, while the final top layer was essentially in uniaxial compression. As the material was specified to have a hardness of HRC 60 to a minimum of 0.183 mm, it was therefore decided that varying material properties with material depth was unnecessary. The mesh in the smallest section at the surface is hidden, because at the scale shown in the figure the elements are too small to be seen.

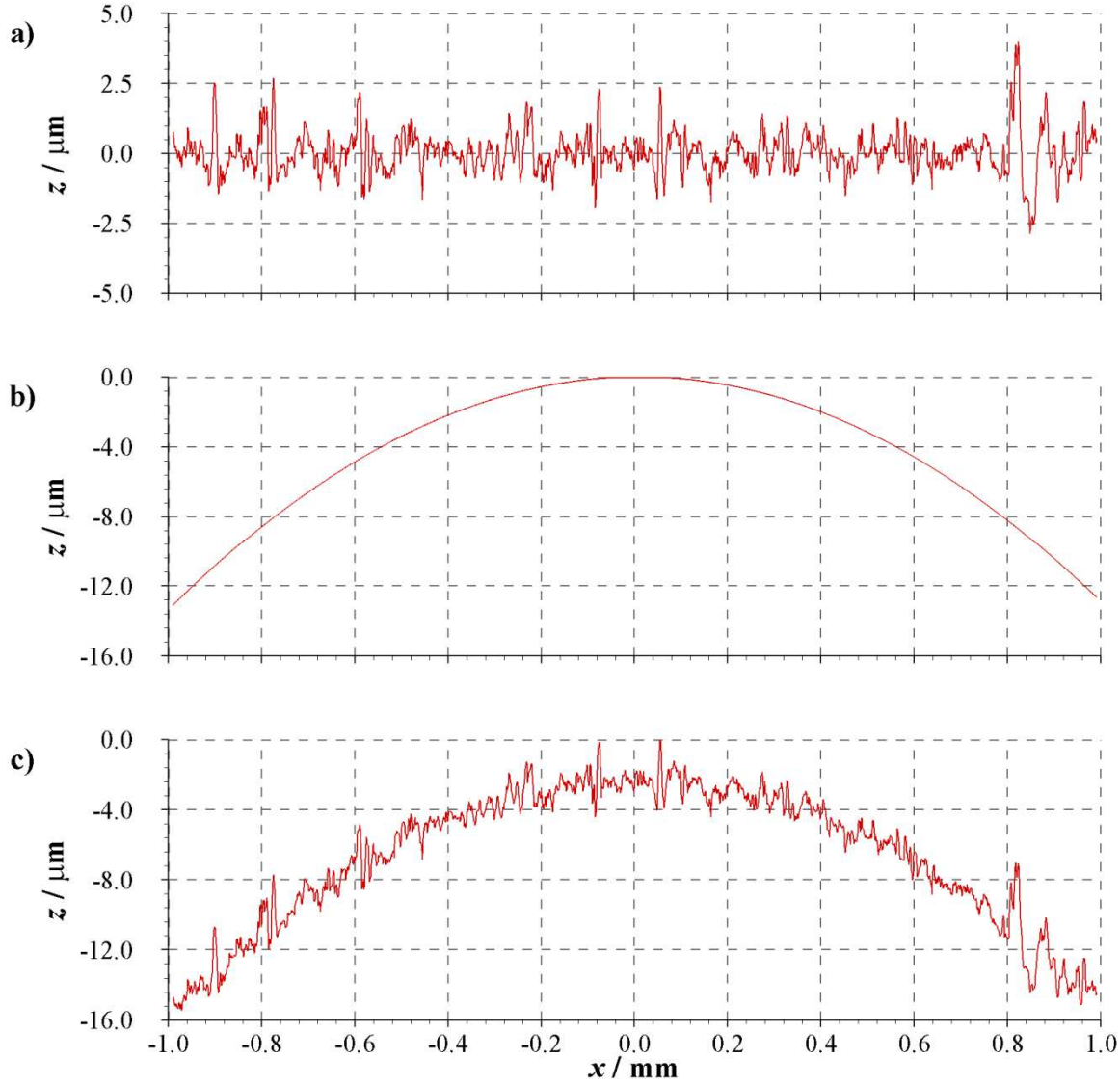

Figure 5.9 - Creation of rough surface roller; a) Filtered test disk roughness profile, b) Smooth roller profile, c) Filtered test disk roughness profile superimposed on smooth roller profile.

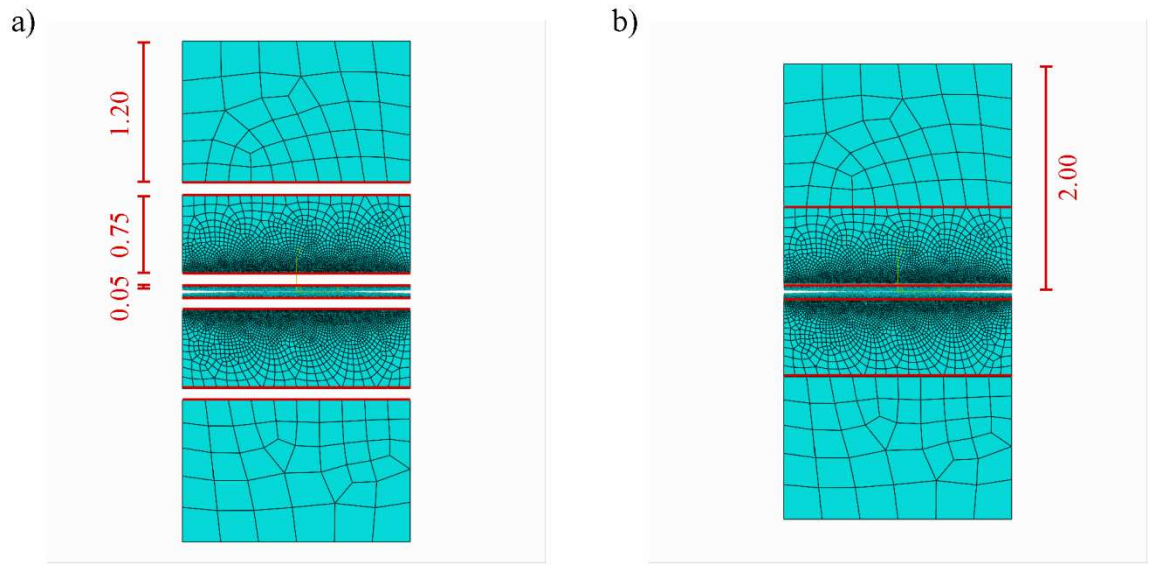

Figure 5.10 - Screenshot of rough roller contact model, showing mesh discontinuities and surface ties (red); a) before final assembly, b) after final assembly. All dimensions in millimetres.

For each of the combined rough and smooth rollers, the total minimum depth was 2.0 mm above the rough surface, as shown in Figure 5.10b, in order to avoid interaction between the field outputs around the surface and the effects of the model boundary. The size of the elements for the rough surfaced roller was approximately 1.0 µm at the contact, resulting in an accuracy of ± 0.5 µm at the edges of each asperity contact. The elements used were fully integrated elements, and the ALE Adaptive Meshing settings were continued from the model experimentation study. Due to computational resource limits, the absolute penetration tolerance was increased from previous models, allowing maximum penetration of 10^{-9} m. Surface elements were assessed for distortion and excess penetration to ensure model validity. This was trailed through comparison of a single load case, and differences between the results were found to be negligible.

The plastic materials properties used the yield stress estimated experimentally in Section 5.2.2.2, giving a yield strength, σ_y, of 2.550 GPa. Initially, the material properties were defined to be elastic-perfectly plastic, but difficulties were encountered in getting the model to complete successfully due to the numerical difficulties caused by the incompressibility of elastic-perfectly plastic material. This

material definition can result in volumetric locking as previously described in Chapter 3, Section 3.4.1.2. The plastic behaviour was modified from the elastic-perfectly plastic case used previously to include linear strain hardening behaviour of E_T / E = 0.01; which gave a close approximation to elastic-perfectly plastic behaviour without the numerical difficulties of incompressibility, which lead to solution problems at asperity contacts. These material properties were also varied to test the effects on the results. The yield strength was modified by ± 10%, giving additional yield strengths of 2.295GPa and 2.805GPa while the linear strain hardening behaviour was changed to E_T / E = 0.05 for each yield strength too. This range of strain hardening behaviour reflects those typically found in engineering steels (Kogut and Etsion 2002). The remaining modelling details are similar to those used in previous models. The summary of the test disk contact model can be seen in Table 5.7.

Table 5.7 - Test disk contact model summary.

Part	2D rough roller – Imported test disk surface profiles
	2D rough roller middle section
	2D rough roller end section
	2D smooth roller
	2D smooth roller middle section
	2D smooth roller end section
Property	Rough: E = 200 GPa, ν = 0.3, σ_y = 2.295GPa, 2.550 GPa, 2.805 GPa E_T / E = 0.01, 0.05
	Smooth: E = 200 GPa, ν = 0.3
Assembly	Model boundaries aligned. Parts on the verge of contact
Step	Initial (required), Contact, Load, Removal
	ALE Adaptive Meshing – Frequency = 1, Remeshing sweeps = 10
Interaction	Frictionless
	Augmented Lagrange Constraint Enforcement Method
	Finite Sliding
	Surface-to-Surface
	Absolute Penetration Tolerance = 1×10^{-9}m
	Surface ties applied to adjacent surfaces of constituent roller parts
Load	800 N, 2700 N, 6480 N total load, applied as a distributed load acting on bottom edge of smooth surface part
Boundary Conditions	Small vertical displacement applied to bottom edge of smooth surface part to initiate contact
	Top edge of rough surface part restrained (U_x = U_y = 0)
	Side edges of rough and smooth surface parts restrained in y-axis (U_x = 0)
Mesh	Partitioned around contact area
	Plane Strain Elements
	Linear Elements
	Fully integrated elements

In order to validate the finite element analysis of each full contact, the residual profiles from the measured disk and numerical model were correlated and compared. For each contact, the profiles were correlated by aligning the measured initial and residual profiles from outside of the contact region, using the Vickers hardness indentation as a reference. The profiles inside the contact region were then adjusted using identifiable local valley features.

For simplicity, the application of nominal Hertzian contact pressures of 1.0 GPa, 1.5 GPa, and 2.0 GPa will be referred to in the text as Load Case 1, 2 and 3 respectively, while each of the surfaces subject to these load cases will be referred to as Surface 1, 2 and 3. It would be impractical to show and discuss results for the entire contact for each load case, so three sections of each surface have been selected for presentation. These sections have been chosen to both to show a range of asperity contacts that occur in each load case, and to show sections of the surface from across the entire contact region. Typically sections were chosen from around the contact centre line, and one from either side, to illustrate the agreement under a range of loading conditions.

For Load Case 1 and Surface 1, these sections are from x = –0.29 mm to x = –0.19 mm, from x = –0.13 mm to x = –0.03 mm, and from x = 0.25 mm to x = 0.35 mm. These sections will subsequently be referred to as Sections 1a, 1b and 1c respectively. For Load Case 2 and Surface 2, these sections are from x = –0.36 mm to x = –0.26 mm, from x = –0.10 mm to x = 0.00 mm, and from x = 0.32 mm to x = 0.42 mm. These sections will subsequently be referred to as Sections 2a, 2b and 2c respectively. For Load Case 3 and Surface 3, these sections are from x = –0.26 mm to x = –0.16 mm, from x = –0.06 mm to x = 0.04 mm, and from x = 0.43 mm to x = 0.53 mm. These sections will subsequently be referred to as Sections 3a, 3b and 3c, respectively.

5.4.2. 1.0 GPa nominal Hertzian contact pressure model results

5.4.2.1. Resolution results

Surface 1 was simulated with Load Case 1 with mesh resolutions of both 0.5 µm and 1.0 µm, in order to check the dependency of the results on the resolution. Figure 5.11a, b and c show the residual profiles for each of the resolution models for Sections 1a, 1b and 1c respectively, as well as the initial and measured profiles. It can be seen that for each of the sections shown that the 0.5 µm and 1.0 µm resolutions show good agreement with each other, and good agreement with the measured residual profile. Small differences between the measured residual profile and each of the simulated results are noticeable in some locations however, primarily in local valley features where material

has been forced into a valley as a result of the plastic flow in the vicinity of the loaded contact. This can be seen in Figure 5.11a, Figure 5.11b and Figure 5.11c at x = –0.228 mm, x = –0.072 mm and x = 0.277 mm respectively.

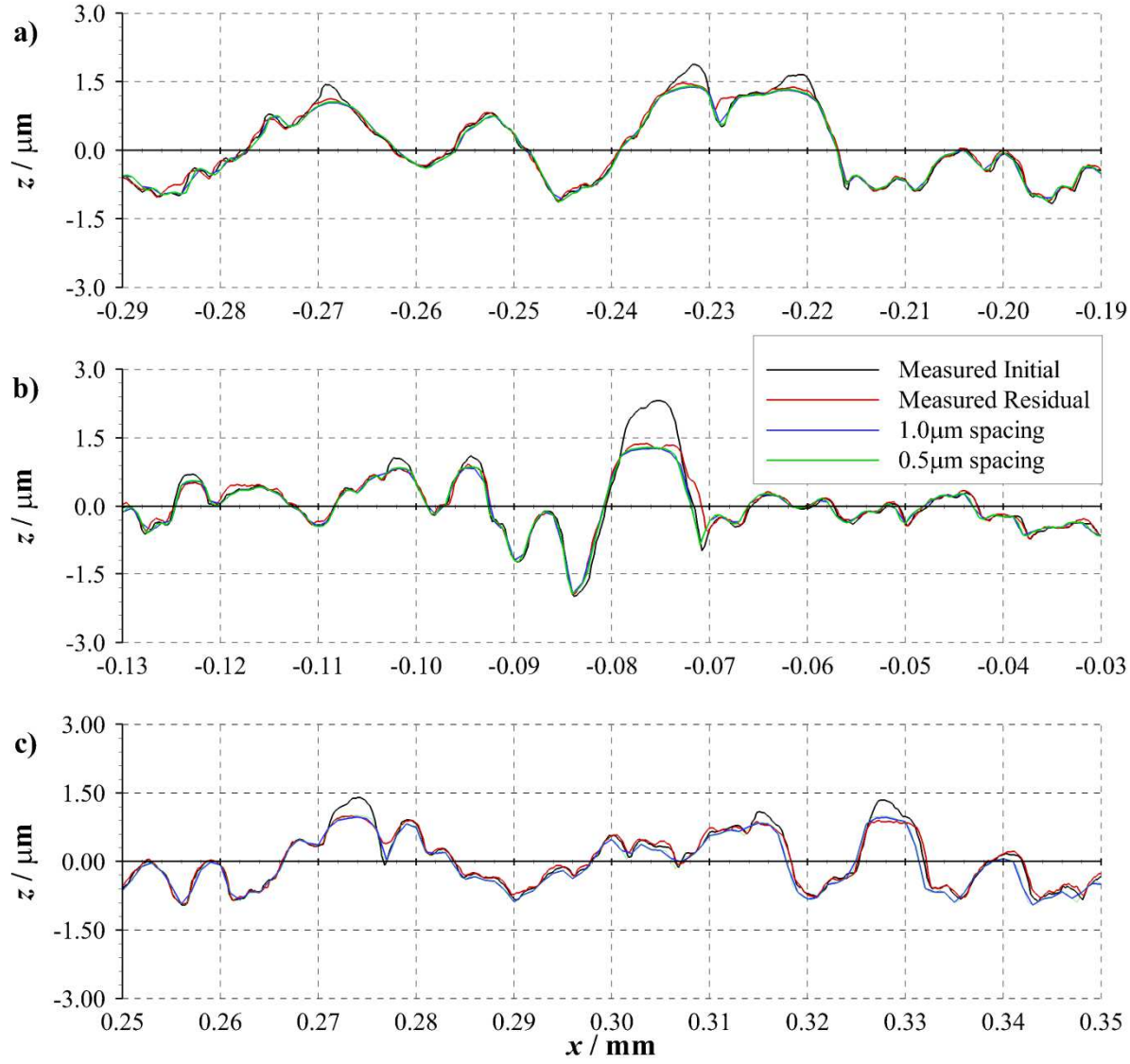

Figure 5.11 - Residual profiles for sections of the rough roller, also showing effect of resolution; a) Section 1a, b) Section 1b, c) Section 1c. Also shown are the initial and residual measured profiles. σ_y = 2.550 GPa and E_T / E = 0.01 for each resolution.

Figure 5.12 shows the residual von Mises stress contours for each of the 1.0 µm and 0.5 µm resolution models, for Section 1b. It can be seen that over most of the zone shown the von Mises stress values in the subsurface material follow the same distribution in both models. The main difference between the two models is in the region of high magnitude stress at the surface of the

deformed asperity between x = –0.083 mm and x = –0.071 mm. At approximately x = –0.0745 mm, a small region of slightly higher magnitude stress is seen to occur in the 1.0 µm resolution model. The difference between the peak stresses at this location is relatively small, at $0.22\sigma_y$.

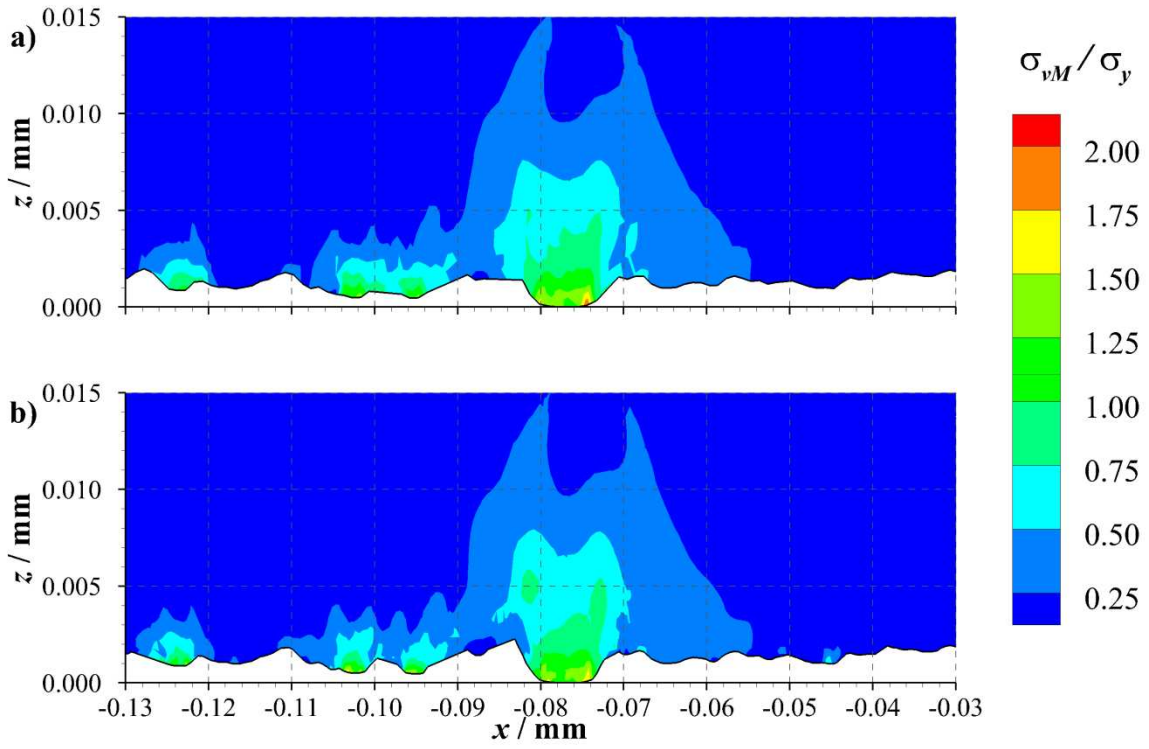

Figure 5.12 - Contours of normalised residual von Mises stress for Section 1b; a) 1.0 µm resolution, b) 0.5 µm resolution. σ_y = 2.550 GPa and E_T / E = 0.01 for each resolution.

Figure 5.13 shows the contours of normalised residual direct stress in the tangential direction for the 1.0 µm and 0.5 µm resolution models, for Section 1b. As with the contours of residual von Mises stress, the stress distributions in the subsurface material are generally similar between each of the models. The main differences occur in the size of the regions of subsurface tension at x = –0.123 mm, z = 0.005 mm and x = –0.103 mm, z = 0.005 mm. In each case, these regions are larger in the 0.5 µm resolution model. At the surface, for the heavily loaded asperity between x = –0.083 mm and x = –0.071 mm, the region in which the highest stress occurs is slightly larger in the 0.5 µm resolution model. Slightly higher magnitude stresses are also seen to occur at the asperities at approximately x = –0.103 mm and x = –0.095 mm.

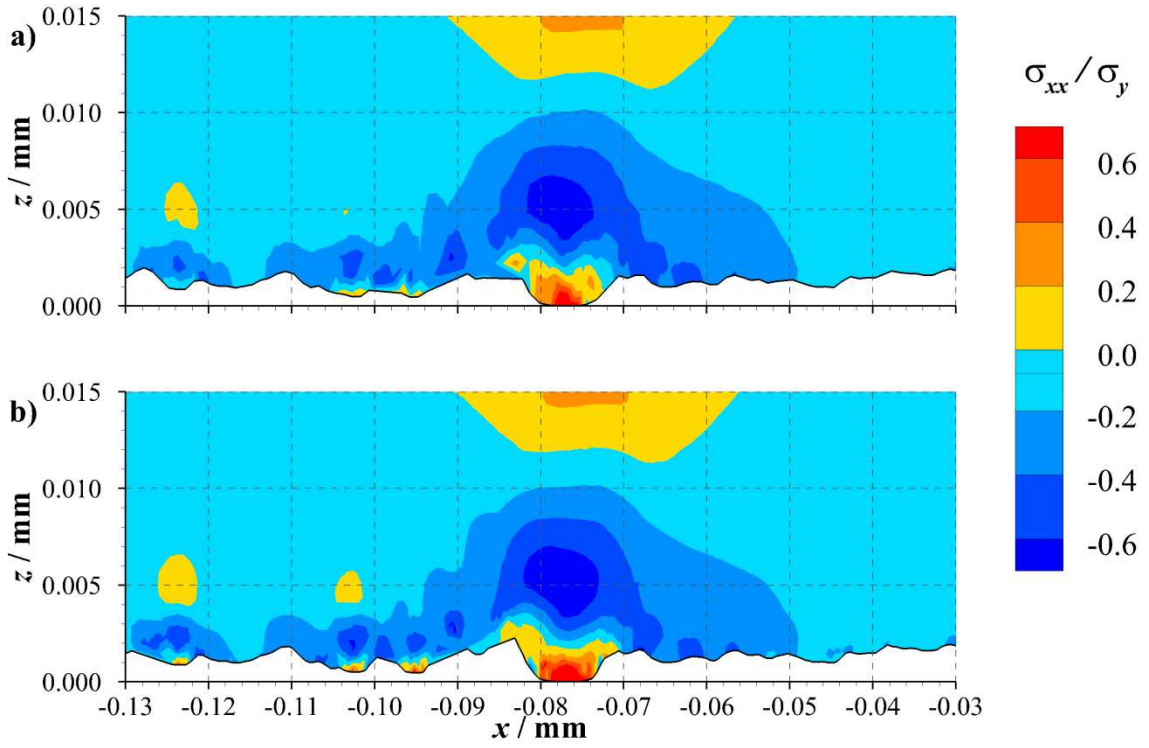

Figure 5.13 - Contours of normalised residual direct stress in the tangential direction for Section 1b; a) 1.0 µm resolution, b) 0.5 µm resolution. σ_y = 2.550 GPa and E_T / E = 0.01 for each resolution.

As a result of the study of the mesh resolution, it was decided that a 1.0 µm resolution was sufficient to model the contacts accurately, whilst maintaining reasonable computation times. Additionally, surfaces using a 0.5 µm resolution were found to have more element distortion. This did not appear to introduce any error in this particular case, but in order to maintain a robust methodology, reduced element distortion was preferable. Therefore, the remainder of the results discussed, both for this surface and Surfaces 2 and 3, therefore utilised a mesh resolution of 1.0 µm.

5.4.2.2. Residual results

Figure 5.14, Figure 5.15 and Figure 5.16 show the residual profiles of Sections 1a, 1b and 1c of Surface 1 after simulations assuming yield strengths of σ_y = 2.295 GPa, σ_y = 2.550 GPa, and σ_y = 2.805 GPa. Also shown are the measured initial and residual profiles. Each yield strength was tested for both E_T / E = 0.01 and E_T / E = 0.05, which covers the practical range for engineering steels (Kogut and Etsion 2002). Also shown are magnified views of individual asperity features, showing the

difference between each of the material property sets in greater detail. As previously found in Chapter 4, increasing E_T / E results in smaller magnitude residual deflections, because a greater proportion of the loaded strain is elastic. This is most evident at the asperity tips, where the residual deflections are greatest.

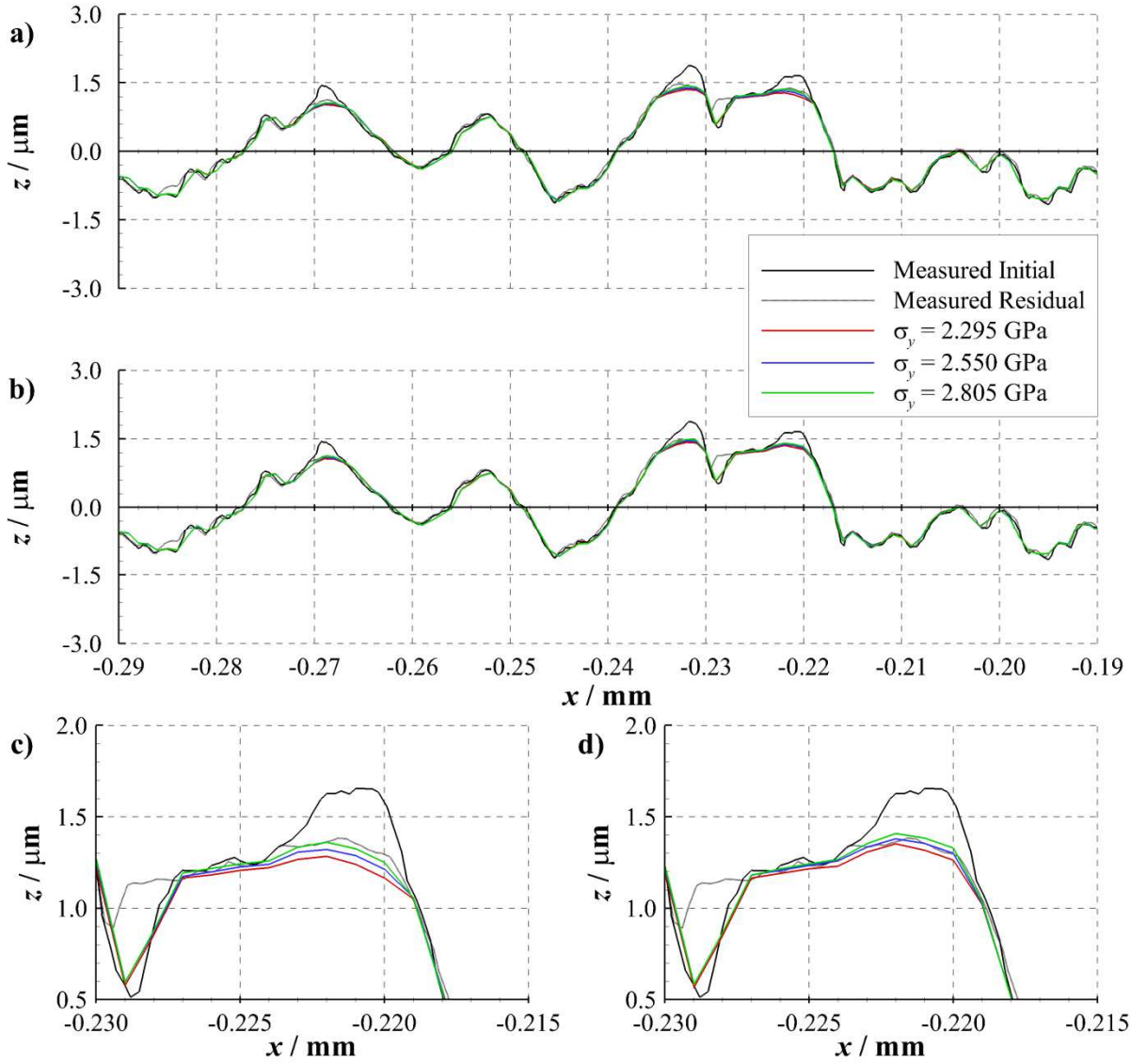

Figure 5.14 - Residual profiles for Section 1a showing effect of yield strength; a) E_T / E=0.01, b) E_T / E = 0.05, c) Magnified view of E_T / E = 0.01 for x = –0.230 to x = –0.215 mm, d) Magnified view of E_T / E = 0.05 for x = –0.230 to x = –0.215 mm. Also shown are the initial and residual measured profiles.

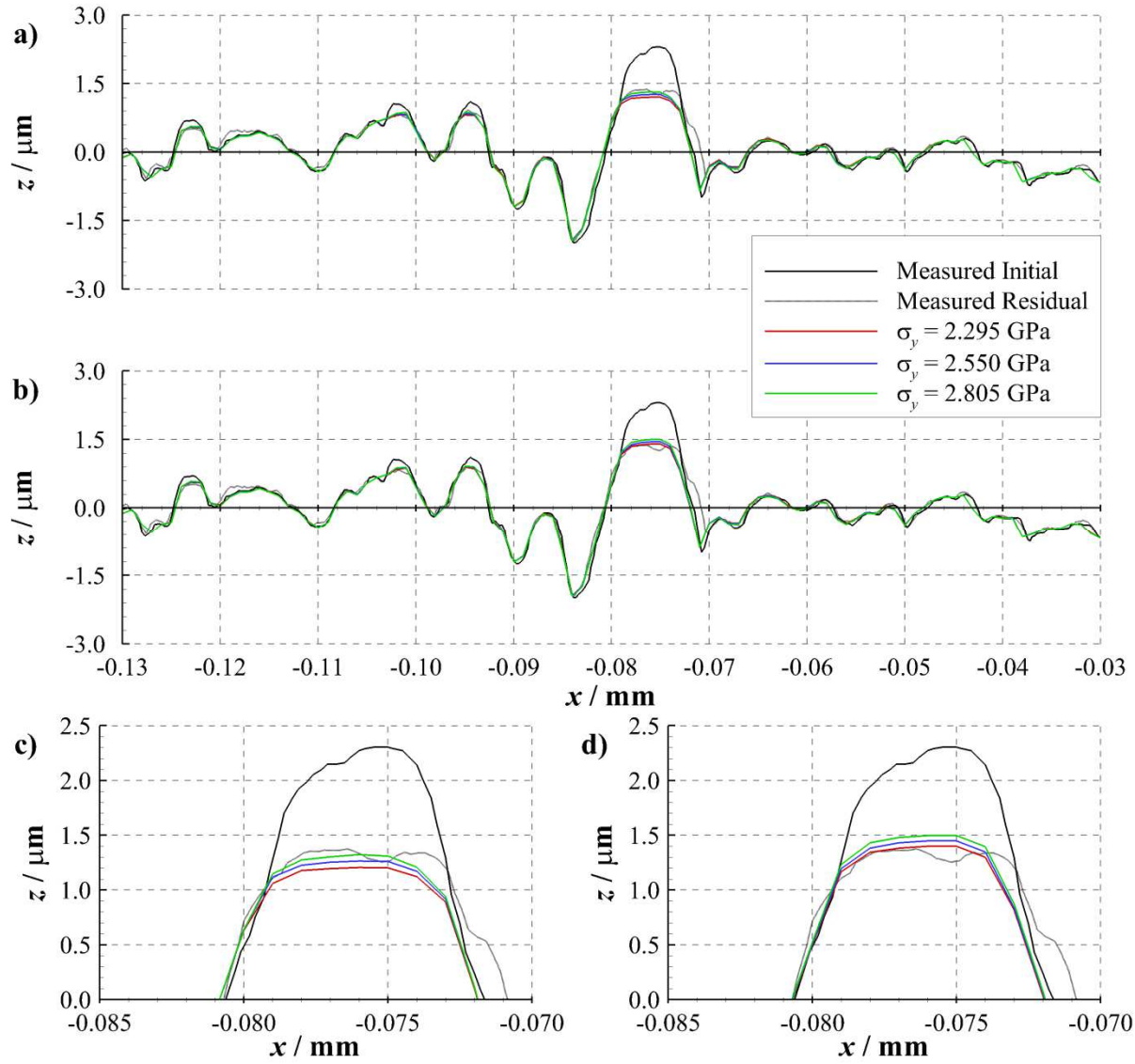

Figure 5.15 - Residual profiles for Section 1b showing effect of yield strength; a) E_T / E = 0.01, b) E_T / E = 0.05, c) Magnified view of E_T / E = 0.01 for x = −0.085 to x = −0.070 mm, d) Magnified view of E_T / E = 0.05 for x = −0.085 to x = −0.070 mm. Also shown are the initial and residual measured profiles.

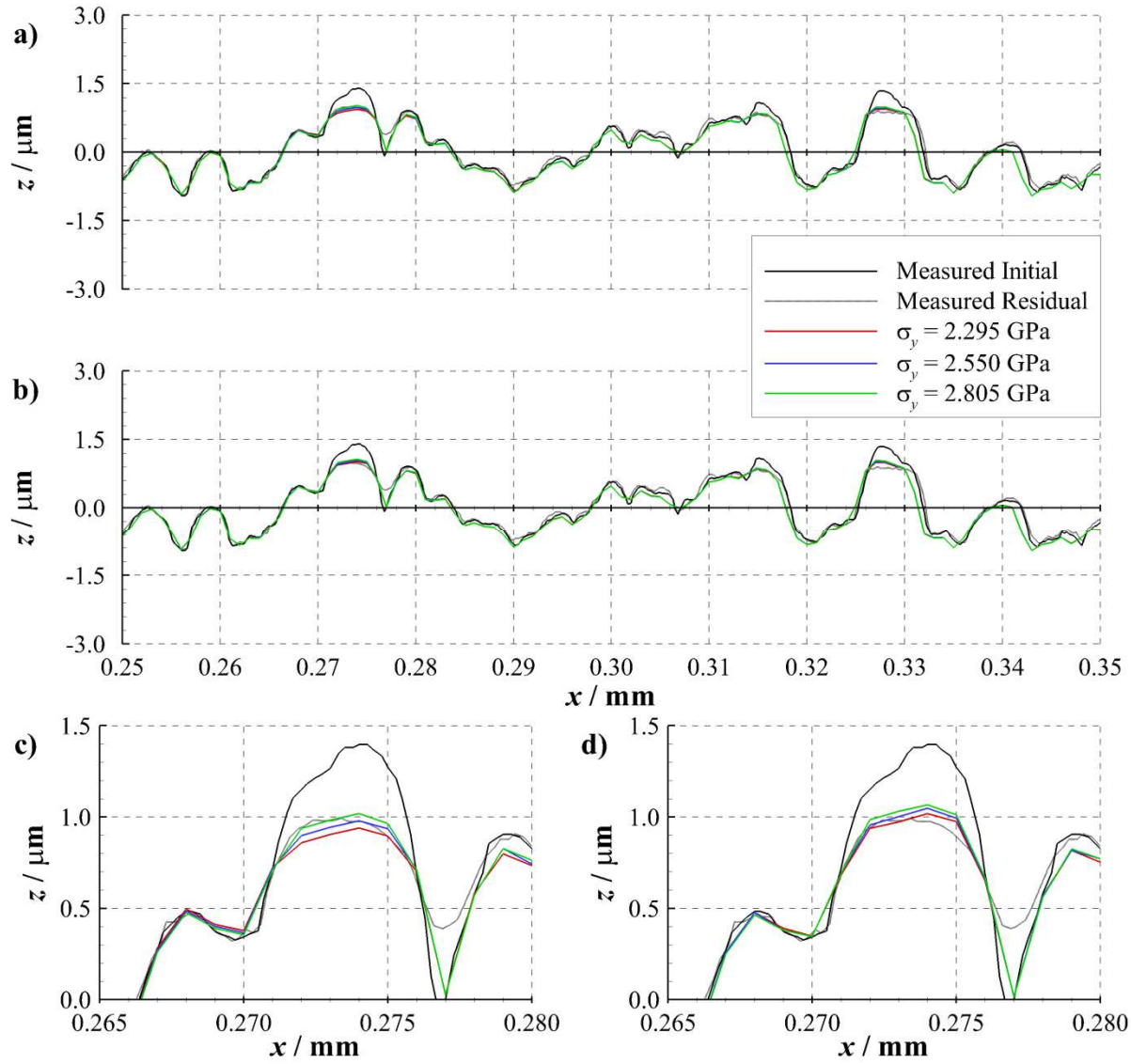

Figure 5.16 - Residual profiles for Section 1c showing effect of yield strength; a) E_T / E = 0.01, b) E_T / E = 0.05, c) Magnified view of E_T / E = 0.01 for x = 0.265 to x = 0.280 mm, d) Magnified view of E_T / E = 0.05 for x = 0.265 to x = 0.280 mm. Also shown are the initial and residual measured profiles.

It can be seen in each figure that for each ratio of E_T / E, a closely related family of profiles are produced for the range of yield strengths tested. The largest magnitude residual deflections are seen to occur for the lowest of the yield strengths tested, σ_y = 2.295GPa, while the smallest deflections are seen for the largest tested yield strength, σ_y = 2.805GPa. This is not unexpected, as for a given magnitude of stress, a larger proportion of the strain is plastic for the lowest yield strength, and vice versa for the highest yield strength.

Whilst each of the choices of yield strength and linear strain hardening behaviour offer good approximations to the residual deflections seen across the contact, some combinations more closely reflected the residual profile measured from the disk itself. In Figure 5.14a, for E_T / E = 0.01, the closest profile to the measured residual profile is given by σ_y = 2.805 GPa. This is not only significantly over the disk specification outlined in Table 5.2 of a surface hardness of HRC 60 to 63 (σ_y = 2.21GPa to σ_y = 2.65GPa), but above any of the measured hardness values in Table 5.3 and Table 5.4. While the lower value of yield strength tested, σ_y = 2.295GPa, is lower than those measured, it is within the specification of the disks. It is therefore suggested that either σ_y = 2.295 GPa or σ_y = 2.550 GPa be considered in preference to σ_y = 2.805 GPa. By examining the profiles of the E_T / E = 0.05 material in Figure 5.14b, it can be seen that the deflections predicted for the two lower yield strengths provide a more accurate approximation to the measured residual profile. Similar behaviour can be seen in Figure 5.15, where for E_T / E = 0.01 in Figure 5.15a, the profile for σ_y = 2.805 GPa provides the closest agreement. However, by considering the results for E_T / E = 0.05 in Figure 5.15b, the residual profiles for the materials with σ_y = 2.295 GPa and σ_y = 2.550GPa provide better agreement with the experimental result. In Figure 5.16, the same trend of behaviour is seen for the asperity between x = 0.271 mm and x = 0.276 mm, where the most accurate approximations are provided by σ_y = 2.805 GPa for E_T / E = 0.01 in Figure 5.16a, and σ_y = 2.295 GPa and σ_y = 2.550 GPa for E_T / E = 0.05 in Figure 5.16b. However, for the asperity between x = 0.326 mm and x = 0.331 mm each of the tested material combinations underestimates the magnitude of residual deformation. As this position of the profile is near the edge of the predicted contact area for a nominal Hertzian contact pressure of 1.0 GPa, it is thought that this may be attributable to slight discrepancies in loading, or imprecise location of the contact centre when creating the finite element model. It is therefore suggested that the material combination which gives the best agreement with the experimental results is either σ_y = 2.295 GPa or σ_y = 2.550 GPa with linear strain hardening behaviour of E_T / E = 0.05.

Figure 5.17 shows contours of normalised residual von Mises stress for the three sections of Surface 1. Figure 5.17a, b and c show the contours for Section 1a, 1b and 1c respectively. It can be seen that larger residual deflections result in larger regions of high magnitude residual stress. This can be seen in particular in Figure 5.17b for the asperity feature between x = –0.082 mm and x = –0.070 mm, which experienced the largest residual deflection of the asperities shown. The surrounding region shows the largest region of high magnitude von Mises stress, of the order of the yield strength, shown in red. Additionally, the subsurface material beneath this asperity feature experiences residual stress to a larger depth, with residual von Mises stress above $0.10\sigma_y$ at a depth of z = 0.019 mm. Asperities with less residual deflection still experience regions of high magnitude residual stress. This can be seen in Figure 5.17a between x = –0.272 mm and x = –0.266 mm, in Figure 5.17b between x = –0.104 mm and x = –0.101 mm and in Figure 5.17c between x = 0.270 mm and x = 0.275 mm. However, the effect on subsurface material is less pronounced, with stresses of above $0.1\sigma_y$ limited to depth of approximately z = 0.010 mm for each of these regions. One instance of a very lightly loaded asperity can be seen in Figure 5.17a, at x = –0.253 mm. Little residual deflection can be seen in the roughness profile at this location in Figure 5.14. However, the residual stress contour suggests a lightly loaded contact, as residual stresses occur. Figure 5.17a also shows how contact of neighbouring asperity features can result in interaction of stress contours, which can be seen between contacts x = –0.234 mm and x = –0.231 mm and between x = –0.226 mm and x = –0.222 mm, with a region of increased magnitude “linking” the two contact regions at approximately x = -0.227 mm, z = 0.004 mm.

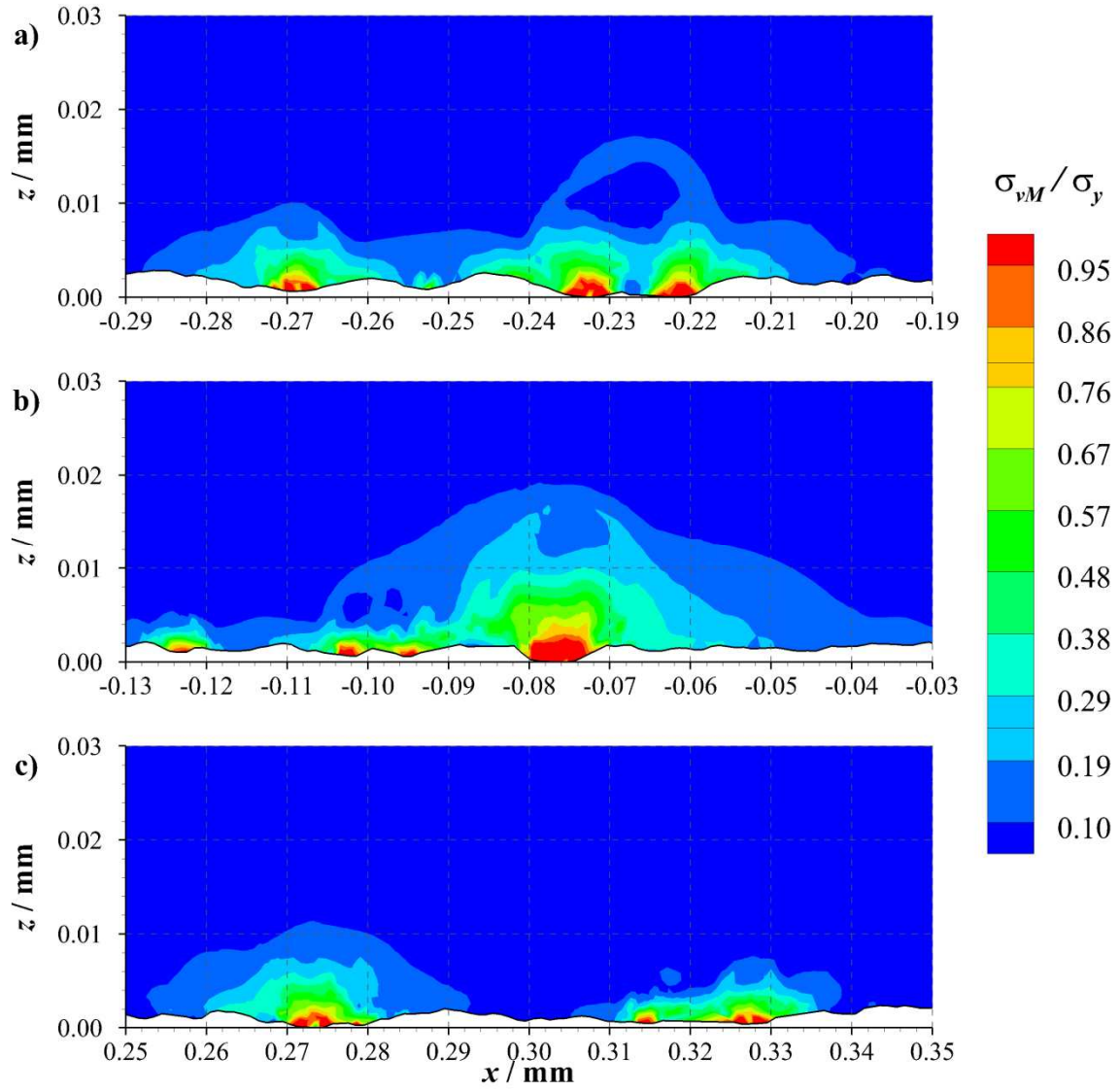

Figure 5.17 - Contours of normalised residual von Mises stress; a) Section 1a, b) Section 1b, c) Section 1c. σ_y = 2.550 GPa and E_T / E = 0.05 for each section.

Figure 5.18 shows contours of the normalised residual direct stress in the tangential direction for the three sections of Surface 1. Figure 5.18a, b and c show the contours for Section 1a, 1b and 1c respectively. As in the von Mises stress contours, the heavily loaded asperity feature between x = –0.082 mm and x = –0.070 mm in Figure 5.18b shows the largest region of surface tensile stress, and it could be suggested that the surface stress is related to the amount of residual deflection of the asperity. However, asperity features between x = –0.234 mm and x = –0.231 mm, and between x = –0.226 mm and x = –0.222 mm in Figure 5.18a, and between x = 0.272 mm and x = 0.275 mm, and

between x = 0.326 mm and x = 0.330 mm in Figure 5.18c each experience similar magnitudes of residual deflection, whilst exhibiting different levels of surface tensile stress, suggesting that the residual change in asperity height is not the only factor to be taken into account.

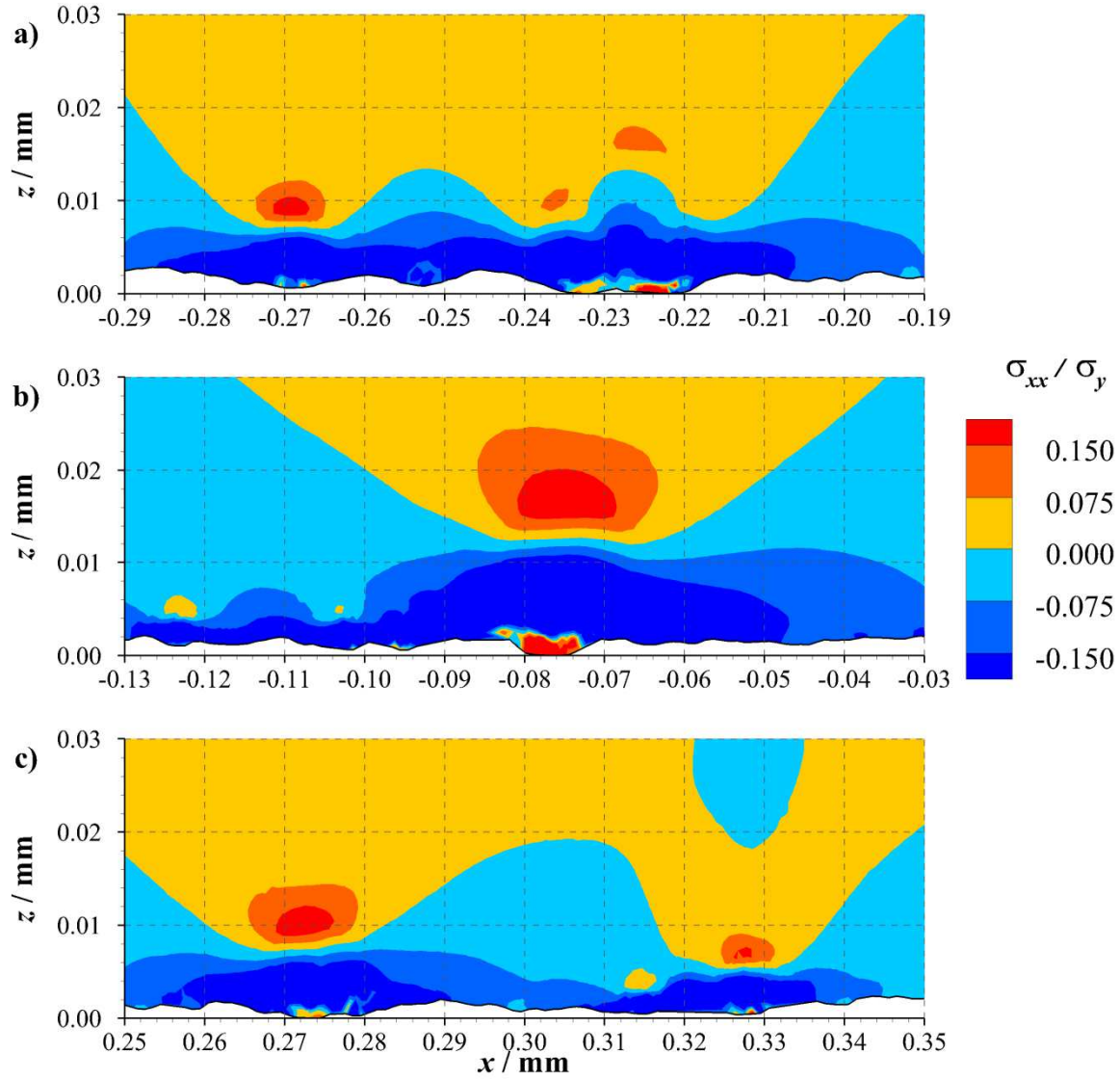

Figure 5.18 - Contours of normalised residual direct stress in the tangential direction; a) Section 1a, b) Section 1b, c) Section 1c. σ_y = 2.550 GPa and E_T / E = 0.05 for each section.

In the subsurface material a band of compressive stress separates these surface tensile stresses from subsurface regions of tension found to occur beneath asperity contacts. As with the surface tensile stress, this appears to be related to the amount of residual deflection occurring for each asperity. This can be seen beneath the heavily loaded asperity feature between x = –0.082 mm and x = –0.070

mm, where the largest region of high magnitude tensile stress in the sections shown can be seen. However, with other asperity features that experience similar residual deflections, differences can be seen in the subsurface tensile stresses as well as those at the surface. It is suggested that this is related to the proximity of other asperity contacts. The more isolated asperity contacts between x = –0.272 mm and x = –0.266 mm in Figure 5.18a and between x = 0.270 mm and x = 0.275 mm in Figure 5.18c result in single "peaks" of subsurface tensile stress. In Figure 5.18a, the two neighbouring asperity features between x = –0.234 mm and x = –0.231 mm and between x = –0.226 mm and x = –0.222 mm cause interaction in the stress contours, resulting in two subsurface "peaks" at approximately x = –0.236 mm and x = –0.216 mm at a depth of z = 0.01 mm, separated by a region of compressive stress. Additionally, the magnitude of residual deflection seems to be reflected in the depth at which the peak residual tensile stress occurs. In Figure 5.18b, the peak surface tensile stress occurs at a depth of approximately z = 0.018mm beneath the heavily loaded asperity feature. In Figure 5.18b and Figure 5.18c it occurs at approximately z = 0.01 mm. The subsurface tensile stresses shown do extend beyond the depth shown in each of the figures, but are typically restricted to the bottom layer of the model previously shown in Figure 5.10. This is a depth of approximately 50 µm. The peak subsurface tensile stresses are found to occur in the material depth plotted.

5.4.2.3. Loaded results

Figure 5.19 shows contours of normalised von Mises stress for the three sections of Surface 1. Figure 5.19a, b and c show the contours for Section 1a, 1b and 1c respectively. Each of the asperity contact regions previously discussed are apparent in the form of high magnitude von Mises stresses, showing plastic material behaviour. From the residual results, it can be seen that the majority of the residual von Mises stresses greater than $0.1\sigma_y$ are in regions with von Mises stress greater than $0.95\sigma_y$ whilst under load. In the residual von Mises stress contours, only contact for which plasticity had occurred were detectable. However, under load, contacts resulting in elastic stress can be seen. Examples of these contacts can be seen in Figure 5.19b between x = –0.048 mm and x = –0.042 mm,

and between x = 0.298 mm and x = 0.300 mm in Figure 5.19c. Interaction can again be seen to occur between the two neighbouring asperity features between x = –0.234 mm and x = –0.231 mm and between x = –0.226 mm and x = –0.222 mm in Figure 5.19a. This interaction results in yielding material at similar depths (z = 0.016mm) to the heavily loaded asperity feature in Figure 5.19b between x = –0.082 mm and x = –0.070 mm.

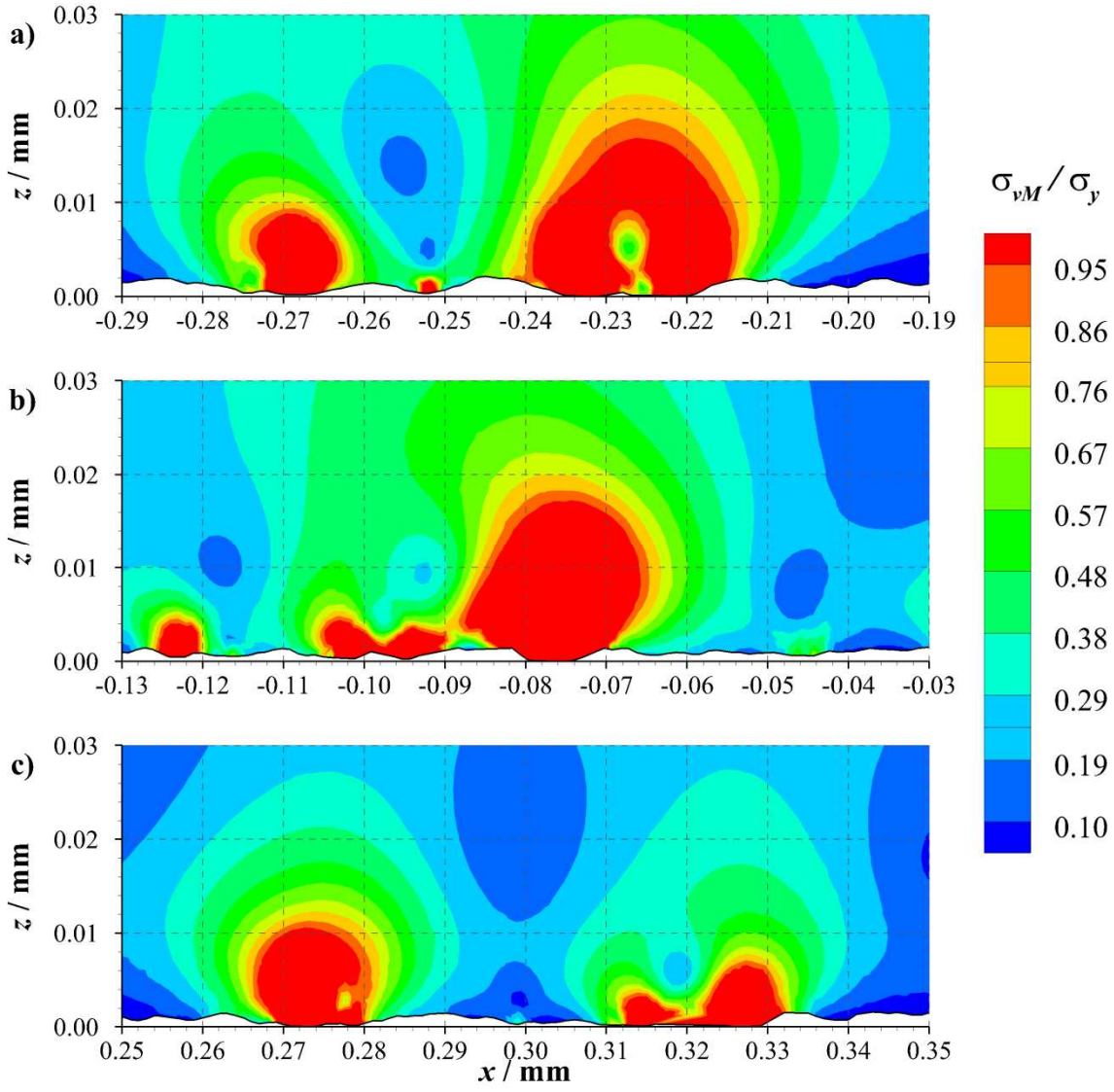

Figure 5.19 - Contours of normalised von Mises stress; a) Section 1a, b) Section 1b, c) Section 1c. σ_y = 2.550 GPa and E_T / E = 0.05 for each section.

Figure 5.20 shows contours of the normalised direct stress in the tangential direction for each of the three sections of Surface 1. Figure 5.20a, b and c show the contours for Section 1a, 1b and 1c

respectively. It can be seen that while the surface is under load, the direct stresses in the tangential direction are predominantly compressive. The largest magnitude compressive stresses can be found to occur at the surface, in the regions in which contact occurs. As previously shown in Figure 5.18, these regions have tensile stresses after loading, and so under repeated loading undergo cyclic variation between compressive and tensile stress, potentially leading to surface crack initiation and propagation.

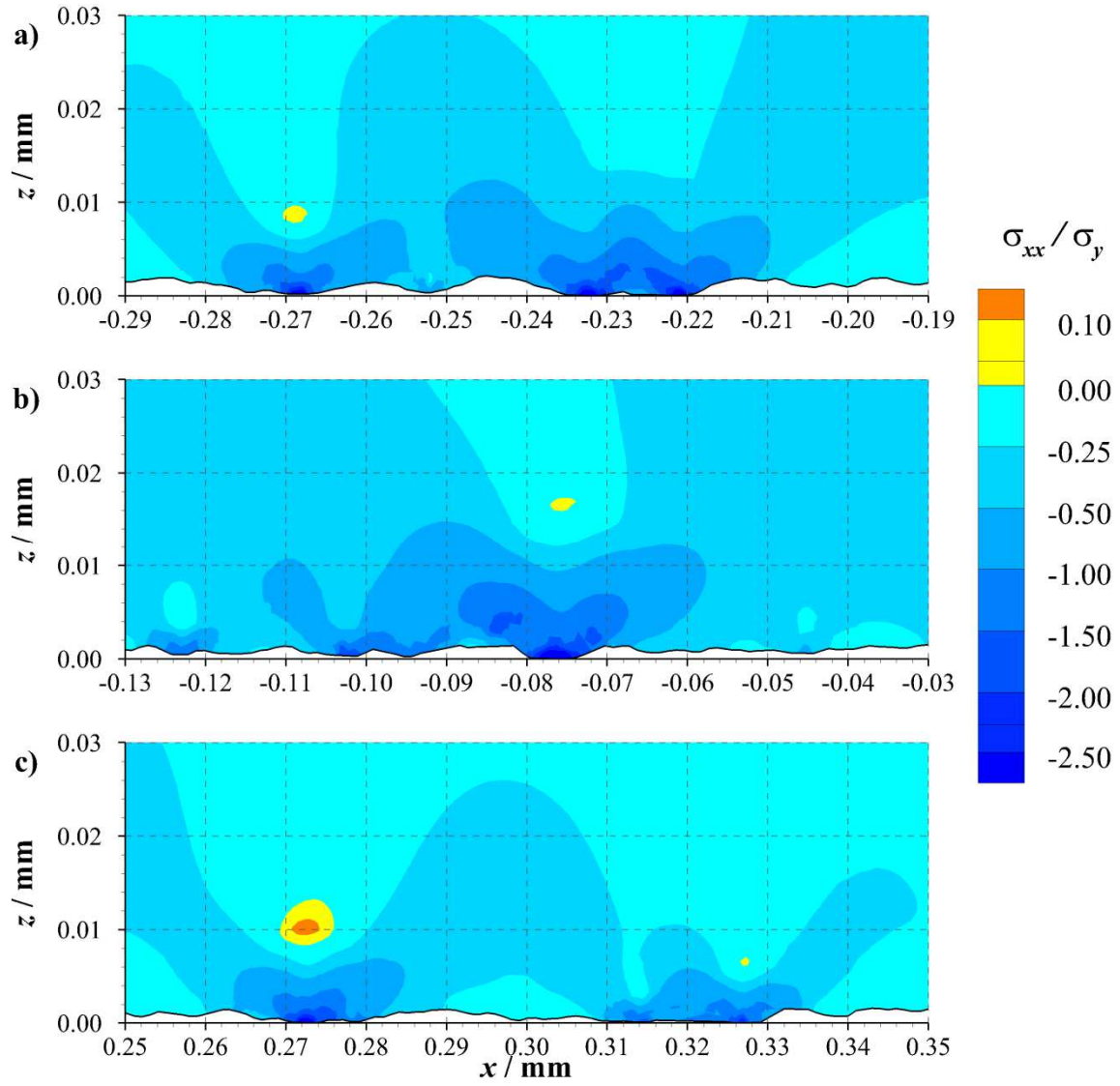

Figure 5.20 - Contours of normalised direct stress in the tangential direction; a) Section 1a, b) Section 1b, c) Section 1c. σ_y = 2.550 GPa and E_T / E = 0.05 for each section.

In the subsurface material, the magnitude of compressive stress reduces in regions away from the direct contact zone. In some locations, small regions of tensile stress can also been found to occur. This can be seen in Figure 5.20a at x = –0.269 mm, z = 0.009 mm, in Figure 5.20b at x = –0.076 mm, z = 0.016 mm and in Figure 5.20c at x = 0.272 mm, z = 0.010 mm. These regions correlate with the regions of highest magnitude residual tensile stress shown in Figure 5.18. The small magnitude compressive stresses (0.00σ_y to -0.25σ_y) in the subsurface material also following similar contours to the regions of residual tensile stress. However, while the highest magnitude of tensile stress under load can be seen in Figure 5.20c at x = 0.272 mm, z = 0.010 mm, the largest residual tensile stress is found in Figure 5.18b at x = –0.005 mm, z = 0.017 mm.

5.4.3. 1.5GPa nominal Hertzian contact pressure model results

5.4.3.1. Residual results

Figure 5.21 shows the residual profiles of the three sections of Surface 2 after loading with Load Case 2. Figure 5.21a, b and c show the residual profiles for Section 2a, 2b and 2c, respectively. Each figure shows the as-measured initial and residual profiles from the ground disk, as well as the residual profile created using the present modelling techniques. The plastic material properties used for the simulation were a yield strength, σ_y, of 2.550 GPa, and strain hardening behaviour of E_T/E = 0.05. These properties were chosen as a result of the range of properties tested in Section 5.4.2.

Good agreement is found between the present model and the measured residual profile across a number of locations, although in some places discrepancies can be found. Overall, the agreement between the finite element analysis and the experimental results is not as consistent as was previously found for Load Case 1 in Section 5.4.2. An example of this can be seen in Figure 5.21a between x = –0.357 mm and x = –0.351 mm where the present model overestimates the deflection of the asperity. However, in Figure 5.21b, the present model underestimates the deflection of the asperity between x = –0.047 mm and x = –0.044 mm. This kind of variation between over- and underestimating the magnitude of asperity deflections occurs throughout the contact region. This

deviation is evident in the difficulty in consistently aligning local valley features. For example, in Figure 5.21a, good agreement is seen between all profiles in the unloaded section of roughness between x = –0.306 mm and x = –0.280 mm. However, from approximately x = –0.280 mm to x = –0.260 mm, the present model profile can be seen to be beneath both measured profiles, and in some instances, the measured residual profile is above the initial measured profile.

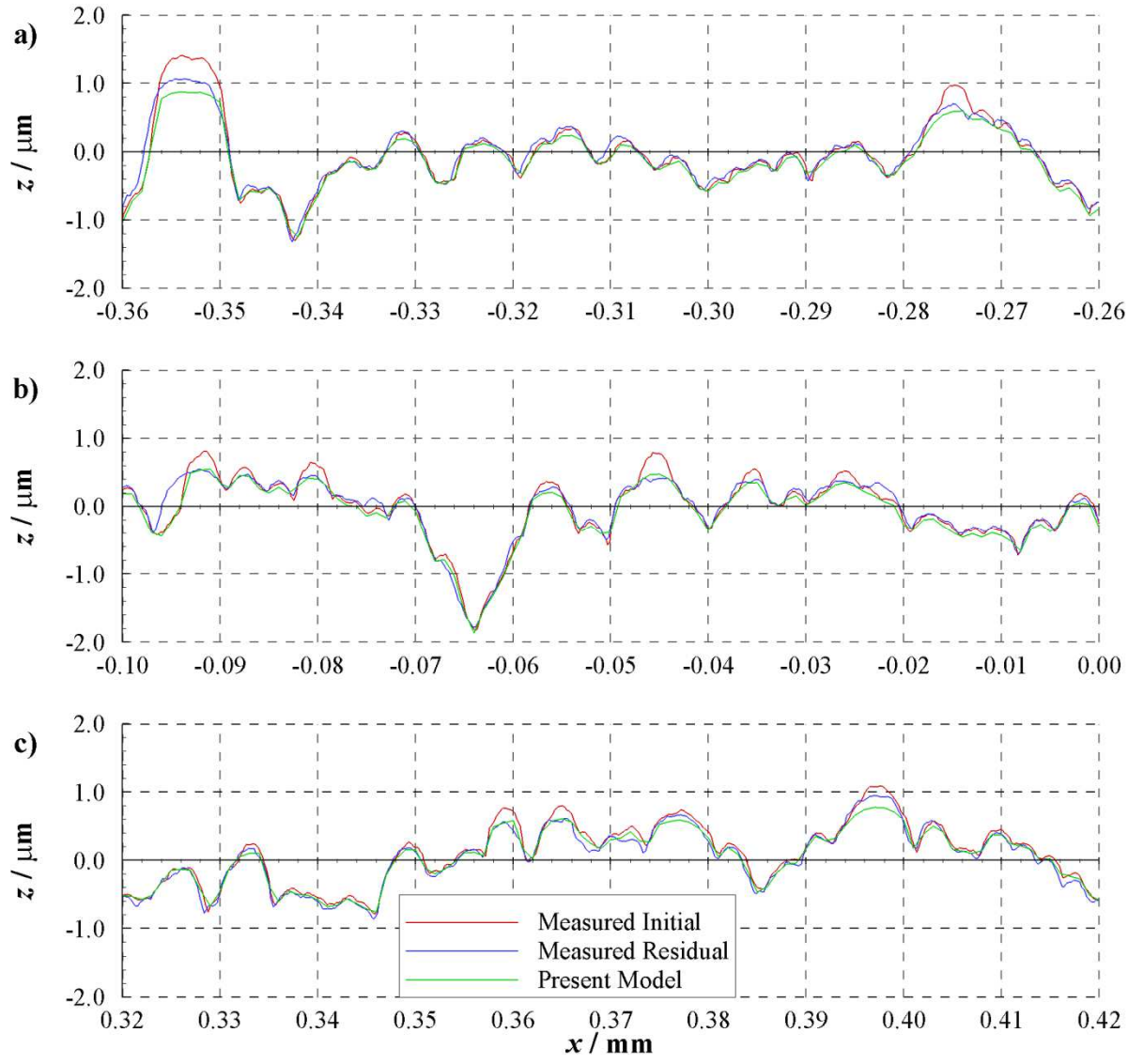

Figure 5.21 - Residual profiles for sections of the rough roller; a) Section 2a, b) Section 2b, c) Section 2c. Also shown are the initial and residual measured profiles. σ_y = 2.550 GPa and E_T / E = 0.05 for each section.

This is not an isolated incident, and a larger discrepancy between measured profiles can be seen between x = –0.097 mm and x = –0.094 mm in Figure 5.21b. It is thought that these issues may originate in the way the raw roughness profiles are treated using a Gaussian filter. For a higher load, there is a greater change in the measured roughness profile and so there will be a bigger change between the mean surface heights produced by the filter for the two profiles. Another potential cause for difference is in the contact counter face. In the experiments, the case-carburised, ground disks were opposed by a nitrided, superfinished disk. In the finite element analysis, this disk was idealised as a perfectly smooth, elastic surface. Although relatively small in comparison to the ground disk, the superfinished disk will still have rough features. The stress in the disk may also be sufficient to cause material yield. Using hardness tests as in Table 5.5, the yield strength of the nitrided disk was found to be approximately 2.86 GPa. While plasticity at lower loads is restricted to asperity features, at higher loads, plasticity in the counter surface may be significant, and be a factor in the discrepancies between the analysis and experimental results.

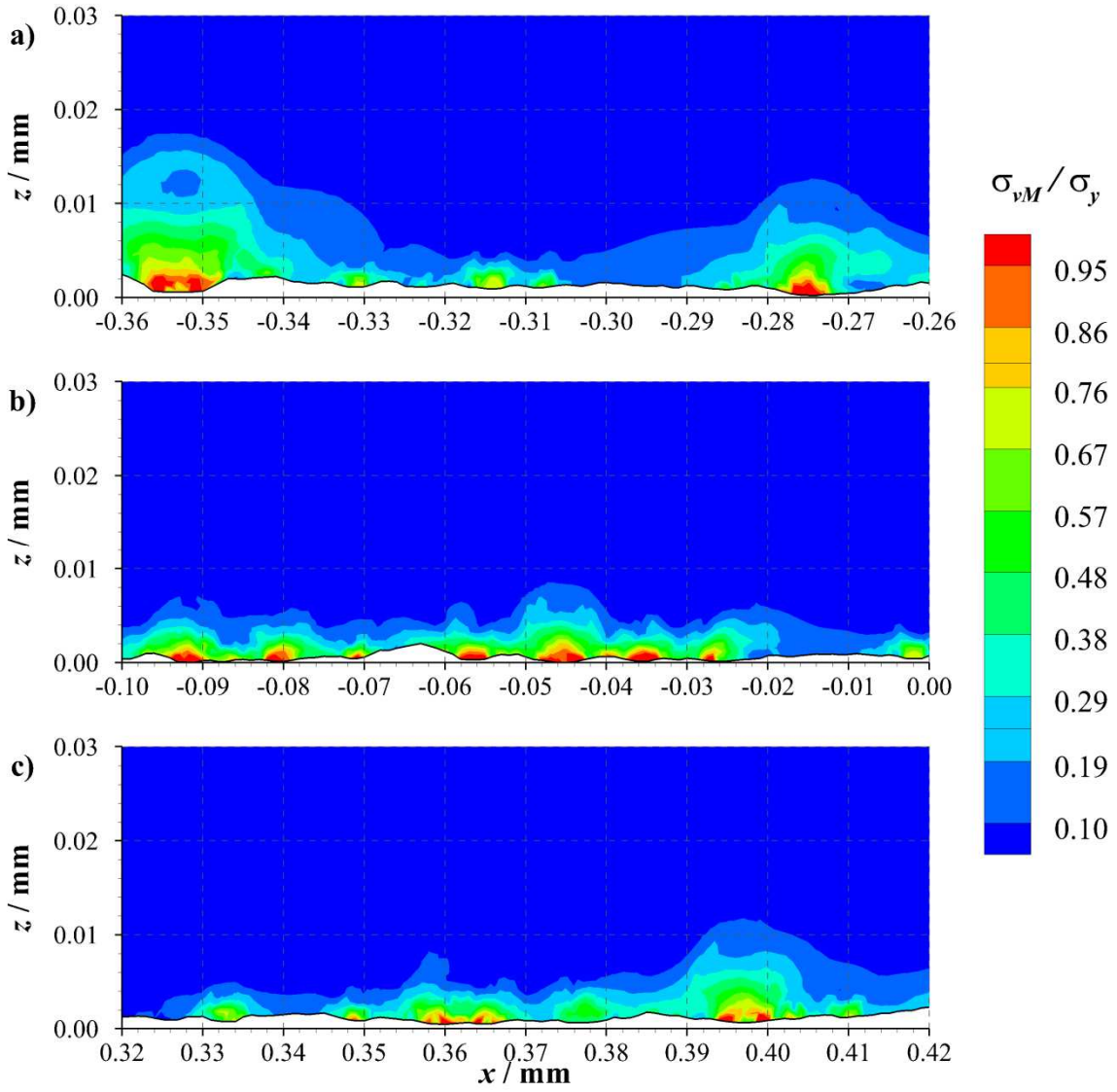

Figure 5.22 - Contours of normalised residual von Mises stress; a) Section 2a, b) Section 2b, c) Section 2c. σ_y = 2.550 GPa and E_T / E = 0.05 for each section.

Figure 5.22 shows contours of residual normalised von Mises stress for each of the three sections of Surface 2. Figure 5.22a, b and c show the contours for Section 2a, 2b and 2c, respectively. As previously shown in Figure 5.17, the majority of the high magnitude residual von Mises stress occurs in close proximity to the surface, with the highest magnitudes occurring as a result of heavily loaded contacts, and large plastic deflections. In comparison to the results from Load Case 1, asperity contacts are more frequent and have less space between them, as a result of the increased load. Therefore, more interaction between contacts occurs. This is evident in Figure 5.22a and Figure

5.22b, where no surface material shows a level of von Mises stress less than $0.1\sigma_y$, with only a small section between x = 0.320 mm and x = 0.325 mm in Figure 5.22c showing such low levels of von Mises stress. The depth in which von Mises stress less than $0.1\sigma_y$ occurs is similar to that found in Load Case 1, limited to approximately z = 0.02 mm beneath the surface. Micropits are typically found to have characteristics depths of around 10 µm (Oila and Bull 2005; Cardoso *et al*. 2009), which is the depth to which higher magnitude stresses (>$0.48\sigma_y$) are found to occur.

Figure 5.23 shows contours of residual normalised direct stress in the tangential direction for each of the three sections of Surface 2. Figure 5.23a, b and c show the contours for Section 2, 2b and 2c, respectively. The contours follow a similar pattern to those seen in Figure 5.18 for Load Case 1. Regions of tensile stress are found to occur at the surface in locations where the surface has been loaded and has experienced residual deflection. A band of compressive stress separates these regions of tensile stress at the surface from regions of tensile stress in the subsurface material. Despite the increase in nominal Hertzian contact pressure, the magnitude of the stresses remains similar to that previously found in Figure 5.18. At the surface, the regions of tensile stress extend no more than approximately 2.0 µm into the material, while the subsurface peak tensile stresses occur at depths between z = 0.010 mm and z = 0.020 mm.

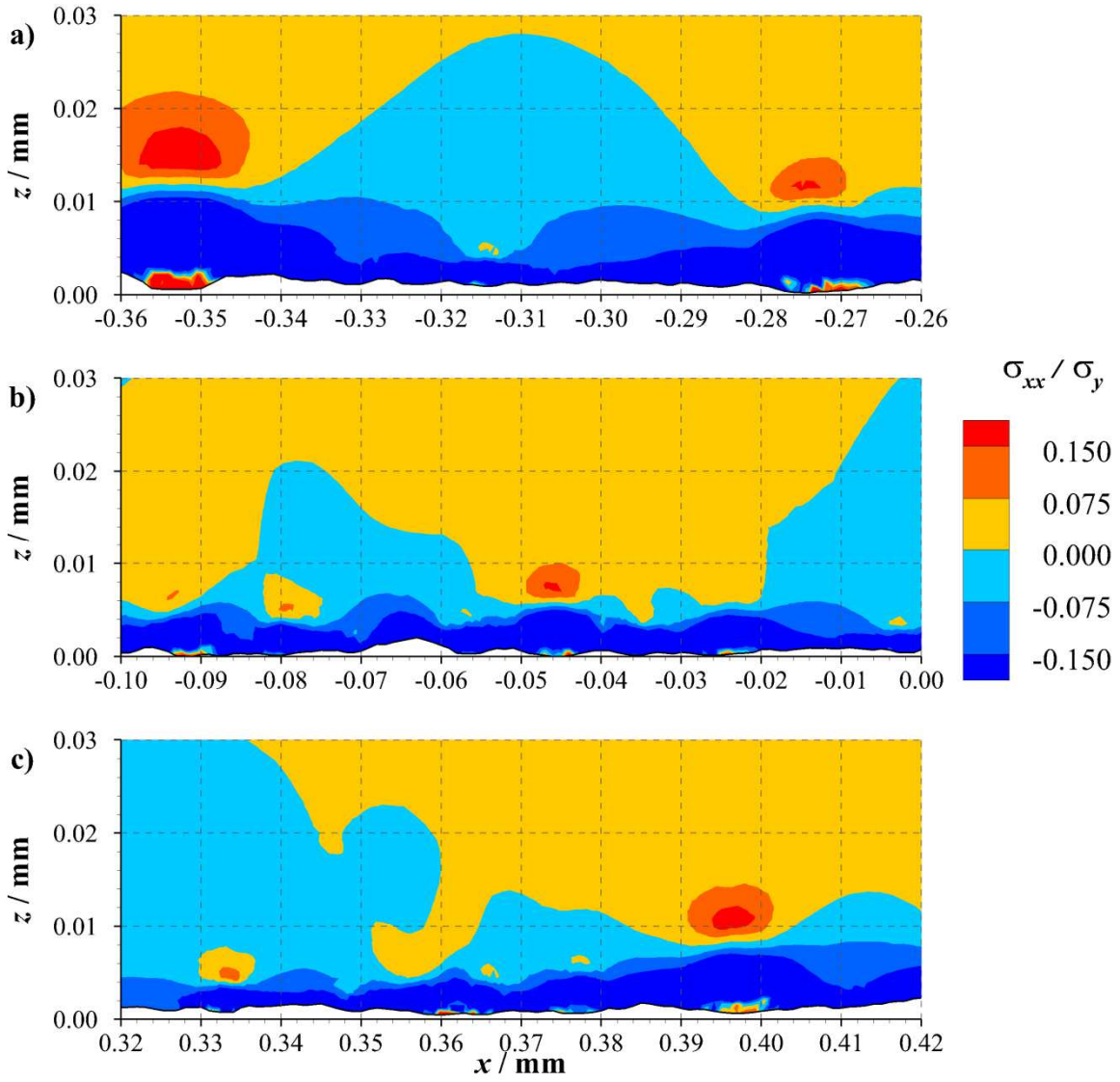

Figure 5.23 - Contours of normalised residual direct stress in the tangential direction; a) Section 2a, b) Section 2b, c) Section 2c. σ_y = 2.550 GPa and E_T / E = 0.05 for each section.

5.4.3.2. Loaded results

Figure 5.24 shows contours of normalised von Mises stress for each of the three sections of Surface 2. Figure 5.24a, b and c show the contours for Section 2a, 2b and 2c, respectively. In comparison to the results obtained for Load Case 1, a larger proportion of the rough surface is in contact, resulting in material yield. The maximum depth in which plastic behaviour occurs is approximately z = 0.014mm at x = –0.352 mm in Figure 5.24a. Only very heavily loaded asperity features showed plasticity beyond this depth in Figure 5.19. As before, in comparison to the residual results for Load

Case 2, it can be seen that residual von Mises stresses of $0.1\sigma_y$ are found in regions where yielding has occurred, with the von Mises stress exceeding $0.95\sigma_y$ in Figure 5.24.

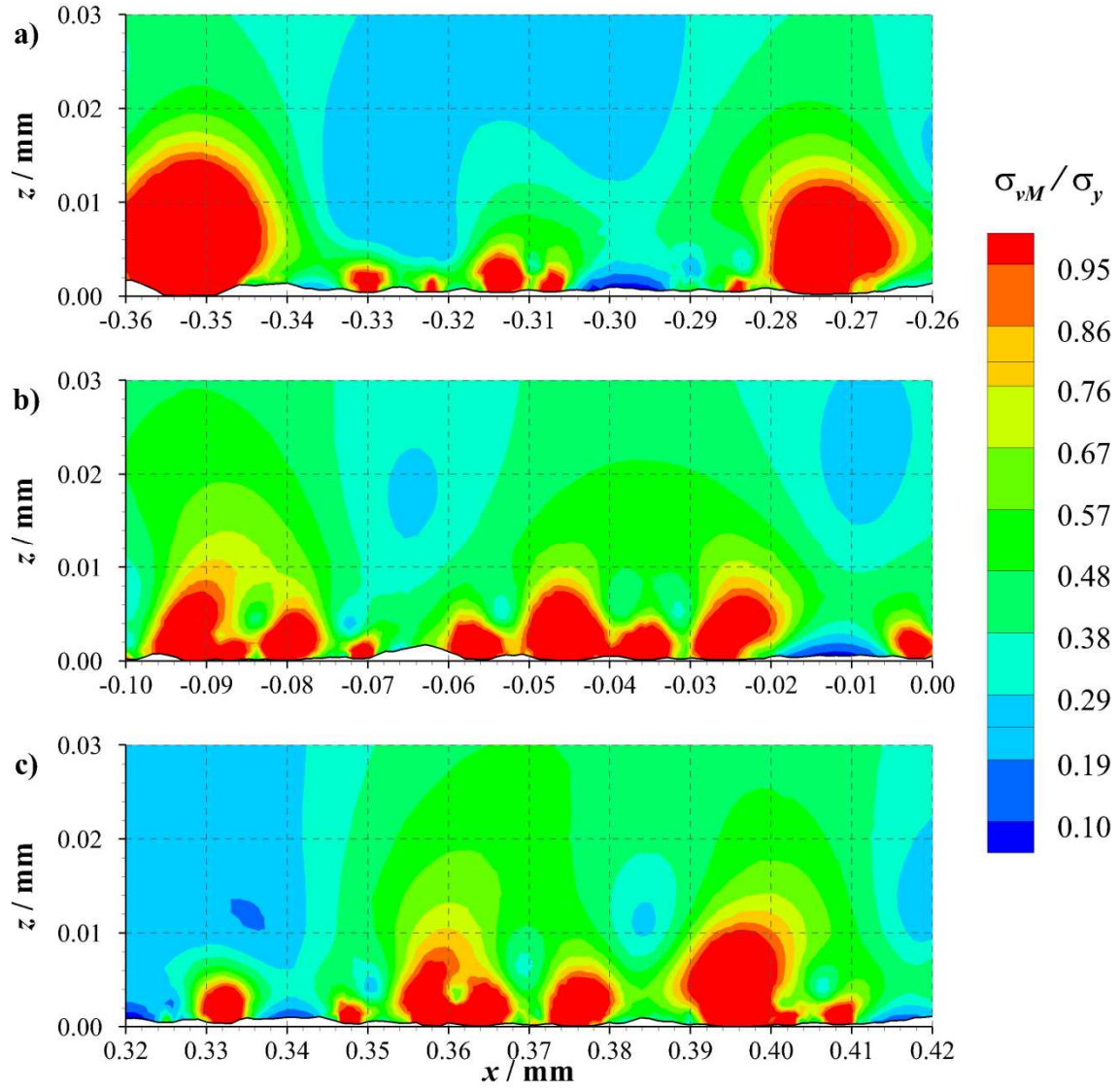

Figure 5.24 - Contours of normalised von Mises stress; a) Section 2a, b) Section 2b, c) Section 2c. σ_y = 2.550 GPa and E_T / E = 0.05 for each section.

Figure 5.25 shows contours of normalised direct stress in the tangential direction for each of the three sections of Surface 2. Figure 5.25a, b and c show the contours for Section 2a, 2b and 2c, respectively. As previously shown for Load Case 1, the majority of the direct stress in the tangential direction is compressive whilst under load. The highest magnitude compressive stresses are found to occur at the surface of contacting asperity features. While previously in Figure 5.20, some regions of

tensile stress were found to occur in the subsurface material directly above these contacting asperities, in the sections shown in Figure 5.25, this does not occur. However, these regions show the smallest magnitude compressive stresses found to occur. This is a common trend as a result of the increase in load from Load Case 1 to Load Case 2. Stresses are typically found to be more compressive. This is particularly true for the section shown in Figure 5.25b, where the majority of the stress is between $-0.50\sigma_y$ and $-1.00\sigma_y$. At a nominal Hertzian contact pressure of 1.0 GPa, the majority of the stress was in the two contour bands between $0.00\sigma_y$ and $-0.50\sigma_y$.

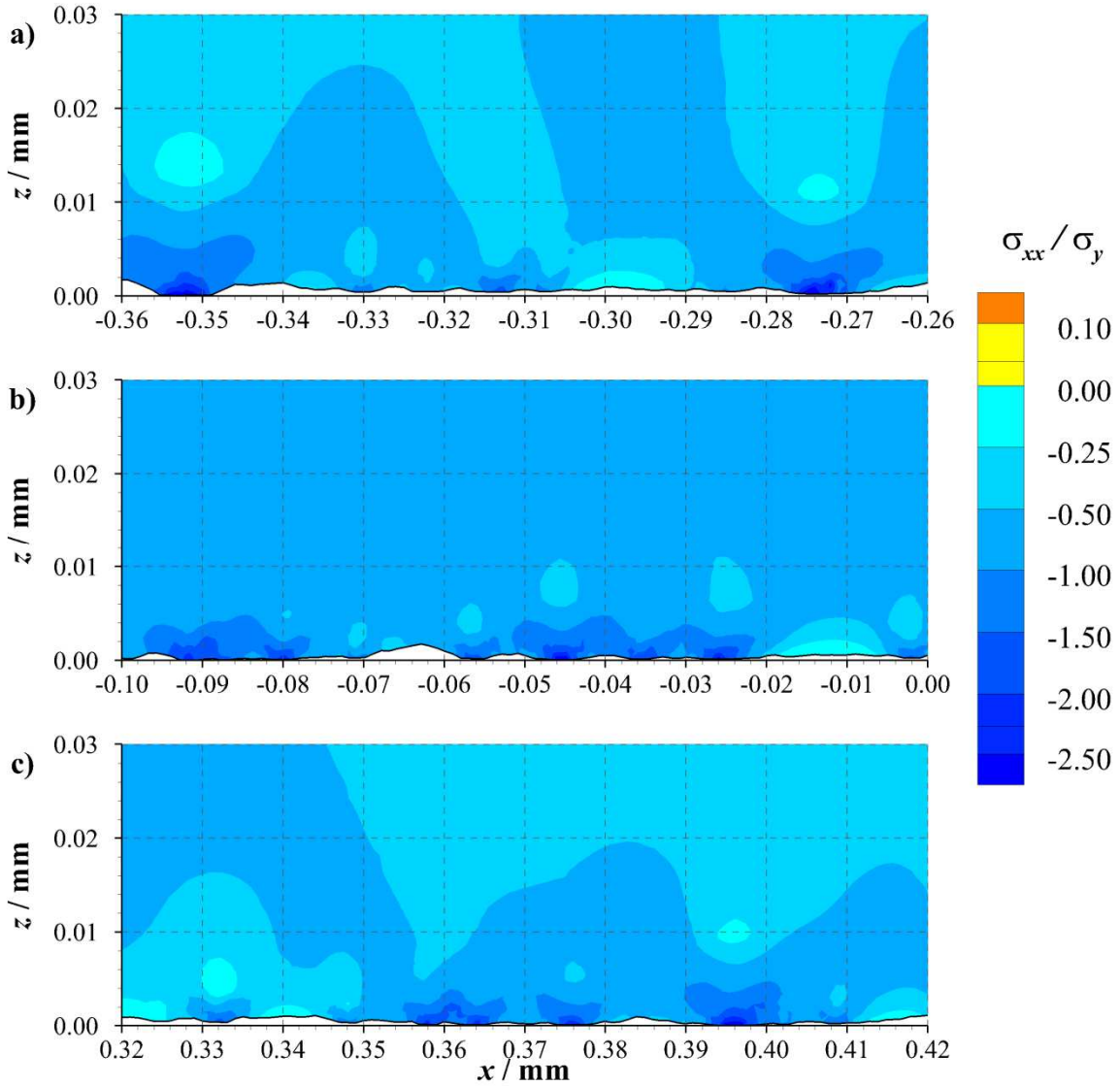

Figure 5.25 - Contours of normalised direct stress in the tangential direction; a) Section 2a, b) Section 2b, c) Section 2c. σ_y = 2.550 GPa and E_T / E = 0.05 for each section.

5.4.4. 2.0GPa nominal Hertzian contact pressure model results

5.4.4.1. Residual results

Figure 5.26 shows the residual profiles of the three sections of Surface 3 after loading with Load Case 3. Figure 5.26a, b and c show the residual profiles for Section 3a, 3b and 3c, respectively. Each figure shows the as-measured initial and residual profiles from the ground disk, as well as the residual profile created using the present modelling techniques. As with Load Case 2, the plastic material properties used for the simulation were a yield strength, σ_y, of 2.550 GPa, and strain hardening behaviour of E_T/E = 0.05. These properties were chosen as a result of the range of properties tested in Section 5.4.2.

As with Load Case 2, good agreement between the experimental residual profile and the residual profile from the present model can be seen, although some differences are present in some locations. As before, the present model can be seen to both underestimate and overestimate the residual deflections in neighbouring locations of the surface after loading. Examples of underestimating the deflection can be seen in Figure 5.26a from x = –0.232 mm to x = –0.226 mm and x = –0.209 mm to x = –0.204 mm, and in Figure 5.26c from x = 0.511 mm to x = 0.514 mm. Overestimating can be seen to occur in Figure 5.26a from x = –0.191 mm to x = –0.189 mm, and x = –0.181 mm to x = –0.178 mm, and in Figure 5.26c from x = 0.444 mm to x = 0.447 mm, and x = 0.462 mm to x = 0.466 mm. More consistent agreement can be found in Figure 5.26b, although still not to the extent as found with Load Case 1. Figure 5.26b also shows instances of apparent positive deflection in the measured residual profile. This can be seen from x = –0.039 mm to x = –0.036 mm, and x = –0.016 mm to x = –0.010 mm where the measured residual profile can be seen above the measured initial profile. As previously discussed, it is thought that the Gaussian filter may be a factor in these differences, although debris or vibrational interference with the measuring equipment may also contribute, as well as the idealisation of the contact counter surface. When repeated were

measurements were made of the same surface profile, the results were found to be near identical, further suggesting that the filtering process may be the source of the discrepancies.

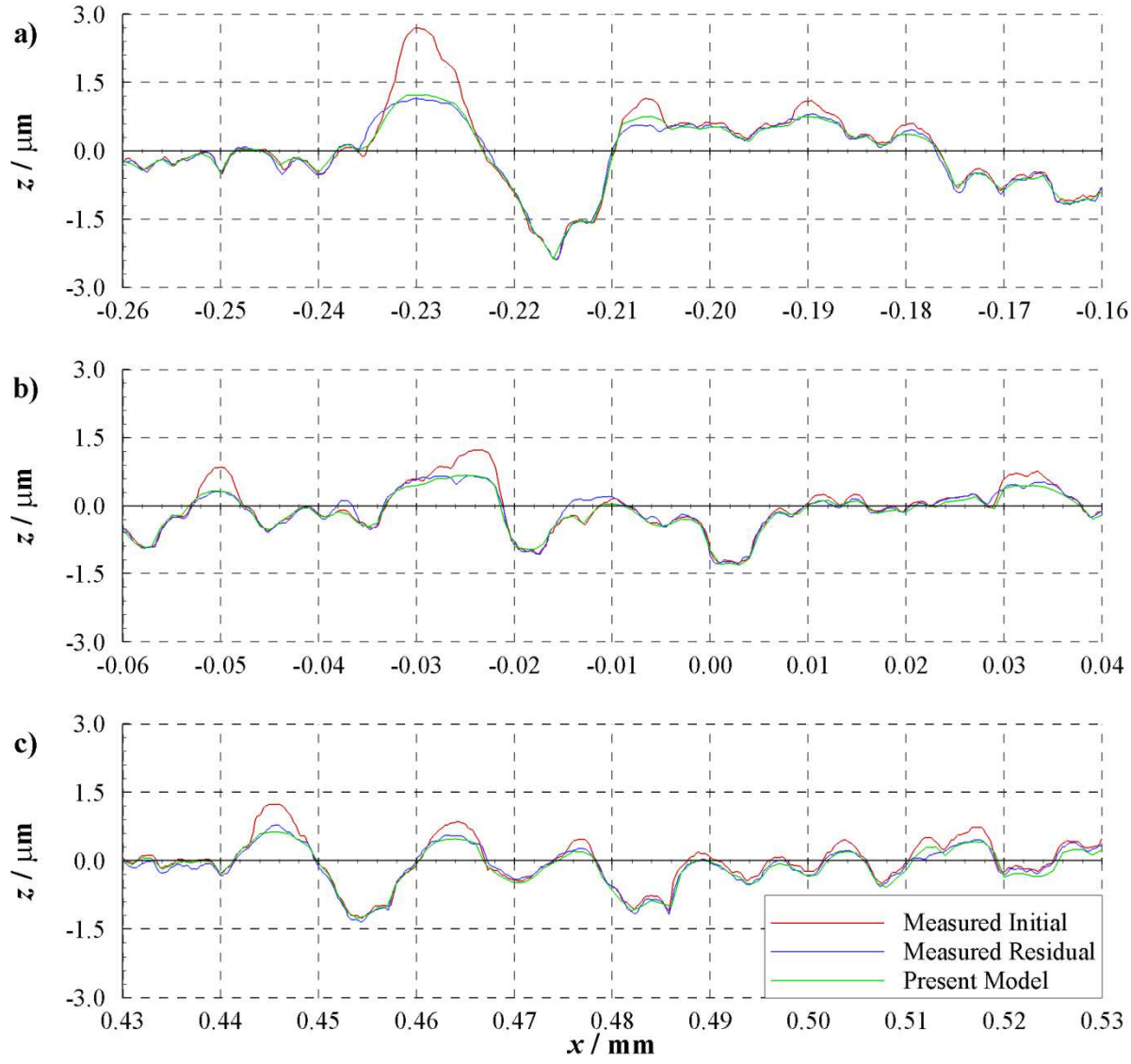

Figure 5.26 - Residual profiles for sections of the rough roller; a) Section 3a, b) Section 3b, c) Section 3c. Also shown are the initial and residual measured profiles. σ_y = 2.550 GPa and E_T / E = 0.05 for each section.

Figure 5.27 shows contours of residual normalised von Mises stress for each of the three sections of Surface 3. Figure 5.27a, b and c show the contours for Section 3a, 3b and 3c, respectively. The stress contours follow similar trends to those already seen for Load Case 1 and 2. The highest magnitude von Mises stresses are found to occur in regions at the surface where heavily loaded asperity contacts have occurred. With the increased load, a larger proportion of the asperity features experienced contact, and as a result more interaction between stress fields has occurred. In Load Case 1, some regions of the surface have von Mises stress of less than $0.1\sigma_y$. In Load Case 2, the surface has von Mises stresses greater than $0.1\sigma_y$ throughout. In Figure 5.27, the von Mises stress at the surface increases further still, with the von Mises stress exceeding $0.19\sigma_y$ across each of the sections of roughness shown. The depth to which the residual von Mises stress is greater than $0.1\sigma_y$ is similar to that found to occur in previous load cases. In both Figure 5.27b and Figure 5.27b, all the von Mises stress zone exceeding $0.1\sigma_y$ is limited to a depth of approximately z = 0.02mm. This depth is exceeded only between x = –0.245 mm and x = –0.215 mm in Figure 5.27a. This feature, shown in Figure 5.26a between x = –0.235 mm and x = –0.223 mm, shows the largest residual deflection of any feature shown from any of the specified load cases, at approximately 1.5 µm, so it is not unexpected for this extreme to be found.

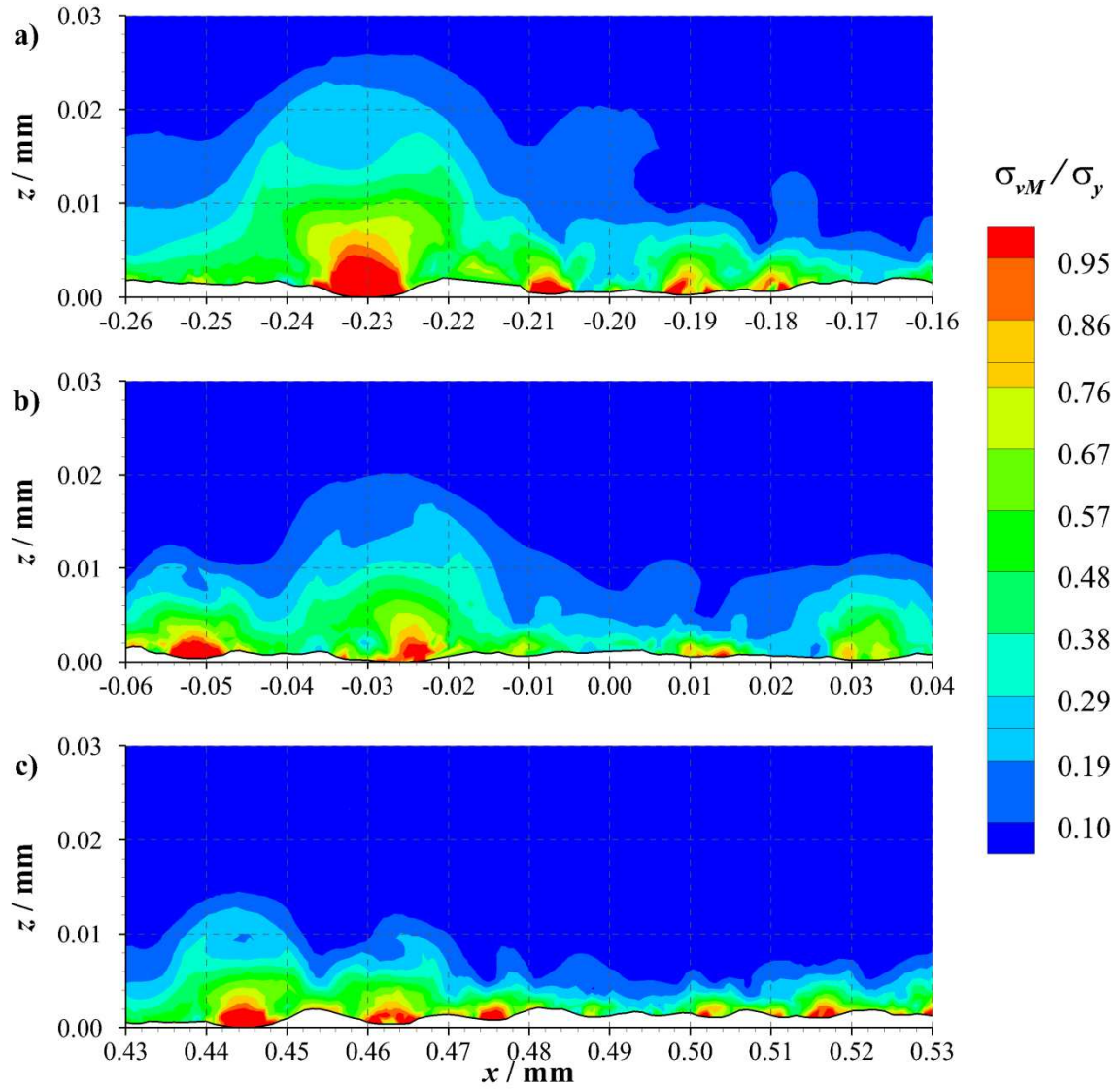

Figure 5.27 - Contours of normalised residual von Mises stress; a) Section 3a, b) Section 3b, c) Section 3c. σ_y = 2.550 GPa and E_T / E = 0.05 for each section.

Figure 5.28 shows contours of residual normalised direct stress in the tangential direction for each of the three sections of Surface 3. Figure 5.28a, b and c show the contours for Section 3a, 3b and 3c, respectively. As before, the stress contours follow similar patterns to those previously seen in Load Cases 1 and 2. Regions of tensile stress at the surface where asperity contacts have occurred are separated from subsurface regions of tension by a band of compressive stress. The peak magnitudes of these subsurface tensile stresses occur directly above where asperity contacts occur, with more heavily loaded contacts resulting in larger regions of tensile stress of higher magnitudes. As a result of the increase in load, several differences are noticeable in the subsurface stresses found in the sections of roughness shown. For previous loads, the band of compressive stresses of the order $-0.075\sigma_y$ and above are typically restricted to depths of approximately z = 0.012 mm. While this is true for Figure 5.28c, the highly compressive band in Figure 5.28b and Figure 5.28a extends to z = 0.014 mm and z = 0.016 mm, respectively. These peak stresses within the subsurface tensile regions can also be found deeper in the material as a result of the heavy loading. While previously the peak subsurface tensile stresses have been found to occur between z = 0.01 mm and z = 0.02 mm, Figure 5.28 shows the peak tensile stress occurring at a depth of approximately z = 0.024 mm. However, despite the increase in load, the magnitude of the stress remains similar across each of the load cases tested.

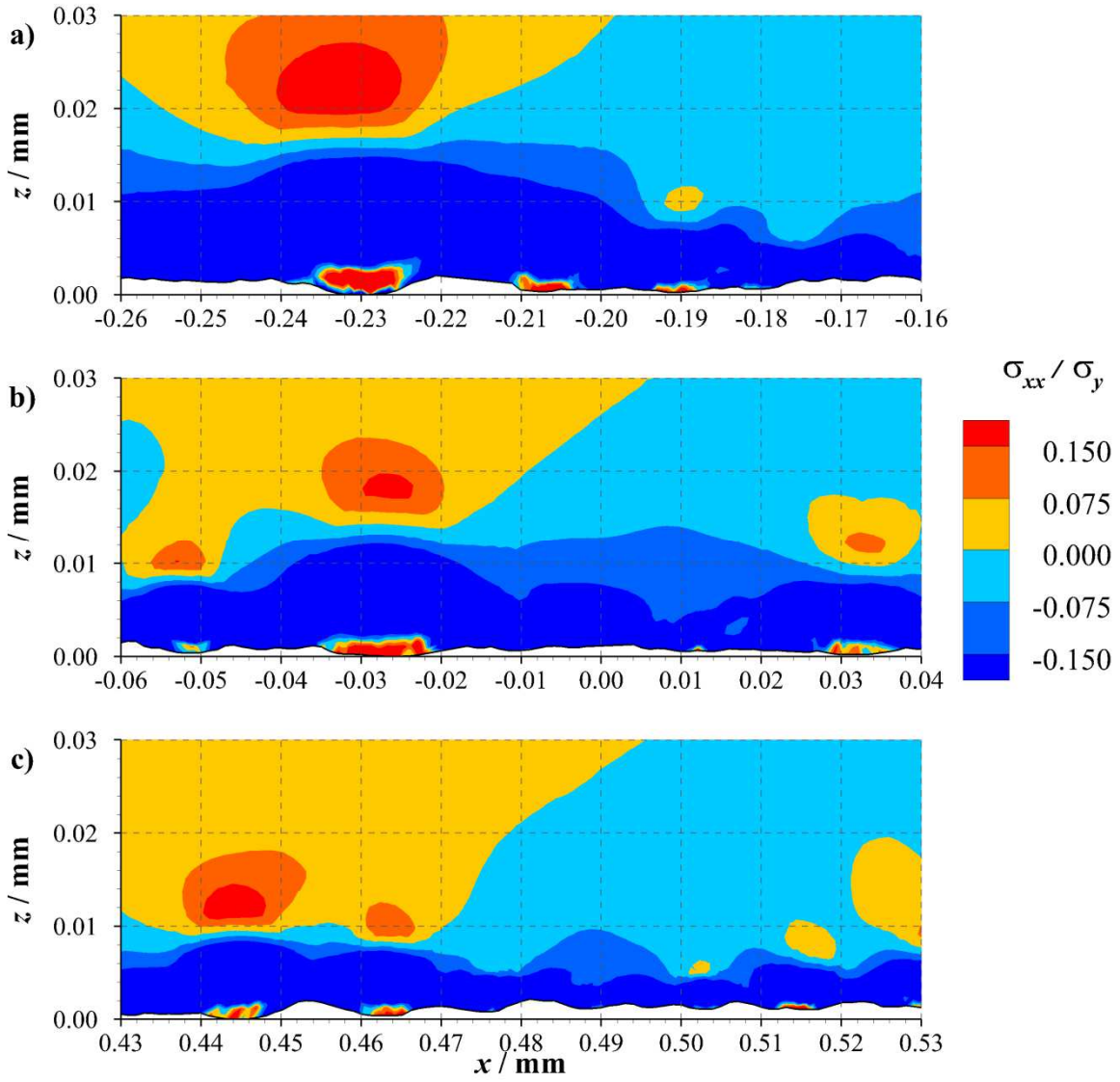

Figure 5.28 - Contours of normalised residual direct stress in the tangential direction; a) Section 3a, b) Section 3b, c) Section 3c. σ_y = 2.550 GPa and E_T / E = 0.05 for each section.

5.4.4.2. Loaded results

Figure 5.29 shows contours of normalised von Mises stress for each of the three sections of Surface 3. Figure 5.29a, b and c show the contours for Section 3a, 3b and 3c, respectively. Patterns observed in Load Cases 1 and 2 can again be found to occur. With the increase in pressure, a larger proportion of the asperity features are in contact, with the more prominent asperities carrying a greater load. This can be seen in Figure 5.29, where a larger proportion of the section width experiences von Mises stress greater than $0.95\sigma_y$, and to a greater depth. In previous load cases, the extent of the plastically deforming materials is limited to approximately z = 0.016 mm. However, in Figure 5.29a,

plastic material can be seen a depth of z = 0.024 mm at x = –0.230 mm. As has previously been discussed, these regions of yielding material correlate with the regions of residual von Mises greater than $0.1\sigma_y$ in Figure 5.27. Outside of these plastically deforming regions, it can be seen that the bulk subsurface material exhibits a higher magnitude of von Mises stress than lighter load cases. For Load Cases 1 and 2, a significant proportion of material had von Mises below $0.38\sigma_y$. The only major region of stress less than $0.38\sigma_y$ in each of the sections shown in Figure 5.29 can be seen in Figure 5.29c between x = 0.472 mm and x = 0.496 mm at depths greater than z = 0.005 mm.

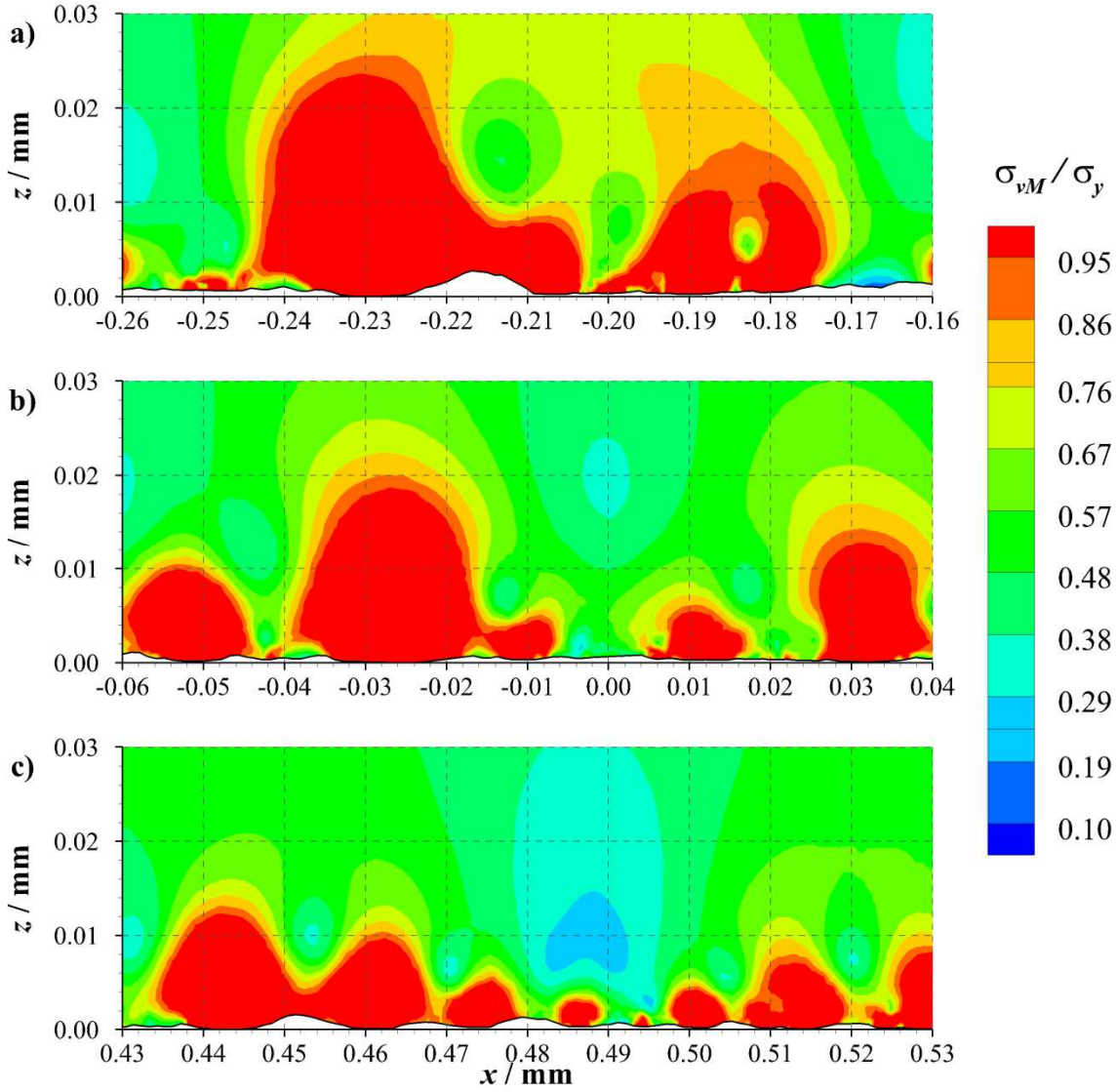

Figure 5.29 - Contours of normalised von Mises stress; a) Section 3a, b) Section 3b, c) Section 3c. σ_y = 2.550 GPa and E_T / E = 0.05 for each section.

Figure 5.30 shows contours of normalised direct stress in the tangential direction for each of the three sections of Surface 3. Figure 5.30a, b and c show the contours for Section 3a, 3b and 3c, respectively. As previously shown for lighter load cases, the stresses are predominantly compressive, with the highest magnitude compressive stresses located at the surface of loaded asperity contacts. Increasing the load from Load Case 1 to Load Case 2 resulted in small regions of tension no longer occurring, and this trend continues in that the stresses generally become more compressive. The bulk of the subsurface material has a compressive stress between $0.5\sigma_y$ and $1.0\sigma_y$. Above each asperity contact, regions of compressive stress between $0.25\sigma_y$ and $0.50\sigma_y$ can be found as the tensile regions previously found have been replaced by the lower compressive stresses. At the surface, the regions of high magnitude compressive stress, greater than $2.00\sigma_y$, extend to greater depths than previously found. An example of this behaviour can be seen at x = –0.214 mm where this magnitude of stress extends to a depth of z = 0.017 mm, whereas for lighter loads this level of stress did not typically extend beyond z = 0.010 mm.

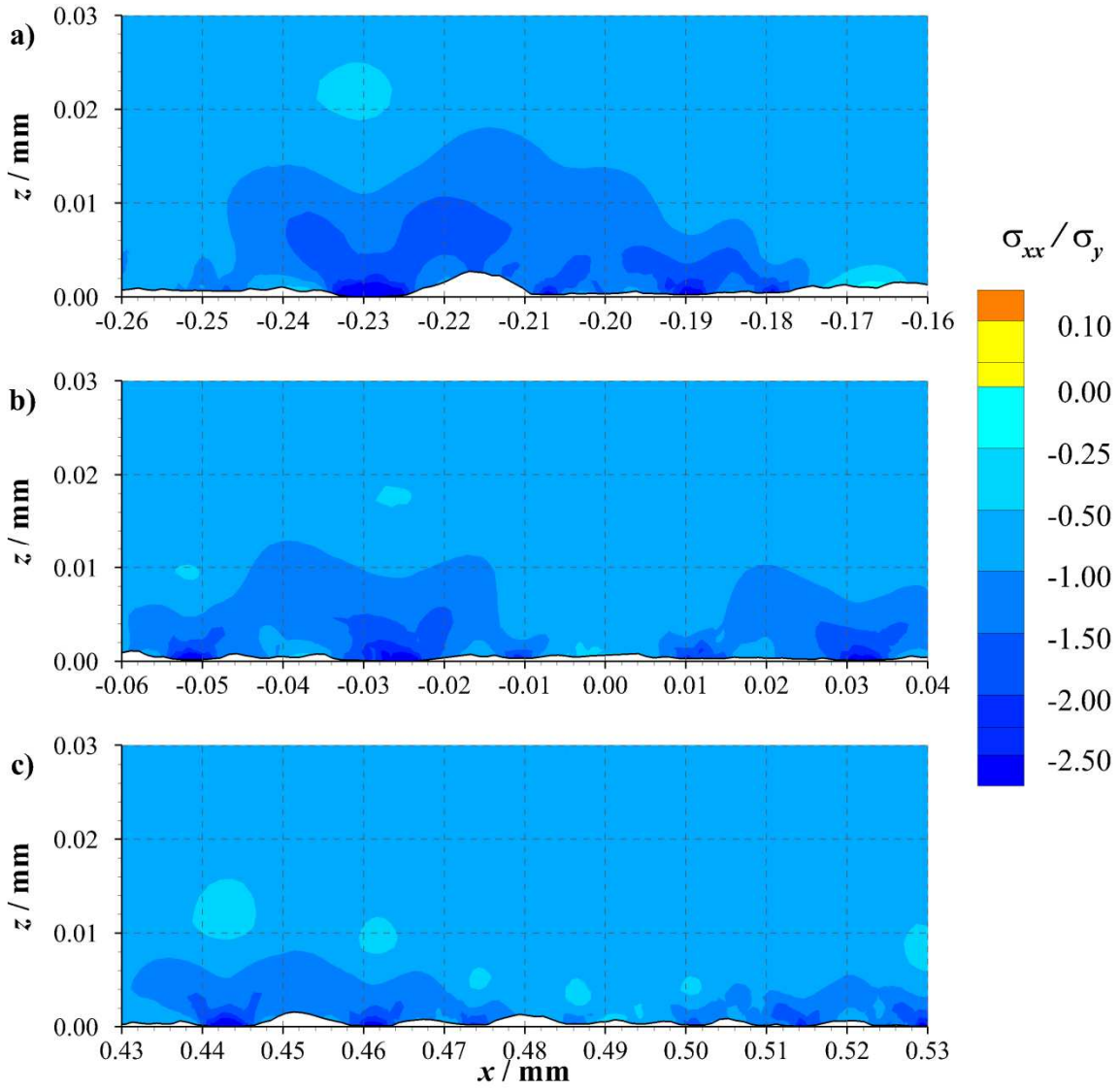

Figure 5.30 - Contours of normalised direct stress in the tangential direction; a) Section 3a, b) Section 3b, c) Section 3c. σ_y = 2.550 GPa and E_T / E = 0.05 for each section.

5.5. Conclusions

This chapter has detailed the experimental procedure used to acquire the initial and residual surface profiles from a ground disk subject to three different loads in contact with a nitrided superfinished disk. This twin disk test rig arrangement was used to approximate the contact of two gear teeth. These profiles were then used to create rough surfaced roller parts using Abaqus and loaded against a smooth elastic counter face before the load was subsequently removed. These models were created using the techniques tested in Chapter 3 and used for multiple load applications and

tangential loading simulations in Chapter 4. Residual profiles from the models were then generated and compared with the results achieved by experiment. In general, good agreement was found between the current modelling techniques and the results obtained from experiment. Load Case 1 was used to simulate a range of material properties, testing both the yield strength and linear strain hardening behaviour. As a result of this investigation, the most suitable material properties were selected and carried forward for heavier load cases. It was in these heavier loading models that some discrepancies were found to occur. For Load Case 2 and Load Case 3, the simulations were found to both slightly underestimate and overestimate the residual deflection of neighbouring asperity contacts. Additionally, some instances of the measured residual profile being above the measured residual profile suggested a positive deflection. This is thought to be a result of the processing of the profiles using a Gaussian filter or factors such as debris or vibrational interference in the experimental procedure, and time constraints have meant that no work in this area has been performed. A further cause for discrepancies may be as a result of the idealised approximation of the nitrided, superfinished contact counter face. While the counter face is a smoother, harder body, some roughness features will exist. These may result in an alternative distribution of the loading across the surfaces that may result in an altered pattern of stresses and deformations. Furthermore, while the yield strength of the counter face may be higher, the loading may result in plasticity that the current assumptions associated with the model do not account for.

Under load, the von Mises stress contours showed that yield occurred as a result of heavily loaded asperity contacts. The regions of plastic behaviour grew in size and depth as the nominal Hertzian contact pressure was increased, with further interaction between asperities. The von Mises stress outside of the plastic regions was found to be of higher magnitude in the larger nominal Hertzian contact pressure models. Upon removal of the load, the regions where plasticity occurred were found to result in elevated residual von Mises stress.

As previously discussed in Chapter 4, the contours of direct stress in the tangential direction showed residual tensile stresses occurring both at the surface and subsurface. These tensile regions of stress were aligned with heavily loaded asperity contacts, with larger magnitude stresses occurring as a result of larger plastic deformations. Peak subsurface tensile stresses were found to occur between approximately 10 μm to 20 μm beneath the surface. Whilst under load, the overwhelming majority of the material is under a compressive state of stress. When a surface is subject to repeated load applications, this cyclic loading between compressive and tensile stress may potentially lead to the initiation and propagation of fatigue cracks at the surface, and could be a significant factor in initiating micropitting failures.

Further analysis of real rough surface contacts and asperity level contact modelling

6.1. Introduction

This chapter details the study of individual asperity contacts within the entire contact region of the experimental disk contacts discussed in Chapter 5. This analysis consists of three sections. The first section analyses and discusses in detail the residual stress found as result of the contacts modelled previously in Chapter 5. In Chapter 1, a review of the literature revealed experimental studies of surface crack initiation, propagation and micropitting failures. This section of the chapter attempts to determine trends in the residual stresses that may explain the findings in these studies.

The second section of the chapter is a parametric analysis of the rough surfaces previously studied in Chapter 5. The aim of this analysis is to provide a tool that can approximately predict the residual stresses at the surface of an asperity subject to a measured residual deflection. Each of the circumferential positions, referred to as Surfaces 1, 2 and 3, were loaded at nominal Hertzian contact pressures of 0.5 GPa, 1.0 GPa, 1.5 GPa, and 2.0 GPa, and the loaded rough surface profiles and stress field outputs extracted. Subsequently, the loads were removed and the residual surface profiles and stress field outputs extracted. Relationships between changes in asperity geometry, applied loading and surface stresses were explored. The geometric parameters considered were derived from the initial, loaded, and residual rough surface profiles. These included the maximum asperity deflection normal to the surface and the residual land width. Combinations of these parameters were investigated, looking for relationships between them and the residual stresses found at the surface. The stress components considered were the von Mises stress, the maximum principal stress and the direct stress in the tangential direction.

The final part of the chapter examines 0.1 mm sections of the rough surfaces and compares the results to those found from the whole contact analysis from Chapter 5. Each section of roughness was loaded with the equivalent distributed load to that applied in the complete contact model. This aimed to evaluate to what extent smaller, less computationally intensive, simulations could provide similar solutions to those obtained from the whole contact models.

6.2. The implications of residual stress on operating life

6.2.1. Introduction

In Chapter 1, the research of the causes of several phenomena found to occur in the operating life of surfaces was discussed. This covered running-in, which happens in the early stages of operating life, as well as causes of surface failure such as surface cracking and micropitting. Factors that affect these surface failures are varied, including material properties, the magnitude of the contact pressure, the surface finish or roughness, the sliding velocity or slide/roll ratio, the lubricant properties or additives and temperature (Oila and Bull 2005). In this section, the apparent connections between the residual stresses as a result of initial contact and the findings found in the literature will be examined.

6.2.2. Discussion

Micropitting and pitting failures are distinguished by the scale of the failure characteristics. Micropits are typically considered to be up to around 10 µm deep (Höhn *et al*. 1996), while pitting failures are typically larger, of the order of several millimetres, as shown in Figure 6.1 (Olver 2005). While both phenomena occur as a result of surface cracks, pitting occurs as these cracks propagate further into the depth of the material, while micropitting occurs as a result of cracks remaining relatively near the surface (Höhn and Michaelis 2004). Therefore, the stresses at both the surface and in the subsurface region of asperity contacts will be considered to determine possible causes. Crack initiation is thought to occur as a result of some kind of stress concentration (Callister 2003).

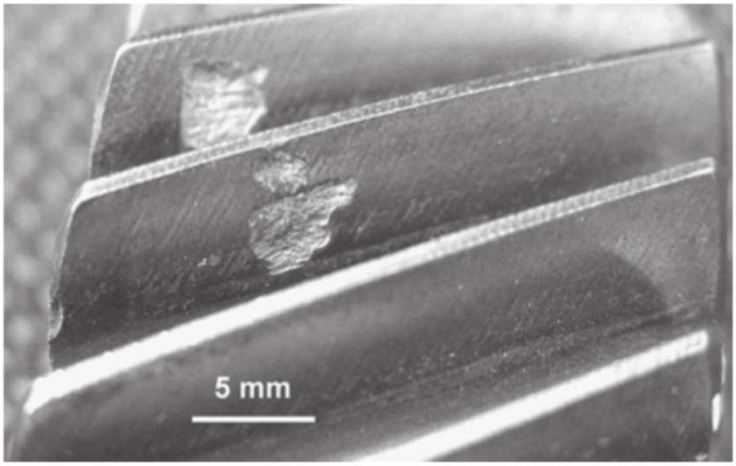

Figure 6.1 - Pitting due to rolling contact fatigue of helical gear tooth (Olver 2005).

Figure 6.2 shows the vector plots of the normalised residual maximum principal stress at, and just below, the surface for three asperities from Surfaces 1, 2 and 3 as defined in Chapter 5. The plots show only positive (tensile) maximum principal stress values. In areas where no vector is shown the maximum principal stress is compressive. The sections of roughness of which these asperities are part have been previously discussed in Chapter 5 as part of Sections 1b, 2a and 3c. These asperity features are located at x = −0.0850 mm to x = −0.0650 mm, x = −0.3625 mm to x = −0.3425 mm, and x = 0.4350 mm to x = 0.4550 mm on each surface respectively, and are shown in Figure 6.2a, b and c. Figure 6.2 shows tensile stresses only for clarity. Compressive stresses have been suppressed. It can be seen that elevated magnitudes of maximum principal stress can be seen to occur at the surface for each of the asperities shown. Furthermore, the peak stress occurs towards the edge of the heavily deformed regions. This can be seen at approximately x = −0.075 mm in Figure 6.2a, x = −0.351 mm in Figure 6.2b, and x = 0.446 mm in Figure 6.2c.

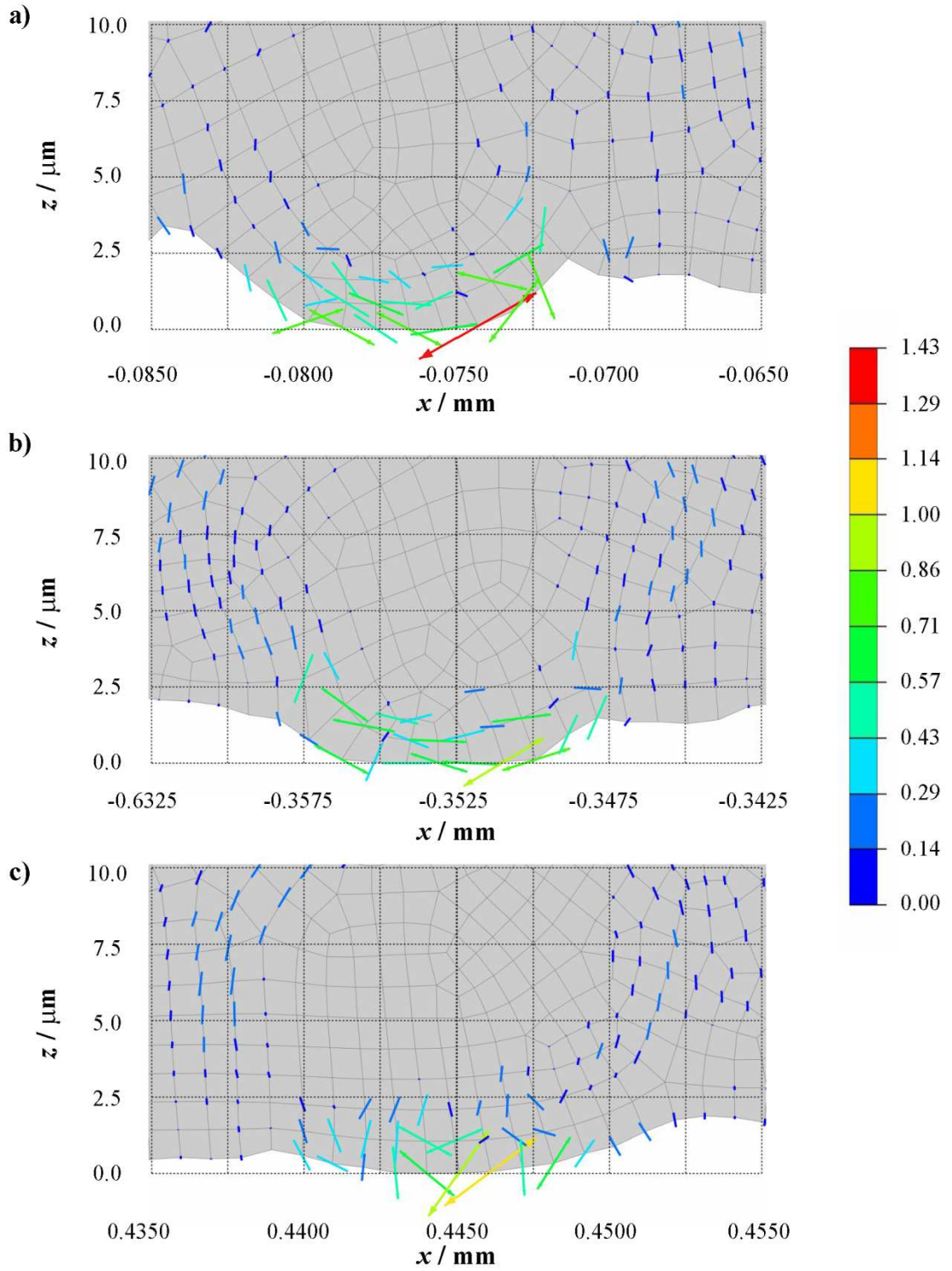

Figure 6.2 - Normalised positive residual maximum principal stress vectors at the surface; a) Surface 1, b) Surface 2, c) Surface 3. σ_y = 2.550 GPa and E_T / E = 0.05 for each surface.

In previous chapters, the surface stresses have been discussed in terms of von Mises stress and direct stress in the tangential direction. By examining the principal stress at the surface, the direction

of the stress in relation to the surface can be found. This is important with regards to surface cracking and micropitting as a characteristic relationship has been found. In the early stages of growth, micropitting cracks are usually shallowly inclined to the surface (Olver *et al*. 2004), as illustrated in Figure 6.3. The angle of these cracks is often stated as being between 10° and 30° to the tangent at the surface, orientated against the sliding direction, originating at the edge of loaded asperities and the neighbouring valley features (Dawson 1968; Olver 2005; Oila and Bull 2005). However, Bull *et al*. (1999) and D'Errico (2011) have reported angles in the range of 35° to 55° to the tangent.

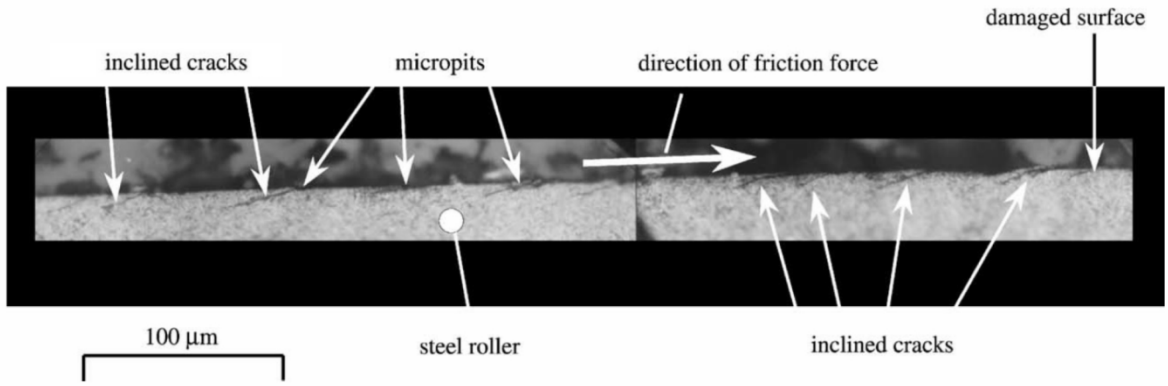

Figure 6.3 - Cross section of typically micropitted surface in hard steel, showing relationship of crack inclination to direction of friction force (Olver *et al*. 2004).

It can be seen that the maximum principal stress vectors act at angles perpendicular to this proposed range. Vectors perpendicular to the proposed range of 35° to 55° are more typically found at the centre of asperities, while the shallower angles such as 10° to 30° are more frequently seen at the edges. If crack initiation/propagation is expected to occur perpendicular to the stress vector, similar to a Mode I crack opening (Broek 1974), then it would be expected that for each of the asperities shown, that cracks would grow from the edge of the asperity towards the centre. While this can be seen in Figure 6.3, at the scale shown, this is not particularly clear. However, this can be seen to have occurred in both Figure 6.4 and Figure 6.5a. Micropitting "wear" occurs as the cracks propagate until they come across the surface, or another crack, resulting in a progressively larger

area becoming covered with micropits, resulting in a stained or frosted appearance on the surface (Ahlroos *et al*. 2009).

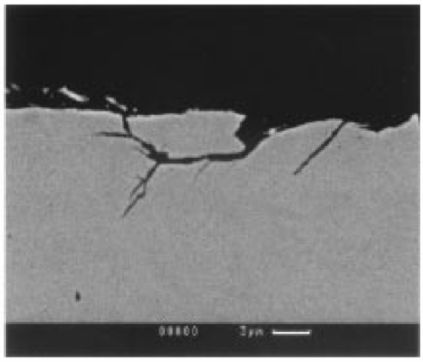

Figure 6.4 - Micrograph of a section taken through a region of micropits showing the crack path taken during the micropitting process (Bull *et al*. 1999).

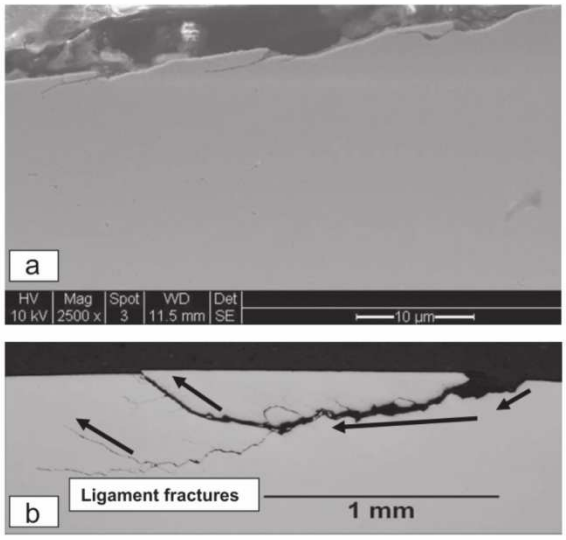

Figure 6.5 - Formation of a) micropits and b) macro pits from the growth of micro-cracks and the subsequent fracture of ligaments above the cracks in an uncoated gear subjected to contact fatigue (Moorthy and Shaw 2013).

Another phenomenon seen both in Figure 6.4 and Figure 6.5b is the development of a crack further into the subsurface material beyond the depth of typical micropitting failures. This increasing depth of the cracks may develop the micropitting into a larger scale pitting failure. It also has the potential

to extend across the surface, perhaps linking to an adjacent micropit, covering more of the surface area with micropitting features. Figure 6.6, Figure 6.7 and Figure 6.8 show the vector plots of the normalised residual maximum principal stress in the subsurface material for the three asperities in Figure 6.2a, b and c, respectively. As a result of the different scale, these figures now show the roughness from x = −0.0900 mm to x = −0.0600 mm, x = −0.3675 mm to x = −0.3375 mm, and x = 0.4300 mm to x = 0.4600 mm from Surfaces 1, 2, and 3, respectively. As before, only tensile stresses are shown; compressive stresses have been suppressed to improve clarity. Annotations have been made to each of these figures that suggest the direction in which cracks could initiate and propagate. The initiation arrows correspond well with the micropitting features previously discussed, while the propagation arrows show the two ways in which these cracks can progress; either deep into the subsurface material as can be seen occurring in Figure 6.4, or in a direction closer to parallel with the surface as in Figure 6.5. It can be seen that for each asperity that at depths between approximately z = 12 μm and z = 22 μm, the maximum principal stress vectors are oriented approximately tangential to the surface, encouraging vertical crack growth into the subsurface material. At depths less than z = 10 μm the principal stress vectors are more perpendicular to the surface encouraging crack propagation tangential to the surface and a progressive development of micropitting features across the surface as cracks meet one another.

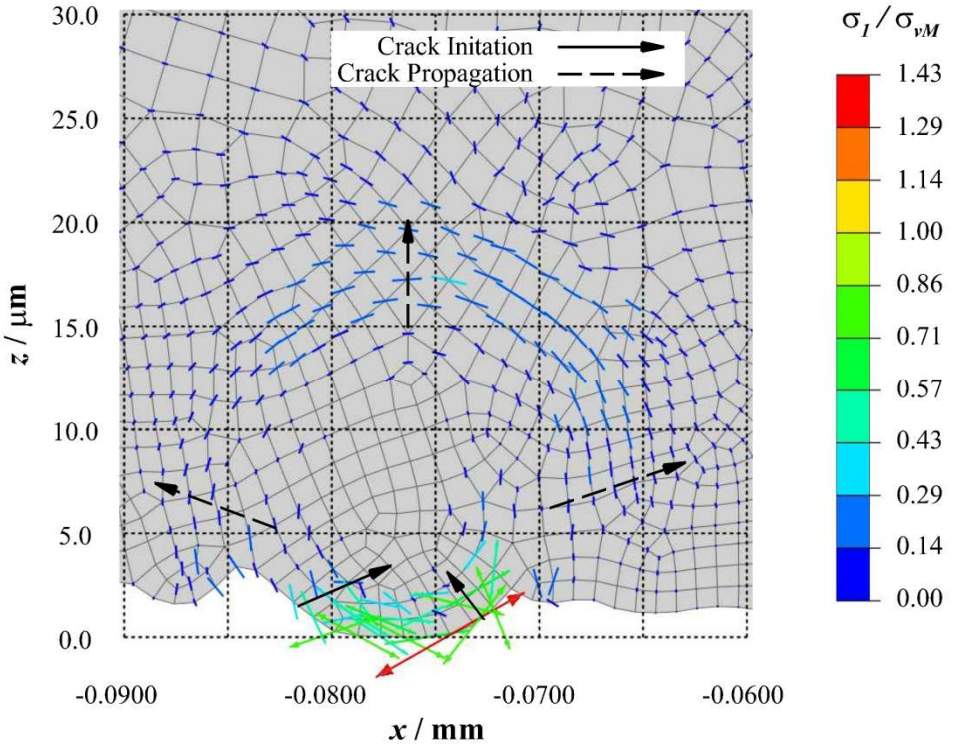

Figure 6.6 - Normalised positive residual maximum principal stress vectors in the subsurface material for asperity feature on Surface 1. σ_y = 2.550 GPa and E_T / E = 0.05.

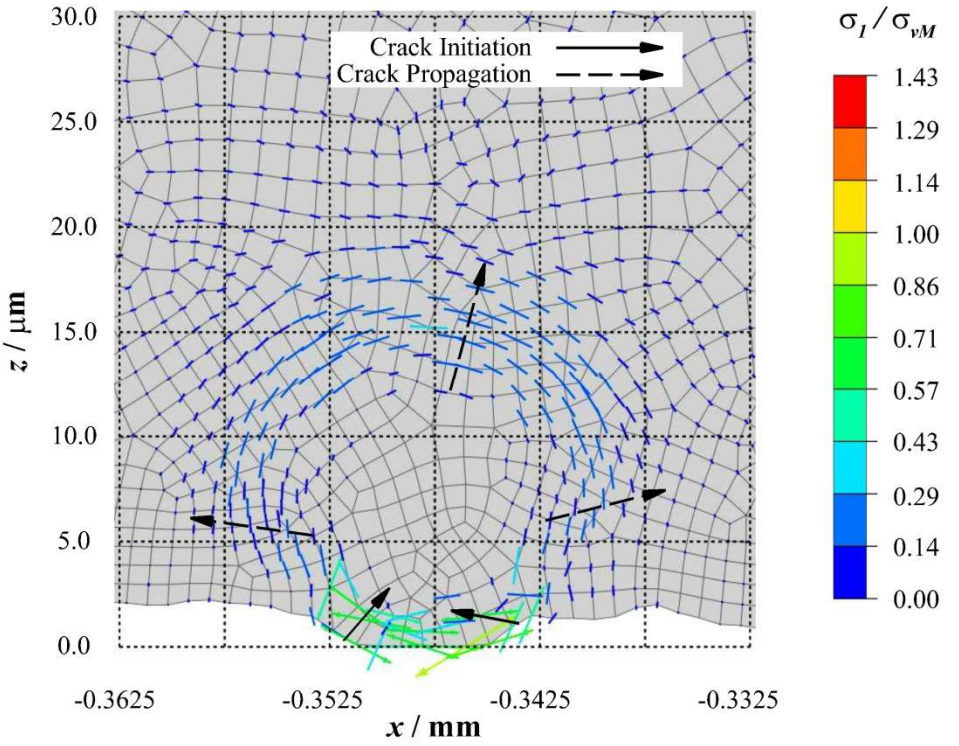

Figure 6.7 - Normalised positive residual maximum principal stress vectors in the subsurface material for asperity feature on Surface 2. σ_y = 2.550 GPa and E_T / E = 0.05.

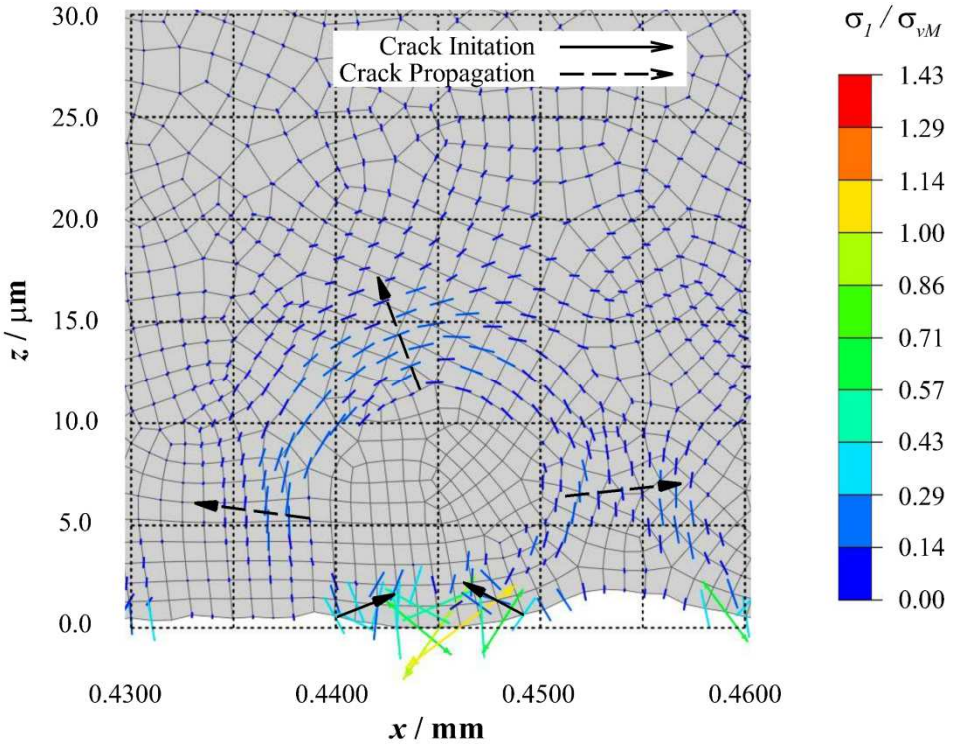

Figure 6.8 - Normalised positive residual maximum principal stress vectors in the subsurface material for asperity feature on Surface 3. σ_y = 2.550 GPa and E_T / E = 0.05.

The relative magnitude of the stresses in each region should also be noted. Those found at the surface are typically found to be of the order of the yield strength. The difference between asperities is noticeable, with greater plastic deformation resulting in larger magnitudes of stress at the surface. This is illustrated by the fact that the greatest magnitude stress is found in Figure 6.6. In the subsurface material, the stresses are significantly smaller, with peak stresses around half the yield strength. However, the magnitude of the subsurface stresses seems to be less sensitive to the degree of plastic deformation.

In work by Zhou *et al*. (1989), a model based on accumulated strain energy was created that proposed that increasing the load applied to the surface reduced the time taken for cracks to initiate and propagate, as illustrated in Figure 6.9. It can be seen that crack initiation life significantly reduces as a result of increased contact pressure, and this may be as a result of the increased magnitude of stress found at the surface as seen in Figure 6.6. Conversely, the crack propagation life

is less sensitive to the increased pressure, decreasing significantly less as the pressure is increased. It could be suggested that the crack initiation and propagation is proportional to the magnitude of the maximum principal stress, with relatively early crack initiation occurring as a result of high stress from large amounts of plastic deformation. Crack propagation then proceeds relatively slowly as a result of the smaller magnitude stresses found in the subsurface material. This can be seen in Figure 6.9 as the crack propagation life becomes an increasingly large proportion of the total contact fatigue life at higher contact pressures.

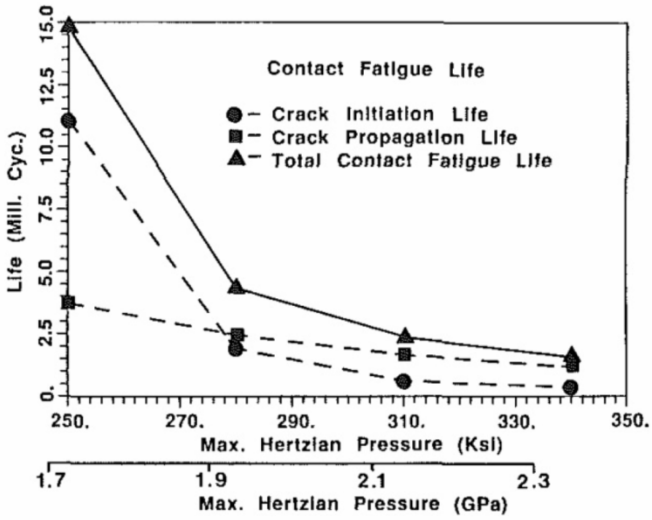

Figure 6.9 - Contact fatigue life from crack initiation to propagation (Zhou *et al*. 1989).

It should be noted that these links are predominantly speculative, while also ignoring many other aspects that are thought to be factors in cracking and micropitting failures. For example, the effect of rolling/sliding contact and trapping pressurised lubricant within cracks Bower (1988), the effect of heat generated by plastic deformation resulting in the metallurgical phase change of gear material known as martensite decay (Oila *et al*. 2005), or the effect the chemical interactions between the contacting surfaces and the lubricant, or additives included in the lubricant (O'Connor 2005). These factors have not been considered when considering the potential effects of the residual stress found to occur as a result of initial surface contacts, as may be expected to occur in the running-in process.

6.3. Parametric analysis of real rough surface contact

6.3.1. Model details

The complete contact models described in Section 5.4.1 were carried forward for further simulations. The aim of this further analysis was to determine characteristic behaviour that linked the magnitude of residual deflection of asperity features and the residual stresses found at the surface. In determining this relationship, the magnitude of residual stress at the surface would be able to be predicted from measuring the surface profile, and in turn be used in fatigue analysis of the surface. In Chapter 5, a combination of a yield strength of σ_y = 2.550 GPa and linear strain hardening behaviour of E_T / E = 0.05, were found to provide the most accurate solutions in comparison with the experimental residual deflections. These material properties were therefore used for the parametric analysis simulations. The only changes made were in the applied load. The remainder of the model settings remained consistent with those previously detailed. Previously, each surface was loaded only with the equivalent load from the twin-disk test rig. Surface 1, Surface 2 and Surface 3 were loaded with nominal Hertzian contact pressures of 1.0 GPa, 1.5 GPa and 2.0 GPa respectively. For this study, each of these surfaces was tested with a range of loads, simulating nominal Hertzian contact pressures of 0.5 GPa, 1.0 GPa, 1.5 GPa, and 2.0 GPa for each of the surfaces. This equates to total applied loads of 220 N, 800 N, 2700 N, and 6480 N, respectively. These loads were then applied as distributed loads by dividing the total load by the application length, the width of the rough roller parts. The remainder of the model details remain as previously discussed in Chapter 5. These are summarised in Table 6.1.

Table 6.1 - Test disk parametric analysis contact model summary.

Part	2D rough roller – Imported test disk surface profiles
	2D rough roller middle section
	2D rough roller end section
	2D smooth roller
	2D smooth roller middle section
	2D smooth roller end section
Property	Rough: E = 200 GPa, ν = 0.3, σ_y = 2.550 GPa, E_T / E = 0.05
	Smooth: E = 200 GPa, ν = 0.3
Assembly	Model boundaries aligned. Parts on the verge of contact
Step	Initial (required), Contact, Load, Removal
	ALE Adaptive Meshing – Frequency = 1, Remeshing sweeps = 10
Interaction	Frictionless
	Augmented Lagrange Constraint Enforcement Method
	Finite Sliding
	Surface-to-Surface
	Absolute Penetration Tolerance = 1x10^{-6}m
	Surface ties applied to adjacent surfaces of constituent roller parts
Load	220 N, 800 N, 2700 N, 6480 N total load, applied as a distributed load acting on bottom edge of smooth surface part
Boundary Conditions	Small vertical displacement applied to bottom edge of smooth surface part to initiate contact
	Top edge of rough surface part restrained (U_x = U_y = 0)
	Side edges of rough and smooth surface parts restrained in y-axis (U_x = 0)
Mesh	Partitioned around contact area
	Plane Strain Elements
	Linear Elements
	Fully integrated elements

6.3.2. Parametric analysis

The aim of the parametric analysis was to investigate the relationship between residual stresses found at the surface of asperities subjected to a measured residual deflection. This would provide a tool for approximating the residual stresses in other work in the research group on fatigue life of rough surface contacts. After each simulation was completed, a number of outputs were extracted from the results. These outputs were used to characterise the change of shape experienced by each asperity as a result of the load applied to it, and the surface residual stresses that occurred as a

result. The region over which stresses were considered extended to 1 µm (one node spacing) outside of the deflected region. It was found that the peak stresses were typically confined to this region for each asperity contact. In order to distinguish between differently shaped asperities experiencing similar residual deflections, the width over which residual deflection normal to the surface occurred was also recorded. Also calculated were the peak and average height differences between the initial and residual asperity profiles. Each of the parameters considered is defined below for an asperity subject to plastic contact.

- Residual asperity land width, $L_{residual}$ – The width over which residual deflection normal to the surface occurs for the asperity.
- Maximum residual deflection, Δz_{max} – The maximum residual deflection normal to the surface for the asperity.

These two parameters are illustrated in Figure 6.10.

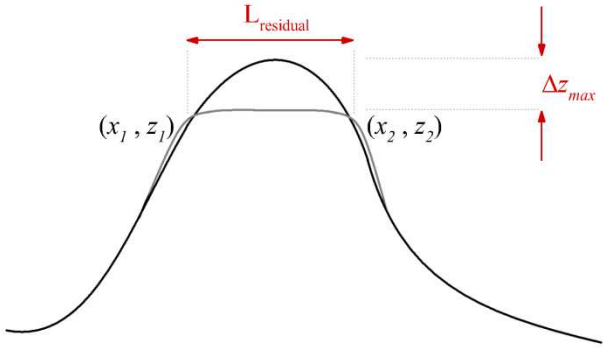

Figure 6.10 - Initial and residual asperity, showing asperity shape parameters $L_{residual}$ and Δz_{max}.

The following parameters were calculated using field outputs obtained from the Abaqus contact analyses.

- Average residual deflection, Δz_{avg} – The average height difference between the initial asperity, and the residual asperity. Calculated by dividing the sum of the asperity deflections normal to the surface by the residual asperity land width.

- Peak residual von Mises stress, σ_{vM} – Peak residual von Mises stress at the surface for each asperity considered.
- Peak residual maximum principal stress, σ_1 – Peak normalised residual maximum principal stress at the surface for each asperity considered.
- Peak residual direct stress in the tangential direction, σ_{xx} – Peak normalised residual direct stress in the tangential direction for each asperity considered.

Each of the stress components was normalised by the yield strength, σ_y.

6.3.3. Parametric analysis results

6.3.3.1. Von Mises stress

Figure 6.11 shows the relationship between the peak normalised residual von Mises stress at the surface, and the peak residual asperity deflection in the z-direction for each of the surfaces and loads combined. As the results are plotted on logarithmic scales, it follows that if the relationship between the two parameters was a standard power law function, then a linear trend would be expected. As can be seen, in the figure there is a linear trend, albeit with some scatter, so the relationship can accurately be defined approximately using a power law. Large amounts of variation can be seen to occur for small amounts of asperity deflection, but these are not significant as interest is focussed on high values of von Mises stress.

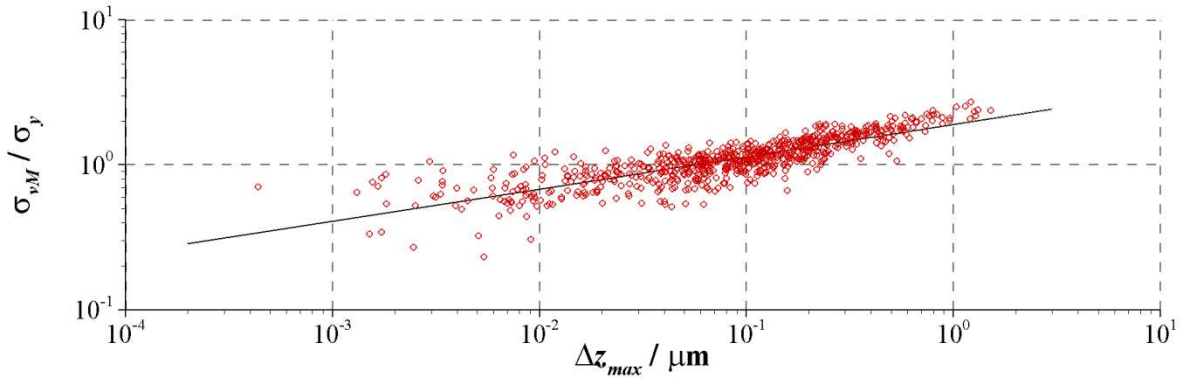

Figure 6.11 - Normalised peak residual von Mises stress at the surface vs. maximum normal deflection for all surfaces using logarithmic axes.

This variation in the results for the large number of asperities with small residual deflections distorts the trendline found by using a least squares power law, as shown in Figure 6.11. This is also shown in Figure 6.12, which plots the same results but on linear axes and highlights the difference between the trendline and the results found for large asperity deflections. A large number of data points exist in the region where Δz_{max} is less than 0.25 µm. The least-squares trend line attempts to reduce the distance from the trendline to each data point and so places undesirable weighting on these data points, when greater interest is in those having experienced larger residual deflections, as these asperities are more prone to surface failure. As a result, it can be seen that the least-squares trend line in Figure 6.12 is particularly poor at predicting behaviour of asperities with Δz_{max} greater than approximately 0.5 µm. Therefore, a trendline will be manually created in order to approximate trends in behaviour. A curve will be defined of the form in Equation 6.1.

$$y = K\,x^n \qquad \textbf{Eq. 6.1}$$

Where the constant K, and index n, will be manually manipulated to qualitatively provide a trendline to the set of data that captures the large stress values correctly.

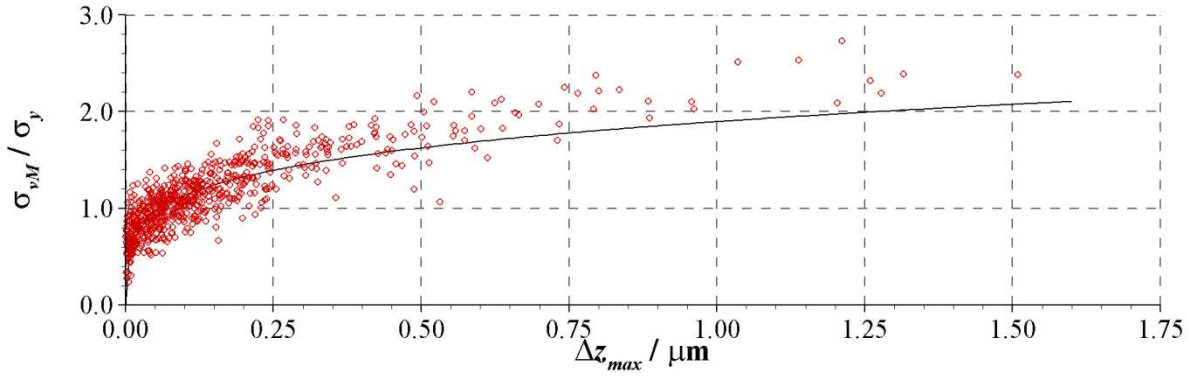

Figure 6.12 - Normalised peak residual von Mises stress at the surface vs. maximum normal deflection for all surfaces using linear axes.

Figure 6.13 shows the relationship between the normalised peak residual von Mises stress at the surface, and the peak residual asperity deflection in the z-direction for Surface 1, 2 and 3, and also for the combined data, in Figure 6.13a, b, c and d respectively. Also shown in each of the figures is the manually manipulated power law shown in Equation 6.2.

$$\frac{\sigma_{vM}}{\sigma_y} = 2.2\ \Delta z_{\max}{}^{0.3} \qquad \textbf{Eq. 6.2}$$

It can be seen that this manually manipulated power law offers a better representation of the behaviour for each of the surfaces. The manipulated power law closely follows the least squares trendline for small asperity residual deflections, but deviates as residual deflection increases. This manipulated trendline more accurately represents the behaviour of these asperities.

In comparing Figure 6.13a, b and c, differences in how each surface reacts to the same set of loads can be seen. In particular, Surface 2 appears to carry the load differently to Surfaces 1 and 3, with only one asperity exceeding Δz_{max} of approximately 0.51 µm. This suggests that Surface 2 carries the load over a larger number of asperities, carrying less load, resulting in less residual deflection. This is further supported in that 278 asperities are plotted in Figure 6.13b for Surface 2 in comparison to 234 and 192 asperities in Figure 6.13a and c for Surfaces 1 and 3. Therefore, on average, each asperity in Surfaces 1 and 3 carries more of the load, and would be expected to deflect more.

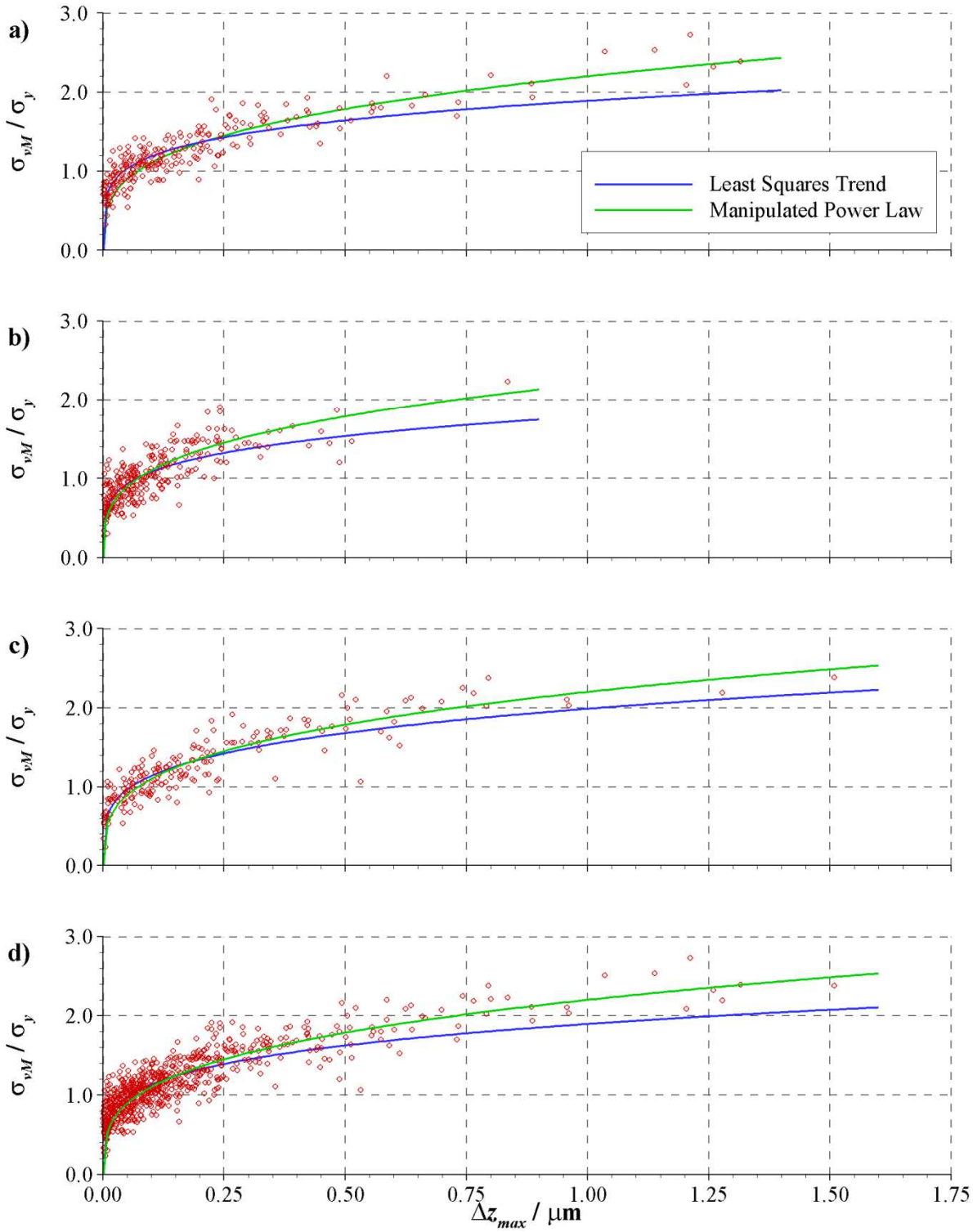

Figure 6.13 - Normalised peak residual von Mises stress at the surface vs. maximum residual normal deflection; a) Surface 1, b) Surface 2, c) Surface 3, d) Combined results. Both the least squares and modified trendlines are also plotted.

Similar analysis was performed to investigate the relationship between the normalised peak residual von Mises stress at the surface and the average residual normal deflection of asperities. However, it

became apparent that the results achieved were similar to those already discussed for the maximum residual deflection and that the mount of scatter was not reduced. The manually manipulated power law relationship between the normalised peak residual von Mises stress at the surface and the average residual deflection is shown in Equation 6.3. The power remains the same as that for the maximum residual deflection. The difference between the relationships is only found in the different constant.

$$\frac{\sigma_{vM}}{\sigma_y} = 2.8\,\Delta z_{\mathrm{avg}}{}^{0.3} \qquad \text{Eq. 6.3}$$

6.3.3.2. Maximum principal stress

Figure 6.14 shows the relationship between the normalised peak residual maximum principal stress at the surface, and the peak residual asperity deflection in the z-direction for each of the surfaces and loads combined. The results are plotted on logarithmic scales, and suggest an approximate power law relationship due to the general linear trend. Again there is scatter in the data, but this is somewhat smaller than previously shown in Figure 6.11.

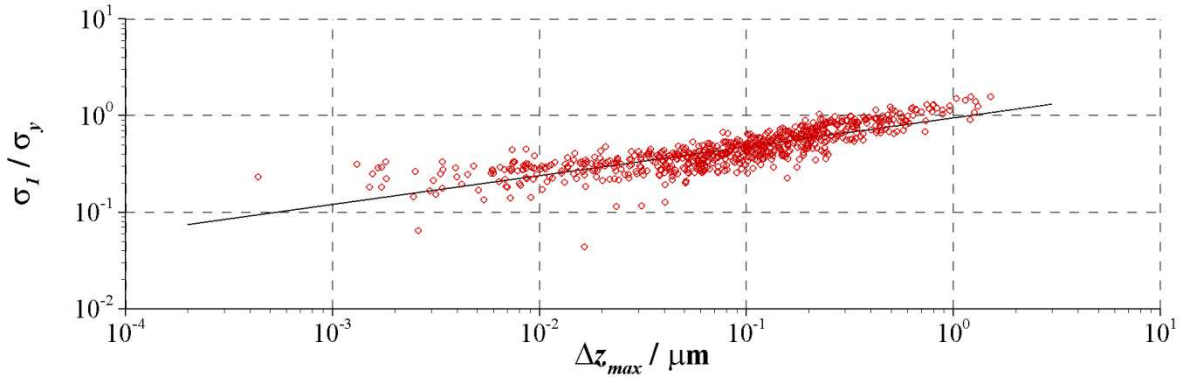

Figure 6.14 - Normalised peak residual maximum principal stress at the surface vs. maximum normal deflection for all surfaces.

This variation in the results for asperities with small residual deflections distorts the trendline found by using a least squares power law, as shown in Figure 6.14. This is also shown in Figure 6.15, which

plots the results on linear axes. This highlights the difference between the trendline and the results found for large asperity deflections. As before, the majority of asperities can be found in the region where Δz_{max} is less than 0.25 µm, distorting the least squares trendline. It can be seen that the least squares trend line in Figure 6.15 is poor at predicting behaviour of asperities with Δz_{max} greater than approximately 0.3 µm. Therefore, a trendline will be manually created in order to approximate trends in behaviour. A curve will again be defined of the form as previously shown in Equation 6.1.

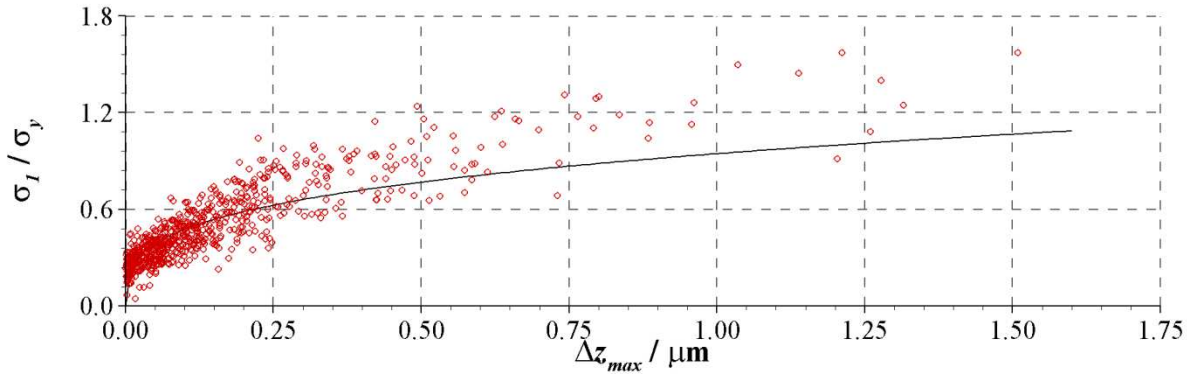

Figure 6.15 - Normalised peak residual maximum principal stress at the surface vs. maximum normal deflection for all surfaces using linear axes.

Figure 6.16 shows the relationship between the normalised peak residual maximum principal stress at the surface, and the peak residual asperity deflection in the z-direction for Surface 1, 2 and 3, and for the combined data, in Figure 6.16a, b, c and d respectively. Also shown in each of the figures is the manually manipulated power law shown in Equation 6.4.

$$\frac{\sigma_1}{\sigma_y} = 1.2\ \Delta z_{\max}{}^{0.4} \qquad \textbf{Eq. 6.4}$$

It can be seen that this manually manipulated power law offers a better representation of the behaviour for each of the surfaces. It follows the least squares trend line closely for small asperity residual deflections, but deviates as residual deflection increases and represents the behaviour of these asperities more accurately. Similar differences between the surfaces can be observed as previously discussed. Surface 2 carries the applied set of loads over a larger number of asperities that typically deflect less than those found in Surfaces 1 and 3.

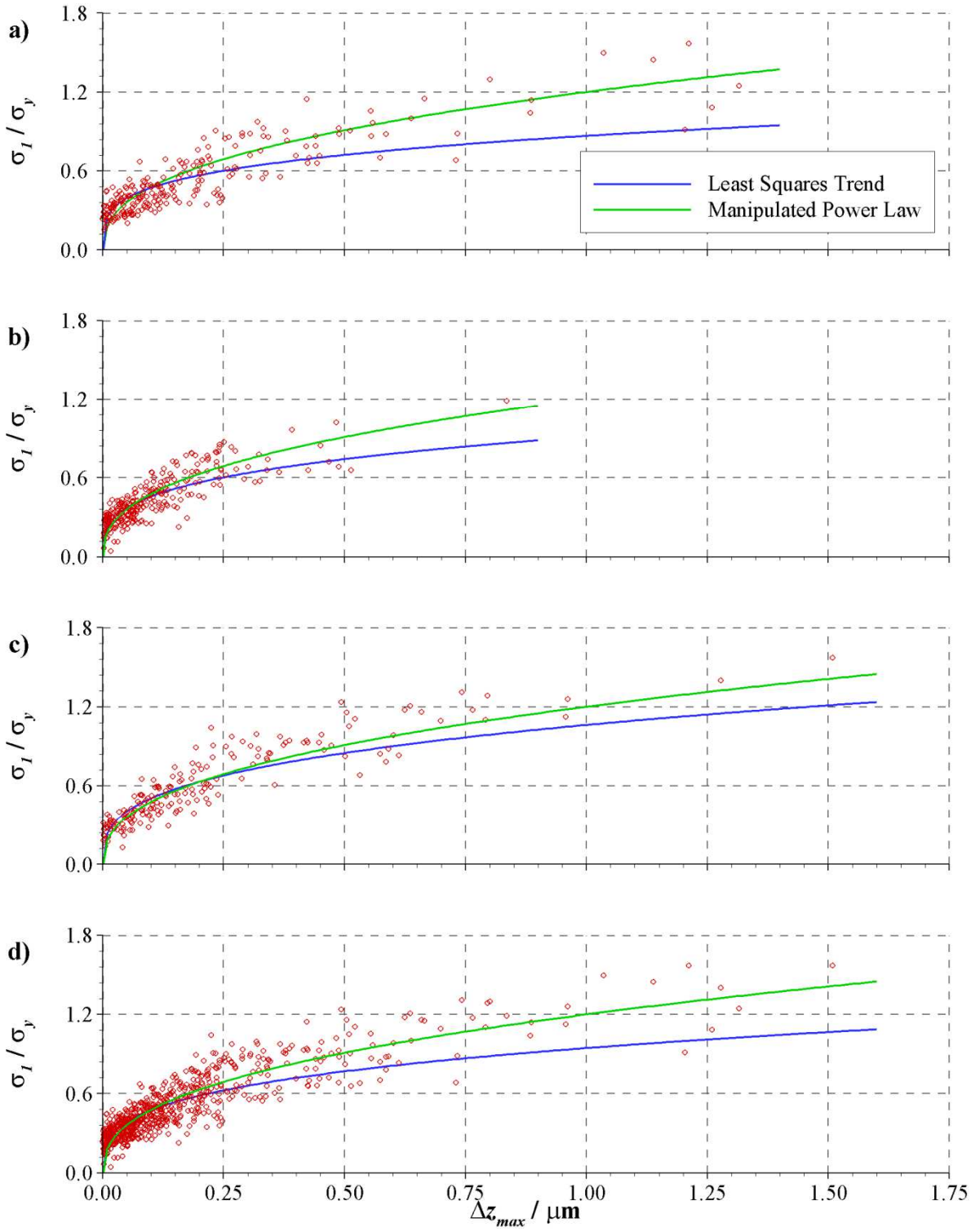

Figure 6.16 - Normalised peak residual maximum principal stress at the surface vs. maximum residual normal deflection; a) Surface 1, b) Surface 2, c) Surface 3, d) Combined results. Both the least squares and modified trendlines are also plotted.

Similar analyses were performed to investigate the relationship between the normalised peak residual maximum principal stress at the surface and the average residual normal deflection of

asperities. It also became apparent that the results achieved were similar to those already discussed for the maximum residual deflection. The manually manipulated power law between the normalised peak residual maximum principal stress at the surface and the average residual deflection is shown in Equation 6.5. The power remains the same as that for the maximum residual deflection. The difference between the relationships is only found in the different constant. As with the von Mises stress, the constant was found to increase approximately 26% when considering the average residual deflection in comparison to the maximum residual deflection.

$$\frac{\sigma_1}{\sigma_y} = 1.6\ \Delta z_{\text{avg}}{}^{0.4} \qquad \text{Eq. 6.5}$$

6.3.3.3. Direct stress in the tangential direction

Similar analysis was performed to examine the relationship between the normalised peak residual direct stress in the tangential direction and the maximum residual deflection of asperities normal to the surface. However, little correlation was seen to occur between the two parameters in comparison to those already discussed for the von Mises and maximum principal stresses. Given the links between the maximum principal stress vectors and crack initiation, propagation and micropitting discussed previously in Section 6.2.2, it is therefore proposed that the direct stress in the tangential direction is not a critical parameter in determining these surface failures. Maximum principal stress appears to be more significant and it is recommended that this is considered for future work.

6.4. Asperity contact modelling

6.4.1. Model details

In Chapter 5, for each nominal Hertzian contact pressure, three sections of the rough surface were examined in further detail. For Surface 1, these sections were for x = −0.29 mm to x = −0.19 mm, x = −0.13 mm to x = −0.03 mm and x = 0.25 to x = 0.35 mm and were first shown in Section 5.4.2.1. in Figure 5.10. For Surface 2, the sections were for x = −0.36 mm to x = −0.26 mm, x = −0.10 mm to x = 0.00 mm and x = 0.32 to x = 0.42 mm and were first shown in Section 5.4.3.1. in Figure 5.20. For Surface 3 the sections were for x = −0.26 mm to x = −0.16 mm, x = −0.06 mm to x = 0.04 mm and x = 0.43 to x = 0.53 mm and were first shown in Section 5.4.4.1. in Figure 5.25. Each of these nine sections of roughness, including the form of the 38.1 mm radius roller, was used to create individual rough surface contact models of widths of 0.1 mm. For the opposing counterface in each model, the corresponding section of the smooth roller was used, ensuring that the radius of relative curvature was the same in the 0.1 mm section models as in the complete contact models.

Parts were then created in a similar manner to the complete contact models. For each rough and smooth surface roller, two constituent parts were created and connected using surface ties. This allowed a more rapid transition in element size, reducing computational cost, as was previously utilised in the complete contact models in Chapter 5. Where possible, the meshes from the complete contact models were replicated. Meshing seeding was used in order to control the element sizes at the surface and boundaries. Model boundaries were then aligned, and the parts adjusted to be on the verge of contact. The top edge of the rough surface roller was restrained in both the x- and y-axis directions, while the sides were restrained in the x-axis direction only. To initiate contact, a small vertical displacement was applied, before being removed in the subsequent load application step. A distributed load was then applied in place of the displacement. For each asperity contact model, the load was equivalent to the load experienced by the section of roughness in the experimentally verified simulation. This was determined by requesting the contact force

output in the complete contact model simulations and summing the forces at each of the appropriate nodes in each section. This total load was then divided by the width of the asperity model, in this case 0.1 mm, to achieve the required distributed load. In the final removal step, this distributed load was then removed, leaving the residual results.

The remainder of the asperity contact model details were consistent with those used in previous models, based upon the methods tested in Chapter 3. These details are summarised in Table 6.2.

Table 6.2 - Asperity contact model summary.

Part	2D rough roller – Imported test disk surface profiles
	2D rough roller end section
	2D smooth roller
	2D smooth roller end section
Property	Rough: E = 200 GPa, ν = 0.3, σ_y = 2.550 GPa, E_T / E = 0.05
	Smooth: E = 200 GPa, ν = 0.3
Assembly	Model boundaries aligned. Parts on the verge of contact
Step	Initial (required), Contact, Load, Removal
	ALE Adaptive Meshing – Frequency = 1, Remeshing sweeps = 10
Interaction	Frictionless
	Augmented Lagrange Constraint Enforcement Method
	Finite Sliding
	Surface-to-Surface
	Absolute Penetration Tolerance = 1x10^{-6}m
	Surface ties applied to adjacent surfaces of constituent roller parts
Load	Total loads determined from experimentally verified complete contact models, applied as a distributed load acting on bottom edge of smooth surface part
Boundary Conditions	Small vertical displacement applied to bottom edge of smooth surface part to initiate contact
	Top edge of rough surface part restrained (U_x = U_y = 0)
	Side edges of rough and smooth surface parts restrained in y-axis (U_x = 0)
Mesh	Partitioned around contact area
	Plane Strain Elements
	Linear Elements
	Fully integrated elements

6.4.2. Loaded results

6.4.2.1. Surface 1

Figure 6.17 shows the loaded roughness profile and normalised contact pressure distributions for both the complete contact model and asperity contact model for the section of roughness between x = −0.29 mm and x = −0.19 mm. The load applied to the section of roughness in the asperity contact model was equivalent to that found to be applied to the same section of roughness in the complete contact model subject to a nominal Hertzian contact pressure of 1.0 GPa.

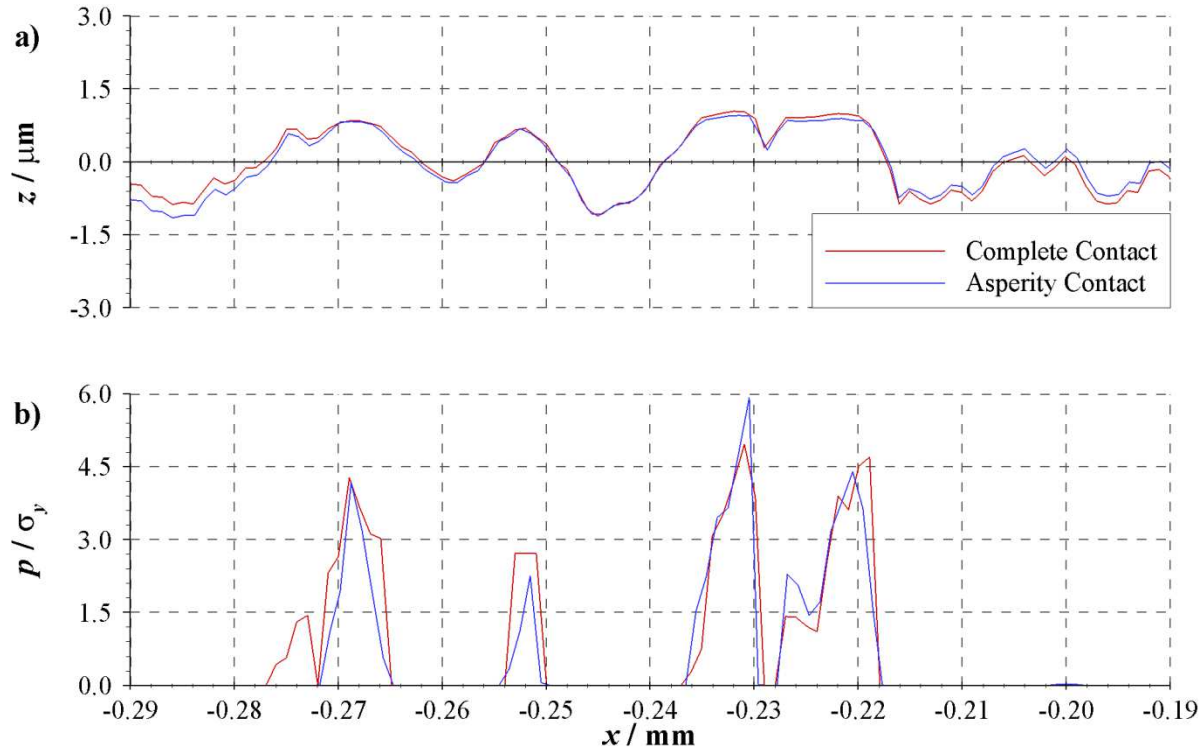

Figure 6.17 - Comparison of complete contact model and asperity contact model for section of roughness from x = −0.29 mm to x = −0.19 mm; a) loaded surface roughness profile, b) normalised contact pressure. σ_y = 2.550 GPa and E_T / E = 0.05 for each model.

Figure 6.17a shows the loaded roughness profiles for both the complete contact and asperity models. Whilst agreement is generally good, noticeable differences can still be seen. Most prominent is the way in which the asperity contact model profile exhibits more of the form of the surface, the 38.1 mm radius disk, in the results. This can be seen at the edges of the profiles,

between x = −0.29 mm and x = −0.28 mm where the asperity contact model profile is beneath the complete contact model, and between x = −0.20 mm and x = −0.19 mm where it is above. In the complete contact model, the surfaces first contact at approximately x = 0.00 mm. As the load is increased, the surfaces outside of the contact begin to conform more as a result of the contact. As such, when the section of roughness shown in Figure 6.17a is in contact, the radius of relative curvature is larger (i.e. “flatter”) than before any contact occurs.

This phenomenon can also be seen in the contact pressure distributions in Figure 6.17b. As a result of the evolved contact geometry of the complete contact model, an asperity contact can be found between x = −0.277 mm and x = −0.272 mm which does not occur in the asperity contact model. Higher peak pressures can be found to occur in the asperity contact model at x = −0.231 mm and x = −0.237 mm, illustrating how the two different models result in variations in the way the surface carries the applied load.

Figure 6.18 shows the loaded normalised von Mises stress contours for the section of roughness between x = −0.29 mm and x = −0.19 mm in the complete contact model and in the asperity contact model previously shown in Figure 6.17. The stress distributions again show the small differences in how the two models carry the applied load. The largest region of high von Mises stress (> $0.95\sigma_y$) occurs between approximately x = −0.240 mm and x = −0.215 mm, to a depth of z = 0.016 mm in the complete contact model in Figure 6.18a. In the asperity contact model in Figure 6.18b, this region extends to an increased depth of z = 0.023 mm, suggesting heavier loading of the asperity feature at the surface. The high stress regions between x = −0.272 mm and x = −0.266 mm and at x = −0.252 mm however reduce in size in comparing the complete contact model to the asperity model, suggesting reduced loading of these asperity features. This further confirms the explanation regarding the change in shape of the contact geometry in the complete contact model.

Aside from the differences that are attributable to differences in contact geometry, differences are seen close to the asperity contact model boundaries, at x = −0.29 mm and x = −0.19 mm. In the

asperity contact model, a larger proportion of the material at these boundaries can be seen to be at a von Mises stress of $0.19\sigma_y$ or less. In the complete contact model the majority of this material has a von Mises stress between $0.19\sigma_y$ and $0.29\sigma_y$. It is suggested that this difference is due to the interaction of the stresses with those due to neighbouring asperity contacts. In the asperity contact model, these boundaries are effectively lines of symmetry. In the complete contact model, unique asperity contacts occur beyond these boundaries, accounting for the differences.

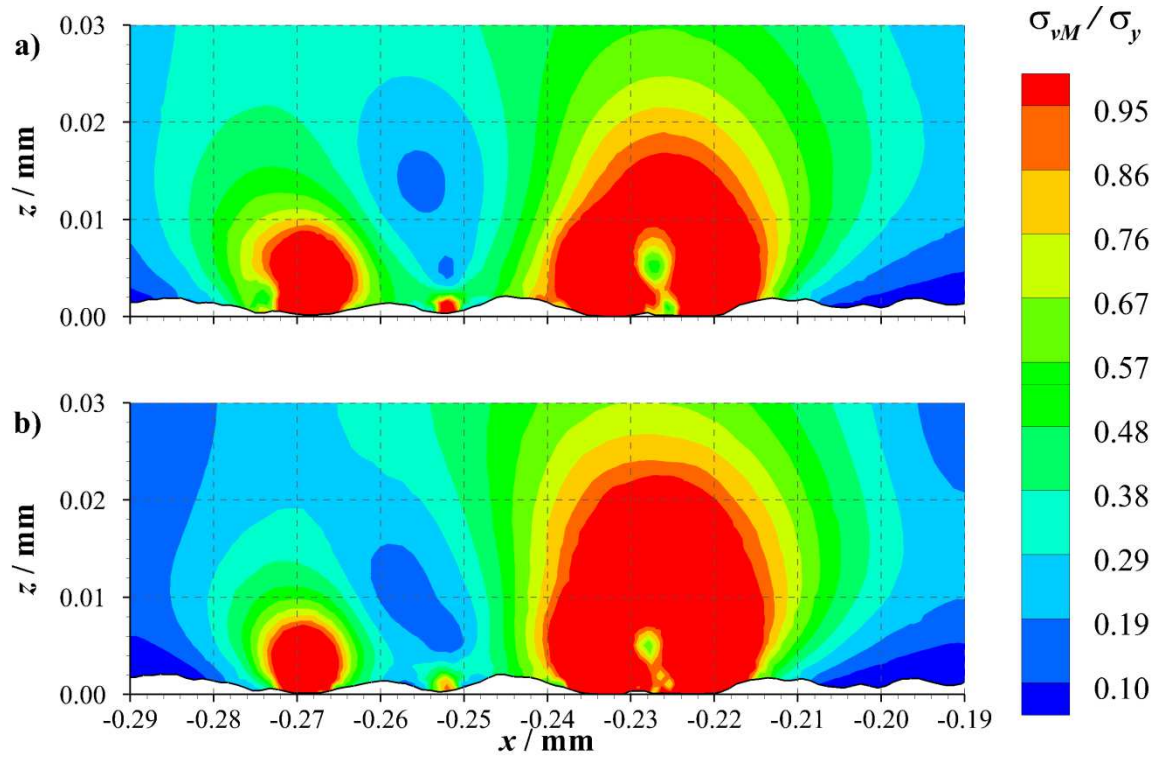

Figure 6.18 - Contours of normalised von Mises stress for section of roughness from x = −0.29 mm to x = −0.19 mm; a) complete contact model, b) asperity contact model. σ_y = 2.550 GPa and E_T / E = 0.05 for each model.

Figure 6.19 shows the contours of loaded normalised direct stress in the tangential directions for the section of roughness between x = −0.29 mm and x = −0.19 mm in the complete contact model and in the asperity contact model first shown in Figure 6.17. In general, good agreement can be seen to occur between the complete contact model and the asperity contact model, albeit with some small differences. The majority of the material in each model is in a compressive state, with the highest magnitude compressive stresses occurring at the surface where asperity contacts occur. The main

differences occur at the model boundaries, primarily at x = −0.29 mm, and in the regions of subsurface tensile stress. In the complete contact model, only one region of subsurface tensile stress can be found, at approximately x = −0.269 mm, z = 0.009 mm in Figure 6.19a. For the asperity contact model in Figure 6.19b, the peak magnitude of this region of tensile stress increases from > $0.00\sigma_y$ to > $0.10\sigma_y$. An additional region of subsurface tensile stress can also be found to occur at x = −0.228 mm, z = 0.023 mm.

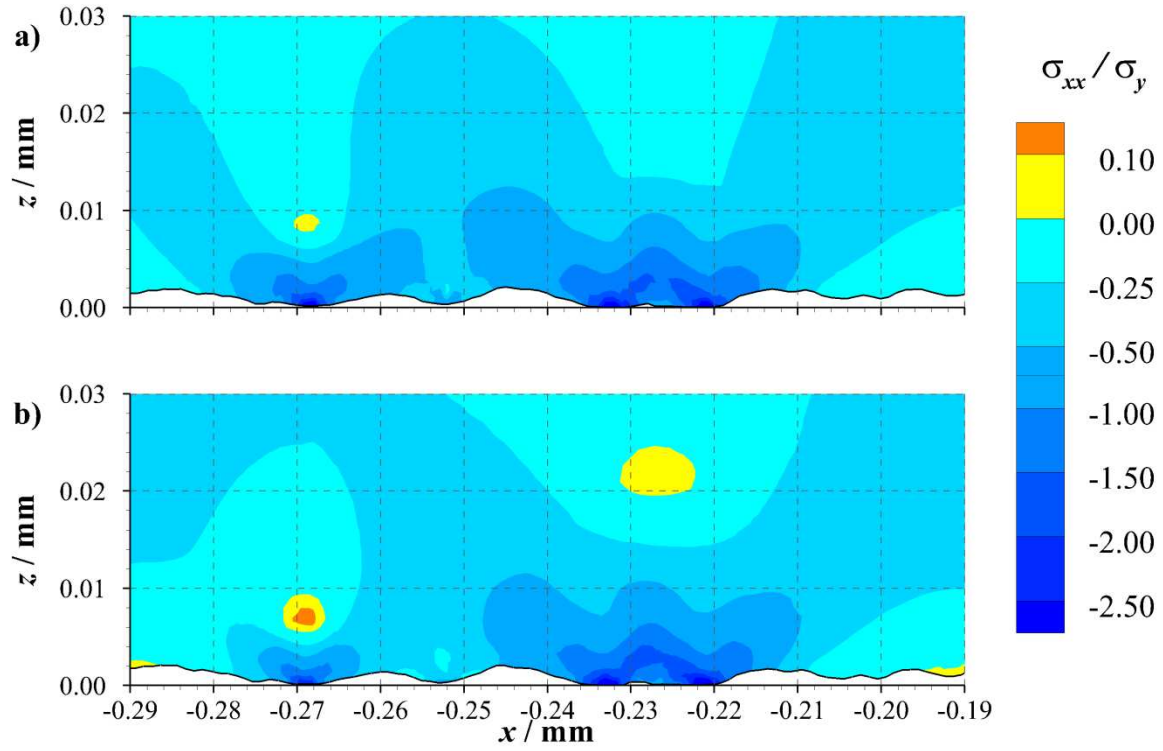

Figure 6.19 - Contours of normalised direct stress in the tangential direction for section of roughness from x = −0.29 mm to x = −0.19 mm; a) complete contact model, b) asperity contact model. σ_y = 2.550 GPa and E_T / E = 0.05 for each model.

6.4.2.2. Surface 2

Figure 6.20 shows the loaded roughness profile and normalised contact pressure distributions for both the complete contact model and asperity contact model for the section of roughness between x = −0.10 mm and x = 0.00 mm. The load applied to the section of roughness in the asperity contact model was equivalent to that found to be applied to the same section of roughness in the complete contact model subject to a nominal Hertzian contact pressure of 1.5 GPa.

Good agreement is found to occur for both the loaded surface roughness profile shown in Figure 6.20a and the contact pressure distribution in Figure 6.20b. Small differences can been seen to occur in the contact pressure distributions in proximity to the asperity contact model boundaries at x = −0.10 mm and x = 0.00 mm. Examples of this can be found at x = −0.10 mm, x = −0.09 mm and x = −0.05 mm. In contrast to behaviour discussed in Section 6.4.2.1, the contact geometry of the complete contact model does not change significantly in comparison with the asperity contact model. This is because the section of roughness shown is located at the centre of the contact, resulting in little difference between the two models.

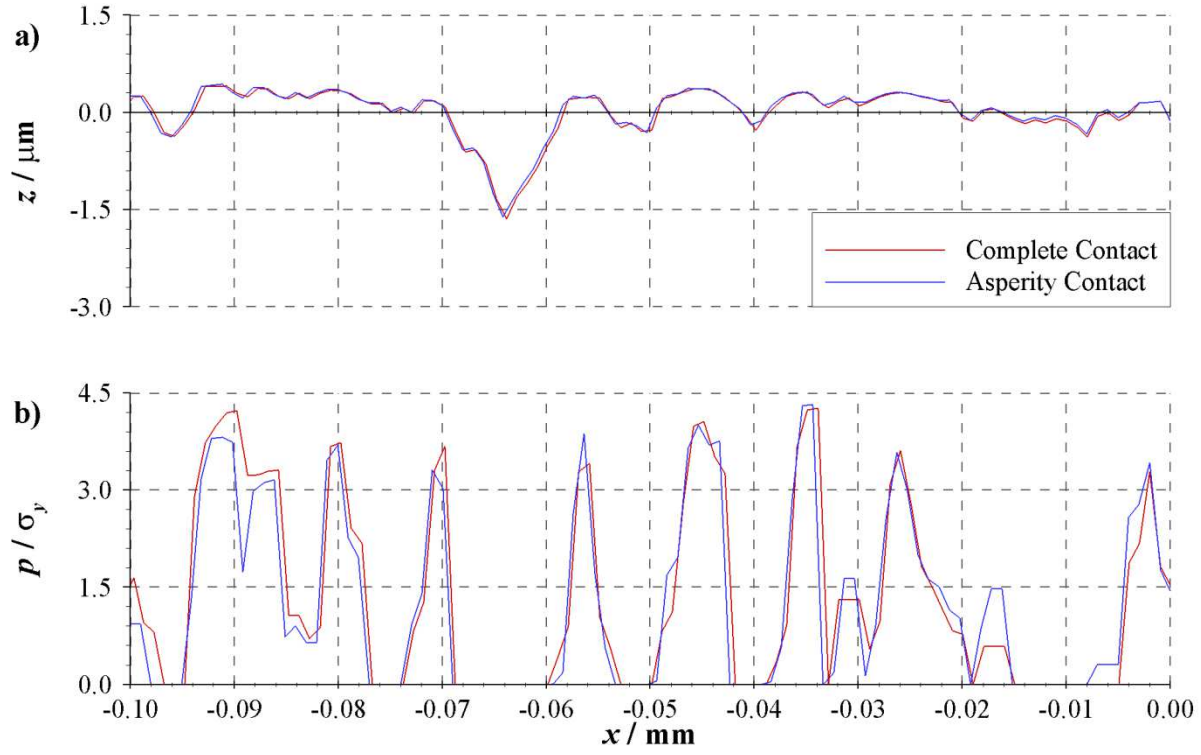

Figure 6.20 - Comparison of complete contact model and asperity contact model for section of roughness from x = −0.10 mm to x = 0.00 mm; a) loaded surface roughness profile, b) normalised contact pressure. σ_y = 2.550 GPa and E_T / E = 0.05 for each model.

Figure 6.21 shows the loaded normalised von Mises stress contours for the section of roughness between x = −0.10 mm and x = 0.00 mm in the complete contact model and in the asperity contact model previously shown in Figure 6.20. Better agreement between the two models is seen to occur for this section of roughness than previously shown in Figure 6.18. As previously discussed, this is

thought to be due to the location of the section of roughness relative to the centre of the contact. As this section is close to the centre, the contact geometry has not changed when the section of roughness is brought into contact. As a result, the asperity contact model provides a better approximation to the complete contact model conditions. Nevertheless, some differences in the stress distributions can still be observed. Two examples of these difference can be seen between x = −0.090 mm and x = −0.082 mm and between x = −0.05 mm and x = −0.02 mm at a depth of approximately z = 0.012 mm. The residual von Mises stress in these locations is higher in the asperity contact model than the complete contact model. Each region of yielding material, $\sigma_{vM} > 0.95\sigma_y$, extends slightly deeper into the subsurface material in the asperity contact model. As previously discussed, the model boundaries of the asperity contact model again affect the results nearby. For example, the region of high von Mises stress between x = −0.004 mm and x = 0.000 mm in Figure 6.21a extends to a depth of approximately z = 0.004 mm. In Figure 6.21b, this region extends to a depth of z = 0.008 mm. As a result of the line of symmetry at x = 0.000 mm in the asperity contact model, a neighbouring asperity contact occurs in close proximity, and the interaction results in a significant change in localised von Mises stress.

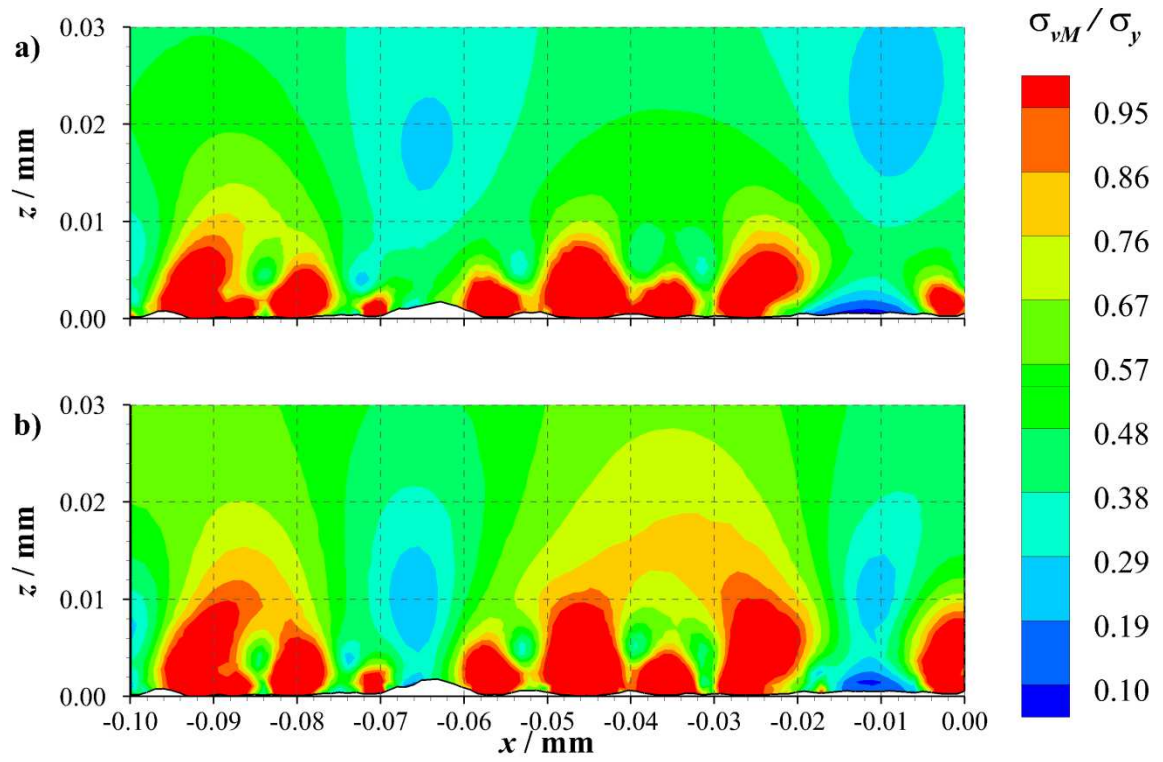

Figure 6.21 - Contours of normalised von Mises stress for section of roughness from x = −0.10 mm to x = 0.00 mm; a) complete contact model, b) asperity contact model. σ_y = 2.550 GPa and E_T / E = 0.05 for each model.

Figure 6.22 shows the contours of loaded normalised direct stress in the tangential directions for the section of roughness between x = −0.10 mm and x = 0.00 mm in the complete contact model and in the asperity contact model first shown in Figure 6.20. The pattern of high compressive stresses at the surface where asperity contacts occur is found in each model, with reduced magnitude compressive stresses in the subsurface material. The region of small magnitude compressive stress in the valley feature between x = −0.017 mm and x = −0.006 mm in the complete contact model results in Figure 6.22a becomes a small region of surface tensile stress in the asperity contact model shown in Figure 6.22b. This trend towards tensile stresses or smaller magnitude compressive stresses is seen to occur in the bulk subsurface material. The majority of the subsurface material is between $-0.50\sigma_y$ and $-1.00\sigma_y$ in the complete contact model, and between $-0.25\sigma_y$ and $-0.50\sigma_y$ in the asperity contact model. However, the contours plotted are slightly unrepresentative of the

differences between the two models. The stresses are predominantly just under and just over $-0.50\sigma_y$ in Figure 6.22a and b respectively.

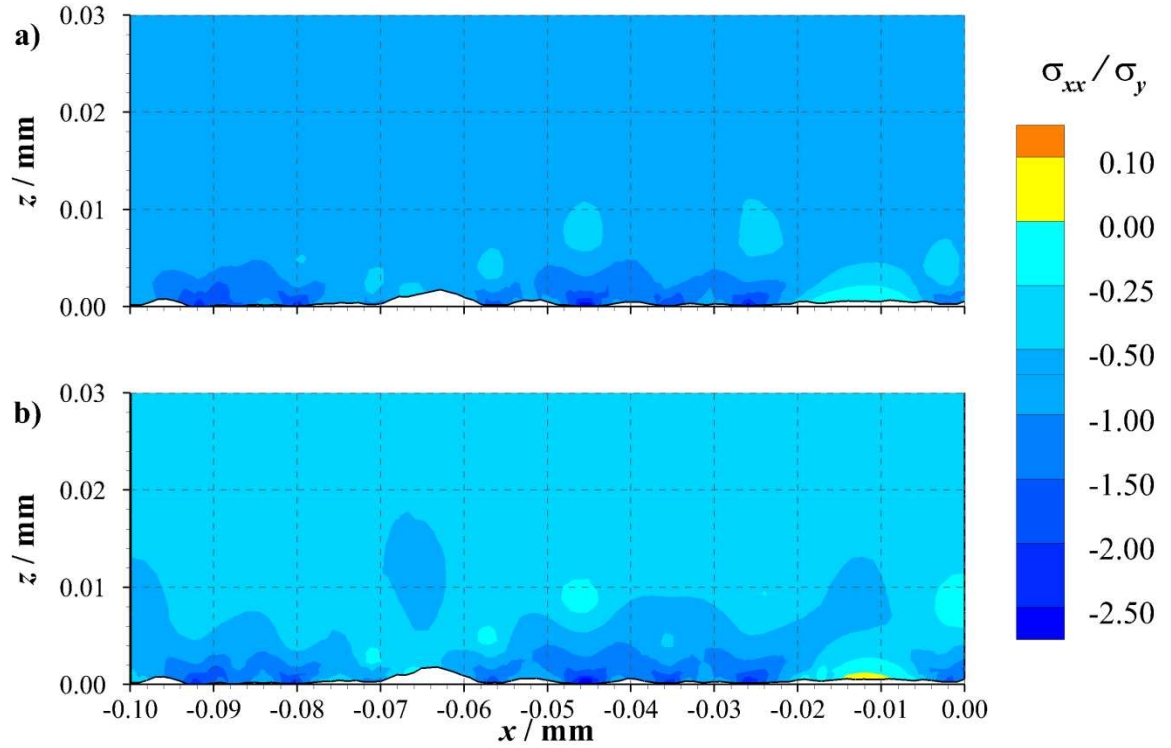

Figure 6.22 - Contours of normalised direct stress in the tangential direction for section of roughness from x = −0.10 mm to x = 0.00 mm; a) complete contact model, b) asperity contact model. σ_y = 2.550 GPa and E_T / E = 0.05 for each model.

6.4.2.3. Surface 3

Figure 6.23 shows the loaded roughness profile and normalised contact pressure distributions for both the complete contact model and asperity contact model for the section of roughness between x = 0.43 mm and x = 0.53 mm. The load applied to the section of roughness in the asperity contact model was equivalent to that found to be applied to the same section of roughness in the complete contact model subject to a nominal Hertzian contact pressure of 2.0 GPa.

Reasonable agreement in the loaded roughness profiles in Figure 6.23a can be seen, although relatively large differences still occur. The profiles were aligned using the clearly identifiable local valley features at approximately x = 0.453 mm, x = 0.469 mm and x = 0.481 mm. Despite this, other

local valley features do not align, such as the one at x = 0.439 mm and that between x = 0.519 mm and x = 0.524 mm, suggesting the section of roughness as a whole deflects differently in each model. Asperity deflections appear to be of larger magnitude in the asperity model, such as between x = 0.459 mm and x = 0.466 mm, although some of the difference may be attributable to the differences previously discussed across the whole section of roughness.

Figure 6.23b shows the contact pressure distributions for each of the models. Good agreement can be seen between the models, especially in the centre of the section of roughness, between approximately x = 0.440 mm and x = 0.510 mm. Differences are seen between the models outside of this region. Between x = 0.430 mm and x = 0.440 mm, the contact pressures in the asperity contact model can be seen to exceed those in the complete contact model. In contrast, for x = 0.510 mm to x = 0.530 mm, the contact pressures in the asperity contact model are less than those in the complete contact model. This illustrates the difference in the way the two models carry the applied load. Due to the boundary conditions used in the asperity contact model, it is effectively mirrored at x = 0.430 mm. This is not reflective of the conditions in the complete contact model. The asperity contact model boundary conditions are less applicable the further away from the contact centre. As the section of roughness shown in Figure 6.23 is the farthest from the contact centre of the sections considered, it could be expected that the largest differences between the models would occur for this case.

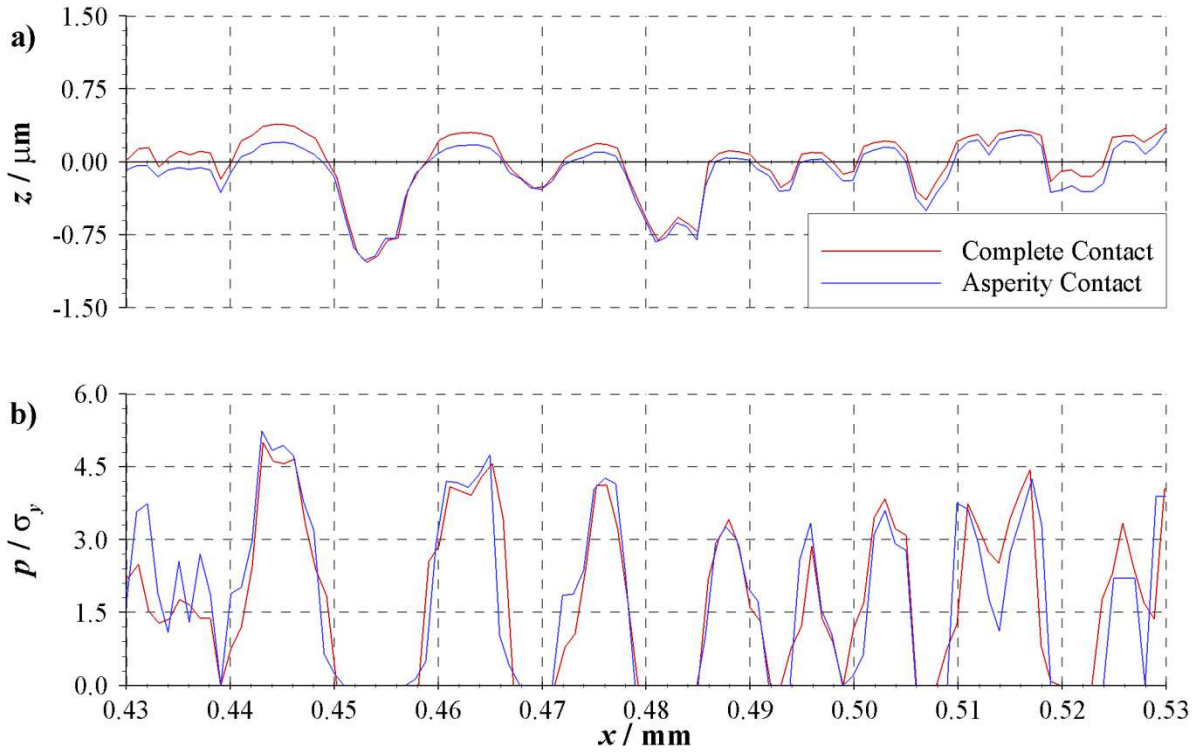

Figure 6.23 - Comparison of complete contact model and asperity contact model for section of roughness from x = 0.43 mm to x = 0.53 mm; a) loaded surface roughness profile, b) normalised contact pressure. σ_y = 2.550 GPa and E_T / E = 0.05 for each model.

Figure 6.24 shows the loaded, normalised von Mises stress contours for the section of roughness between x = 0.43 mm and x = 0.53 mm in the complete contact model and in the asperity contact model previously shown in Figure 6.23. This section of roughness shows the least agreement between the two models. In particular, the stress distributions at all depths between x = 0.430 mm and x = 0.480 mm are significantly different. Between x = 0.480 mm and x = 0.520 mm, differences are noticeable, but the stress results are comparable. Finally, between x = 0.520 mm and x = 0.530 mm, larger differences are again found. These differences can be attributed to the differences in the boundary conditions at x = 0.43 mm and x = 0.53 mm. As previously discussed, the contact pressures in the asperity contact model between x = 0.430 mm and x = 0.440 mm exceed those in the complete contact model, so a larger region of material plasticity, and von Mises stress greater than $0.95\sigma_y$, is not unexpected. However, this is furthered by the symmetrical boundary condition effectively creating a cylindrical line contact, with the centre at x = 0.43 mm, elevating subsurface

stresses. The surface form at this point is not continuous as in a cylinder, creating a point at the centre of the contact, acting as a further stress raiser. For x = 0.520 mm to x = 0.530 mm, the asperity contact model has lower contact pressures than in the complete contact model, and this is reflected in the differences in the stress distributions. In the complete contact model, von Mises stress higher than $0.95\sigma_y$ is found at the surface between x = 0.522 mm and x = 0.530 mm, extending to a depth of z = 0.008 mm at x = 0.530 mm. In the asperity contact model, this region is split into two distinct regions of stress greater than $0.95\sigma_y$ at approximately x = 0.526 mm and x = 0.530 mm. Neither of these regions extends beyond a depth of z = 0.002 mm. In between these regions, from x = 0.480 mm to x = 0.520 mm, the stress distributions are not dissimilar. Regions of high von Mises stress, greater than $0.95\sigma_y$, are in similar locations and of similar width. However, they extend deeper into the subsurface material. This is a trend seen both in Figure 6.18 and Figure 6.21.

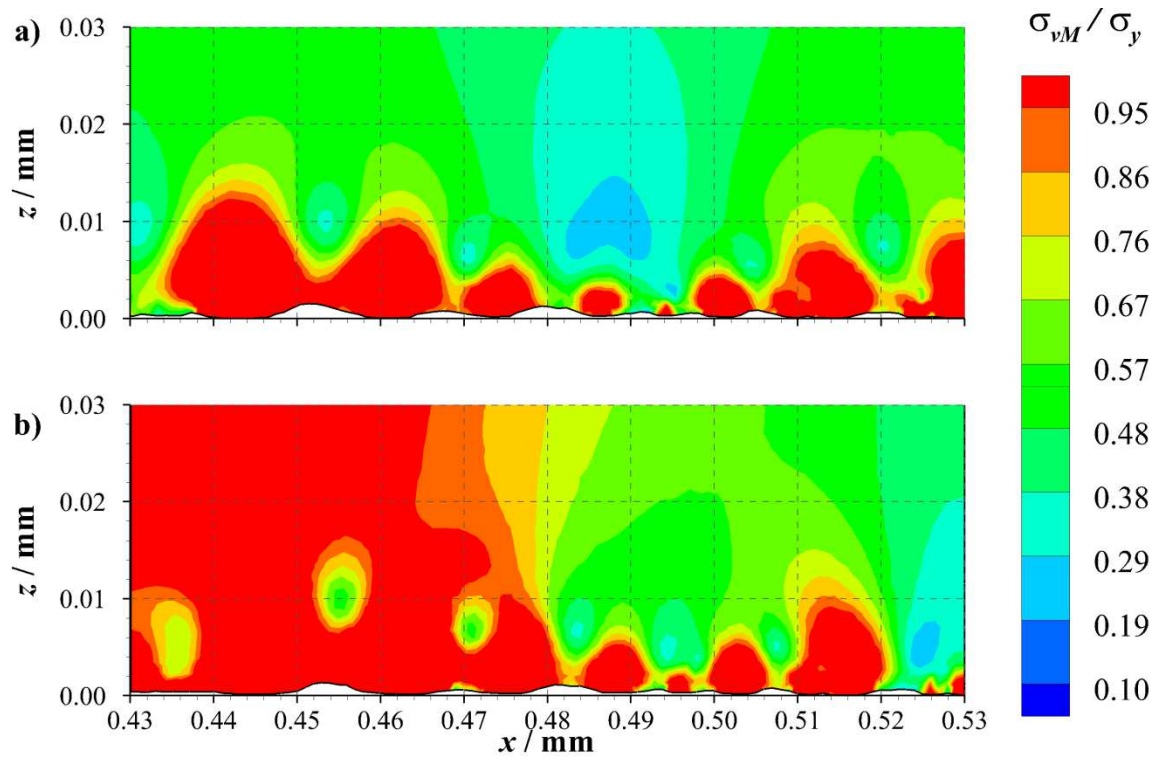

Figure 6.24 - Contours of normalised von Mises stress for section of roughness from x = 0.43 mm to x = 0.53 mm; a) complete contact model, b) asperity contact model. σ_y = 2.550 GPa and E_T / E = 0.05 for each model.

Figure 6.25 shows the contours of loaded normalised direct stress in the tangential directions for the section of roughness between x = 0.43 mm and x = 0.53 mm in the complete contact model and in the asperity contact model first shown in Figure 6.23. In comparison with the major differences seen in the von Mises stress distributions, relatively good agreement can be seen in the direct stress in the tangential direction. The main differences again occur towards the boundaries of the section of roughness. The region between x = 0.430 mm and x = 0.440 mm has higher contact pressures in the asperity contact model, and the region between x = 0.430 mm and x = 0.480 mm has higher magnitudes of von Mises stress. In the contours of direct stress in the tangential direction, this region is found to have higher magnitudes of compressive stress at the surface, and in the subsurface region close to the surface (z < 0.01 mm).

The region between x = 0.520 mm and x = 0.530 mm has lower contact pressures in the asperity contact model and lower magnitudes of von Mises stress than in the complete contact model. In the contours of direct stress in the tangential direction, this is reflected in lower magnitudes of compressive stress, both at the surface and to depths of approximately z = 0.01 mm in the subsurface material. Nonetheless, some similarities are still seen between the two models. Subsurface regions of low magnitude compressive stress are found to occur directly beneath moderately loaded contacts. Examples of these can be seen at approximately x = 0.488 mm and x = 0.502 mm. These regions have been eliminated from the subsurface region in the more heavily loaded regions as previously discussed.

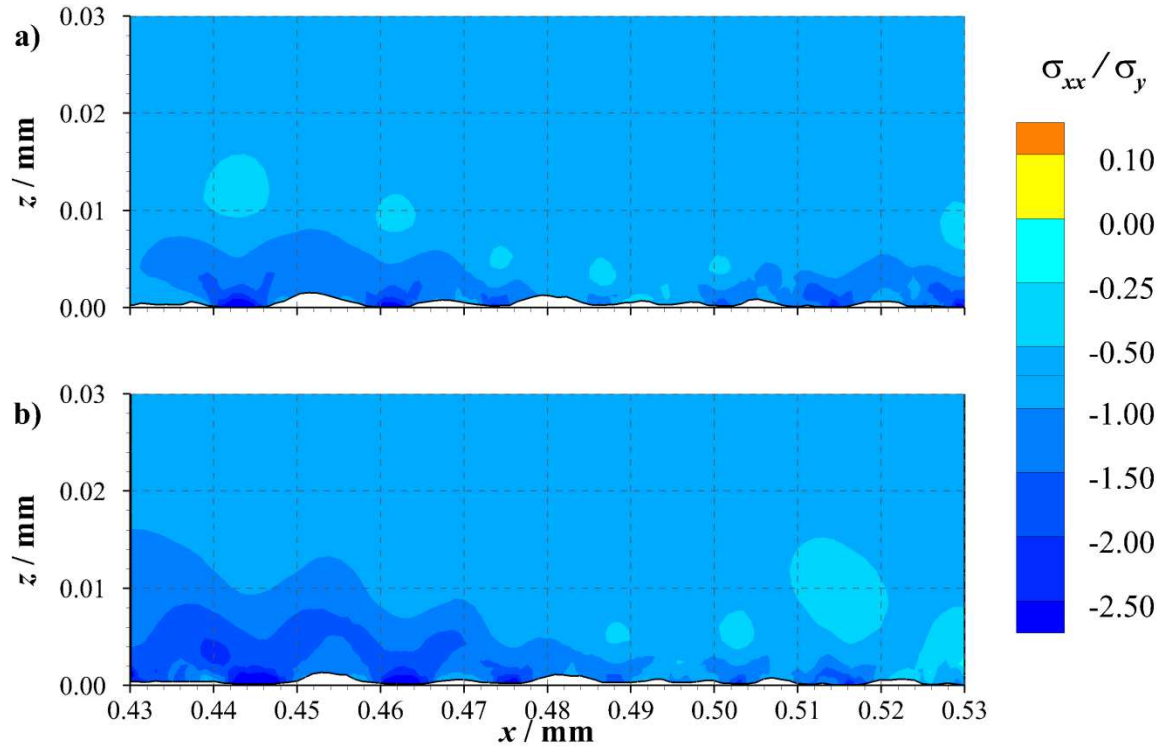

Figure 6.25 - Contours of normalised direct stress in the tangential direction for section of roughness from x = 0.43 mm to x = 0.53 mm; a) complete contact model, b) asperity contact model. σ_y = 2.550 GPa and E_T / E = 0.05 for each model.

6.4.3. Residual results

6.4.3.1. Surface 1

Figure 6.26 shows the residual roughness profile for both the complete contact model and asperity contact model for the section of roughness between x = −0.29 mm and x = −0.19 mm. The load applied to the section of roughness in the asperity contact model was equivalent to that found to be applied to the same section of roughness in the complete contact model subject to a nominal Hertzian contact pressure of 1.0 GPa. The load profiles were previously shown in Figure 6.17.

Three distinct regions of residual deflection can be seen to occur in both the complete contact and asperity contact models. These can be seen between x = −0.271 mm and x = −0.268 mm, x = −0.235 mm and x = −0.230 mm and x = −0.228 mm and x = −0.219 mm. Good agreement between the two models can be seen to occur for the first region of residual deflection, although the asperity contact

predicts increased deflection in comparison to the complete contact model. This is not unexpected as the profile under load was found to predict larger deflections. It was suggested that this increased deflection was due to a difference in the way the surface carried the load in each model, as a result of the contact geometry in the complete contact model changing for sections of roughness away from the contact centre. This difference is not so apparent in the residual profiles for this section of roughness, except for the small difference in magnitude of residual deflections for the two asperities.

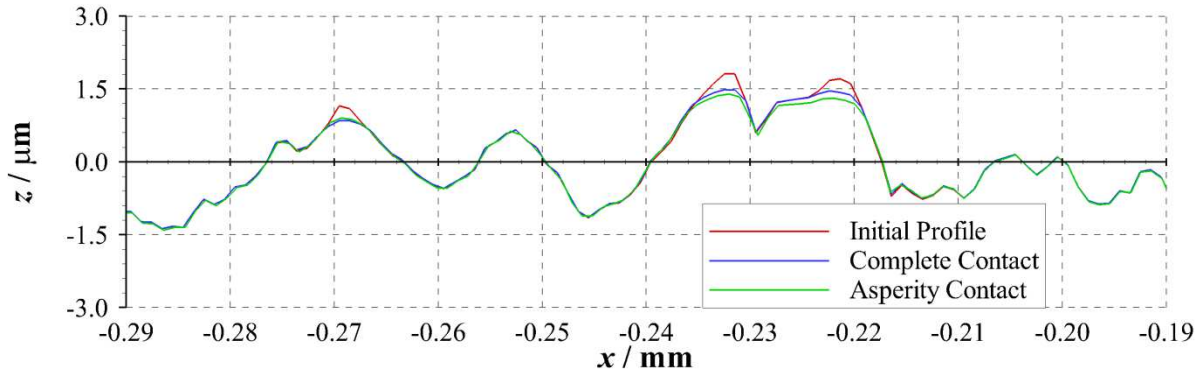

Figure 6.26 - Comparison of residual surface roughness profiles from complete contact model and asperity contact model for section of roughness from x = –0.29 mm to x = –0.19 mm. σ_y = 2.550 GPa and E_T / E = 0.05 for each model.

Figure 6.27 shows the residual normalised von Mises stress contours for the section of roughness between x = −0.29 mm and x = −0.19 mm in the complete contact model and in the asperity contact model previously shown in Figure 6.26. In each model, the regions of von Mises stress greater than $0.1\sigma_y$ align well with regions of material yield under the applied load shown in Figure 6.18. As previously discussed, these regions of plasticity extend deeper into the subsurface material in the asperity contact model than the complete contact model, and this is reflected in the residual stresses. Von Mises stresses greater than $0.1\sigma_y$ extend to a subsurface depth of z = 0.016 mm in the complete contact model in Figure 6.27a, while this region extends to a depth of z = 0.023 mm in the asperity contact model in Figure 6.27b. The effects of the asperity contact model boundaries can also be seen. At depths less than z = 0.010 mm, the residual von Mises stress exceeded $0.1\sigma_y$ at each

of the model boundaries in the asperity contact model. This did not occur in these locations in the complete contact model.

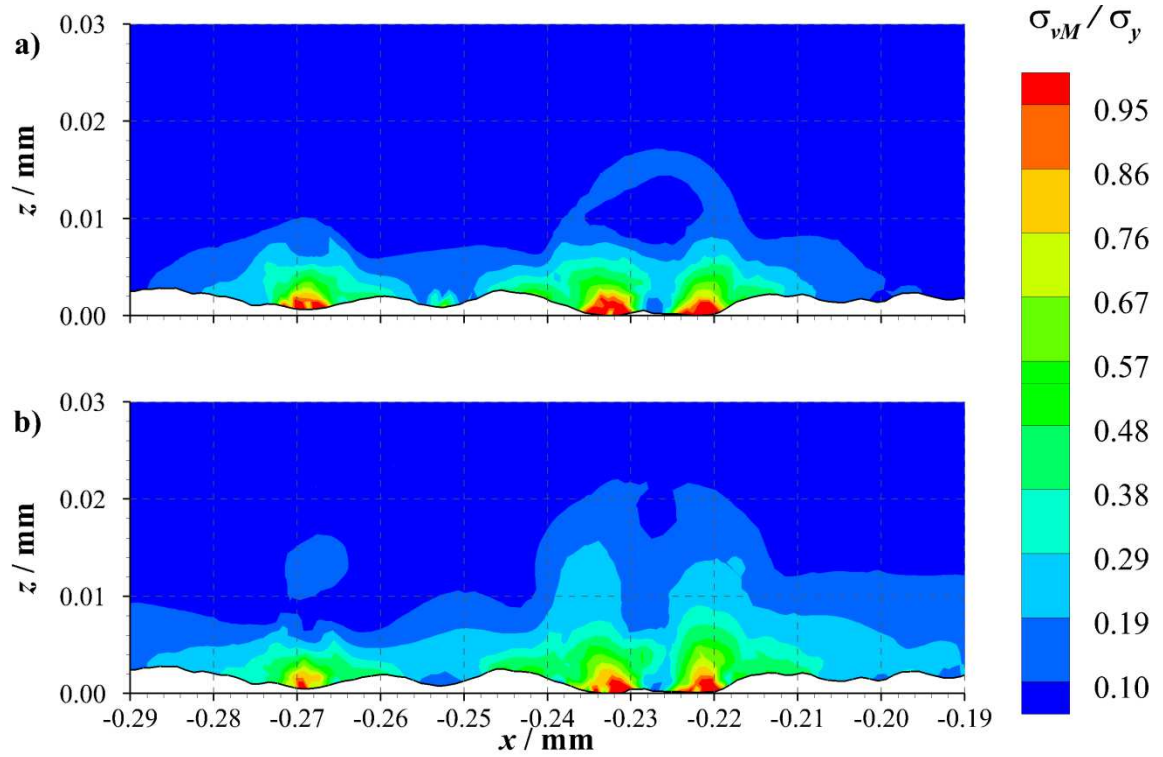

Figure 6.27 - Contours of normalised residual von Mises stress for section of roughness from x = −0.29 mm to x = −0.19 mm; a) complete contact model, b) asperity contact model. σ_y = 2.550 GPa and E_T / E = 0.05 for each model.

Figure 6.28 shows the contours of residual normalised direct stress in the tangential direction for the section of roughness between x = −0.29 mm and x = −0.19 mm in the complete contact model and in the asperity contact model previously shown in Figure 6.26. Both models show regions of tensile stress at the surface where asperity contacts have occurred, and beneath the surface, with the highest magnitude tensile stresses typically occurring directly beneath these contacts. These two regions of tensile stress are separated by a band of compressive stress. As previously discussed, the asperities between x = −0.235 mm and x = −0.230 mm and x = −0.228 mm and x = −0.219 mm carry more of the applied load and deflect more in the asperity contact model than in the complete contact model. As a result of this a larger region of high magnitude subsurface tensile stress can be found at approximately x = −0.227 mm, z = 0.023 mm in Figure 6.28a in comparison to the complete

contact model in Figure 6.28b. In contrast, the region of tensile stress at x = −0.269 mm, z = 0.009 mm in the complete contact model is reduced in size and magnitude in the asperity contact model. Furthermore, in the asperity contact model, less interaction between the subsurface tensile stress regions in seen to occur, with the two regions separated by compressive stress. At the surface, because of the reduction in load carried by the asperity at approximately x = −0.269 mm, no tensile stress is found to occur at the surface, whilst increased magnitude tensile stresses are found for the asperities between x = −0.235 mm and x = −0.230 mm and x = −0.228 mm and x = −0.219 mm. The symmetrical boundaries of the asperity contact model result in a deeper, higher magnitude band of compressive stress between the surface and subsurface tensile stress regions.

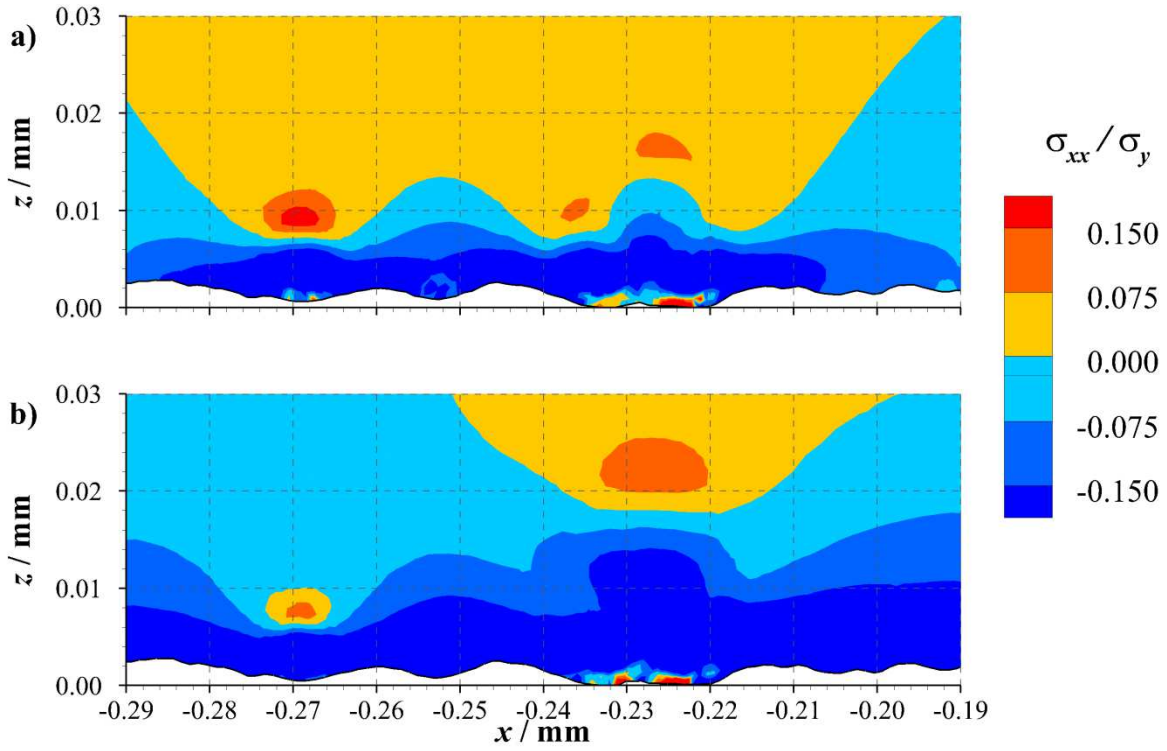

Figure 6.28 - Contours of normalised residual direct stress in the tangential direction for section of roughness from x = −0.29 mm to x = −0.19 mm; a) complete contact model, b) asperity contact model. σ_y = 2.550 GPa and E_T / E = 0.05 for each model.

6.4.3.2. Surface 2

Figure 6.29 shows the residual roughness profile for both the complete contact model and asperity contact model for the section of roughness between x = −0.10 mm and x = 0.00 mm. The load applied to the section of roughness in the asperity contact model was equivalent to that found to be applied to the same section of roughness in the complete contact model subject to a nominal Hertzian contact pressure of 1.5 GPa.

Seven regions of significant residual deflection can be seen to occur in each of the models, at approximately x = −0.093 mm, x = −0.081 mm, x = −0.057 mm, x = −0.045 mm, x = −0.035 mm, x = −0.026 mm, and x = −0.002 mm. Good agreement is observed in the magnitude of the residual deflections seen at each of these locations, and in the shape of the residual profile for this section of the rough surface. As previously discussed, this section of roughness is at the centre of the contact, and as a result the contact geometry in the complete contact model does not change before the section of roughness is loaded. As a result, the agreement between the two models is excellent.

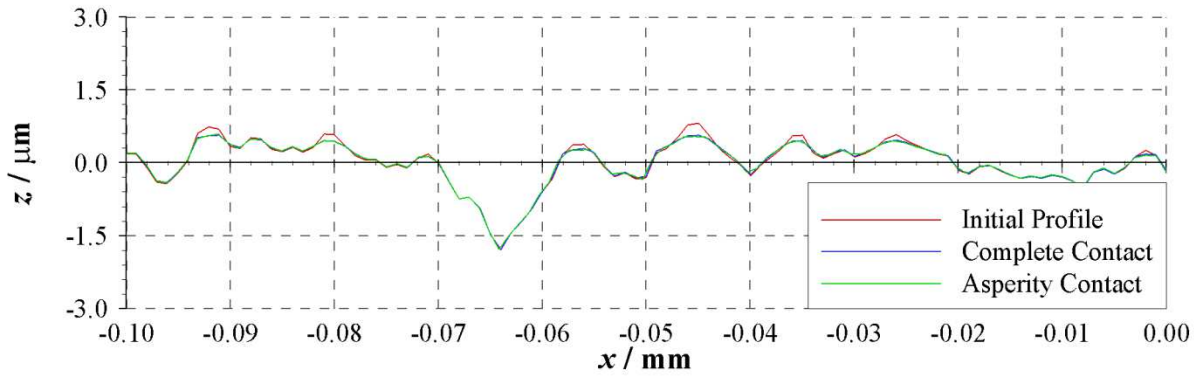

Figure 6.29 - Comparison of residual surface roughness profiles from complete contact model and asperity contact model for section of roughness from x = −0.10 mm to x = 0.00 mm. σ_y = 2.550 GPa and E_T / E = 0.05 for each model.

Figure 6.30 shows the residual normalised von Mises stress contours for the section of roughness between x = −0.10 mm and x = 0.00 mm in the complete contact model and in the asperity contact model previously shown in Figure 6.29. As found previously, the regions of residual von Mises stress greater than $0.1\sigma_y$ align well with the regions of material plasticity under load, von Mises stress

greater than $0.95\sigma_y$, in Figure 6.21. Whilst under load, it was found that for the asperity contact model, material yielded to a slightly lower depth. This can be seen in the residual stress distributions where a stress of between $0.1\sigma_y$ and $0.19\sigma_y$ can be found at a depth of z = 0.010 mm in the asperity contact model in Figure 6.30b. In the complete contact model, this stress extends to a depth of z = 0.008 mm, but less often. Whilst under load, the most prominent difference between the two models occurred at the surface between x = −0.004 mm and x = 0.000 mm. The region of von Mises stress greater than $0.95\sigma_y$ was significantly larger in the asperity contact model than in the complete contact model. In the residual results this was found to occur once more as the magnitude of von Mises stress in this location is significantly greater. Von Mises stress greater than $0.1\sigma_y$ is also found to occur to a greater depth in this location in the asperity contact model. A further effect of this difference is in the interaction of von Mises stress fields in the region between x = −0.02 mm and x = −0.01 mm at depths up to z = 0.01 mm. In the complete contact model, the majority of this material has a von Mises stress of $0.19\sigma_y$ or less. In the asperity contact model, a significant amount of the material has von Mises stress greater than $0.19\sigma_y$, and in some cases exceeds $0.29\sigma_y$. As previously discussed, this is thought to be due to the boundary of the asperity contact model occurring at x = 0.00 mm.

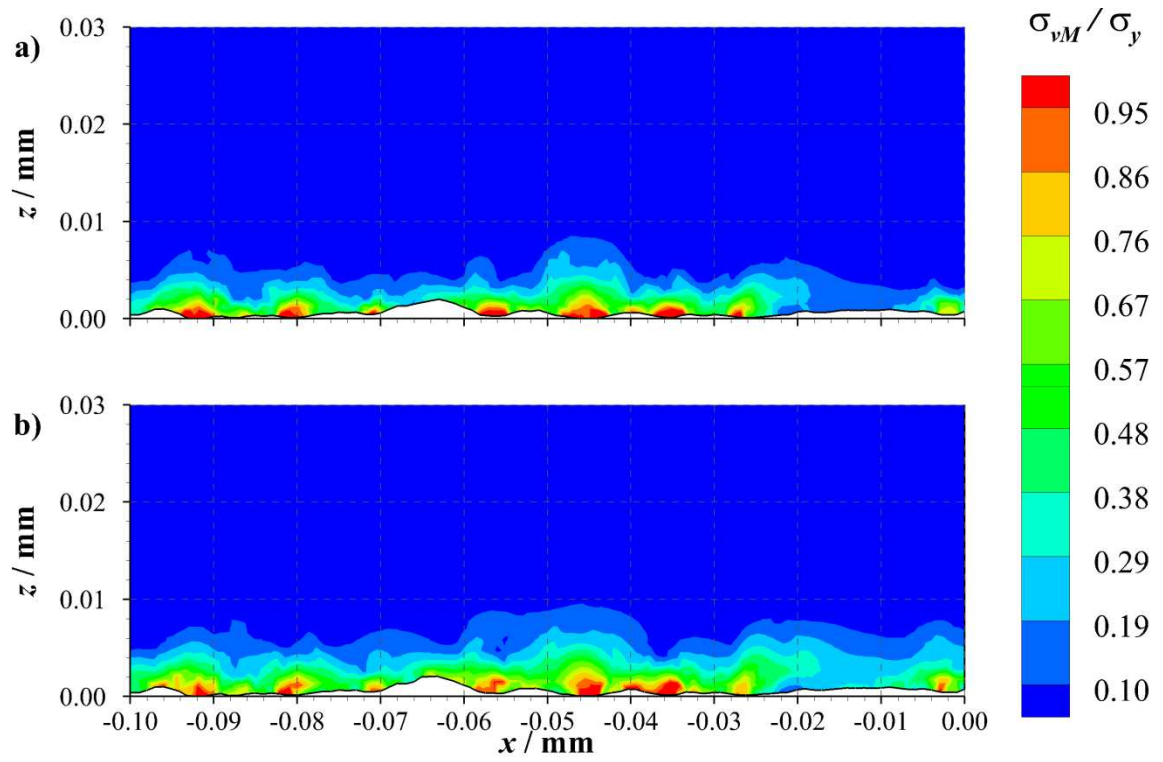

Figure 6.30 - Contours of normalised residual von Mises stress for section of roughness from x = −0.10 mm to x = 0.00 mm; a) complete contact model, b) asperity contact model. σ_y = 2.550 GPa and E_T / E = 0.05 for each model.

Figure 6.31 shows the contours of residual normalised direct stress in the tangential direction for the section of roughness between x = −0.10 mm and x = 0.00 mm in the complete contact model and in the asperity contact model previously shown in Figure 6.29. As has previously been shown, regions of tensile stress at the surface are separated from regions of subsurface tensile stress by a band of compressive stress. In the complete contact model in Figure 6.31a, the regions of surface tensile stress are fairly small, and yet in the asperity contact model Figure 6.31b, these regions of tension disappear almost entirely. This is not dissimilar to what was seen previously in Figure 6.28 at x = −0.269 mm. A similar trend is seen in that the band of compressive stress is found to be thicker and extends to a greater depth in the asperity contact model. However, the regions of peak subsurface tensile stress remain consistent in each model. In particular, this can be seen at approximately x = −0.046 mm, where the peak tensile stress differs in depth by approximately 0.002 mm. Some seemingly large differences occur in the subsurface material, for example between x = −0.10 mm

and x = −0.08 mm and a depth greater than z = 0.02 mm, where the stress is found to be tensile in the complete contact model, but compressive in the asperity contact model. These stresses are of very small magnitude, and as such the difference is actually very small.

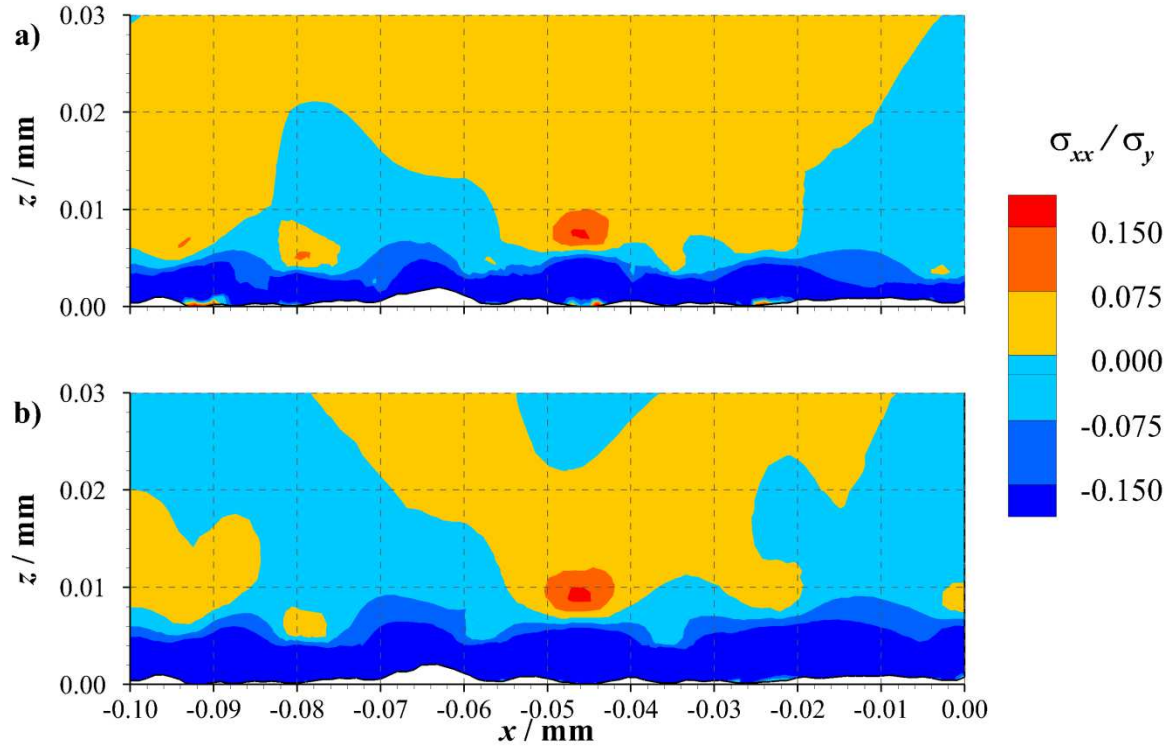

Figure 6.31 - Contours of normalised residual direct stress in the tangential direction for section of roughness from x = −0.10 mm to x = 0.00 mm; a) complete contact model, b) asperity contact model. σ_y = 2.550 GPa and E_T / E = 0.05 for each model.

6.4.3.3. Surface 3

Figure 6.32 shows the residual roughness profile for both the complete contact model and asperity contact model for the section of roughness between x = 0.43 mm and x = 0.53 mm. The load applied to the section of roughness in the asperity contact model was equivalent to that found to be applied to the same section of roughness in the complete contact model subject to a nominal Hertzian contact pressure of 2.0 GPa.

Partial agreement can be seen to occur across the residual profile. It has previously been discussed how the asperity contact model has larger contact pressures than the complete contact model

between x = 0.430 mm and x = 0.440 mm, and a larger amount of material yield occurs between x = 0.430 mm and x = 0.480 mm. Therefore it is unsurprising that larger asperity deflection can be seen to occur for asperities in these regions in the asperity contact model. This can be seen for the asperities from x = 0.440 mm to x = 0.448 mm and x = 0.460 mm to x = 0.465 mm. Across the remainder of the section of roughness, good agreement is seen to occur between the two models.

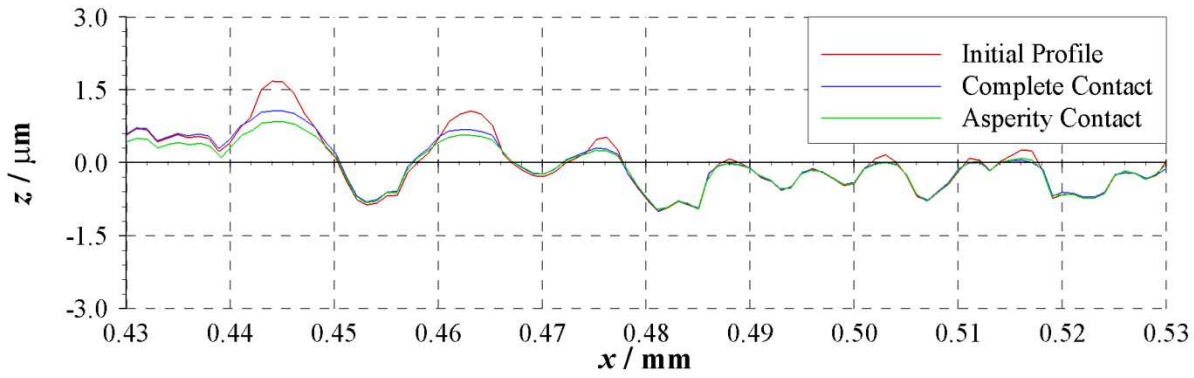

Figure 6.32 - Comparison of residual surface roughness profiles from complete contact model and asperity contact model for section of roughness from x = 0.43 mm to x = 0.53 mm. σ_y = 2.550 GPa and E_T / E = 0.05 for each model.

Figure 6.33 shows the residual normalised von Mises stress contours for the section of roughness between x = 0.43 mm and x = 0.53 mm in the complete contact model and in the asperity contact model previously shown in Figure 6.32. Better agreement is found to occur for the section of roughness than was found whilst under load. However, the effects of the extended regions of material plasticity in the asperity contact model whilst under load are evident in the residual stress contours. In the complete contact model, beneath a depth of approximately z = 0.014 mm, the von Mises stress is below $0.1\sigma_y$. However, as a result of the extended region of material yield between x = 0.43 and x = 0.48 mm under load, larger residual stresses remain over the corresponding region in Figure 6.33b. This can be seen in particular between x = 0.43 mm and x = 0.45 mm where the von Mises stress is between $0.19\sigma_y$ and $0.29\sigma_y$ at a depth of z = 0.03 mm. Despite this major difference, the stress distributions throughout the rest of the material display reasonable agreement between models. The main difference is the depth to which stresses of between $0.1\sigma_y$ to $0.19\sigma_y$ extend. For

example, at x = 0.516 mm stresses of this magnitude extend only to a depth of approximately z = 0.007 mm in the complete contact model. But to a depth of approximately z = 0.025 mm in the asperity contact model. Residual stresses of higher magnitudes, greater than $0.48\sigma_y$ are restricted to similar depths of approximately z = 0.005 mm. However, as previously discussed, regions of plasticity extend slightly deeper into the subsurface material in the asperity contact models. As a result, elevated von Mises stresses extend into the corresponding regions once the load has been removed.

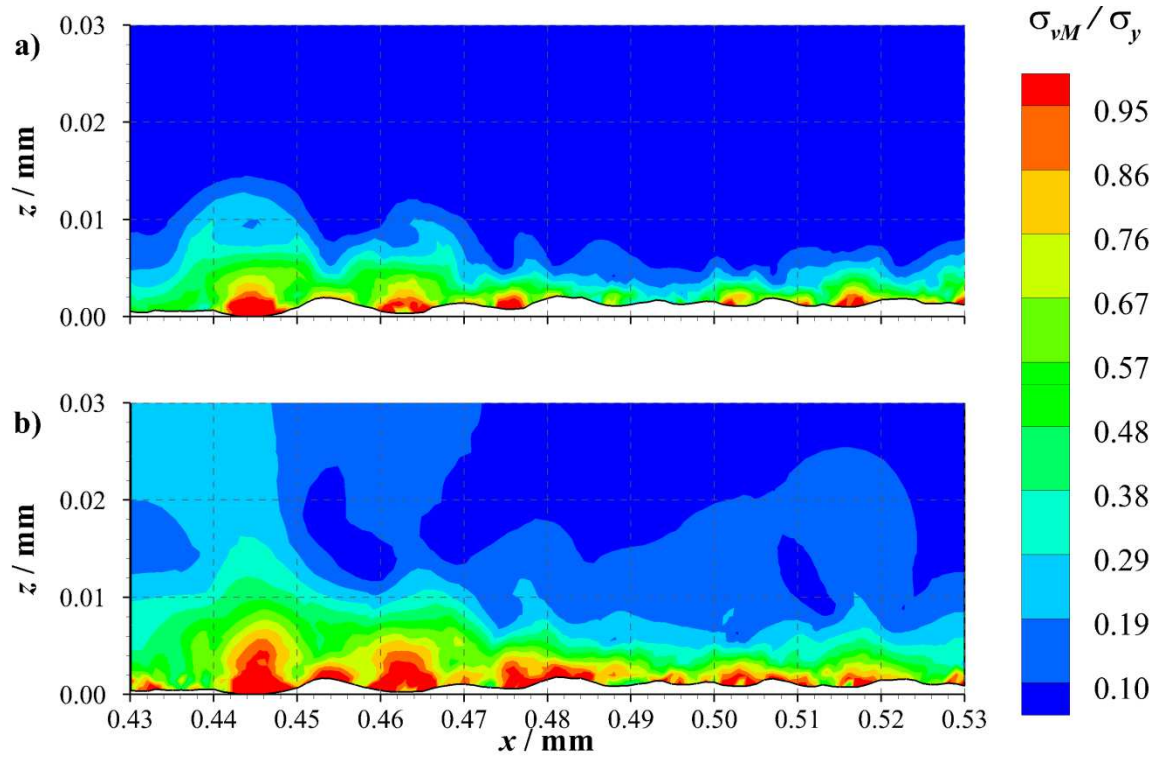

Figure 6.33 - Contours of normalised residual von Mises stress for section of roughness from x = 0.43 mm to x = 0.53 mm; a) complete contact model, b) asperity contact model. σ_y = 2.550 GPa and E_T / E = 0.05 for each model.

Figure 6.34 shows the contours of normalised residual direct stress in the tangential direction for the section of roughness between x = 0.43 mm and x = 0.53 mm in the complete contact model and in the asperity contact model previously shown in Figure 6.32. Very little agreement can be found between the models. In the complete contact model in Figure 6.34a, regions of tensile stress occur both at the surface and beneath the surface. The majority of the asperity contact model shown in Figure 6.34b is under compressive stress, with significantly smaller regions of surface and subsurface

tension. The only similarity between the two models is in the regions of subsurface tension. The tensile region at x = 0.463 mm, z = 0.012 mm in the complete contact model is also found in the asperity contact model, albeit at a smaller magnitude. The regions of tension in the complete contact model at x = 0.445 mm, z = 0.015 mm and x = 0.516 mm, z = 0.008 mm are instead regions of low magnitude compressive stress in the asperity contact model.

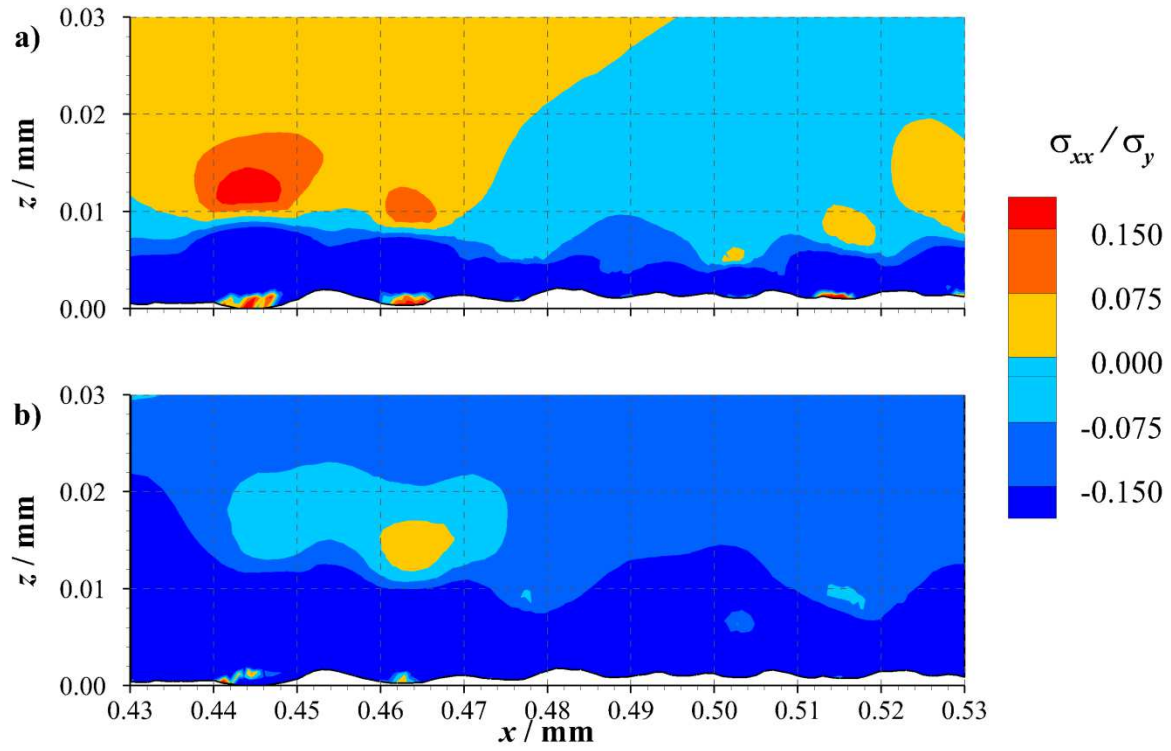

Figure 6.34 - Contours of normalised residual direct stress in the tangential direction for section of roughness from x = 0.43 mm to x = 0.53 mm; a) complete contact model, b) asperity contact model. σ_y = 2.550 GPa and E_T / E = 0.05 for each model.

6.5. Conclusions

This chapter has described the analysis of individual asperity contacts within a complete contact. The analysis consisted of discussion of residual stresses found in the complete contact models described in Chapter 5, parametric analysis of complete contacts subject to a range of nominal Hertzian contact pressures, and the simulation of sections of roughness from contact surfaces to assess the difference between complete contact models and smaller, less computationally intensive asperity contact models.

Links between experimental findings on surface cracking and pitting failure and locations of the maximum principal stresses both at the surface and in the subsurface material were found. It is proposed that the maximum principal stresses at the surface are typically found at orientations perpendicular to characteristic crack growth. Subsurface principal stresses normal to the surface are also found at depths where cracks have been found to penetrate into the deeper subsurface material.

The parametric analysis studied the relationships between residual stresses found to occur at the surface and the maximum residual deflection normal to the surface of the associated asperity. It was found that a pure power law relationship could not accurately represent the results found from the contact simulations. Furthermore, the trend lines that were found as a result of the least squares method were dominated by the number of asperities that experienced small residual deflections. The result is a particularly poor prediction of the stresses found for asperities with large asperity deflections. These asperities were of greater interest, as it is thought that the increased stresses affect fatigue life more significantly. As a result, manually manipulated power laws were defined that more accurately represented this region of the results.

The comparison of the complete contact models and asperity contacts models showed that when considered correctly, smaller, less computationally intensive simulations of limited widths of roughness can provide very similar results to those found from modelling an entire contact. These

asperity contact models were found to most accurately agree with the complete contact model for sections of roughness close to the contact centre. For sections of roughness far from the contact centre, the agreement was found to decline due to the boundary conditions implemented in the asperity contact models. These boundary conditions were not sufficient to provide an equivalent solution. However, the asperity contact models using sections of roughness from the centre of the contact gave excellent agreement.

Conclusions and future work

7.1. Summary of work

This thesis has been concerned with the investigation of the contact of real rough surfaces, typical of those found on the teeth of gears. In the early stages of operating life, freshly manufactured surfaces undergo a process known as running-in, where relatively large amounts of plastic deformation occurs. This thesis has modelled elastic-plastic contact based on measured profiles to investigate the residual stresses induced by this plastic deformation. As part of this investigation, both theoretical work, in the form of finite element analysis, and experimental work have been undertaken.

Finite element modelling techniques were initially developed using known contact problems for verification. This included comparisons with pre-existing studies from the literature for both elastic and elastic-plastic contact of spheres, cylinders and sinusoidal surfaces. After developing a method for importing as-measured, rough surface profiles into Abaqus, profiles from unrun and run gear surfaces were used in contact simulations. Difficulties were encountered in the simulations for unrun surfaces, where more aggressive surface features are found. These difficulties involved excessive element distortions as a result of larger relative asperity deflections. In turn, these distortions resulted in excessive surface penetrations and extreme contact pressure events that were judged to be unsatisfactory. A number of new modelling techniques were trialled in response to these factors, improving the robustness of the contact models.

Using these developed modelling techniques, unrun surface profiles were used in an investigation of multiple load applications, and of the effect of tangential loading including friction. The aim of the multiple load applications was to simulate the process of running-in. The results of this investigation showed that the overwhelming majority of residual asperity shape change occurred in the first loading cycle. Subsequent loading cycles resulted in repeated application of contact pressure and

stress in both the loaded and residual states. Deformation under load was predominantly elastic in the second and subsequent applications of the same load. In studying the effect of tangential loads, it was found that the coefficient of friction had to be defined as unrealistically large for noticeable effects to be seen in the contact behaviour. For more realistic coefficients of friction, only small differences could be found. Where differences did occur, it was found that peak stresses were closer to the surface than in equivalent simulations having only normal load.

Alongside the finite element analysis, an experimental procedure for the contact of two crowned, rough disks was established. The aim of the experimental programme was to provide verifiable deformation of rough surface profiles that could be recreated using Abaqus. To simplify the model, the test disks were carefully chosen. The first disk was nitrided and superfinished. This was simulated in Abaqus as a smooth, perfectly elastic solid. The second disk was case carburised with a ground surface finish, typical of the specification of gear teeth surfaces. This was simulated as a rough, elastic-plastic solid in Abaqus. Surface profiles were taken at three circumferential positions, before being loaded with nominal Hertzian contact pressures of 1.0 GPa, 1.5 GPa, and 2.0 GPa respectively. Residual surface profiles were measured after loading and correlated with the initial profiles using undeformed asperity peaks and valley features. These loads were recreated in Abaqus and the residual surface geometry of the finite element analysis and experiment compared. Good agreement was generally found to occur.

In the loaded state, stresses were typically found to be compressive. Upon removal of the load, regions of residual tensile stress were found to occur in the proximity of heavily deformed asperities. These were found both at the surface and subsurface. Surface tensile stresses were in regions where crack initiation has been found to occur in test gears, with the orientation of the maximum principal stress found to be perpendicular to the typical direction of crack growth in micropitting. The regions of subsurface tension occurred at depths characteristic of the progression of micropitting to macro

pitting failure. Cyclic loading of compressive and tensile stress has the potential to aid crack initiation and propagation.

Parametric analysis was used to explore the relationship between residual surface stresses and the maximum residual deflection normal to the surface of an asperity. The aim of this analysis was to provide a tool that could approximately predict residual surface stresses as a result of a measured residual deflection. This would then be used alongside other work in the research group investigating the fatigue life of rough surface contacts. A pure power law did not accurately describe the data, and a trend line generated using the least squares method was distorted by the higher number of asperities with small residual deflections. This resulted in poor prediction of residual stresses for asperities experiencing larger residual deflections. Manually manipulated trend lines were therefore used to describe the results.

7.2. Conclusions

- Finite element analysis can provide accurate residual deformation of asperities in comparison with experimental results.
- Repeated applications of the same load resulted in predominantly elastic behaviour.
- Tangential loading caused little change in contact behaviour at practical coefficients of friction.
- Large plastic deformation of asperities resulted in surface and subsurface regions of residual tensile stress.
- The location of these residual tensile stresses aligns well with experimental studies of the location of crack initiation and propagation typically found in micropitting.

7.3. Suggestions for future work

The work in this thesis has been part of a wider area of research within the research group at Cardiff University. This research is concerned with an investigation of the fatigue life of rough surfaces operating under mixed lubrication conditions. The current work in the analysis of the fatigue of rough surfaces has considered elastic bodies with no residual stresses as a result of running-in (Evans *et al*. 2012). In the future, the work described in this thesis could be incorporated with the fatigue life analysis to superimpose the residual stresses, as a result of plastic deformation during initial running-in, with the cyclic elastic contact stresses of a typical operating life cycle. This will allow the investigation of the impact of residual stresses as a result of running-in on the subsequent fatigue life of rough surfaces.

In the work discussed in Chapter 4 regarding the running-in process of a surface, it was found that the majority of plastic deformation occurred within the first application of any given load. In correlating contact of real rough surfaces of test disks with finite element analysis, only single applications of load were performed. It may be of interest to further investigate the plastic deformation contribution to the running-in process by performing multiple applications of the same load to confirm whether the results achieved in Chapter 4 can be replicated in experimental tests. Additional care would be required in order to ensure than the load was applied to the same circumferential location each time. In a single load application, this was less crucial due to the length of profiles measured to detect the contact region.

While good agreement between the results from finite element analysis and experiment has been found, a number of assumptions and simplifications have been made. In the future, these should be reconsidered. In the present model, asperity features were considered to be two-dimensional, to allow simple modelling of a plane strain problem. In many manufacturing processes, such as grinding, this is not an unreasonable assumption, as shown by the agreement found in this research. However, asperities are generally three-dimensional features and modelling them as such will

provide more accurate solutions. To introduce three-dimensional surfaces to Abaqus, modifications to the current excel macros and python scripts are needed to consider y-coordinates, as well as x and z. Yastrebov *et al*. (2011) and Olshevskiy *et al*. (2012) have both used finite element analysis to model three-dimensional roughness. Both have encountered considerable simulation time difficulties and so an appraisal of computational resources would be recommended if such models were to be created.

In the current model, simple material properties are assumed, either utilising elastic-perfectly plastic properties, or varying degrees of linear strain hardening. In reality, material behaviour is more complex, and there are a number of ways in which this can be implemented in Abaqus models. Assuming that the user knows the complete stress-strain behaviour for the material, the simplest option would be to approximate the stress-strain curve using a number of linear sections. This would be implemented in the same manner as the linear strain-hardening behaviour previously discussed, but consist of additional rows defining the plastic behaviour. A more complex method would be to create a user-defined material using a UMAT user subroutine (Abaqus 2010a). To develop the knowledge to create user-defined materials it is recommended that simple materials, such as purely elastic, elastic-perfectly plastic and linear strain hardening types are created first. These user-defined materials can then be compared with those defined using Abaqus/CAE as described in this thesis. Subsequently, the more complex behaviour of real engineering materials can be measured and used within Abaqus with the aim of obtaining more accurate results.

In the comparison with experimental results, the best agreement was found to occur for a nominal Hertzian contact pressure of 1.0 GPa. With increased pressure, while reasonable agreement was found to occur, inconsistencies in the under and over prediction of plastic deformation was seen to occur. It was proposed in the discussion of these results that the way in which the profiles were filtered could be a contributing factor in these differences. With increased pressure, larger asperity deformation occurs, which in turn results in a greater effect upon the mean line of the roughness. In

comparing initial and residual profiles with different mean lines used for filtering, the comparison at high pressures may not be as equivalent as at lower pressures. It is suggested that for comparisons in the future, a new method of filtering profiles be developed in order to eliminate any contribution of the filtering process to the differences seen.

An issue with finite element analysis is the potential for error in determining the contact area. The precision with which the edge of a contact is detected is limited to plus or minus the element size. In a single contact problem, this effect can be more fully accounted for by using more elements of reduced size to reduce the potential for error to an acceptable limit. For contact of rough surfaces, the number of elements required is already significant and so increasing the number of surface elements is not always practical. To solve this issue, another form of adaptive meshing could provide a solution. Adaptive remeshing is an automated iterative process, that runs the prescribed analysis multiple times, altering the mesh between analyses based on specified rules that can be defined by the user. The process will repeatedly iterate until a set number of cycles is complete, or until targets are met. These targets are output variable based, and are essentially mesh dependency checks, judging the difference in output parameters between simulations. Once the difference is below a prescribed limit, the process is complete and terminates. For example, the user may choose the von Mises stress as the variable of interest, ensuring that heavily loaded regions become more densely meshed. An example of this can be seen in Figure 7.1.

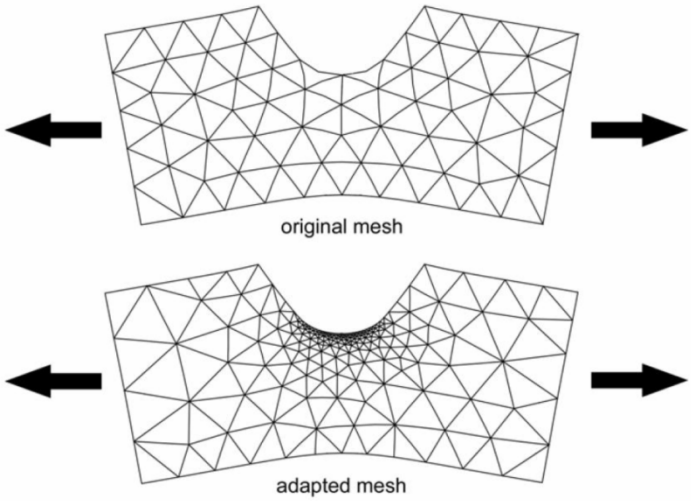

Figure 7.1 - Stress raiser mesh before and after refinement (Abaqus 2010a).

As contacts are heavily loaded, this will ensure more elements in contact regions, enhancing the accuracy of the contact dimension. An increased number of elements around the contact regions will also result in an increased resolution of stresses, which may be advantageous for studying phenomena such as micropitting which occurs on a scale of just a few microns. The process can also work in reverse, increasing element size in regions where little activity occurs. It should be noted that adaptive meshing requires triangular elements, either alongside or in combination with quadrilateral elements in order to be implemented. The effect of using triangular elements should be fully evaluated before proceeding with such an investigation.

Assuming that triangular elements are found to be suitable, the implementation of adaptive meshing is relatively simple. In the **Mesh** module, the user must select **Adaptivity** from the toolbar, and create a **Remeshing Rule**, defining the regions and step in which the adaptation is required. In the subsequent menu, a number of options become available that are described in much greater detail within the Abaqus User's Manual (Abaqus 2010a). These include the error indicator (such as von Mises stress, or plastic strain), the error tolerance, minimum and maximum element size, the maximum total number of elements and the rate of refinement/coarsening allowed during the

process. To submit standard analyses, the **Job** module is used to create and submit Jobs. To use adaptive meshing, the **Job** module is still used, but an **Adaptivity Process** is created and submitted instead. Upon creating the Adaptivity Process, the user can specify the maximum number of iterations that will be performed by Abaqus. Abaqus will then initially proceed as in a standard analysis until the first iteration is completed. The mesh is then automatically altered using the specified remeshing rules, before submitting and running the job again. This will be repeated until the error targets are met or the maximum number of iterations is achieved.

References

Abaqus 2010a. *Abaqus 6.10 - Analysis User's Manual*. Providence, RI, USA.: Dassault Systèmes, Simulia Corp.

Abaqus 2010b. *Abaqus 6.10 - Benchmarks Manual*. Providence, RI, USA.: Dassault Systèmes, Simulia Corp.

Abaqus 2010c. *Abaqus 6.10 - Scripting Reference Manual*. Providence, RI, USA.: Dassault Systèmes, Simulia Corp.

Abaqus 2010d. *Abaqus 6.10 - Scripting User's Manual*. Providence, RI, USA.: Dassault Systèmes, Simulia Corp.

Abaqus 2010e. *Abaqus 6.10 - Theory Manual*. Providence, RI, USA.: Dassault Systèmes, Simulia Corp.

Abbott, E.J. and Firestone, F.A. 1933. Specifying surface quality: a method based on accurate measurement and comparison. *Mechanical Engineering* 55, pp. 569–572.

Abdo, J. and Farhang, K. 2005. Elastic-plastic contact model for rough surfaces based on plastic asperity concept. *International Journal of Non-Linear Mechanics* 40(4), pp. 495–506.

Abudaia, F.B., Evans, J.T. and Shaw, B.A. 2005. Spherical indentation fatigue cracking. *Materials Science and Engineering A* 391(1-2), pp. 181–187.

Ahlroos, T., Ronkainen, H., Helle, A., Parikka, R., Virta, J. and Varjus, S. 2009. Twin disc micropitting tests. *Tribology International* 42(10), pp. 1460–1466.

Akyuz, F.A. and Merwin, J.E. 1968. Solution of nonlinear problems of elastoplasticity by the finite element method. *AIAA Journal* 6(10), pp. 1825–1831.

Alanou, M.P. 2006. Study of parameters influencing surface distress of gears. Cardiff University.

Amontons, G. 1699. On the resistance originating in machines. *French Royal Academy of Sciences*, pp. 206–22.

Amzallag, C., Gerey, J.P., Robert, J.L. and Bahuaud, J. 1994. Standardization of the rainflow counting method for fatigue analysis. *International Journal of Fatigue* 16(4), pp. 287–293.

Archard, J.F. 1957. Elastic deformation and the laws of friction. *Proceedings of the Royal Society of London. Series A, Mathematical and Physical Sciences* 243(1233), pp. 190–205.

Bailey, D.M. and Sayles, R.S. 1991. Effect of Roughness and Sliding Friction on Contact Stresses. *Journal of Tribology* 113, pp. 729–738.

Barber, G.C., Lee, J.C. and Ludema, K.C. 1987. Materials and surface finish effects in the breaking-in process of engines. *Journal of Engineering for Gas Turbines and Power* 109, pp. 380–387.

Barber, J.R. 2002. *Elasticity*. 2nd ed. Dordrecht: Kluwer Academic Publishers.

Barragan de Ling, F., Evans, H.P. and Snidle, R.W. 1989. Micro-Elastohydrodynamic Lubrication of Circumferentially Finished Rollers: The Influence of Temperature and Roughness. *Journal of Tribology* 111, pp. 730–736.

Beghini, E., Dwyer-Joyce, R.S., Ioannides, E., Jacobson, B., Lubrecht, A.A. and Tripp, J.H. 1992. Elastic/plastic contact and endurance life prediction. *Journal of Physics, D: Applied Physics* 379(25), pp. 379–383.

Benyajati, C., Olver, A. V and Hamer, C.J. 2003. An experimental study of micropitting, using a new miniature test-rig. *Tribology Series* 43, pp. 601–610.

Bhargava, V., Hahn, G.T. and Rubin, C.A. 1985a. An Elastic-Plastic Finite Element Model of Rolling Contact, Part 1: Analysis of Single Contacts. *Journal of Applied Mechanics* 52, pp. 67–74.

Bhargava, V., Hahn, G.T. and Rubin, C.A. 1985b. An Elastic-Plastic Finite Element Model of Rolling Contact, Part 2: Analysis of Repeated Contacts. *Journal of Applied Mechanics* 52, pp. 75–82.

Bhushan, B. 1985. The real area of contact in polymeric magnetic media—II: Experimental data and analysis. *ASLE Transactions* 28, pp. 181–197.

Bhushan, B. and Dugger, M.T. 1990. Real contact area measurements on magnetic rigid disks. *Wear* 137, pp. 41–50.

Bosman, R., Hol, J. and Schipper, D.J. 2011. Running-in of metallic surfaces in the boundary lubrication regime. *Wear* 271(7-8), pp. 1134–1146.

Boucly, V., Nélias, D. and Green, I. 2007. Modeling of the rolling and sliding contact between two asperities. *Journal of Tribology* 129, pp. 235–245.

Bowden, F.P. and Tabor, D. 1950. *The Friction and Lubrication of Solids, Part I*. Oxford: Clarendon Press.

Bowden, F.P. and Tabor, D. 1964. *The Friction and Lubrication of Solids, Part II*. Oxford: Oxford University Press Inc.

Bower, A.F. 1988. The influence of crack face friction and trapped fluid on surface initiated rolling contact fatigue cracks. *Journal of Tribology* 110, pp. 704–711.

BP 1969. *Lubrication Theory and its Application*. London: BP Trading Limited.

Broek, D. 1974. *Elementary engineering fracture mechanics*. 1st ed. Leyden: Noordhoff International Publishing.

Bryant, M.J., Evans, H.P. and Snidle, R.W. 2012. Plastic deformation in rough surface line contacts—a finite element study. *Tribology International* 46(1), pp. 269–278.

Bull, S.J., Evans, J.T., Shaw, B.A. and Hofmann, D.A. 1999. The effect of the white layer on micro-pitting and surface contact fatigue failure of nitrided gears. *Proceedings of the Institution of Mechanical Engineers, Part J: Journal of Engineering Tribology* 213(4), pp. 305–313.

Bush, A.W. and Gibson, R.D. 1975. The elastic contact of a rough surface. *Wear* 35(1), pp. 87–111.

Callister, W.D. 2003. *Materials Science and Engineering: An Introduction*. 6th ed. John Wiley & Sons, Inc.

Cardoso, N.F.R., Martins, R.R., Seabra, J.H.O., Igartua, A., Rodríguez, J.C. and Luther, R. 2009. Micropitting performance of nitrided steel gears lubricated with mineral and ester oils. *Tribology International* 42(1), pp. 77–87.

Carnes, K., Gresham, R.M., Canter, N. and Anderson, M. 2005. The Ten Greatest Events in Tribology History. *Tribology and Lubrication Technology* (June), pp. 38–47.

Chang, W.R. 1997. An elastic-plastic contact model for a rough surface with an ion-plated soft metallic coating. *Wear* 212, pp. 229–237.

Chang, W.R., Etsion, I. and Bogy, D.B. 1987. An Elastic-Plastic Model for the Contact of Rough Surfaces. *Journal of Tribology* 109(2), p. 257.

Chaudhri, M.M., Hutchings, I.M. and Makin, P.L. 1984. Plastic compression of spheres. *Philosophical Magazine A* 49(4), pp. 493–503.

Chen, W.W., Wang, Q.J., Wang, F., Keer, L.M. and Cao, J. 2008. Three-Dimensional Repeated Elasto-Plastic Point Contacts, Rolling, and Sliding. *Journal of Applied Mechanics* 75, p. 021021.

Chow, L.S.H. and Cheng, H.S. 1976. The effect of surface roughness on the average film thickness between lubricated rollers. *Journal of Lubrication Technology* 98(1), pp. 117–124.

Chung, J.C. 2010. Elastic–plastic contact analysis of an ellipsoid and a rigid flat. *Tribology International* 43(1-2), pp. 491–502.

Ciavarella, M., Delfine, V. and Demelio, G. 2006. A “re-vitalized” Greenwood and Williamson model of elastic contact between fractal surfaces. *Journal of the Mechanics and Physics of Solids* 54(12), pp. 2569–2591.

Ciavarella, M., Demelio, G., Barber, J.R. and Jang, Y.H. 2000. Linear elastic contact of the Weierstrass profile. *Proceedings of the Royal Society A: Mathematical, Physical and Engineering Sciences* 456(1994), pp. 387–405.

Ciavarella, M., Greenwood, J.A. and Paggi, M. 2008. Inclusion of “interaction” in the Greenwood and Williamson contact theory. *Wear* 265(5-6), pp. 729–734.

Cole, S.J. and Sayles, R.S. 1992. A Numerical Model for the Contact of Layered Elastic Bodies With Real Rough Surfaces. *Journal of Tribology* 114(2), p. 334.

D’Errico, F. 2011. Micropitting Damage Mechanism on Hardened and Tempered, Nitrided, and Carburizing Steels. *Materials and Manufacturing Processes* 26(1), pp. 7–13.

Davies, C.N. 2005. Effects of non-Newtonian rheology on the line contact elastohydrodynamic lubrication problem. Cardiff University.

Dawson, P.H. 1962. Effect of metallic contact on the pitting of lubricated rolling surfaces. *Journal of Mechanical Engineering Science* 4, pp. 16–21.

Dawson, P.H. 1968. Rolling contact fatigue crack initiation in a 0.3 per cent carbon steel. *Proceedings of the Institution of Mechanical Engineers* 183, pp. 75–86.

Dawson, P.H. 1961. The pitting of lubricated gear teeth and rollers. *Power Transmission* 30(351), p. 208.

Dowson, D. 1979a. *History of Tribology*. Longman Ltd.

Dowson, D. 1977. Men of Tribology: Leonardo da Vinci (1452-1519). *Journal of Lubrication Technology* 99(4), pp. 382–386.

Dowson, D. 1979b. Men of Tribology: William Bate Hardy (1864-1934), Arnold Sommerfeld (1868-1951). *Journal of Lubrication Technology* 101, pp. 393–397.

Dowson, D. and Higginson, G.R. 1959. A Numerical Solution to Elasto-Hydrodynamic Problem. *Journal of Mechanical Engineering Science* 1(1), pp. 6–15.

Dumas, G. and Baronet, C.N. 1971. Elastoplastic indentation of half-space by an infinitely long rigid circular cylinder. *International Journal of Mechanical Sciences* 13, pp. 519–530.

Etsion, I., Kligerman, Y. and Kadin, Y. 2005. Unloading of an elastic-plastic loaded spherical contact. *International Journal of Solids and Structures* 42, pp. 3716–3729.

Evans, H.P., Snidle, R.W., Sharif, K.J. and Bryant, M.J. 2012. Predictive modelling of fatigue failure in concentrated lubricated contacts. *Faraday Discussions* 156(1), pp. 105–121.

Evseev, D.G., Medvedev, B.M. and Grigoriyan, G.G. 1991. Modification of the elastic-plastic model for the contact of rough surfaces. *Wear* 150(1), pp. 79–88.

Fatemi, A. and Darrell, F. 1988. Critical plan approach to multiaxial fatigue damage including out-of-phase loading. *Fatigue and Fracture of Engineering Materials and Structures* 11(3), pp. 149–165.

Faulkner, A. and Arnell, R.D. 2000. The development of a finite element model to simulate the sliding interaction between two, three-dimensional, elastoplastic, hemispherical asperities. *Wear* 242, pp. 114–122.

Follansbee, P.S. and Sinclair, G.B. 1984. Quasi-static normal indentation of an elasto-plastic half-space by a rigid sphere - I. Analysis. *International Journal of Solids and Structures* 20(1), pp. 81–91.

Ford, H. 1963. *Advanced mechanics of materials*. London: Longmans.

Franse, A.G., Tangena, A.G. and Wijnhoven, P.J.M. 1985. The influence of asperity deformation and surface roughness on the coefficient of friction during sliding. In: Dowson, D., Taylor, C. M., Godet, M., and Berthe, D. eds. *Proc. 12th Leeds-Lyon Symposium on Tribology*. London: Butterworths.

Freeth, T., Bitsakis, Y., Moussas, X., Seiradakis, J.H., Tselikas, A., Mangou, H., Zafeiropoulou, M., Hadland, R., Bate, D., Ramsey, A., Allen, M., Crawley, A., Hockley, P., Malzbender, T., Gelb, D., Ambrisco, W. and Edmunds, M.G. 2006. Decoding the ancient Greek astronomical calculator known as the Antikythera Mechanism. *Nature* 444, pp. 587–591.

Gao, Y.F., Bower, A.F., Kim, K.S., Lev, L. and Cheng, Y.T. 2006. The behavior of an elastic–perfectly plastic sinusoidal surface under contact loading. *Wear* 261(2), pp. 145–154.

Gay, R.J. 2010. Personal communication.

Gelinck, E.R.M. and Schipper, D.J. 1999. Deformation of Rough Line Contacts. *Journal of Tribology* 121, pp. 449–454.

Gong, Z.-Q. and Komvopoulos, K. 2003. Effect of surface patterning on contact deformation of elastic-plastic layered media. *Journal of Tribology* 125(1), pp. 16–24.

Green, I. 2005. Poisson ratio effects and critical valus in spherical and cylindrical Hertzian contacts. *International Journal of Applied Mechanics and Engineering* 10(3), pp. 451–462.

Greenwood, J.A., Putignano, C. and Ciavarella, M. 2011. A Greenwood & Williamson theory for line contact. *Wear* 270(3-4), pp. 332–334.

Greenwood, J.A. and Tripp, J.H. 1970. The contact of two nominally flat rough surfaces. *Proceedings of the Institution of Mechanical Engineers* 185(1970), pp. 625–633.

Greenwood, J.A. and Tripp, J.H. 1967. The elastic contact of rough spheres. *Journal of Applied Mechanics* 34, pp. 153–159.

Greenwood, J.A. and Williamson, J.B.P. 1966. Contact of Nominally Flat Surfaces. *Proceedings of the Royal Society of London. Series A, Mathematical and Physical Sciences (1934-1990)* 295(1442), pp. 300–319.

Grubin, A.N. and Vinogradova, I.E. 1949. Investigation of the Contact of Machine Components. *Central Scientific Research Institute for Technology and Mechanical Engineering* Book No 30(DSIR Translation No 337).

Hamrock, B.J. and Anderson, W.J. 1983. NASA Reference Publication 1105. *Rolling-element bearings*.

Hamrock, B.J., Jacobson, B.O. and Schmid, S.R. 2005. *Fundamentals of machine elements*. 2nd ed. Boston, MA: McGraw-Hill Higher Education.

Handzel-Powierza, Z., Klimczak, T. and Polijaniuk, A. 1992. On the experimental verification of the Greenwood-Williamson model for the contact of rough surfaces. *Wear* 154(1), pp. 115–124.

Hardy, C., Baronet, C.N. and Tordion, G. V 1971. The elasto-plastic indentation of a half-space by a rigid sphere. *International Journal for Numerical Methods in Engineering* 3(4), pp. 451–462.

Hardy, W.B. and Doubleday, I. 1922. Boundary lubrication. The paraffin series. *Proceedings of the Royal Society of London. Series A* 100(707), pp. 550–574.

Hertz, H. 1882. On the contact of elastic solids. *J. reine angew. Math* 92, pp. 156–171.

Hill, R., Storakers, B. and Zdunek, A.B. 1989. A theoretical study of the Brinell hardness test. *Proceedings of the Royal Society A: Mathematical, Physical and Engineering Sciences* 423, pp. 301–330.

Höhn, B.R. and Michaelis, K. 2004. Influence of oil temperature on gear failures. *Tribology International* 37(2), pp. 103–109.

Höhn, B.R., Oster, P. and Emmert, S. 1996. Micropitting in Case-Carburized Gears-FZG Micro-pitting Test. *Proceedings of International Conference on Gears* 1230, pp. 331–344.

Holmes, M.J.A., Evans, H.P., Hughes, T.G. and Snidle, R.W. 2003a. Transient elastohydrodynamic point contact analysis using a new coupled differential deflection method Part 1 : theory and validation. *Proceedings of the Institution of Mechanical Engineers, Part J: Journal of Engineering Tribology* 217, pp. 289–303.

Holmes, M.J.A., Evans, H.P., Hughes, T.G. and Snidle, R.W. 2003b. Transient elastohydrodynamic point contact analysis using a new coupled differential deflection method Part 2 : results. *Proceedings of the Institution of Mechanical Engineers, Part J: Journal of Engineering Tribology* 217, pp. 305–321.

Holmes, M.J.A., Evans, H.P. and Snidle, R.W. 2005. Analysis of Mixed Lubrication Effects in Simulated Gear Tooth Contacts. *Journal of Tribology* 127(1), p. 61.

Horng, J.H. 1998. An Elliptic Elastic-Plastic Asperity Microcontact Model for Rough Surfaces. *Journal of Tribology* 120(1), pp. 82–88.

Horng, J.H., Len, M.L. and Lee, J.S. 2002. The contact characteristics of rough surfaces in line contact during running-in process. *Wear* 253(9-10), pp. 899–913.

Hu, Y.Z., Barber, G.C. and D, Z. 1999. Numerical Analysis for the Elastic Contact of Real Rough Surfaces. *Tribology Transactions* 42(3), pp. 443–452.

Hu, Y.Z. and Tonder, K. 1992. Simulation of 3-D random rough surface by 2-D digital filter and Fourier analysis. *International Journal of Machine Tools and Manufacture* 32(1-2), pp. 83–90.

Hu, Y.Z. and Zhu, D. 2000. A full numerical solution to the mixed lubrication in point contacts. *Journal of Tribology* 122(January), pp. 1–9.

Hutchings, I.M. 2003. *Tribology: Friction and Wear of Engineering Materials*. Oxford: Butterworth-Heinemann.

Hyun, S., Pei, L., Molinari, J.F. and Robbins, M.O. 2004. Finite-element analysis of contact between elastic self-affine surfaces. *Physical Review E* 70(2), p. 026117.

Ioannides, E. and Harris, T.A. 1985. A new fatigue life model for rolling bearings. *Journal of Tribology* 107(84), pp. 367–377.

Ishlinksky, A.J. 1944. The axi-symmetrical problem in plasticity and the Brinell test. *PMM* 8, p. 201.

Ismail, R., Tauviqirrahman, M., Jamari and Schipper, D.J. 2010. Two-Dimensional Finite Element Analysis on Running-in of Elastic-Plastic Rolling Contact. In: *AIP Conference Proceedings*. pp. 190–193.

Jackson, R.L., Chusoipin, I. and Green, I. 2005. A Finite Element Study of the Residual Stress and Deformation in Hemispherical Contacts. *Journal of Tribology* 127(3), pp. 484–493.

Jackson, R.L., Duvvuru, R., Meghani, H. and Mahajan, M. 2007. An analysis of elasto-plastic sliding spherical asperity interaction. *Wear* 262, pp. 210–219.

Jackson, R.L. and Green, I. 2005. A Finite Element Study of Elasto-Plastic Hemispherical Contact Against a Rigid Flat. *Journal of Tribology* 127(2), pp. 343–354.

Jackson, R.L. and Green, I. 2006. A statistical model of elasto-plastic asperity contact between rough surfaces. *Tribology International* 39(9), pp. 906–914.

Jackson, R.L. and Green, I. 2007. Discussion: "Experimental investigtion of fully plastic contact of a sphere against a hard flat" (Jamari, J, and Schipper, D. J., 2006, ASME J. Tribol., 128, pp. 230-235). *Journal of Tribology* 129, p. 700.

Jackson, R.L. and Green, I. 2011. On the Modeling of Elastic Contact between Rough Surfaces. *Tribology Transactions* 54(2), pp. 300–314.

Jackson, R.L., Krithivasan, V. and Wilson, W.E. 2008. The pressure to cause complete contact between elastic–plastic sinusoidal surfaces. *Proceedings of the Institution of Mechanical Engineers, Part J: Journal of Engineering Tribology* 222(7), pp. 857–863.

Jamari, J., de Rooij, M.B. and Schipper, D.J. 2007. Plastic Deterministic Contact of Rough Surfaces. *Journal of Tribology* 129(4), p. 957.

Jamari, J. and Schipper, D.J. 2006a. An elastic–plastic contact model of ellipsoid bodies. *Tribology Letters* 21(3), pp. 262–271.

Jamari, J. and Schipper, D.J. 2007a. Deformation due to contact between a rough surface and a smooth ball. *Wear* 262(1-2), pp. 138–145.

Jamari, J. and Schipper, D.J. 2008. Deterministic repeated contact of rough surfaces. *Wear* 264(3-4), pp. 349–358.

Jamari, J. and Schipper, D.J. 2006b. Experimental investigation of fully plastic contact of a sphere against a hard flat. *Journal of Tribology* 128(2), pp. 230–235.

Jamari, J. and Schipper, D.J. 2007b. Plastic deformation and contact area of an elastic-plastic contact of ellipsoid bodies after unloading. *Tribology International* 40(8), pp. 1311–1318.

James, S.R. 1989. Hominid Use of Fire in the Lower and Middle Pleistocene: A Review of the Evidence. *Current Anthropology* 30(1), pp. 1–26.

Jeng, Y.R., Lin, Z.W. and Shyu, S.H. 2004. Changes of Surface Topography During Running-In Process. *Journal of Tribology* 126(3), p. 620.

Jiang, X., Hua, D.Y., Cheng, H.S., Ai, X. and Lee, S.C. 1999. A mixed elastohydrodynamic lubrication model with asperity contact. *Journal of Tribology* 121, pp. 481–491.

Johnson, K.L. 1968. An experimental determination of the contact stresses between plastically deformed cylinders and spheres. In: Heyman, J. and Leckie, F. A. eds. *Engineering Plasticity*. Cambridge: Cambridge University Press.

Johnson, K.L. 1985. *Contact Mechanics*. Cambridge: Cambridge University Press.

Johnson, K.L. 1995. Contact mechanics and the wear of metals. *Wear* 190, pp. 162–170.

Johnson, K.L., Greenwood, J.A. and Higginson, J.G. 1985. The contact of elastic regular wavy surfaces. *International Journal of Mechanical Sciences* 27(6), pp. 383–396.

Jost, P.H. 1966. *Lubrication (Tribology) Education and Research. A Report on the Present Position and Industry Needs*. London.

Kadin, Y., Kligerman, Y. and Etsion, I. 2006. Multiple loading–unloading of an elastic–plastic spherical contact. *International Journal of Solids and Structures* 43, pp. 7119–7127.

Kadin, Y., Kligerman, Y. and Etsion, I. 2006. Unloading an elastic–plastic contact of rough surfaces. *Journal of the Mechanics and Physics of Solids* 54(12), pp. 2652–2674.

Karami, G., Evans, H.P. and Snidle, R.W. 1987. Elastohydrodynamic lubrication of circumferentially finished rollers having sinusoidal roughness. *Proceedings of the Institution of Mechanical Engineers, Part C: Journal of Mechanical Engineering Science* 201(1), pp. 29–36.

Kim, T.W., Bhushan, B. and Cho, Y.J. 2006. The contact behavior of elastic/plastic non-Gaussian rough surfaces. *Tribology Letters* 22(1), pp. 1–13.

Kingsbury, A. 1914. U.S. Patent No. 1,117,504.

Kogut, L. and Etsion, I. 2003. A finite element based elastic-plastic model for the contact of rough surfaces. *Tribology Transactions* 46(3), pp. 383–390.

Kogut, L. and Etsion, I. 2002. Elastic-Plastic Contact Analysis of a Sphere and a Rigid Flat. *Journal of Applied Mechanics* 69(5), p. 657.

Komvopoulos, K. and Choi, D. 1992. Elastic finite element analysis of multi-asperity contacts. *Journal of Tribology* 114, pp. 823–831.

Kral, E.R., Komvopoulos, K. and Bogy, D.B. 1993. Elastic-Plastic Finite Element Analysis of Repeated Indentation of a Half-Space by a Rigid Sphere. *Journal of Applied Mechanics* 60, p. 829.

Kral, E.R., Komvopoulos, K. and Bogy, D.B. 1995a. Finite Element Analysis of Repeated Indentation of an Elastic-Plastic Layered Medium by a Rigid Sphere, Part I: Surface Results. *Journal of Applied Mechanics* 62, pp. 20–28.

Kral, E.R., Komvopoulos, K. and Bogy, D.B. 1995b. Finite Element Analysis of Repeated Indentation of an Elastic-Plastic Layered Medium by a Rigid Sphere, Part II: Subsurface Results. *Journal of Applied Mechanics* 62, pp. 29–42.

Krithivasan, V. and Jackson, R.L. 2007. An analysis of three-dimensional elasto-plastic sinusoidal contact. *Tribology Letters* 27(1), pp. 31–43.

Kucharski, S., Klimczak, T., Polijaniuk, A. and Kaczmarek, J. 1994. Finite-elements model for the contact of rough surfaces. *Wear* 177, pp. 1–13.

Kulkarni, S.M., Hahn, G.T., Rubin, C.A. and Bhargava, V. 1991. Elasto-Plastic Finite Element Analysis of Three-Dimensional Pure Rolling Contact Above the Shakedown Limit. *Journal of Applied Mechanics* 58, pp. 347–353.

Kulkarni, S.M., Hahn, G.T., Rubin, C.A. and Bhargava, V. 1990. Elastoplastic Finite Element Analysis of Three-Dimensional, Pure Rolling Contact at the Shakedown Limit. *Journal of Applied Mechanics* 57, pp. 57–65.

Lainé, E., Olver, A. V and Beveridge, T.A. 2008. Effect of lubricants on micropitting and wear. *Tribology International* 41(11), pp. 1049–1055.

Larsson, J., Biwa, S. and Storåkers, B. 1999. Inelastic flattening of rough surfaces. *Mechanics of Materialsaterials* 31, pp. 29–41.

Lee, C.H. and Kobayashi, S. 1970. Elastoplastic analysis of plane-strain and axisymmetric flat punch indentation by the finite-element method. *International Journal of Mechanical Sciences* 12(4), pp. 349–370.

Lee, C.H., Masaki, S. and Kobayashi, S. 1972. Analysis of ball indentation. *International Journal of Mechanical Sciences* 14, pp. 417–426.

Liang, X., Kaiyuan, J., Yongqing, J. and Darong, C. 1993. Variations in Contact Stress Distribution of Real Rough Surfaces During Running-In. *Journal of Tribology* 115(4), p. 602.

Lin, F. and Tseng, A. 1998. A finite element analysis of elasto-plastic contact problems in metal forming. *Materials and Design* 19, pp. 99–108.

Lin, L.P. and Lin, J.F. 2006. A New Method for Elastic-Plastic Contact Analysis of a Deformable Sphere and a Rigid Flat. *Journal of Tribology* 128(2), pp. 221–229.

Lin, L.P. and Lin, J.F. 2007. An Elliptical Elastic-Plastic Microcontact Model Developed for an Ellipsoid in Contact With a Smooth Rigid Flat. *Journal of Tribology* 129(4), pp. 772–782.

Liu, G., Zhu, J., Yu, L. and Wang, Q.J. 2001. Elasto-Plastic Contact of Rough Surfaces. *Tribology Transactions* 44(3), pp. 437–443.

Liu, S., Wang, Q. and Liu, G. 2000. A versatile method of discrete convolution and FFT (DC-FFT) for contact analyses. *Wear* 243, pp. 101–111.

Lo, C.C. 1969. Elastic contact of rough cylinders. *International Journal of Mechanical Sciences* 11(1), pp. 105–115.

Lode, W. 1926. Versuche über den Einfluß der mittleren Hauptspannung auf das Fließen der Metalle Eisen, Kupfer und Nickel. *Zeitschrift für Physik* 36, pp. 913–939.

Lugt, P.M. and Morales-Espejel, G.E. 2011. A review of elasto-hydrodynamic lubrication theory. *Tribology Transactions* 54(3), pp. 470–496.

Majumdar, A. and Bhushan, B. 1991. Fractal model of elastic-plastic contact between rough surfaces. *Journal of Tribology* 113, pp. 1–11.

Majumdar, A. and Bhushan, B. 1990. Role of Fractal Geometry in Roughness Characterization and Contact Mechanics of Surfaces. *Journal ofTribology* 112, pp. 205–216.

Manners, W. 2008. Plastic deformation of a sinusoidal surface. *Wear* 264(1-2), pp. 60–68.

McCool, J. 1986. Comparison of model for the contact of rough surfaces. *Wear* 107(1), pp. 37–60.

McCool, J. 2000. Extending the capability of the Greenwood Williamson microcontact model. *Journal of Tribology* 122, pp. 496–502.

Meheux, M., Minfray, C., Ville, F., Mogne, T.L., Lubrecht, A.A., Martin, J.M., Lieurade, H.P. and Thoquenne, G. 2010. Effect of lubricant additives in rolling contact fatigue. *Proceedings of the Institution of Mechanical Engineers, Part J: Journal of Engineering Tribology* 224, pp. 947–955.

Mendelson, A. 1968. *Plasticity: Theory and Application*. New York: The Macmillan Company.

Merritt, H. 1935. Worm gear performance. *Proceedings of the Institution of Mechanical Engineers*, pp. 127–194.

Merwin, J.E. and Johnson, K.L. 1963. An analysis of plastic deformation in rolling contact. *Proceedings of the Institution of Mechanical Engineers* 177(25), pp. 676–690.

Mesarovic, S.D. and Fleck, N.A. 2000. Frictionless indentation of dissimilar elastic–plastic spheres. *International Journal of Solids and Structures* 37, pp. 7071–7091.

Mesarovic, S.D. and Fleck, N.A. 1999. Spherical indentation of elastic-plastic solids. *Proceedings of the Royal Society A: Mathematical, Physical and Engineering Sciences* 455, pp. 2707–2728.

Meyers, M.A. and Chawla, K.K. 2009. *Mechanical behavior of materials*. 2nd ed. Cambridge; New York: Cambridge University Press.

Michell, A.G.M. 1950. *Lubrication: its principles and practice*. Blackie.

Mihailidis, A., Bakolas, V. and Drivakos, N. 2001. Subsurface stress field of a dry line contact. *Wear* 249(7), pp. 546–556.

Mikic, B.B. 1974. Thermal contact resistance; theoretical considerations. *International Journal of Heat and Mass Transfer* 17(2), pp. 205–214.

Miller, G.R., Keer, L.M. and Cheng, H.S. 1985. On the Mechanics of Fatigue Crack Growth Due to Contact Loading. *Proceedings of the Royal Society A: Mathematical, Physical and Engineering Sciences* 397(1813), pp. 197–209.

Von Mises, R. 1913. Mechanik der festen Körper im plastisch deformablen Zustand. *Göttin. Nachr. Math. Phys.* 1, pp. 582–592.

Moorthy, V. and Shaw, B.A. 2013. An observation on the initiation of micro-pitting damage in as-ground and coated gears during contact fatigue. *Wear* 297(1-2), pp. 878–884.

Mulvihill, D.M., Kartal, M.E., Nowell, D. and Hills, D.A. 2011. An elastic–plastic asperity interaction model for sliding friction. *Tribology International* 44, pp. 1679–1694.

Nowell, D. and Hills, D.A. 1989. Hertzian contact of ground surfaces. *Journal of Tribology* 111, pp. 175–179.

O'Connor, B. 2005. The influence of additive chemistry on micropitting. *Gear Technology*, pp. 34–41.

Oila, A. and Bull, S.J. 2005. Assessment of the factors influencing micropitting in rolling/sliding contacts. *Wear* 258(10), pp. 1510–1524.

Oila, A., Shaw, B.A., Aylott, C.J. and Bull, S.J. 2005. Martensite decay in micropitted gears. *Proceedings of the Institution of Mechanical Engineers, Part J: Journal of Engineering Tribology* 219(2), pp. 77–83.

Olshevskiy, A., Yang, H.I. and Kim, C.W. 2012. Finite element simulation of inelastic contact for arbitrarily shaped rough bodies. *Proceedings of the Institution of Mechanical Engineers, Part C: Journal of Mechanical Engineering Science* 226(3), pp. 595–606.

Olver, A. V 2005. The Mechanism of Rolling Contact Fatigue: An Update. *Proceedings of the Institution of Mechanical Engineers, Part J: Journal of Engineering Tribology* 219(5), pp. 313–330.

Olver, A. V, Tiew, L.K., Medina, S. and Choo, J.W. 2004. Direct observations of a micropit in an elastohydrodynamic contact. *Wear* 256(1-2), pp. 168–175.

Onions, R.A. and Archard, J.F. 1974. Pitting of gears and discs. *Proceedings of the Institution of Mechanical Engineers* 188, pp. 673–682.

Onions, R.A. and Archard, J.F. 1973. The contact of surfaces having a random structure. *Journal of Physics D: Applied Physics* 6(3), pp. 289–304.

Ovcharenko, A., Halperin, G., Verberne, G. and Etsion, I. 2007. In situ investigation of the contact area in elastic-plastic spherical contact during loading-unloading. *Tribology Letters* 25(2), pp. 153–160.

Patching, M.J. 1994. The effect of surface roughness on the micro-elastohydrodynamic lubrication and scuffing performance of aerospace gear tooth contacts. University of Wales College of Cardiff.

Patir, N. 1978. A numerical procedure for random generation of rough surfaces. *Wear* 47(2), pp. 263–277.

Pei, L., Hyun, S., Molinari, J.F. and Robbins, M.O. 2005. Finite element modeling of elasto-plastic contact between rough surfaces. *Journal of the Mechanics and Physics of Solids* 53(11), pp. 2385–2409.

Petrov, N. 1883. Friction in Machines and the Effect of the Lubricant. *Inzh. Zh., St. Peterb* 1, pp. 71–140.

Poon, C.Y. and Sayles, R.S. 1994a. Contact Analysis of a Smooth Ball on an Anisotropic Rough Surface. *Journal of Tribology* 116, pp. 850–859.

Poon, C.Y. and Sayles, R.S. 1994b. Numerical Contact Model of a Smooth Ball on an Anisotropic Rough Surface. *Journal of Tribology* 116, pp. 194–201.

Pullen, J. and Williamson, J.B.P. 1972. On the Plastic Contact of Rough Surfaces. *Proceedings of the Royal Society A: Mathematical, Physical and Engineering Sciences* 327(1569), pp. 159–173.

Reynolds, O. 1886. On the Theory of Lubrication and Its Application to Mr. Beauchamp Tower's Experiments, Including an Experimental Determination of the Viscosity of Olive Oil. *Proceedings of the Royal Society of …* 177, pp. 157–234.

Ros, M. and Eichinger, A. 1929. Versuche zur klaerung der frage der bruchefhar III, mettalle, eidgenoss. *Material pruf. Und Versuchsantalt Industriell Bauwek und Geerbe, Diskussionsbericht* 34, pp. 3–59.

Sabelkin, V. and Mall, S. 2007. Elastic–Plastic Multi-Asperity Contact Analysis of Cylinder-on-Flat Configuration. *Journal of Tribology* 129(2), p. 292.

Seabra, J. and Berthe, D. 1987. Influence of surface waviness and roughness on the normal pressure distribution in the Hertzian contact. *Journal of Tribology* 109, pp. 462–469.

Shankar, S. and Mayuram, M.M. 2008a. A Finite Element Based Study on the Elastic-Plastic Transition Behavior in a Hemisphere in Contact With a Rigid Flat. *Journal of Tribology* 130(4), p. 044502.

Shankar, S. and Mayuram, M.M. 2008b. Effect of strain hardening in elastic–plastic transition behavior in a hemisphere in contact with a rigid flat. *International Journal of Solids and Structures* 45(10), pp. 3009–3020.

Sinclair, G.B., Follansbee, P.S. and Johnson, K.L. 1985. Quasi-static normal indentation of an elasto-plastic half-space by a rigid sphere - II. Results. *International Journal of Solids and Structures* 21(8), pp. 865–888.

Snidle, R.W. and Evans, H.P. 1994. A simple method of elastic contact simulation. *Proceedings of the Institution of Mechanical Engineers, Part J: Journal of Engineering Tribology* 208, pp. 291–293.

Snidle, R.W. and Evans, H.P. 2009. Some aspects of gear tribology. *Proceedings of the Institution of Mechanical Engineers, Part C: Journal of Mechanical Engineering Science* 223(1), pp. 103–141.

Snidle, R.W., Rossides, S.D. and Dyson, A. 1984. The failure of elastohydrodynamic lubrication. *Proceedings of the Royal Society of London, Series A: Mathematical and Physical Sciences* 395(1809), pp. 291–311.

Sommerfeld, A. 1904. Zur hydrodynamischen theorie der Schmiermittelreibung. *Z. Math. Phys* 50, pp. 97–155.

Stanley, H.M. and Kato, T. 1997. An FFT-based method for rough surface contact. *Journal of Tribology* 119, pp. 481–485.

Sundaram, N. and Farris, T.N. 2009. Multiple Contacts of Similar Elastic Materials. *Journal of Tribology* 131(2), p. 021405.

Swahn, H., Becker, P.C. and Vingsbo, O. 1976. Martensite decay during rolling contact fatigue in ball bearings. *Metallurgical Transactions A* 7(8), pp. 1099–1110.

Tabor, D. 1951. *The Hardness of Metals*. Oxford: Oxford University Press Inc.

Taljat, B. and Pharr, G.M. 2004. Development of pile-up during spherical indentation of elastic–plastic solids. *International Journal of Solids and Structures* 41(14), pp. 3891–3904.

Tao, J., Hughes, T.G., Evans, H.P., Snidle, R.W., Hopkinson, N.A., Talks, M. and Starbuck, J.M. 2003. Elastohydrodynamic Lubrication Analysis of Gear Tooth Surfaces From Micropitting Tests. *Journal of Tribology* 125(2), p. 267.

Taylor, G.I. and Quinney, H. 1931. The Plastic Distortion of Metals. *Philosophical Transactions of the Royal Society A: Mathematical, Physical and Engineering Sciences* 230, pp. 323–362.

Teer, D.G. and Arnell, R.D. 1975a. Friction Theories. In: Halling, J. ed. *Principles of Tribology*. London and Basingstoke: The Macmillan Press Ltd., pp. 72–93.

Teer, D.G. and Arnell, R.D. 1975b. Wear. In: Halling, J. ed. *Principles of Tribology*. London and Basingstoke: The Macmillan Press Ltd., pp. 94–127.

Tian, H. and Saka, N. 1991. Finite element analysis of an elastic-plastic two-layer half-space: normal contact. *Wear* 148, pp. 47–68.

Tower, B. 1883. First report on friction experiments. *Proceedings of the Institution of Mechanical Engineers* 34, pp. 632–659.

Tower, B. 1885. Research Committee on Friction Second Report on Friction Experiments. *Proceedings of the Institution of Mechanical Engineers* 36, pp. 58–70.

Townsend, D.P., Zaretsky, E. V and Scibbe, H.W. 1986. Lubricant and additive effects on spur gear fatigue life. *Journal of Tribology* 108, pp. 468–475.

Tresca, H. 1864. Mémoire sur l'écoulement des corps solides soumis à de fortes pressions. *C.R. Acad. Sci. Paris* 59, p. 754.

Tripp, J.H., Van Kuilenburg, J., Morales-Espejel, G.E. and Lugt, P.M. 2003. Frequency response functions and rough surface stress analysis. *Tribology Transactions* 46(3), pp. 376–382.

Vergne, P., Villechaise, B. and Berthe, D. 1985. Elastic behavior of multiple contacts: asperity interaction. *Journal of Tribology* 107, pp. 224–228.

Vijaywargiya, R. and Green, I. 2007. A finite element study of the deformations, forces, stress formations, and energy losses in sliding cylindrical contacts. *International Journal of Non-Linear Mechanics* 42(7), pp. 914–927.

Wang, F. and Keer, L.M. 2005. Numerical Simulation for Three Dimensional Elastic-Plastic Contact With Hardening Behavior. *Journal of Tribology* 127, pp. 494–502.

Wang, F.S., Block, J.M., Chen, W.W., Martini, A., Zhou, K., Keer, L.M. and Wang, Q.J. 2009. A Multilevel Model for Elastic-Plastic Contact Between a Sphere and a Flat Rough Surface. *Journal of Tribology* 131(2), p. 021409.

Wang, Z.J., Wang, W.Z., Hu, Y.Z. and Wang, H. 2010. A Numerical Elastic-Plastic Contact Model for Rough Surfaces. *Tribology Transactions* 53, pp. 224–238.

Warren, T. and Krajcinovic, D. 1996. Random cantor set models for the elastic-perfectly plastic contact of rough surfaces. *Wear* 196, pp. 1–15.

Way, S. 1935. Pitting due to rolling contact. *Journal of Applied Mechanics* 2(2), pp. 49–58.

Webster, M.N. and Sayles, R.S. 1986. A Numerical Model for the Elastic Frictionless Contact of Real Rough Surfaces. *Journal of Tribology* 108(3), p. 314.

Westergaard, H.M. 1939. Bearing pressures and cracks. *Journal of Applied Mechanics* 6, pp. 49–53.

Whitehouse, D.J. and Archard, J.F. 1970. The properties of random surfaces of significance in their contact. *Proceedings of the Royal Society of London. Series A, Mathematical and Physical Sciences* 316(1524), pp. 97–121.

Whomes, T.L. and Halling, J. 1975. Elastohydrodynamic Lubrication. In: Halling, J. ed. *Principles of Tribology*. London and Basingstoke: The Macmillan Press Ltd., pp. 288–307.

Williams, J.E. 1994. *Engineering Tribology*. Oxford: Oxford University Press Inc.

Williamson, J.B.P. and Hunt, R.T. 1972. Asperity Persistence and the Real Area of Contact Between Rough Surfaces. *Proceedings of the Royal Society A: Mathematical, Physical and Engineering Sciences* 327(1569), pp. 147–157.

Wilson, W.E., Angadi, S.V. and Jackson, R.L. 2010. Surface separation and contact resistance considering sinusoidal elastic-plastic multi-scale rough surface contact. *Wear* 268(1-2), pp. 190–201.

Yamada, K., Takeda, N., Kagami, J. and Naoi, T. 1978. Mechanisms of elastic contact and friction between rough surfaces. *Wear* 48, pp. 15–34.

Yastrebov, V.A., Durand, J., Proudhon, H. and Cailletaud, G. 2011. Rough surface contact analysis by means of the Finite Element Method and of a new reduced model. *Comptes Rendus Mécanique* 339(7-8), pp. 473–490.

Yu, M.M.H. and Bhushan, B. 1996. Contact analysis of three-dimensional rough surfaces under frictionless and frictional contact. *Wear* 200(1-2), pp. 265–280.

Zhao, Y., Maietta, D.M. and Chang, L. 2000. An asperity microcontact model incorporating the transition from elastic deformation to fully plastic flow. *Journal of Tribology* 122, pp. 86–93.

Zhou, R.S., Cheng, H.S. and Mura, T. 1989. Micropitting in rolling and sliding contact under mixed lubrication. *Journal of Tribology* 111, pp. 605–613.

Zhu, D. and Hu, Y. 2001a. Effects of rough surface topography and orientation on the characteristics of EHD and mixed lubrication in both circular and elliptical contacts. *Tribology Transactions* 44(3), pp. 391–398.

Zhu, D. and Hu, Y.Z. 2001b. A computer program package for the prediction of EHL and mixed lubrication characteristics, friction, subsurface stresses and flash temperatures based on measured. *Tribology Transactions* 44(3), pp. 383–390.

Zhu, D. and Hu, Y.Z. 1999. The study of transition from full film elastohydrodynamic to mixed and boundary lubrication. In: Cheng, H. S. ed. *Proc. STLE/ASME: Tribology Surveillance*. pp. 150–156.

Zhu, D., Martini, A., Wang, W., Hu, Y., Lisowsky, B. and Wang, Q.J. 2007. Simulation of Sliding Wear in Mixed Lubrication. *Journal of Tribology* 129(3), p. 544.

Zhuravlev, V.A. 1940. On the question of theoretical justification of the Amontons-Coulomb law for friction of unlubricated surfaces. *Zh. Tekh. Fiz.* 10(17), pp. 1447–1452.

Importing profiles into Abaqus/CAE

A.1. Introduction

In order to simulate the contact of real rough surfaces, measured rough surface profiles must be available within Abaqus. For the user to create these parts using the simple CAD tools available within Abaqus/CAE would be a time consuming and monotonous task. To provide an effective to solution to this task, macros were used in Microsoft Excel to create a Python script that would create a part with the required profile coordinates in Abaqus (Gay 2010).

A.2. User Guide

The solution consists of two files: an Excel workbook, containing embedded macros to write a python script file, and the base python script file itself. The Excel workbook allows the user to specify the profile data, and the Abaqus part dimensions, while the base python file consists of the code that is required for every part creation. It is recommended that a copy of this python file is kept separate, and renamed, for reference and in the event of difficulties. Before opening and using the embedded macro script, the Excel workbook and associated python file(s), must be located on the D drive, in a folder named “talysurf2abaqus” (i.e. D:\talysurf2abaqus\).

A.2.1. In Excel

The excel spreadsheet consists of four sheets: “options”, “results here”, “transform” and “out”. Figure A.1 shows the sheet “results here”, where the required rough surface profile data is to be entered. For the surface roughness to be to-scale, each of the coordinates must be in the same units. In the example shown, both the *x* and *z* coordinates are specified in millimetres. Furthermore, if the profile is still in raw, as measured format, any filtering or smoothing should be performed prior to using the transformation spreadsheet. Column A consists of the *x*-coordinate, while column B consists of the *z*-coordinate, i.e. the profile height. However, it should be noted that the macros do

not use the *x*-coordinates in column A, it is purely for user reference. The macro assumes that the profile starts at *x*=0mm (or other units) in cell B1. The following points are then spaced in the *x*-direction by the "Resolution" input in the "options" sheet.

Figure A.2 shows the sheet "options", where the details of the part to be created in Abaqus are entered. The cells highlighted in yellow show the cells that must be completed by the user. The *x*-coordinate of the start and end of the profile required in Abaqus must be specified in C22 and E22 respectively. It is here in which the *x*-coordinate data becomes useful to the user. If only a portion of the profile data imported to the "results here" sheet is required, then the *x*-coordinate data in column A allows simple selection of the required profile section. As previously stated, the spacing between points in the *x*-direction is defined in C26. Each of these is to be specified in millimetres. In the example shown, the spacing between points is 0.25µm, ranging from 0.0mm to 0.5mm. The remaining box to be filled in by the user is C24. This defines the depth of the part that will be created above the rough surface in the *z*-direction, again, specified in millimetres. In the example shown, the part created will extend 0.5mm beyond the imported rough surface to the part boundary. However, this is relatively unimportant as the part can be modified further once in Abaqus.

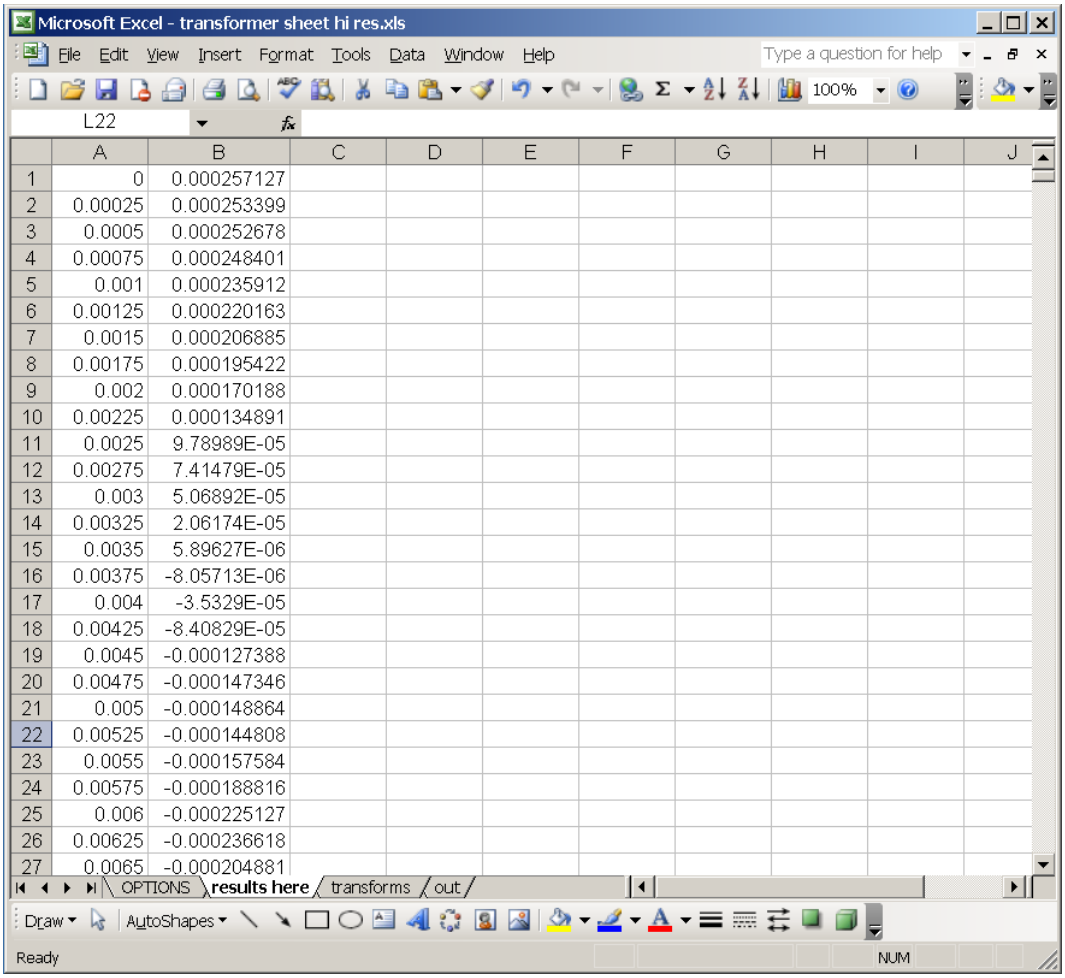

	A	B
1	0	0.000257127
2	0.00025	0.000253399
3	0.0005	0.000252678
4	0.00075	0.000248401
5	0.001	0.000235912
6	0.00125	0.000220163
7	0.0015	0.000206885
8	0.00175	0.000195422
9	0.002	0.000170188
10	0.00225	0.000134891
11	0.0025	9.78989E-05
12	0.00275	7.41479E-05
13	0.003	5.06892E-05
14	0.00325	2.06174E-05
15	0.0035	5.89627E-06
16	0.00375	-8.05713E-06
17	0.004	-3.5329E-05
18	0.00425	-8.40829E-05
19	0.0045	-0.000127388
20	0.00475	-0.000147346
21	0.005	-0.000148864
22	0.00525	-0.000144808
23	0.0055	-0.000157584
24	0.00575	-0.000188816
25	0.006	-0.000225127
26	0.00625	-0.000236618
27	0.0065	-0.000204881

Figure A.1 - Results Sheet.

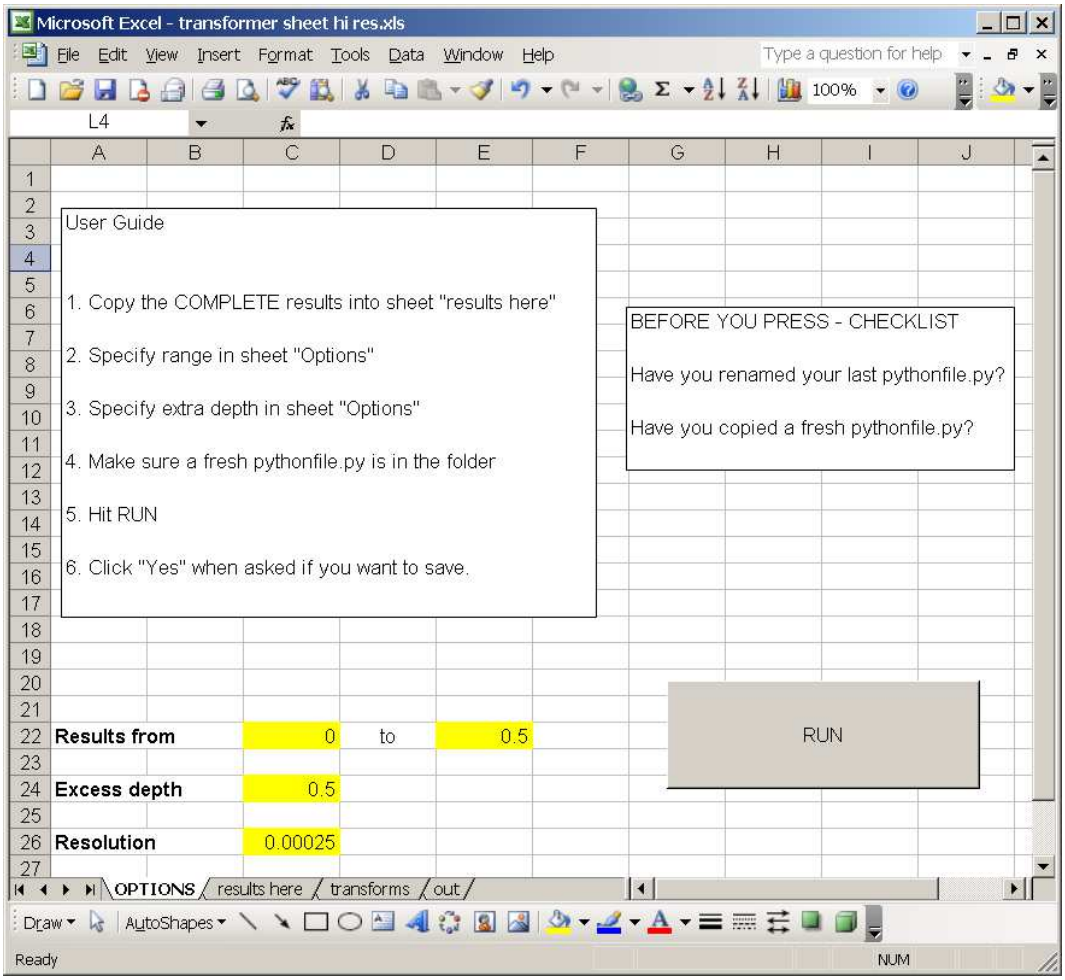

Figure A.2 - Options Sheet.

The sheets “transform” and “out” should be left unchanged by the user unless modifications to the code are to be performed. The “transform” sheet contains the code to transform the specified rough surface profile and part dimensions into the required coordinates for Abaqus. It then uses these coordinates with the required Sketcher command (Abaqus 2010c) to draw straight lines between the points. These commands are then written in the “out” sheet, which consists of the entire part creation command list required to draw a part in Abaqus. This command list is then written to a generically named python scripting file, named python.py. This file contains required initial commands for Abaqus, and overwrites the part creation command lines each time the user clicks the “Run” button in the “options” sheet. Each of these regions is labelled in Figure A.3. It is therefore important to copy and rename the python script file if overwriting subsequently would be

undesirable. For further details on writing script for use with Abaqus, it is recommended that users refer to the Abaqus Scripting User's Manual (Abaqus 2010d).

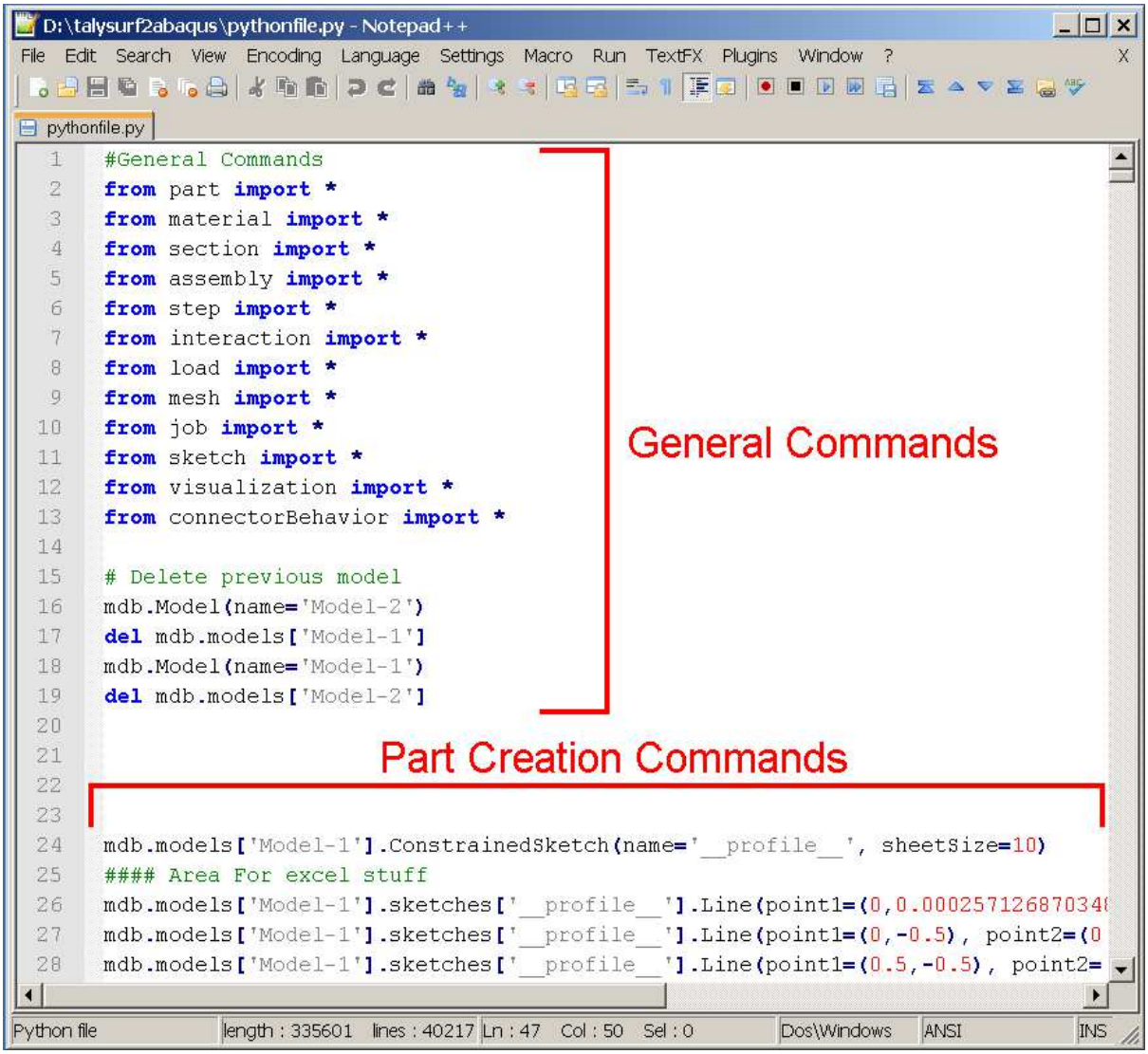

Figure A.3 - Python Script File Layout.

A step by step guide to use the excel workbook is shown in Table A.1.

Table A.1 - Step by step guide to using excel workbook.

1.	Insert profile data in millimetres in sheet “results here”.
2.	Define starting and finishing *x*-coordinate in millimetres for Abaqus part in cells C22 and E22 in sheet “options”. The macros consider cell B1 to be at *x*=0mm.
3.	Define depth of part in millimetres beyond the rough surface in cell C24 in sheet “options”.
4.	Select *x*-direction spacing of inserted profile data in cell C26 in sheet “options”.
5.	Click “Run” in sheet “options”.
6.	Python.py file is updated with new profile data to be run in Abaqus.

A.2.2. In Abaqus

Once the python script file has been created using the macros in the excel workbook, Abaqus/CAE can be opened, and a new model created. Select “File” from the taskbar at the top of the window, and choose the “Run script” option. This will open a separate explorer window that will allow the user to select the previously created python script file (.py file extension). The script will then run and create a 2D deformable part based on the roughness profile and details specified by the user. If necessary, the user can then modify the part as required and proceed with creating a finite element model in Abaqus/CAE in the same way as with any other part.

Publications

Title	Plastic deformation in rough surface line contact - a finite element study
Authors	M.J. Bryant, H.P. Evans, R.W. Snidle
Journal	Tribology International
Year	2012
Volume (Issue)	46(1)
Pages	269-278
Abstract	The paper describes an elastic–plastic finite element (EPFE) analysis of line contact between a cylinder and rigid plane using commercial software. The range of loading demonstrates the transition from purely elastic to fully plastic contact behaviour, revealing the residual deformations and stress fields upon unloading. A multiple contact configuration was analysed in the form of sinusoidal roughness. Results obtained under elastic conditions were validated by comparison with theoretical solutions. This model was extended by replacing the sinusoidal surface with a real roughness profile. Modelling multiple contacts indicates the influence of adjacent surface ‘‘asperities’’ on contact pressure and residual stress distributions.

Title	Predictive modelling of fatigue failure in concentrated lubricated contacts
Authors	H.P. Evans, R.W. Snidle, K.J. Sharif, M.J. Bryant
Journal	Faraday Discussions
Year	2012
Volume (Issue)	156(1)
Pages	105-121
Abstract	Reducing frictional losses in response to the energy agenda will require use of less viscous lubricants causing hydrodynamically-lubricated bearings to operate with thinner films leading to ‘‘mixed lubrication’’ conditions in which a degree of direct interaction occurs between surfaces protected only by boundary tribofilms. The paper considers the consequences of thinner films and mixed lubrication for concentrated contacts such as those occurring between the teeth of power transmission gears and in rolling element bearings. Surface fatigue in gears remains a serious problem in demanding applications, and its solution will become more pressing with the tendency towards thinner oils. The particular form of failure examined here is micropitting, which is identified as a fatigue phenomenon occurring at the scale of the surface roughness asperities. It has emerged recently as a systemic difficulty in the operation of large scale wind turbines where it occurs in both power transmission gears and their support bearings. Predictive physical modelling of these contacts requires a transient mixed lubrication analysis for conditions in which the predicted lubricant film thickness is of the same order or significantly less than the height of surface roughness features. Numerical solvers have therefore been developed which are

cont.	able to deal with situations in which transient solid contacts occur between surface asperity features under realistic engineering conditions. Results of the analysis, which reveal the detailed time-varying behaviour of pressure and film clearance, have been used to predict fatigue and damage accumulation at the scale of surface asperity features with the aim of improving understanding of the micropitting phenomenon. The possible consequences on fatigue of residual stress fields resulting from plastic deformation of surface asperities is also considered.

Title	Dry elasto-plastic contact of nominally flat surfaces
Authors	A.V. Manoylov, M.J. Bryant, H.P. Evans
Journal	Tribology International
Year	2013
Volume (Issue)	*Article in press*
Pages	
Abstract	In mixed lubrication the lubricant film is not sufficiently thick to prevent contact between the working surfaces. As a result, the influence of the surface roughness on the pressure distribution becomes significant with large pressures being generated in the interaction regions of the most prominent surface asperities. In addition the flow of lubricant is obstructed by the asperities and therefore the flow cannot be described by the classical Reynolds equation for smooth surfaces. The flow of lubricant between rough surfaces was studied by e.g. Patir and Cheng, who introduced flow factors to modify the Reynolds equation so as to take roughness effects into account in an averaged way and this approach has been subsequently generalised to incorporate an homogenised Reynolds equation. These methods take account of roughness based on the distribution of gap between the loaded surfaces obtained from a dry contact analysis. This paper presents a method to solve dry contact problems for this purpose in the case of plane surfaces using a simple elastic–plastic model at the asperity contacts and a differential formulation for the elastic deflection, and provides validation for the method in terms of comparison with the results of an elastic–plastic rough surface contact analysis obtained using a finite element analysis.